



**University
of Southampton**

School of Engineering Sciences

A dissertation submitted for the degree of
Doctor of Philosophy

A NUMERICAL STUDY OF INSTABILITY AND VORTEX BREAKDOWN OF SWIRLING FLOW

Dario Amirante

DECEMBER 2007

Abstract

Direct numerical simulations of both axisymmetric and three-dimensional highly swirling flows are conducted to study the vortex breakdown phenomenon and the onset of helical instabilities.

The enduring debate on the physical reasons underlying the breakdown of slender vortices has widely involved theoretical, experimental and computational studies. In the present investigation, we are motivated by the necessity to evaluate the range of applicability of recent studies which have correlated the global response of this class of flows to their local stability characteristics. In synthesis, the dynamics of the unsteady structures developing in swirling flows are explained according to simplified theories which assume the flow to be locally parallel. These results, which might be considered as the natural extension of concepts well established for two-dimensional jets and wakes, appear to be quite surprising if applied to swirling flows in breakdown configuration. In fact, the presence of one or more large regions of recirculating flow (the vortex bubbles) renders the assumption of near parallelism strongly violated.

Inspired by this observation, we have carried out a numerical investigation in order to study the evolution of self-sustained oscillations. For this purpose, a finite difference code has been developed and later adapted to perform linear analysis around a given parallel swirling flow. Successively, a comparative study between the global and local analysis methodologies has been conducted. The novelty of the work is represented by the use of simple filtering techniques which can be implicitly activated if the cylindrical coordinates are employed. These have made possible to focus on the nonlinear evolution of higher order modes. Following this strategy, we have identified an instability mechanism which cannot be explained by the local theory and whose existence is clearly associated with the presence of recirculating flow. The result is considered important since it provides a further contribution to the general understanding of the global modes.

Throughout this thesis we have followed a bottom-up approach in terms of the assumptions undertaken. The general stability properties of swirling flows are initially revisited based on 1D models. The hypothesis of one-dimensionality has been later replaced by that of axisymmetry. Real swirling flows are examined in the final chapter for Reynolds numbers in the range of those generally employed in the physical experiments.

Acknowledgements

First and foremost, I wish to thank my supervisor, Professor Kai H. Luo, for introducing me to computational fluid dynamics, and for giving me the opportunity to work in the field of hydrodynamic stability. I appreciate his constant and careful supervision, his expert advice, the support received at all moments of difficulty and the enthusiasm expressed for every single achievement.

Other people have contributed to my education at the University of Southampton. In particular, I am very thankful to Dr. Richard Sandberg, for all the profitable, endless discussions we have had in his office. I also wish to thank my friends and colleagues, Michele Lombardi, Raul Machado, Ernesto Monaco, Jun Xia, Giuliano Bordignon and Matteo Franchin for the help received in many circumstances and for having made my time in the office more enjoyable.

Finally, my thoughts go to my family and my fiancée Maria Rosa: not a single word of this work would have been possible without their love and support.

1944

1944

1944

1944

1944

Al mio papà

1944

1944

1944

1944

1944

1944

1944

1944

1944

1944

1944

1944

1944

1944

1944

1944

1944

1944

Contents

List of figures	ii
List of tables	x
Nomenclature	xi
1 Literature review	1
1.1 Introduction	1
1.2 Vortex breakdown	2
1.3 Physical mechanisms of vortex instability	8
1.4 Concepts of linear analysis	9
1.5 Present research	13
2 Numerical method	16
2.1 Governing equations	16
2.1.1 Navier-Stokes equations in cylindrical coordinates	16
2.1.2 Linearised Navier-Stokes around a 1D base flow	18
2.2 Spatial discretisation	21
2.2.1 Non-homogeneous directions	21
2.2.2 Homogeneous directions	25
2.3 Time advancement	28
2.3.1 Explicit method	28
2.3.2 Dual Time Stepping	34
2.4 Boundary conditions	36
2.5 Axis treatment	41
2.6 Coordinates transformation	45
3 Vortex core dynamics	49
3.1 The Batchelor vortex	49
3.1.1 Formulation and diagnostic tools	49
3.1.2 Validation: results at $Re=667$, $q=0.8$	53
3.1.3 Effect of the swirl	58
3.2 Kelvin waves	64

3.2.1	Linear analysis	65
3.2.2	The bulging mode	69
3.2.3	Vorticity considerations	76
3.2.4	The critical state	79
3.2.5	The bending modes	81
3.3	Kelvin-Helmholtz instabilities	83
3.3.1	Formulation	83
3.3.2	Analytical results	85
3.3.3	Numerical results	89
4	Axisymmetric vortex breakdown	92
4.1	Problem formulation	92
4.2	Physical observations	95
4.3	Effect of the swirl	99
4.4	Effect of Reynolds number	103
4.5	Bifurcation diagram	106
4.6	Effect of the coflow	109
4.7	Testing a simple criterion	110
5	Three-dimensional direct numerical simulations	115
5.1	Results at $Re=200$	115
5.1.1	Helical vortex breakdown	115
5.1.2	Double-helical vortex breakdown	121
5.1.3	Local stability analysis	127
5.1.4	Response to controlled perturbations	133
5.2	Results at $Re=400$	139
5.2.1	Spatial DNS	139
5.2.2	Wave packet analysis	144
5.3	Results at $Re=800$	148
5.3.1	Evolution from a columnar vortex	148
5.3.2	Evolution from the axisymmetric breakdown state	155
5.3.3	Wave packet analysis	161
5.4	Higher wavenumber structures	164
5.5	Vortex breakdown in a constricted pipe	168
5.6	Effect of compressibility	171
	Conclusions	173
	Future work	176
	Bibliography	179

List of Figures

1.1	Experimental observation of an axisymmetric bubble followed by spiral breakdown. From the gallery of fluid mechanics, Cambridge University.	3
1.2	Typical bifurcation diagrams of an axisymmetric swirling flow.	4
1.3	Production of axial circulation gradient due to the radial flow divergence in an axisymmetric swirling flow with $dL/dr > 0$	6
1.4	Schematic representation of the impulse response of an unstable medium. Left: convective instability. Right: absolute instability.	11
2.1	Butterfly algorithm of the Fast Fourier Transform.	25
2.2	Stability region of the Runge-Kutta 4-th order scheme, visualised by isocontour of the amplification factor $ \dot{z} $ for $ \dot{z} = 1, 2, \dots, 10$. Blue regions are the most damped.	29
2.3	Fourier symbol obtained keeping constant the values $CFL_{zr}^{(2)} = 0.3, CFL_{\theta}^{(1)} = 0.4, CFL_{\theta}^{(2)} = 0.1$, and increasing the $CFL_{zr}^{(1)}$ from 0.4 (blue curve) to 0.9 (red curve). The linear stability is lost because some frequencies lie outside the stability region of the Runge Kutta 4-th order.	30
2.4	Plot of the modified phase vs the real phase for first derivatives approximations: spectral method (black curve), sixth-order compact method (red curve) and second-order central differences (blue curve).	31
2.5	Fourier symbol $ \dot{z}^{(1)} + \dot{z}^{(2)} $ calculated for $CFL^{(1)} = 0.5, CFL^{(2)} = 0.05$ (green curve), $CFL^{(1)} = 0.6, CFL^{(2)} = 0.1$ (blue curve) and $CFL^{(1)} = 0.8, CFL^{(2)} = 0.2$ (red curve).	32
2.6	Boundary type definition.	39
3.1	Axial velocity profile of the Batchelor vortex, corresponding to equation (3.2) with (a): $a = 0$ (jet) and (b): $a = -1.2$ (wake).	50
3.2	Response of the perturbed Batchelor vortex at $Re=667, q = 0.8, a = 0$. Isosurfaces of radial velocity component at Time=30. $V_r = \pm 0.0002$. The arrow V_z indicates the direction of the base flow.	53

3.3	Response of the perturbed Batchelor vortex at $Re=667$ $q = 0.8, a = 0$. Cross sectional contours of radial velocity component at $z = 19$ and different times. Contours levels are in the range $[-0.0008,+0.0007]$	53
3.4	Temporal stability properties of the Batchelor vortex at $Re=667, q = 0.8, a = 0$, retrieved by LTS. (a): Temporal growth rate $\omega_i(k)$. (b): Real part of the frequency $\omega_r(k)$	55
3.5	Response of the perturbed Batchelor vortex at $Re=667, q = 0.8, a = 0$. Time evolution of the amplitude A associated with different Fourier pairs (m, k) . Top: $m = +3$. Bottom: $m = -3$	56
3.6	Numerical comparisons of growth rate measured by LTS. (a): Grid convergence: the default resolution (black) of table 3.1 vs the higher resolution case (red) reported in the text. (b): Different axis treatments: default method based on the spectral reconstruction on the axis (black) vs the method using a staggered grid (red).	57
3.7	Temporal growth rate ω_i retrieved by LTS for the Batchelor vortex at $Re=667, a = 0$ and different swirl levels. (a): Non-rotating jet $q = 0$ (b): $q = 0.2$ (c): $q = 0.4$ (d): $q = 1$ (e): $q = 1.2$ (f): $q = 1.4$	59
3.8	Effect of the swirl on the temporal growth rate ω_i of negative azimuthal modes. (a): $m = -1$ (b): $m = -2$ (c): $m = -3$ (d): $m = -4$	60
3.9	Representation of the sloped plane where the centrifugal instability occurs for the Batchelor vortex in jet configuration. \mathbf{k} is the wave vector.	61
3.10	Temporal stability characteristics of the Batchelor vortex at $Re=667, q = 0.8, a = -1.2$ modified changing the sign of V_z in the first of (3.2). (a): Temporal growth rate $\omega_i(k)$ of positive azimuthal modes (black curve). For comparison, the red curve is the one of fig. 3.4, pertaining to the negative modes for the jet-like profile with $a = 0$. (b): Real part of the frequency $\omega_r(k)$	62
3.11	Response of the perturbed Batchelor vortex at $Re=667, q = 0.8, a = -1.2$ modified changing the sign of V_z in the first of (3.2). Isosurfaces of radial velocity component at Time=30. $V_r = \pm 0.0002$. The arrow V_z indicates the direction of the base flow.	63
3.12	Complex frequency plane: line intersections between red and green curves represent solutions of the dispersion relation (3.34) with $k = 2, m = 0$	68
3.13	Axisymmetric Kelvin modes sustained by the pure Rankine vortex. (a): Dispersion diagram. (b): Normalised eigenfunctions of the axial velocity perturbation corresponding to the first 4 modes, at $k = 3/2$	69
3.14	Response of the perturbed Rankine vortex at $Re=500$, excited by an axisymmetric perturbation with wavenumber $k = 2\pi$. Contours of azimuthal vorticity revealing the propagation of waves within the vortex core.	71

3.15	Response of the perturbed Rankine vortex at $Re=500$, excited by an axisymmetric perturbation with wavenumber $k = 2\pi$. Evolution of the axial distribution of azimuthal vorticity at different radial locations within the vortex core.	72
3.16	Response of the perturbed Rankine vortex at $Re=500$, excited by an axisymmetric perturbation with wavenumber $k = 2\pi$ (dash) and $k = \pi$ (solid). Radial velocity registered in the center of the vortex tube at $r = 0.3$	73
3.17	Effect of the Reynolds number on the response of the Rankine vortex excited by an axisymmetric perturbation with wavenumber $k = 2\pi$. Contours of azimuthal vorticity at $Time=7.76$	74
3.18	Response of the perturbed Rankine vortex. Normalised eigenfunction computed along the ray $\Delta z/\Delta t = 1$. Solid: $\Delta t = 5$. Dash: $\Delta t = 10$. Dash-dots: $\Delta t = 15$. The red curve is the eigenfunction of the initial disturbance, corresponding to $J_0(\gamma_1)$	75
3.19	Effect of the initial perturbation on the response of the perturbed Rankine vortex. Top: Perturbation defined by (3.36). Bottom: Perturbation defined by (3.37). In both cases the excited wavenumber is $k = 2$	75
3.20	Early evolution of the perturbed Rankine vortex; axial distribution of different perturbation quantities within the core. For the azimuthal vorticity, the maximum amplitude is reached at vortex edge; for the axial vorticity (bottom), the maximum amplitude is near the axis. . . .	78
3.21	Axisymmetric Kelvin modes sustained by a swirling flow defined by a Rankine vortex superimposed on an uniform axial flow field. $S = 1$	80
3.22	Bending Kelvin modes sustained by the pure Rankine vortex. Dispersion diagram for (a): $m = +1$ and (b): $m = -1$	81
3.23	Response of the perturbed Rankine vortex, excited by a wavenumbers pair $(m, k) = (1, 2\pi)$. Azimuthal vorticity contours on the meridional plane $\theta = 0$ at $Time=20$	82
3.24	Response of the perturbed Rankine vortex, excited by a wavenumbers pair $(m, k) = (1, 2\pi)$. Iso-surfaces of radial velocity component: $V_r = \pm 0.0004$. $Time=20$	82
3.25	Complex frequency plane: line intersections between red and green curves represent solutions of the dispersion relation (3.55) with $S = 1, k = 2, m = 0$	85
3.26	Temporal stability properties of Kelvin-Helmholtz axisymmetric mode for levels of swirl ratio $S = 0, 0.2, 0.6, 0.8, 1$. (a): Real part of frequency. (b): Imaginary part of frequency. . .	86
3.27	Temporal stability properties of Kelvin-Helmholtz bending mode $m = +1$ for levels of swirl ratio $S = 0.2, 0.4, 0.6, 1$. (a): Real part of frequency. (b): Imaginary part of frequency. . .	86
3.28	Temporal stability properties of Kelvin-Helmholtz bending mode $m = -1$ for levels of swirl $S = 0, 0.2, 0.3, 0.4$. (a): Real part of frequency. (b): Imaginary part of frequency. . .	87
3.29	Temporal stability properties of Kelvin-Helmholtz bending mode $m = -1$ for levels of swirl $S = 0.4, 0.6, 0.8, 1$. (a): Real part of frequency. (b): Imaginary part of frequency. . .	87

3.30	Temporal growth rate of Kelvin-Helmholtz modes (a) $m = -2$ and (b) $m = -5$ for different levels of swirl.	88
3.31	Growth rate of Kelvin-Helmholtz modes $m = -1, -2, -3, -4$ at the level of swirl $S = 1$	89
3.32	Temporal growth rate ω_i retrieved by LTS for the model (3.57) (a): Non-rotating jet $q = 0$ (b): $q = 0.2$ (c): $q = 0.4$ (d): $q = 2$	90
3.33	Effect of the swirl on the temporal growth rate ω_i of negative azimuthal modes for the model (3.57). (a): Axisymmetric mode $m = 0$ (b): $m = -1$ (c): $m = -2$ (d): $m = -3$ (e): $m = -4$ (f): $m = -5$	91
4.1	Velocity profiles corresponding to (4.1). (a): Axial velocity component for $\alpha = 0.5$ (dash) $\alpha = 1$ (solid) $\alpha = 1.2$ (dash dot). (b): Azimuthal velocity component for $S = 0.5$ (dash) $S = 1$ (solid) $S = 1.2$ (dash dot)	94
4.2	Early evolution of the $Re=200$ $S = 0.95$ case. Streamwise evolution at $Time=2$ of (a): azimuthal velocity near the axis, (b): pressure on the axis, (c): axial velocity on the axis, (d): radial velocity near the axis.	96
4.3	$Re=200$ $S = 0.95$ case. Time evolution of azimuthal vorticity. $Time=400$ corresponds to the final steady solution.	97
4.4	$Re=200$ $S = 0.95$ case. Time evolution of instantaneous streamlines. $Time=400$ corresponds to the final steady solution.	98
4.5	$Re=200$ $S = 0.95$ case. Steady solution: streamwise evolution of (a): azimuthal velocity at $r = 0.5$, (b): pressure on the axis, (c): axial velocity on the axis, (d): radial velocity at $r = 0.5$	99
4.6	Convergence histories at $S = 0.89$ (solid), $S = 0.92$ (dash), $S = 0.95$ (dash-dots), $S = 1.1$ (dots) and $S = 1.3$ (long dash). (a): Time history of rms, (b): Time history of the minimum axial velocity in the flow field.	100
4.7	Steady solutions obtained at different swirl numbers. $Re=200$, $M = 0.5$, $\alpha = 1$	102
4.8	Steady solution obtained at $S = 1.9$ presenting multiple breakdown (two corotating vortices) with a double-celled structure (two counter-rotating vortices) of the first breakdown.	103
4.9	Steady solutions obtained at different Reynolds numbers. $S = 0.95$, $M = 0.5$, $\alpha = 1$	104
4.10	Computed bifurcation diagram at $Re=1000$ (squares), $Re=400$ (triangles) and $Re=200$ (circles).	106
4.11	$Re=400$ case. (a): Evolution of instantaneous streamlines at $S = 0.9$. (b): Streamlines for steady solutions found on branch (II).	107
4.12	$Re=1000$ case. (a): Evolution of instantaneous streamlines at $S = 1$. (b): Streamlines for steady solutions found on branch (II).	108
4.13	Steady solutions obtained at different coflow numbers. $Re=200$, $S = 1.1$, $M = 0.5$	111
4.14	Steady solutions obtained at different coflow numbers. $Re=200$, $S = 0.84$, $M = 0.5$	112

4.15	Application of the vortex breakdown criterion to the $Re=1000$ case (squares) and $Re=200$ case (circles).	114
5.1	$Re=200$ $S = 1.1$ case. Evolution of the axisymmetric vortex breakdown toward a spiral breakdown state.	117
5.2	$Re=200$ $S = 0.89$ case. The axisymmetric vortex breakdown remains helically stable.	118
5.3	$Re=200$ $S = 1.3$ case. Spiral breakdown state with the appearance of double-helical structures.	119
5.4	Unsteadiness of the flow. Comparison between axisymmetric (dash line) and three-dimensional (solid) simulations. (a): $S = 0.95$ (b): $S = 1.1$ (c): $S = 1.3$ (d): $S = 1.5$	120
5.5	$Re=200$ $S = 1.1$ case. (a): Temporal evolution of azimuthal Fourier coefficients for axial velocity (solid), radial velocity (dash) and azimuthal velocity (dash-dots) at the probe $z = 5, r = 0.3$. (b): Temporal evolution of the first azimuthal mode $m = 1$ for the axial velocity measured at different axial positions: $z = 5$ (solid), $z = 10$ (dash), $z = 15$ (dash-dots).	121
5.6	$Re=200$ $S = 1.3$ case. Refer to caption of fig. 5.5.	121
5.7	$Re=200$ $S = 1.1$ case. Iso-surface of vorticity magnitude. $ \xi = 1.57$	122
5.8	$Re=200$ $S = 1.1$ case. Cross sectional contour of the radial velocity component at different axial positions.	122
5.9	$Re=200$ $S = 1.5$ case. The axisymmetric breakdown ultimately evolves toward a double-helical breakdown mode.	123
5.10	$Re=200$ $S = 1.5$ case. Temporal evolution of azimuthal Fourier coefficients for axial velocity (solid), radial velocity (dash) and azimuthal velocity (dash-dots) at different axial positions. (a): $z = 5, r = 0.3$. (b): $z = 10, r = 0.3$	124
5.11	$Re=200$ $S = 1.5$ case. Temporal evolution of a single azimuthal Fourier coefficient for the axial velocity measured at different axial positions: $z = 5$ (solid), $z = 10$ (dash), $z = 15$ (dash-dots). (a): $m = 1$. (b): $m = 2$	124
5.12	$Re=200$ $S = 1.5$ case excited by an “even” perturbation. Temporal evolution of the azimuthal Fourier coefficient $m = 2$ at different axial positions: $z = 4$ (solid), $z = 6$ (dash), $z = 8.5$ (dash-dot), $z = 11$ (dotted), $z = 14$ (long dash), $z = 16$ (dash-dot-dot).	125
5.13	$Re=200$ $S = 1.5$ case perturbed by an “even” perturbation. A double-helical mode contaminates the whole domain.	126
5.14	Independence on the initial condition for the $Re=200$ $S = 1.1$ case: temporal evolution of the azimuthal modes $m = 1$ and $m = 2$ for axial velocity (solid), radial velocity (dash) and azimuthal velocity (dash-dots). Solution starting from the axisymmetric base flow begins at $Time=360$	128
5.15	Base flow used for LTS. Top: streamlines. Bottom: centerline axial velocity (solid) and azimuthal velocity (dash) at $r = 0.5$	130

5.16	Base flow used for LTS: radial distribution of (a): axial velocity, (b): axial vorticity, (c): circulation, at different axial stations z . Solid: $z = 2$; dash: $z = 3$; dash-dot: $z = 4$; dotted: $z = 8$	130
5.17	Response of the perturbed 1D swirling flows obtained extracting velocity profiles at different streamwise positions z from the converged DNS axisymmetric solution. Isocontours of radial velocity perturbation. Time=30.	131
5.18	Temporal growth rate $\omega_i(k)$ of helical modes retrieved by LTS for velocity profiles extracted at different axial stations z	132
5.19	Real part of the frequency $\omega_r(k)$ of helical modes retrieved by LTS for velocity profiles extracted at different axial stations z	132
5.20	Re=200 $S = 1.1$ case subjected to nonlinear forcing ($\epsilon = 10^{-2}$), exciting modes $m = 1..5$ with frequency $\omega_m = m$. Time=500. Top: vorticity isosurface. Bottom: Cross sectional contours of radial velocity component at different axial positions.	134
5.21	Re=200 $S = 1.1$ case subjected to nonlinear ($\epsilon = 10^{-2}$) forcing exciting modes $m = 1..5$ with frequency $\omega_m = m$. Time=500. Time history of modes $m = 1$ (top) $m = 2$ (center) and $m = 3$ (bottom) at different axial stations.	135
5.22	Re=200 $S = 1.1$ case perturbed by linear forcing ($\epsilon = 10^{-6}$) exciting modes $m = 2..5$ with frequencies ($\omega_m = m$). (a): Time history of mode $m = 2$ at different streamwise positions. (b): Time history of mode $m = 3$ at different streamwise positions. (c): Radial velocity component recorded at $z = 10, r = 0.3, \theta = 0$. (d): Corresponding power spectrum density.	136
5.23	Re=200 $S = 1.1$ case. Temporal evolution of mode $m = 2$ at different streamwise positions. (a): Inflow perturbed by linear forcing $\epsilon = 10^{-6}$ exciting mode $m = 2$ with frequency $\omega_2 = 4$ and modes $m = 3..5$ with frequencies $\omega_m = m$. (b): Self-sustained case obtained by an initial "even" perturbation.	137
5.24	Re=400 $S = 0.95$ case. Axisymmetric vortex bubble followed by a spiral breakdown.	141
5.25	Re=400 $S = 0.95, \alpha = 2$ case. Streamwise evolution of the axial velocity profile in the converged axisymmetric solution.	142
5.26	Re=400 $S = 0.95, \alpha = 2$ case subjected to a transient linear forcing ($\epsilon = 10^{-6}$), exciting modes $m = 1..5$ with frequency $\omega_m = m$. Temporal evolution of azimuthal Fourier coefficients for the axial velocity measured at different axial positions. (a): $m = 1$. (b): $m = 2$. (c): $m = 3$	143
5.27	Streamwise distribution of the wave packet amplitude $A_1(z, t)$ as defined by (5.3). (a): LTS performed on velocity profiles extracted at (a): $z = 4$. (b): $z = 2$	145
5.28	Re=400 $S = 0.95$ case. Absolute growth rate $\sigma(V_g)$ of helical modes $m = 1, 2$ retrieved by LTS for velocity profiles extracted at different axial stations z	146

5.29	Streamwise evolution of the local absolute frequency $\omega_{0,r}$ of the helical mode $m = 1$ retrieved by LTS. Blue symbols are used for stations where the instability is convective. Black symbols where the instability is absolute. The horizontal red line represents the frequency measured in the spatial DNS.	147
5.30	Re=800 $S = 0.95$ case. Convergence history within the Dual Time integration.	149
5.31	Re=800 $S = 0.95$ case starting from a columnar vortex. Formation of a double breakdown followed by helical instabilities.	153
5.32	Re=800 $S = 0.95$ case starting from a columnar vortex. Temporal evolution of azimuthal Fourier coefficients for the azimuthal velocity component registered at the different axial stations ($r = 0.3$). (a): $z = 7.5$ (b): $z = 13$ (c): $z = 19$ and (d): Comparison between the growth observed for mode $m = 1$ at different axial stations.	154
5.33	Re=800 $S = 0.95$ case starting from a columnar vortex. (a): Azimuthal velocity component registered at $z = 19, r = 0.3, \theta = 0$ and (b): Corresponding power spectrum density.	155
5.34	Re=800 $S = 0.95$ case starting from the axisymmetric converged solution at Time=360. (a): Azimuthal velocity component registered at $z = 19, r = 0.3, \theta = 0$ and (b): Corresponding power spectrum density.	156
5.35	Re=800 $S = 0.95$ case starting from the axisymmetric converged solution at Time=360. Temporal evolution of azimuthal Fourier coefficients for the velocity component V_θ at (a): $z = 7.5, r = 0.3$ and (b): $z = 19, r = 0.3$	157
5.36	Re=800 $S = 0.95$ case starting from the axisymmetric converged solution at Time=360. Temporal evolution of the first (a) and second (b) azimuthal Fourier coefficients for the velocity component V_θ measured at different axial positions: $z = 7.5$ (black), $z = 13$ (red), $z = 19$ (blue).	157
5.37	Re=800 $S = 0.95$ case starting from the axisymmetric converged solution.	158
5.38	Re=800 $S = 0.95$ case starting from the axisymmetric converged solution. Radial velocity contours on the meridional plane $\theta = 0$. Contour levels in the range $[-0.13;0.27]$	159
5.39	Re=800 $S = 0.95$ case starting from the axisymmetric converged solution. Time=414. Radial velocity contours on cross-sectional planes at different axial stations z	159
5.40	Re=800 $S = 0.95$ case excited by an “even” perturbation. Comparison of temporal growth of modes (a): $m = 2$ and (b): $m = 4$ at different axial stations. Solid: axial velocity; dash: radial velocity; dash-dots: azimuthal velocity.	160
5.41	Re=800 $S = 0.95$ case excited by an “even” perturbation. (a): Azimuthal velocity component registered at $z = 19, r = 0.3, \theta=0$. (b): Corresponding power spectrum density (solid) and replication of fig. 5.34-b (dash).	160
5.42	Re=800 $S = 0.95$ case excited by an “even” perturbation. Iso-surface of vorticity magnitude. $ \xi = 2.18$	162

5.43	Re=800 $S = 0.95$ case excited by an “even” perturbation. The multiple breakdown configuration remains preserved.	162
5.44	Re=800 $S = 0.95$ case. Absolute growth rate $\sigma(V_g)$ of helical modes retrieved by LTS for velocity profiles extracted at different axial stations z	163
5.45	Re=1200 $S = 0.95$ case excited by an “even” perturbation.	165
5.46	Re=1600 $S = 0.95$ excited by a “m4” perturbation. Temporal evolution of mode $m = 4$ at different axial stations.	166
5.47	Re=1600 $S = 1.4$ case excited by a “m4” perturbation. Iso-surface of vorticity magnitude. $ \xi = 3.12$	166
5.48	Re=1600 $S = 1.4$ case excited by an “m=4” perturbation.	167
5.49	Swirling flow in pipe: steady axisymmetric solutions obtained at different swirl numbers. Re=200, $M = 0.5$, $\alpha = 1$	169
5.50	Swirling flow in pipe: Saturated unstable states. Re=200 $M = 0.5$, $\alpha = 1$	170
5.51	Effect of compressibility on the axisymmetric vortex breakdown. Centerline axial velocity at $M = 0.3$ (solid), $M = 0.6$ (dash-dotted) and $M = 0.7$ (dotted). Re=200, S=1.1.	171
5.52	Effect of compressibility on the development of helical instabilities. Temporal evolution of mode $m = 1$ at different axial positions. (a): $z = 4$, $r = 0.3$. (b): $z = 16$, $r = 0.3$. Re=200 $S = 1.1$	172

List of Tables

3.1	Numerical parameters used for linear calculations LTS on the Batchelor vortex.	51
3.2	Comparison of growth rates with previous computations. DCH: Delbende <i>et al.</i> , AL: current study, LSP: Lessen <i>et al.</i> . Top table reports the maximum growth rate $\{\omega_i\}_{max}$. Bottom table reports the most amplified axial wavenumber k_{max}	58
4.1	Grid resolution used for spatial axisymmetric DNS at different Reynolds numbers.	94
5.1	Numerical parameters used for spatial DNS at Re=200.	116
5.2	Linear growth rates measured at $S = 1.1$ and $S = 1.3$. Note the dependence $\hat{\omega}_m \simeq m \hat{\omega}_1$	116
5.3	Numerical parameters used for linear calculations LTS on velocity profiles extracted by DNS.	129
5.4	Numerical parameters used for spatial DNS at Re=800.	148
5.5	Linear growth rate of mode $m = 1$ measured for different Mach numbers.	171

Nomenclature

\bar{r}	radial distance from which the drop of modes is performed in the FFT
\mathbf{q}	heat flux
$\mathbf{R}(\mathbf{W})$	residual of unsteady compressible Navier-Stokes equations
$\mathbf{R}^*(\mathbf{W})$	unsteady residual in a DTS formulation
\mathbf{U}	vector of primitive variables
\mathbf{W}	vector of conservative variables
\dot{z}	amplification factor of the Runge-Kutta scheme
rms	root mean square
\tilde{r}	radial distance fixed to measure the amplitude of a Fourier component pair
∇	nabla differential operator
A	amplitude of a Fourier component pair in LTS
a	external flow parameter defined for the Batchelor vortex
b_r	grid stretching factor
E	total energy per unit mass
H	total enthalpy
I_m, K_m	modified Bessel functions of first and second kind of order m
J_m, Y_m	Bessel functions of first and second kind of order m
k, m	axial and azimuthal wavenumber in a Fourier decomposition
k_{max}	most amplified axial wavenumber in LTS
L	circulation
L_z, L_r	axial and radial length of the cylindrical domain
M	reference Mach number
n_r, n_θ, n_z	number of grid points in the radial, azimuthal and axial directions, respectively
p	static pressure
Pr	reference Prandtl number
q	swirl number as defined for the Batchelor vortex
q_m	amplitude of the m -th azimuthal mode in DNS

r, θ, z	radial, azimuthal and axial coordinates, respectively
r_0, z_0	location in the meridional plane where the initial perturbation is placed
S	swirl number
S_1, S_2	first and second limit point in the bifurcation diagram of an axisymmetric swirling flow
T	temperature
V_g	group velocity
V_r, V_θ, V_z	radial, azimuthal and streamwise velocity components, respectively
CFL	Courant Freidricks Levy parameter
DNS	direct numerical simulation
DTS	dual time stepping
FFT	fast Fourier transform
LTS	linear temporal simulation
Re	reference Reynolds number
$\{\omega_i\}_{max}$	maximum growth rate over all axial wavenumbers in LTS
α	coflow parameter
$\Delta\tau$	pseudo-time step integration used in the DTS
$\Delta r, \Delta\theta, \Delta z$	grid size in the radial, azimuthal and axial directions, respectively
Δt	physical time step
δ	dimensional vortex core size
$\hat{\omega}_m$	growth rate of the m-th azimuthal mode in DNS
μ	molecular kinematic viscosity
Ω	dimensional angular velocity of the solid body rotation
ω	angular frequency in DNS
ω_i	temporal growth rate retrieved by LTS
ω_m	forcing frequency of the m-th azimuthal mode in DNS
ω_r	temporal frequency retrieved by LTS
$\omega_{0,r}$	absolute frequency retrieved by wave packet analysis
Φ	phase associated with a Fourier pair in LTS
ρ	density
σ	absolute growth rate retrieved by wave packet analysis
$\underline{\underline{\tau}}$	stress tensor
ξ_r, ξ_θ, ξ_z	radial, azimuthal and axial vorticity components, respectively
$\{\sigma\}_{max}$	absolute growth rate on the spatio temporal ray of highest amplification

Chapter 1

Literature review

1.1 Introduction

Swirl is known to drastically affect the dynamics of jets and wakes, and is encountered in a variety of technical applications as well as in natural conditions. Due to its practical relevance, it is highly desirable to have a full understanding of how the different physical mechanisms characterising such a configuration can combine, modify and eventually compensate each other. We define a “swirling flow” as the superposition on a pure jet or wake of a vortex with axis parallel to the jet direction. The velocity profile of the swirling flow can induce shear instabilities, *i.e.* Kelvin-Helmholtz instabilities similar to those encountered in non-rotating jets. The introduction of swirl may result in the development of centrifugal instabilities, or even enhance Kelvin-Helmholtz instabilities associated with the additional presence of the azimuthal shear. Finally, under certain conditions, a swirling flow can evolve into what is called “vortex breakdown”, *i.e.* a sudden axial velocity decay occurring in the vortex core, resulting in a region with recirculating fluid.

The recent experimental investigation of Liang and Maxworthy [65] offers an interesting picture for possible dynamical evolutions of the vortical structures arising in a swirling jet at low Reynolds numbers. They analyse the plug flow emerging from a long rotating tube in a stationary environment. Depending on the intensity of the swirl, four different regimes are identified: non-rotating jets, weakly swirling flows, strong swirling flows prior to vortex breakdown and breakdown state. In the absence of rotation, the axial shear generated at the interface between the jet emerging at the inlet and the still fluid, originates a sequence of axisymmetric vortex rings. These structures are seen to move downstream from the inlet, amplifying and pairing before evolving into a full turbulent state. When a moderate swirl is applied, the vortex rings preserve their axisymmetric structure for some axial extent in

proximity of the inlet, before being tilted downstream in the direction opposite to that of the rotation of the jet. The last regime preceding breakdown is found to be very unsteady and irregular. The vortex rings, which dominate the flow field at lower swirl, are replaced by several helical waves coexisting with small scale vortices. The more the flow approaches the breakdown condition, the more it becomes chaotic and the coherent structures difficult to visualise. At a threshold level of swirl, the vortex core of the jet “bursts”: the flow stagnates and forms near the nozzle exit an axisymmetric bubble. The flow field becomes suddenly more regular, helical structures with azimuthal wavenumber $m = 1$ and $m = 2$ become more visible in the rear of the bubble, with the bending spiral $m = 1$ being the dominant.

This thesis consists in a computational study on swirling flows at low Reynolds numbers. As detailed later, the relation between vortex breakdown and vortex stability is quite unclear. Several attempts have been undertaken to regard vortex breakdown as a manifestation of vortex instability. The partial successes which have been obtained, mostly in the axisymmetric framework, cannot provide an explanation for a very simple fact: swirling flows are highly unstable to helical disturbances, whereas the most robust breakdown is found to be axisymmetric. In this introduction, we assume the perspective of Escudier *et al.* [26], and consider a clear separation between the two concepts. The evolution towards a breakdown state determines the base character of the flow, while instabilities represent an important, superimposed detail.

1.2 Vortex breakdown

In one of the first experimental works on vortex breakdown, Harvey [40] describes the phenomenon as the formation of a well confined region of reversed flow, with a shape of a body of revolution located on the axis, imposing the approaching flow to move around it. Figure 1.1 reports the vortex breakdown obtained in the experiment of Sarpkaya [93]: the flow is streaming from the left side, and under the effect of a very intense swirl develops a nearly axisymmetric bubble, acting as a solid obstacle which induces in the rear the distinctive vortex shedding of a wake.

The possibility to generate and eventually control a localised region with reversed flow offers interesting benefits in many industrial applications. For example, the technique can be used as flame-holder in order to stabilise combustion. On the other hand, vortex breakdown can result in undesirable consequences: for example, over delta wings, the presence of

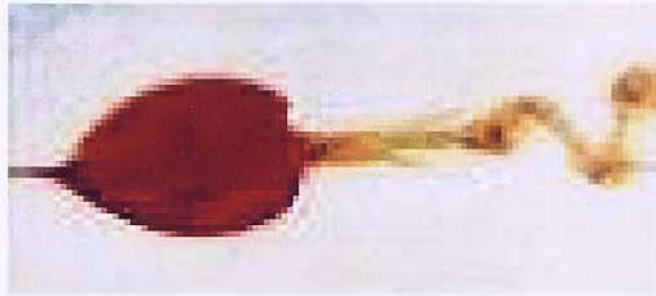


Figure 1.1: Experimental observation of an axisymmetric bubble followed by spiral breakdown. From the gallery of fluid mechanics, Cambridge University.

stagnating fluid at high pressure leads to a deterioration of lift characteristics and to a poor controllability [23].

Despite four decades of theoretical, experimental and numerical studies, a universally accepted explanation of vortex breakdown is still lacking. Among the proposed theories, Ludweig [70] in the early sixties seems to be the first to suggest that breakdown occurs as a consequence of hydrodynamic instabilities, arguing that the formation of the internal stagnation point results from the sensitivity of the vortex core to helical disturbances. In his view, helical instabilities are those responsible for the axial flow decay by means of a transfer of energy: vortex breakdown is therefore seen as an *asymmetric* process, although it may manifest predominant *axisymmetric* features. The initial idea of Ludweig was seeded by the consideration that the classic linear theory highlights a tendency of highly swirling flows to helical instabilities more than to axisymmetric ones, but it was later moderated when the first numerical simulations of swirling jets proved that breakdown can occur even on axisymmetric models [35, 53].

Although the numerical results were not exempt from criticism, this induced theoreticians to consider the possibility that the breakdown process cannot be fully described in the framework of a linear stability analysis, but that other more sophisticated mechanisms should be accounted for. In this context, the work of Leibovich [57], Leibovich & Randall [58] and Kribus & Leibovich [55] is relevant. They formalised an idea originally proposed by Squire [96]. According to these lines of thought, the fundamental nature of vortex breakdown is similar to other well known fluid dynamic phenomena like shock waves and the hydraulic jump. In all these systems waves propagate, and all are based on the concept of critical state. In a swirling flow, even if the stability of the base flow is guaranteed, the restoring effect of the Coriolis force generates longitudinal inertial waves. They are the so

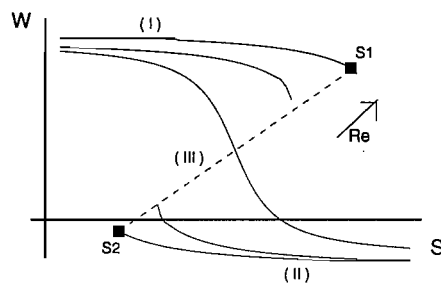


Figure 1.2: Typical bifurcation diagrams of an axisymmetric swirling flow.

called Kelvin waves [66, 90] associated with the presence of a core in a solid body rotation: in the absence of axial velocity, the vortex core behaves as a wave guide for axisymmetric disturbances which propagate marginally in the upstream and downstream direction symmetrically. These waves have a specific group velocity depending on the intensity of the rotation: when the axial velocity is not zero, but bigger than the speed of the inertial waves, any perturbation is convected downstream by the main flow. For a given axial velocity, there exists a critical level of swirl for which an axisymmetric standing wave can be sustained from the base flow [6]. Below the critical level the flow is *supercritical* and waves can only propagate downstream; upstream propagation of energy becomes possible above the critical level, when the flow is said to be *subcritical*.

The critical state is defined referring to a swirling flow which is assumed to be columnar, extending to infinity both upstream and downstream. In real situations the flow is never uniform, but, due to geometrical constraints and viscous diffusion, it has conditions slowly evolving which may lead an initial supercritical flow towards criticality. Whereas if a critical condition is reached, perturbations spreading from the subsequent subcritical region will accumulate and amplify to large value resulting in a possible breakdown. Leibovich [57], using a weakly nonlinear analysis, derives the evolution of waves of finite amplitude in an inviscid vortex core. The wave amplitude is governed by a Korteweg-de Vries equation, whose solutions are the well known *solitons*, waves of permanent form arising from the nonlinear interaction of dispersive waves. The resulting finite wave presents a dependence of the velocity on the amplitude: as it grows it becomes faster and therefore can penetrate the supercritical region, inaccessible for small perturbations. In this scenario, a steady configuration becomes possible only if a mechanism extracting energy from the big wave arises.

Experimental works [26, 93] have revealed a very weak sensitivity to viscosity for high Reynolds numbers. Kribus and Leibovich [55] suggest that non-axisymmetric features can replace viscosity as the most dissipative effect helping to stabilise the wave. Thus, Kribus and Leibovich arrive at the opposite conclusion to that of Ludweig: the energy transfer goes from the axisymmetric wave toward the helical ones and represents the mechanism by which the ‘positional instability’ [59] of the growing axisymmetric bubble is stopped.

The wave theory of Leibovich finds support in two important considerations: first, a tendency of vortex breakdown to migrate upstream during its formation has been observed in numerical [35] as well as in experimental studies [73]. Furthermore, both Sarpkaya [93] and Harvey [40] report in their experiments that if the conditions are assigned trying to minimise the development of vortex instabilities, then the flow morphology may resemble a wave train, with the formation of less intense breakdown states created in the wake of the first bubble. In Leibovich’s view, the secondary breakdowns are the ‘tail’ of the developing soliton. Since they are sequentially smaller, as soon as three-dimensional asymmetries develop, any characteristics of the wave train would be lost, and this explains why even the most recent experiments [9, 32, 65] do not report this flow configuration: depending on differences in the velocity profile of the underlying swirling jet, helical vortex instabilities can develop for values of swirl lower than that needed for a breakdown state. In this case, as in the revisited experiment of Liang and Maxworthy, the possibility to identify the wave train is inhibited. Computational fluid dynamics offers the opportunity to study separately axisymmetric and three-dimensional effects and to analyse their interaction.

The wave theory of Leibovich would also provide some insights into the hysteresis loop that some unsteady axisymmetric simulations have revealed for large Reynolds numbers ($Re \geq 300$) [1, 7, 41, 69]: some quantities, like the minimum axial velocity, when represented as function of the swirl level, show multiple steady solutions. Figure 1.2 illustrates a schematic representation of the minimum axial velocity W obtained for different values of the swirl. Here we remark that $W \leq 0$ indicates breakdown. Starting from a condition with low swirl the solution moves along the branch (I), corresponding to a quasi-columnar configuration until the first folding point S_1 is reached. For $S > S_1$ the solution evolves towards branch (II) and a stagnation point appears. At this stage, a successive reduction of swirl below the critical value S_1 is unable to restore the initial quasi-columnar configuration until a second folding point S_2 is reached.

This behaviour is connected to bifurcating solutions of the *steady* Navier-Stokes equa-

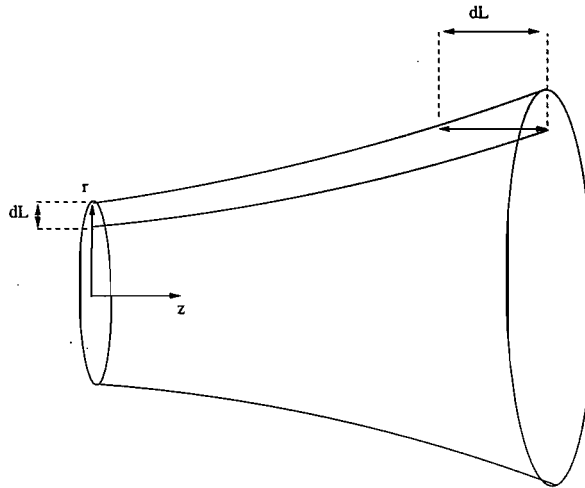


Figure 1.3: Production of axial circulation gradient due to the radial flow divergence in an axisymmetric swirling flow with $dL/dr > 0$.

tions. Wang and Rusak [101] have applied a global variational approach to the inviscid Rankine vortex in a pipe, deriving a bifurcation diagram which resembles the viscous results found by numerical computations. In particular they prove the existence of the two limit points S_1 and S_2 such that for $S_1 < S < S_2$ three solutions exist: solutions on branch (I) representing a columnar flow; solutions on branch (II) representing a well localised region of separated flow; there exists a third branch (III), connecting the two folding points, which describes waves developing in the main flow. This branch is unstable and cannot be obtained as steady solution of a time marching calculation, but could be found using a steady state case in combination with continuation techniques [7, 101].

The numerical computations of Beran [7], Lopez [69] and Herrada *et al.* [41] are seen as a viscous correction of these results. S_1 is the critical point for infinitesimal disturbances, while S_2 is suggested to be a critical state for *finite amplitude* waves. When the Reynolds number is high enough, the flow becomes locally critical, nonlinear waves interact and propagate upstream; in the inviscid limit the only mechanism which may trap the large wave is due to the boundary conditions fixed at the inlet. For moderate Reynolds numbers the dissipative effect of viscosity is no longer negligible, and the large wave can come to rest before approaching the inlet. The corresponding bifurcation diagram is modified, the third branch becomes shorter and eventually disappears, suggesting a relation between the excursion of the breakdown and the multiple steady solutions found.

More recently, Brown and Lopez [12] have proposed an explanation of vortex break-

down based on simpler vorticity considerations. According to these authors, breakdown results from the tilting of axial vorticity into negative azimuthal vorticity. In the vorticity equation, this process is modelled by $\xi_z \frac{\partial V_\theta}{\partial z}$ where ξ_z is the axial vorticity and V_θ the azimuthal component of velocity. If it is enough intense, the appearance of negative azimuthal vorticity can start a positive feedback by vortex stretching. This would reinforce the production of negative ξ_θ leading ultimately the flow to stagnate. Darmofal [19] points out that what is initially necessary to start the process is the establishment of a significant negative axial gradient of circulation. For an open jet, this is achieved by the diffusion of the vortex tube as depicted in figure 1.3. The approaching swirling flow starts blowing in the positive radial direction by vortex diffusion. In accordance with the Kelvin theorem, a loop of particles moves radially preserving the circulation $L = rV_\theta$. If the circulation of the swirling flow increases outward, a negative axial gradient of L is established due to radial divergence of the flow. The mechanism is clearly enhanced when the viscous diffusion is higher. As a consequence, for a given level of swirl, the initial production of azimuthal vorticity would be bigger in magnitude and the positive feedback of Brown and Lopez easier to be activated. The modification of the bifurcation diagram with the Reynolds number is consistent with this theory.

In a completely different approach, much work on breakdown has been done using the boundary layer analogy [7, 39, 41]: from the axisymmetric Navier-Stokes equations, the quasi-cylindrical approximation can be derived by making the assumptions that the flow is steady, the centrifugal force is balanced by the radial pressure gradient, and neglecting the axial derivatives in the viscous terms. The resulting equations are parabolic, and can be integrated marching in the streamwise direction. Similarly to boundary layers calculations, there exists a critical level of swirl for which the system of equations fails to converge. It is found that the critical value obtained in the quasi-cylindrical equations agree very well with that of S_1 found by numerical solutions of the axisymmetric Navier-Stokes equations. Rather than a theory, the boundary layer analogy has to be regarded as a tool, which however is unable to provide information about the structure of the vortex bubble. It has to be pointed out however, that some works [54] report as vortex breakdown state a morphology of the flow resembling the separation occurring in the boundary layer under the effect of an adverse pressure gradient. In that case, it is likely that any wave theory is pointless: vortex breakdown may just be a consequence of the excess of the pressure gradient on the axial momentum flux, as also suggested by Mahesh [72].

1.3 Physical mechanisms of vortex instability

A columnar (1D) swirling flow is defined by functional dependency of the form

$$\begin{aligned} V_r &= 0, \\ V_\theta &= V_\theta(r), \\ V_z &= V_z(r). \end{aligned} \tag{1.1}$$

Depending on the velocity profiles described in (1.1), different physical mechanisms may trigger different responses of the main flow to an external perturbation. When $V_\theta = 0$, (1.1) identifies a cylindrical jet (or wake) without rotation. The presence of a strong shear layer can then originate Kelvin-Helmholtz instabilities. The well known inflection Rayleigh criterion [24] provides a necessary condition for the case of an inviscid, incompressible planar jet¹. When the finite shear layer is replaced by a 2D vortex sheet, the growth rate of a perturbation with wave vector \mathbf{k} is $\frac{1}{2}\mathbf{k} \cdot \Delta \mathbf{V}$ [24] where $\Delta \mathbf{V}$ is the shear vector. In the case of a cylindrical plug flow, for very short waves the axisymmetric mode follows the same law (see, for example, Batchelor and Gill [5]) but the helical modes $m \pm 1$ are more unstable.

In terms of vorticity, the Rayleigh criterion says that a necessary condition is the existence of a local extremum. Stated like this, it is easily extended to circular geometries, *i.e.* to a pure vortex $V_\theta(r)$ in the absence of axial velocity. In that case, the existence of a local extremum in the *axial* vorticity represents a necessary condition for instabilities to two dimensional disturbances of the form $e^{im\theta}$ [24]. These are the spectacular dipoles and tripoles revealed in the experiments of Carnevale and Kloosterziel [13].

In the absence of the destabilising effect produced by the shear, the pure vortex $V_\theta(r)$ can however be unstable by virtue of centrifugal instability. If an axisymmetric perturbation takes place, particles from an inner annulus will move out conserving the angular momentum. When the initial circulation decreases outward, particles will be subjected to a lower pressure gradient unable to balance the centrifugal force and the initial perturbation amplifies. Linear theory provides the following criterion, also known as Rayleigh criterion: a necessary and sufficient condition for the flow to be unstable is that the square of the circulation $L = rV_\theta$ decreases with the radius [24]. A generalisation of this result to the swirling jet with non-zero axial velocity is given by Howard and Gupta [44], but it is necessary although not sufficient and refers to the single axisymmetric centrifugal mode. Conversely,

¹Luo and Sandham [71] have extended the Rayleigh's criterion to a compressible flow, showing that instability can exist even when there is no inflection point.

for a swirling flow one may have *helical* centrifugal instabilities $m \neq 0$ developing in a sloped plane. A sufficient condition has been provided by the asymptotic analysis $|m| \gg 1$ of Leibovich and Stewartson [61]. Emanuel [25] shows that the condition of Leibovich and Stewartson can be regarded as that of Howard and Gupta in the sloped plane containing all the shear components. Thus, the centrifugal instability pertains to helical waves, and can develop even if the pure vortex flow $V_\theta(r)$ (without the axial flow support) is centrifugally stable.

The idea of considering this generalised form of centrifugal instability was originally motivated by the following observation: intuitively, if the destabilising mechanism was a tilted shear effect, accounting for the axial and the azimuthal contribution, the most unstable modes would be expected to be those having the wave vector \mathbf{k} more aligned with the shear. In most of the circumstances, the behaviour has been found to be different, as revealed by the majority of the experiments on vortex breakdown [26, 65, 73, 93] and by the linear analysis of several authors [48, 49, 63, 74].

This scenario, however, lacks completeness, because it does not consider the effect of the swirl on the Kelvin-Helmholtz instabilities. The indications provided by the studies of Loiseleux *et al.* [67] and Gallaire *et al.* [30] are that under the effect of the rotation, the axisymmetric Kelvin-Helmholtz instabilities modify producing helical waves. When the axial shear is particularly intense, these waves follow a behaviour similar to that of the generalised centrifugal instabilities. In other words, as also suggested by Liang and Maxworthy [65], the two different physical mechanisms (shear and centrifugal) combine inducing a similar mode selection. Conversely, if the azimuthal shear dominates, the behaviour may be the opposite, and the most unstable modes are actually those more aligned with the shear.

The main concern regarding these results is that they have been obtained on discontinuous models, and their applicability to real velocity profiles may be questionable.

1.4 Concepts of linear analysis

The classic linear stability analysis of shear flows deals with instabilities developing in a parallel flow, *i.e.* a flow containing only one inhomogeneous spatial direction. For a given two-dimensional (x, y) base flow, if y represents the inhomogeneous cross-stream direction, the standard procedure consists in regarding infinitesimal perturbations as a superposition of elementary waves of the form $\hat{\phi}(y)\exp\{i(kx - \omega t)\}$ with ϕ standing for any perturbation

variable. In the above wave form, k is the complex wavenumber, ω is the complex frequency and $\hat{\phi}(y)$ is the eigenfunction representing the distribution of the perturbation over the cross-stream direction. The evolution of small waves is studied linearising the governing equations around the given base flow. This leads writing for the eigenfunction a single ordinary differential equation, which in most of the cases is of *Sturm-Liouville* type. For simple base flows, enforcing two boundary conditions can allow to write a dispersion relation of the form

$$F(k, \omega, R) = 0 ,$$

where R represents a typical control parameter, for example the Reynolds number. The existence of the eigenfunction $\hat{\phi}$ implies that k and ω have to satisfy the dispersion relation. In a temporal framework, one considers the evolution of waves with prescribed real values of k so that the base flow is unstable if there exists at least one value of k for which $\omega(k, R)$ has a positive imaginary part. In contrast to the temporal analysis, the spatial approach refers to the development in space of waves generated by a localised time-harmonic forcing, thus instability is reached when for a prescribed real frequency ω , the dispersion relation admits a solution $k = k(\omega, R)$ with negative imaginary part.

The above considerations should be complemented with the concepts of absolute and convective instabilities, a distinction originated by plasma physics [8] and formalising the competition between the dispersion mechanism induced by the instability, and the advection due to the base flow. For parallel flows, following the definition of Chomaz [16], the instability is absolute when the response to a localised initial impulse grows indefinitely at *any* axial station x in the laboratory frame; the instability is said to be convective when the response goes to zero in the laboratory frame, but there exists at least one Galilean frame in which the response grows. In other words, the pulse response of an unstable flow originates a wave packet moving in the streamwise direction and confined between two spatio-temporal rays $x/t = V_{\pm}$ representing the edges of the packet (see fig. 1.4). If the velocity of the two edges has opposite sign, the instability is absolute because a mode with zero-group velocity grows along the ray $x/t = 0$, *i.e.* at the source station.

As reviewed by Huerre [46], when the initial pulse is replaced by a continuous harmonic small forcing, the response of a convectively unstable medium consists of a periodic steady state left everywhere and beating at the forcing frequency. Following a generally adopted terminology, these flows behave as spatial amplifiers because the amplitude of the

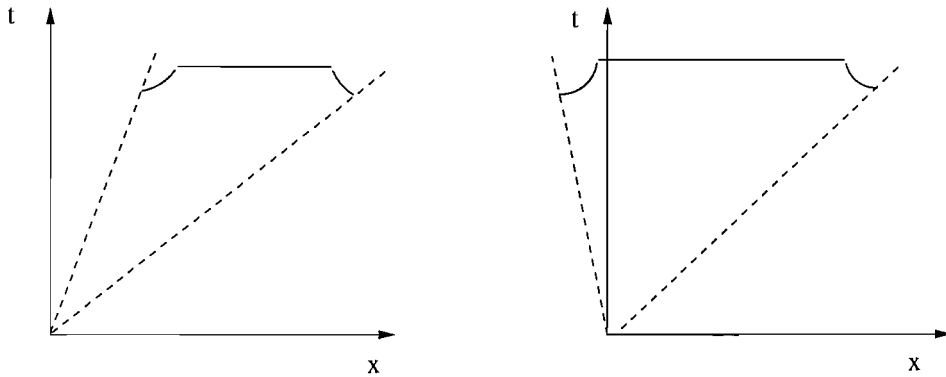


Figure 1.4: Schematic representation of the impulse response of an unstable medium. Left: convective instability. Right: absolute instability.

periodic forcing grows exponentially in space. Conversely, when the flow becomes absolutely unstable, the mode with zero group velocity gives rise to *self-sustained* oscillations tuned at a well defined natural frequency. The self-sustained oscillations overshadow the forcing response, and maintain their natural frequency independently of the forcing applied. If the forcing is suddenly turned off, in the medium which is only convectively unstable the response relaxes to zero, whereas the oscillations in the absolutely unstable flow are preserved (self-sustained).

There exist two methods to determine the nature of a given velocity profile. One possibility is the application of the “pinching criterion” [45]. The dispersion relation is studied in the spatial framework, *i.e.* assigning a real frequency ω and seeking complex values of k . The locus of complex k is made of two distinct branches, solutions corresponding to waves propagating in both the upstream and downstream direction of the forcing station. It can be proved [45] that when the instability becomes absolute, the two branches pinch. Therefore, one has to examine the morphology of the two spatial branches as the control parameter is changed. Alternatively, it is possible to remain in the physical space and evaluate by numerical simulation the flow response to a localised perturbation. Following the evolution of the disturbance along different spatio-temporal rays $\frac{x}{t} = V_g$, one can measure the growth rate along each ray, *i.e.* the absolute growth $\sigma = \sigma(V_g)$. If it is positive at $V_g = 0$, the perturbation grows at the initial disturbance location, and the instability is absolute. The two methods have been shown to produce the same results by Olendraru and Sellier [82].

The applicability of the above concepts to non-parallel flows may be considered straightforward when the inhomogeneity in the streamwise direction (measured by $\frac{d\delta(x)}{dx}$)

where $\delta(x)$ is a typical local length scale) is very small: in that case, the *global* response is affected by the *local* stability characteristics. The amount of studies confirming this result is extremely wide, and the reader is referred to the paper of Huerre and Monkewitz [45] for a review of them. Heated jets [79], or bluffbody wakes [80] are typical flows presenting self-sustained oscillations. The classic example is the vortex shedding past a two-dimensional cylinder. If the Reynolds number exceeds a critical value, the wake of the solid obstacle is seen to distort according to synchronised oscillations. Examples of convectively unstable flows are mixing layer, non-rotating jets and flat plate wakes [45].

In a slowly developing flow, a necessary condition for a global mode to be self-sustained, is the existence of local absolute instability, as first recognised by Koch [51] for wakes, and later confirmed by Chomaz *et al.* [17] on the one-dimensional evolution model described by the Ginzburg-Landau equation. The condition, however, is not sufficient: the localised region of absolute instability can be unable to trigger a global mode if it is of limited axial extent [17].

In the present discussion, the recent work of Pier and Huerre [85] assumes particular relevance: considering a family of slowly varying developing 2D wakes, they show that a nonlinear self-sustained vortex shedding (the global mode) is associated with the existence of a front located at the streamwise station where the transition from convective to absolute instability occurs. The front acts as wave-maker, in the sense that nonlinear waves are sent out with a frequency given by the local absolute frequency at the transition station. It is important to notice that the analysis of Pier and Huerre [85] is fully nonlinear, and it shows that nonlinear effects do not modify either the instability threshold or the frequency of oscillation predicted by the linear absolute instability. This important result, sometimes referred as theory of Pier and Huerre for the generality of the assumptions undertaken (slowly varying flow, strongly nonlinear) relies on the concepts of front selection, as detailed in the work of Delbende and Chomaz [22]. In their computational study on 2D wakes, the localised perturbation is seen to grow initially according to the linear theory. When it is big enough, the growth is compensated by the nonlinear terms and the wave packet saturates. At this point, Delbende and Chomaz find that the edges of the packet are ‘linearly selected’ [22], that is, even after saturation, they travel at a speed equal to that of the precursor linear packet. This condition, which the authors warn to be not universal, excludes the possibility that this class of flows might be absolutely unstable with respect to nonlinear perturbations, and only convectively unstable with respect to linear ones. The above conclusion would explain

a posteriori why the linear theory has accounted so well for the onset of self-sustained oscillations in the wake dynamics.

The distinction between absolute and convective instability may be regarded as a generalisation of the concept of criticality introduced for the neutral Kelvin waves. In spite of this consideration, it appears natural to attempt to interpret vortex breakdown as a manifestation of absolute instability of the axisymmetric mode $m = 0$. Loiseleux *et al.* [67] evaluated the instability character of a swirling jet made of the Rankine vortex superimposed on a plug flow. Applying the pinching criterion, they demonstrated that the swirl promotes absolute instability, but the transitional helical mode (the first to become absolutely unstable) was found to be $m = 1$. The same analysis predicts higher modes to be “more absolutely” unstable as the swirl is increased. Adopting the same procedure, Yin *et al.* [103] have shown that the absolute instability of the Batchelor vortex succeeds in predicting the Strouhal number measured in the experimental breakdown state of Garg and Leibovich [34].

More recently, Gallaire and Chomaz [29] have analysed by direct numerical simulation the velocity profiles modelling the jet used in the experiment of Billant *et al.* [9]. The experiment reveals the presence of double-helical structures in the pre-breakdown stage, suggesting the onset of a self-sustained global mode with azimuthal wavenumber $m = 2$. The analysis of Gallaire and Chomaz shows that under the same conditions of the experiment, the inlet velocity profile is absolutely unstable to $m = 2$. Increasing the swirl, the same analysis should have revealed absolute instability for the axisymmetric mode to account for the breakdown; conversely, the results reveal a sequence of transitional modes $m = 1..5$. Absolute instability of the axisymmetric mode has been determined by Loiseleux *et al.* [68], but for a jet with an azimuthal velocity profile centrifugally unstable. The evaluation of these results leads to the conclusion that the concepts of absolute and convective instabilities appear to be unable to explain the onset of vortex breakdown, although they capture quite well the dynamics of the unsteady structures developing in swirling flows.

1.5 Present research

In this work we have carried out a fairly extensive numerical investigation on vortex breakdown in compressible swirling jets. In a first part, we have tried to gain more physical insights into the base mechanisms present under the effect of the rotation. For this purpose, the stability of parallel swirling flows has been studied by direct numerical simulations

of the linearised Navier-Stokes equations. Selecting appropriate velocity profiles, we have tried to isolate as much as possible the role played by centrifugal instabilities, shear instabilities and the neutral Kelvin waves. The study, presented in chapter 3, has later served as a guideline for the successive spatial simulations, where the assumption of parallelism has been relaxed.

Axisymmetric simulations have been conducted with the specific purpose to determine numerically the bifurcation diagram and to see how it correlates with the flow-field computed. What appears quite unclear is the meaning of the limit point S_2 (cfr. fig. 1.2). The theoretical analysis of Wang and Rusak [101], conducted for the inviscid straight Rankine vortex, suggests S_2 is associated with a full expulsion from the computational domain of the axisymmetric wave. Existing numerical studies [7, 41, 69] have computed the diagram for swirling flows in a nozzle and, possibly due to the pressure gradients imposed by the geometry, they do not show the wave excursions predicted by the analysis of Wang and Rusak. We have therefore deemed important to derive the bifurcation diagram for an open jet. A large number of parametric studies have also been conducted and we have tried to find out which of the elements predicted by the theories of Leibovich [57] and Brown & Lopez [12] are captured by the viscous calculations.

Finally, in the last chapter, we report what we consider the main contribution of the work. The starting point of the analysis is the DNS conducted by Ruith *et al.* [88], showing that in the breakdown state, helical and double-helical structures can actually be self-sustained, *i.e.* generated in a numerical simulation without the introduction of a continuous forcing. In a more recent paper, Gallaire *et al.* [33] apply a local linear analysis to the results of Ruith *et al.*. They consider a base axisymmetric vortex breakdown state, that the DNS has revealed to evolve into a limit cycle with a global mode $m = 1$, and solve the equations linearised around velocity profiles extracted at different streamwise stations. The results seem to confirm the validity of the steep-front theory of Pier and Huerre [85], since they show that the frequency of oscillation revealed in the nonlinear DNS is given by the local absolute frequency at the transition station from convective to absolute. The conclusions of Gallaire *et al.* have also been corroborated by a similar study conducted by Herrada *et al.* [42] on a swirling flow with different velocity profiles. In light of what previously discussed, this should guarantee that swirling flows, in general, behave like the 2D wakes studied by Delbende and Chomaz [22], with the front dynamics linearly selected.

The numerical simulations of Ruith *et al.*, which certainly represent the most complete

computational study on vortex breakdown, leave open the question about the origin of the global mode $m = 2$. It has to be pointed out that their DNS show a notable propensity to the onset of a double-helix. Although the local analysis of Loiseleux *et al.* [67, 68] and that of Gallaire *et al.* [29, 30] do not exclude the possibility of absolute instability for the helical mode $m = 2$, this behaviour seems qualitatively inconsistent with the experimental observations and with other recent computations of three-dimensional vortex breakdown [42, 52]. In most of the cases, the dominant unstable mode in a swirling wake is found to be $m = 1$, a feature considered a well established result in the swirling wake dynamics². In addition, under some conditions, the double-helical structures of Ruith *et al.* show an interesting “axisymmetric unsteadiness”, which the authors report as a three-dimensional effect, not observed in the axisymmetric calculations.

The questions that we have tried to address are the following: are those double-helical structures actually a manifestation of a global mode caused by a localised small perturbation? If so, do they follow the steep-front theory, like the bending mode $m = 1$, *i.e.*, are they associated with a region of local absolute instability? If the answer to these questions were positive, another issue would then arise. Extending the range of control parameters, is it possible to obtain self-sustained global modes with higher azimuthal wavenumber?

Analysing the response of forced and self-sustained swirling jets, and performing local analysis, we have encountered a mechanism which may partially explain the results of Ruith *et al.*. We suggest the existence of self-sustained structures of convective nature: these are associated with the presence of the recirculating region which, if the initial perturbation is introduced *ad hoc*, can dictate the entire dynamics sending out wave packets which are convectively amplified.

The details of the numerical code developed are presented in chapter 2. The code is in cylindrical coordinates, and the computational techniques employed are quite standard. Some care has been required for the axis treatment, and two different methods have been tested. We have also adapted the the Poinot-Lele method [86] for the boundary conditions treatment on curvilinear grids.

²In section 1.3, we cited the double-helix revealed in the experiment of Billant *et al.* [9]. It is not relevant in this context, as it has been obtained in the pre-breakdown state, when the flow configuration is that of a swirling jet.

Chapter 2

Numerical method

2.1 Governing equations

2.1.1 Navier-Stokes equations in cylindrical coordinates

Using as state variables density ρ , momentum $\rho\mathbf{V}$ and energy per unit volume ρE , the time-dependent, compressible Navier-Stokes equations can be written as

$$\begin{aligned}\frac{\partial \rho}{\partial t} + \underline{\nabla} \cdot (\rho \mathbf{V}) &= 0 \\ \frac{\partial(\rho \mathbf{V})}{\partial t} + \underline{\nabla} \cdot [(\rho \mathbf{V}) \mathbf{V} + p \underline{\mathbf{I}}] &= \underline{\nabla} \cdot \underline{\underline{\tau}} \\ \frac{\partial(\rho E)}{\partial t} + \underline{\nabla} \cdot [(\rho E) \mathbf{V} + \mathbf{q} + p \mathbf{V}] &= \underline{\nabla} \cdot (\underline{\underline{\tau}} \cdot \mathbf{V}),\end{aligned}\tag{2.1}$$

where the stress tensor $\underline{\underline{\tau}}$ and the heating flux \mathbf{q} are defined according to the Newton and Fourier laws:

$$\begin{aligned}\underline{\underline{\tau}} &= 2\mu \left\{ \frac{(\underline{\nabla} \mathbf{V}) + (\underline{\nabla} \mathbf{V})^T}{2} - \frac{\underline{\nabla} \cdot \mathbf{V}}{3} \underline{\underline{\mathbf{I}}} \right\}, \\ \mathbf{q} &= -k \underline{\nabla} T.\end{aligned}\tag{2.2}$$

Equations (2.1) can be made dimensionless introducing characteristic values for length L_r , velocity V_r , density ρ_r and temperature T_r . Their exact expression will be discussed later in the context of the specific problem studied. The convective time scale is then L_r/V_r and the characteristic pressure p_r is chosen to be twice the reference dynamic pressure $p_r = \rho_r V_r^2$. In a cylindrical frame of reference (r, θ, z) , the above non-dimensionalisation leads to the following system of equations:

$$\frac{\partial \mathbf{W}}{\partial t} + \frac{\partial \mathbf{F}_z}{\partial z} + \frac{\partial \mathbf{F}_r}{\partial r} + \frac{1}{r} \frac{\partial \mathbf{F}_\theta}{\partial \theta} + \frac{\mathbf{S}}{r} = 0,\tag{2.3}$$

where the non-dimensional state vector \mathbf{W} is $[\rho, \rho V_r, \rho V_\theta, \rho V_z, \rho E]^T$ and the fluxes \mathbf{F} and the source term \mathbf{S} are given by:

$$\mathbf{F}_z = \begin{bmatrix} \rho V_z \\ \rho V_r V_z - \frac{1}{\text{Re}} \tau_{zr} \\ \rho V_\theta V_z - \frac{1}{\text{Re}} \tau_{z\theta} \\ \rho V_z^2 + p - \frac{1}{\text{Re}} \tau_{zz} \\ \left\{ \begin{array}{l} \rho H V_z - \frac{1}{\text{Re}} \\ (\tau_{zr} V_r + \tau_{z\theta} V_\theta + \tau_{zz} V_z) + \\ + \frac{q_z}{(\gamma-1)\text{Re}M^2\text{Pr}} \end{array} \right\} \end{bmatrix} \quad \mathbf{F}_r = \begin{bmatrix} \rho V_r \\ \rho V_r^2 + p - \frac{1}{\text{Re}} \tau_{rr} \\ \rho V_\theta V_r - \frac{1}{\text{Re}} \tau_{r\theta} \\ \rho V_z V_r - \frac{1}{\text{Re}} \tau_{rz} \\ \left\{ \begin{array}{l} \rho H V_r - \frac{1}{\text{Re}} \\ (\tau_{rr} V_r + \tau_{r\theta} V_\theta + \tau_{rz} V_z) + \\ + \frac{q_r}{(\gamma-1)\text{Re}M^2\text{Pr}} \end{array} \right\} \end{bmatrix}$$

$$\mathbf{F}_\theta = \begin{bmatrix} \rho V_\theta \\ \rho V_r V_\theta - \frac{1}{\text{Re}} \tau_{\theta r} \\ \rho V_\theta^2 + p - \frac{1}{\text{Re}} \tau_{\theta\theta} \\ \rho V_z V_\theta - \frac{1}{\text{Re}} \tau_{\theta z} \\ \left\{ \begin{array}{l} \rho H V_\theta - \frac{1}{\text{Re}} \\ (\tau_{\theta r} V_r + \tau_{\theta\theta} V_\theta + \tau_{\theta z} V_z) + \\ + \frac{q_\theta}{(\gamma-1)\text{Re}M^2\text{Pr}} \end{array} \right\} \end{bmatrix} \quad \mathbf{S} = \begin{bmatrix} \rho V_r \\ \rho V_r^2 - \rho V_\theta^2 - \frac{1}{\text{Re}} (\tau_{rr} - \tau_{\theta\theta}) \\ 2\rho V_r V_\theta - \frac{2}{\text{Re}} \tau_{r\theta} \\ \rho V_z V_r - \frac{1}{\text{Re}} \tau_{rz} \\ \left\{ \begin{array}{l} \rho H V_r - \frac{1}{\text{Re}} \\ (\tau_{rr} V_r + \tau_{r\theta} V_\theta + \tau_{rz} V_z) + \\ + \frac{q_r}{(\gamma-1)\text{Re}M^2\text{Pr}} \end{array} \right\} \end{bmatrix}$$

In the above equations we have introduced the total enthalpy $H = E + p/\rho$, and the usual similarities parameters Re, M, Pr defined as:

$$\text{Re} = \left(\frac{\rho V L}{\mu} \right)_r,$$

$$\text{M} = \left(\frac{V}{\sqrt{\gamma R T}} \right)_r,$$

$$\text{Pr} = \left(\frac{c_p \mu}{k} \right)_r.$$

The individual components of the viscous stress-tensor are explicitly obtained from (2.2):

$$\begin{aligned} \tau_{rr} &= 2\mu \left[\frac{\partial V_r}{\partial r} - \frac{\nabla \cdot \mathbf{V}}{3} \right] & \tau_{r\theta} &= \mu \left[\frac{1}{r} \frac{\partial V_r}{\partial \theta} + r \frac{\partial}{\partial r} \left(\frac{V_\theta}{r} \right) \right] \\ \tau_{\theta\theta} &= 2\mu \left[\frac{1}{r} \frac{\partial V_\theta}{\partial \theta} + \frac{V_r}{r} - \frac{\nabla \cdot \mathbf{V}}{3} \right] & \tau_{rz} &= \mu \left[\frac{\partial V_z}{\partial r} + \frac{\partial V_r}{\partial z} \right] \\ \tau_{zz} &= 2\mu \left[\frac{\partial V_z}{\partial z} - \frac{\nabla \cdot \mathbf{V}}{3} \right] & \tau_{\theta z} &= \mu \left[\frac{\partial V_\theta}{\partial z} + \frac{1}{r} \frac{\partial V_z}{\partial \theta} \right], \end{aligned}$$

with the divergence of velocity given by:

$$\nabla \cdot \mathbf{V} = \frac{1}{r} \frac{\partial(rV_r)}{\partial r} + \frac{1}{r} \frac{\partial V_\theta}{\partial \theta} + \frac{\partial V_z}{\partial z}.$$

The pressure is obtained from the non-dimensional equation of state

$$p = \frac{\rho T}{\gamma M^2}. \quad (2.4)$$

Finally, to close the system of equations, the molecular viscosity is computed according to the power law:

$$\mu(T) = T^{0.76}.$$

From a mathematical point of view, the Navier-Stokes equations are hyperbolic in the continuity equation and parabolic in the momentum and energy equations. This makes it possible to solve (2.3) using a *method of lines* approach, in which a spatial discretisation is first introduced giving an approximate solution of all the spatial derivatives. A time integration is then performed to update the solution to a new time level. The main elements to analyse are the spatial derivatives, the time integration technique and the boundary conditions treatment.

2.1.2 Linearised Navier-Stokes around a 1D base flow

Linearisation of Navier-Stokes equations is derived decomposing all variables into a base state $\bar{\Phi}$ value and a disturbance variable Φ' . Subtracting the base flow equations (which are implicitly satisfied), and neglecting all products containing more than one disturbance variable, the resulting equations govern the evolution of small perturbations on a given base flow. Following this procedure, one has:

$$\begin{aligned} \frac{\partial \rho'}{\partial t} + \underline{\nabla} \cdot (\rho' \bar{\mathbf{V}} + \bar{\rho} \mathbf{V}') &= 0 \\ \frac{\partial (\bar{\rho} \mathbf{V}' + \rho' \bar{\mathbf{V}})}{\partial t} + \underline{\nabla} \cdot [\bar{\rho} \bar{\mathbf{V}} \mathbf{V}' + \bar{\rho} \mathbf{V}' \bar{\mathbf{V}} + \rho' \bar{\mathbf{V}} \bar{\mathbf{V}} + p' \underline{\mathbf{I}}] &= \underline{\nabla} \cdot \underline{\underline{\tau}}' \\ \frac{\partial (\rho' \bar{E} + \bar{\rho} E')}{\partial t} + \underline{\nabla} \cdot [\bar{\rho} \bar{H} \mathbf{V}' + \bar{\rho} H' \bar{\mathbf{V}} + \rho' \bar{H} \bar{\mathbf{V}} + \mathbf{q}'] &= \underline{\nabla} \cdot (\underline{\underline{\tau}}' \cdot \mathbf{V}' + \underline{\underline{\tau}}' \cdot \bar{\mathbf{V}}), \end{aligned} \quad (2.5)$$

where

$$\begin{aligned} \underline{\underline{\tau}}' &= 2\bar{\mu}(\underline{\nabla} \mathbf{V}')_0^s + 2\mu'(\underline{\nabla} \bar{\mathbf{V}})_0^s \\ \mathbf{q}' &= -\bar{k} \underline{\nabla} T' - k' \underline{\nabla} \bar{T}, \end{aligned}$$

with $(\underline{\nabla} \mathbf{a})_0^s$ representing the symmetric part with zero trace (the strain) of $(\underline{\nabla} \mathbf{a})$.

If we consider a base axisymmetric ($\frac{\partial}{\partial \theta} = 0$), one-dimensional ($\frac{\partial}{\partial z} = 0$), parallel ($\bar{V}_r = 0$) flow, system (2.5) becomes:

$$\frac{\partial \mathbf{W}}{\partial t} + \frac{\partial \mathbf{A}}{\partial z} + \frac{\partial \mathbf{B}}{\partial r} + \frac{1}{r} \frac{\partial \mathbf{C}}{\partial \theta} + \frac{\mathbf{D}}{r} = 0, \quad (2.6)$$

$$\mathbf{A} = \begin{bmatrix} \bar{\rho}V'_z + \rho'\bar{V}_z \\ \bar{\rho}V'_r\bar{V}_z - \frac{1}{\text{Re}}\tau'_{zr} \\ \rho'\bar{V}_\theta\bar{V}_z + \bar{\rho}V'_\theta\bar{V}_z + \bar{\rho}\bar{V}_\theta V'_z - \frac{1}{\text{Re}}\tau'_{z\theta} \\ \bar{\rho}\bar{V}_z V'_z + \rho'\bar{V}_z\bar{V}_z + \bar{\rho}V'_z\bar{V}_z + p' - \frac{1}{\text{Re}}\tau'_{zz} \\ \left\{ \begin{array}{l} \rho'\bar{H}\bar{V}_z + \bar{\rho}H'\bar{V}_z + \bar{\rho}\bar{H}V'_z \\ -\frac{1}{\text{Re}}(\tau'_{zr}\bar{V}_r + \tau'_{z\theta}\bar{V}_\theta + \tau'_{zz}\bar{V}_z) \\ -\frac{1}{\text{Re}}(\bar{\tau}_{zr}V'_r + \bar{\tau}_{z\theta}V'_\theta + \bar{\tau}_{zz}V'_z) \\ + \frac{q'_z}{(\gamma-1)\text{Re}M^2\text{Pr}} \end{array} \right\} \end{bmatrix}$$

$$\mathbf{B} = \begin{bmatrix} \bar{\rho}V'_r \\ +p' - \frac{1}{\text{Re}}\tau'_{rr} \\ \bar{\rho}\bar{V}_\theta V'_r - \frac{1}{\text{Re}}\tau'_{r\theta} \\ \bar{\rho}\bar{V}_z V'_r - \frac{1}{\text{Re}}\tau'_{rz} \\ \left\{ \begin{array}{l} \bar{\rho}\bar{H}V'_r \\ -\frac{1}{\text{Re}}(\tau'_{rr}\bar{V}_r + \tau'_{r\theta}\bar{V}_\theta + \tau'_{rz}\bar{V}_z) \\ -\frac{1}{\text{Re}}(\bar{\tau}_{rr}V'_r + \bar{\tau}_{r\theta}V'_\theta + \bar{\tau}_{rz}V'_z) \\ + \frac{q'_r}{(\gamma-1)\text{Re}M^2\text{Pr}} \end{array} \right\} \end{bmatrix}$$

$$\mathbf{C} = \begin{bmatrix} \bar{\rho}V'_\theta + \rho'\bar{V}_\theta \\ \bar{\rho}V'_r\bar{V}_\theta - \frac{1}{\text{Re}}\tau'_{\theta r} \\ \rho'\bar{V}_\theta\bar{V}_\theta + \bar{\rho}V'_\theta\bar{V}_\theta + \bar{\rho}\bar{V}_\theta V'_\theta + p' - \frac{1}{\text{Re}}\tau'_{\theta\theta} \\ \rho'\bar{V}_z\bar{V}_\theta + \bar{\rho}V'_z\bar{V}_\theta + \bar{\rho}\bar{V}_z V'_\theta - \frac{1}{\text{Re}}\tau'_{\theta z} \\ \left\{ \begin{array}{l} \rho'\bar{H}\bar{V}_\theta + \bar{\rho}H'\bar{V}_\theta + \bar{\rho}\bar{H}V'_\theta \\ -\frac{1}{\text{Re}}(\tau'_{\theta r}\bar{V}_r + \tau'_{\theta\theta}\bar{V}_\theta + \tau'_{\theta z}\bar{V}_z) \\ -\frac{1}{\text{Re}}(\bar{\tau}_{\theta r}V'_r + \bar{\tau}_{\theta\theta}V'_\theta + \bar{\tau}_{\theta z}V'_z) \\ + \frac{q'_\theta}{(\gamma-1)\text{Re}M^2\text{Pr}} \end{array} \right\} \end{bmatrix}$$

$$\mathbf{D} = \begin{bmatrix} \bar{\rho}V'_r \\ -(\rho'\bar{V}_\theta\bar{V}_\theta + \bar{\rho}V'_\theta\bar{V}_\theta + \bar{\rho}\bar{V}_\theta V'_\theta) - \frac{1}{\text{Re}}(\tau'_{rr} - \tau'_{\theta\theta}) \\ 2\bar{\rho}V'_r\bar{V}_\theta - \frac{2}{\text{Re}}\tau'_{r\theta} \\ \bar{\rho}V'_r\bar{V}_z - \frac{1}{\text{Re}}\tau'_{rz} \\ \left\{ \begin{array}{l} \bar{\rho}\bar{H}V'_r \\ -\frac{1}{\text{Re}}(\tau'_{rr}\bar{V}_r + \tau'_{r\theta}\bar{V}_\theta + \tau'_{rz}\bar{V}_z) + \\ -\frac{1}{\text{Re}}(\bar{\tau}_{rr}V'_r + \bar{\tau}_{r\theta}V'_\theta + \bar{\tau}_{rz}V'_z) \\ + \frac{q'_r}{(\gamma-1)\text{Re}M^2\text{Pr}} \end{array} \right\} \end{bmatrix}$$

In the linearised code, all the derivatives of the base flow are initially computed and stored. Equation (2.6) is integrated in time to give the conservative variables:

$$\mathbf{W} = \begin{bmatrix} W_1 \\ W_2 \\ W_3 \\ W_4 \\ W_5 \end{bmatrix} = \begin{bmatrix} \rho' \\ \bar{\rho} V_r' \\ \bar{\rho} V_\theta' + \rho' \bar{V}_\theta \\ \bar{\rho} V_z' + \rho' \bar{V}_z \\ \bar{\rho} E' + \rho' \bar{E} \end{bmatrix}.$$

Note that the integration time step has to be evaluated according to the general stability criterion of the numerical scheme (cfr. §2.4.1) but referring to the base flow, so it can be calculated only once. After the state vector \mathbf{W} has been updated, the primitive disturbance quantities are deduced from the conservative variables:

$$\mathbf{U} = \begin{bmatrix} U_1 \\ U_2 \\ U_3 \\ U_4 \\ U_5 \end{bmatrix} = \begin{bmatrix} \rho' \\ V_r' \\ V_\theta' \\ V_z' \\ T' \end{bmatrix} = \begin{bmatrix} W_1 \\ W_2/\bar{\rho} \\ (W_3 - W_1 \bar{V}_\theta)/\bar{\rho} \\ (W_4 - W_1 \bar{V}_z)/\bar{\rho} \\ \gamma(\gamma - 1)M^2 \{ (W_5 - \bar{E}W_1) - (\bar{V}_\theta U_3 + \bar{V}_z U_2) \} / \bar{\rho} \end{bmatrix}.$$

Then, the linearised pressure, viscosity and total enthalpy are calculated using the linearised state equation and the linearised power law:

$$\begin{aligned} p' &= \frac{\bar{\rho} T' + \rho' \bar{T}}{\gamma M^2}, \\ \mu' &= \omega \bar{T}^{\omega-1} T', \\ H' &= \frac{T'}{(\gamma - 1)M^2} + (\bar{V}_\theta V_\theta' + \bar{V}_z V_z'). \end{aligned}$$

Since the base flow is assumed to be one-dimensional, direct numerical simulations of the linear equations employ periodic boundary conditions in the streamwise direction. Solutions of (2.6) describe the evolution of small perturbations which need to be explicitly introduced to initiate the state vector \mathbf{W} . In the literature this is referred to as temporal stability analysis by DNS and we will label in this work as Linear Temporal Simulation (LTS) to distinguish from the spatial cases solved by the full nonlinear code (hereafter simply denoted as DNS). LTS results are expected to match with those obtained by solving the dispersion relation of the corresponding problem. Note that the nonlinear code itself may be adapted to carry on

stability analysis in a temporal framework, introducing a body force which compensates the diffusion of the base flow (see, for example Luo and Sandham [71]). However, for highly receptive flows it is problematic to discriminate between linear and nonlinear effects, and some quantities (real and imaginary frequencies) may not be clearly evaluated.

2.2 Spatial discretisation

The code designed for this work is a finite difference code, with spatial discretisation performed using a spectral method in the homogeneous directions and compact methods for the non-homogeneous directions. For spatial calculations, the periodic direction is the azimuthal one θ , whereas for temporal calculations also the streamwise direction z is assumed to be periodic.

2.2.1 Non-homogeneous directions

The compact schemes used were first introduced by Lele [62], and belong to the Pade's scheme family [43]. Let f_i be the value of a function on N points x_i and h the distance between two consecutive points. We solve a system of equations composed of a linear combination of the values f_i of the function and the unknown values of its derivatives f'_i . For example we may write (but it's not the only possible choice):

$$\alpha f'_{i-1} + f'_i + \alpha f'_{i+1} = \frac{1}{h} [a (f_{i+1} - f_{i-1}) + b (f_{i+2} - f_{i-2})] . \quad (2.7)$$

A Taylor expansion for f_i and f'_i can be written as:

$$\begin{aligned} f_{i\pm d} &= f_i \pm \sum_{n=1}^{\infty} \frac{f_i^{(2n-1)}}{(2n-1)!} d^{2n-1} h^{2n-1} + \sum_{n=1}^{\infty} \frac{f_i^{(2n)}}{(2n)!} d^{2n} h^{2n} , \\ f'_{i\pm d} &= f'_i \pm \sum_{n=1}^{\infty} \frac{f_i^{(2n)}}{(2n-1)!} d^{2n-1} h^{2n-1} + \sum_{n=1}^{\infty} \frac{f_i^{(2n+1)}}{(2n)!} d^{2n} h^{2n} . \end{aligned} \quad (2.8)$$

Substituting expressions (2.8) in (2.7) and omitting the index i we get:

$$\begin{aligned} (1 + 2\alpha)f' + 2\alpha \sum_{n=1}^{\infty} \frac{f^{(2n+1)} h^{2n}}{(2n)!} &= \\ &= \frac{1}{h} \left[2a \sum_{n=1}^{\infty} \frac{f^{(2n-1)} h^{2n-1}}{(2n-1)!} + 2b \sum_{n=1}^{\infty} \frac{f^{(2n-1)} (2h)^{2n-1}}{(2n-1)!} \right] . \end{aligned} \quad (2.9)$$

For different values of n , eq (2.9) can be explicitly developed and the coefficients a, b, α can be determined imposing the largest number of terms in each equation equal to zero. The

first non zero term will give the truncation error of the final formula. For $n = 1, 2, 3$ this leads to the following relations:

$$\begin{aligned} n = 1 &\Rightarrow 2\alpha = 2a + 4b - 1 & \epsilon &= \frac{\alpha f^{(3)} h^2}{1!}, \\ n = 2 &\Rightarrow 3\alpha = a + 8b & \epsilon &= \frac{2\alpha f^{(5)} h^4}{4!}, \\ n = 3 &\Rightarrow 10\alpha = 2a + 64b & \epsilon &= \frac{2\alpha f^{(7)} h^6}{6!}. \end{aligned} \quad (2.10)$$

Coefficients obtained from set (2.10) are then substituted in (2.7) resulting in a sixth order formula which can be used in all the points except for the first two close to the boundaries ($i = 1, 2$ and $i = N - 1, N$) for which the initial linear combination has to be different. More precisely, for $i = 2$ and $i = N - 1$ we can assume

$$\alpha f'_{i-1} + f'_i + \alpha f'_{i+1} = \frac{a}{h} (f_{i+1} - f_{i-1}) \quad (2.11)$$

and, applying the same procedure, we get

$$\begin{aligned} k = 1 &\Rightarrow 1 + 2\alpha = 2 & \epsilon &= \frac{2\alpha f^{(3)} h^2}{2!}, \\ k = 2 &\Rightarrow 3\alpha = a & \epsilon &= \frac{2\alpha f^{(5)} h^4}{4!}, \end{aligned} \quad (2.12)$$

whereas the points on the boundaries need a one-side discretisation formula like:

$$\begin{aligned} f'_1 + \alpha_1 f'_2 &= \frac{1}{h} [a_1 f_1 + b_1 f_2 + c_1 f_3 + d_1 f_4], \\ f'_N + \alpha_N f'_N &= \frac{1}{h} [a_N f_N + b_N f_{N-1} + c_N f_{N-2} + d_N f_{N-3}]. \end{aligned} \quad (2.13)$$

The system obtained in this case is

$$\begin{aligned} k = 1 &\Rightarrow a + b + c + d = 2 \\ k = 2 &\Rightarrow [1 + \alpha] = \pm b \pm 2c \pm 3d & \epsilon &= \frac{\alpha f^{(2)} h}{1!} \\ k = 3 &\Rightarrow \pm\alpha = \frac{1}{2!}b + \frac{2^2}{2!}c + \frac{3^2}{2!}d & \epsilon &= \frac{\alpha f^{(3)} h^2}{2!} \\ k = 4 &\Rightarrow \frac{1}{2!}\alpha = \pm \frac{1}{3!}b \pm \frac{2^3}{3!}c \pm \frac{3^3}{3!}d & \epsilon &= \frac{\alpha f^{(4)} h^3}{3!}, \end{aligned} \quad (2.14)$$

where positive signs hold for $i = 1$ and negative for $i = N$. The final formula is of third order accuracy. System (2.14) is undetermined, meaning that a fourth order accuracy may be reached imposing an additional relation. However, as also reported by Carpenter *et al.* [14], we have found that when used in conjunction with (2.7) and (2.11) the fourth order formula

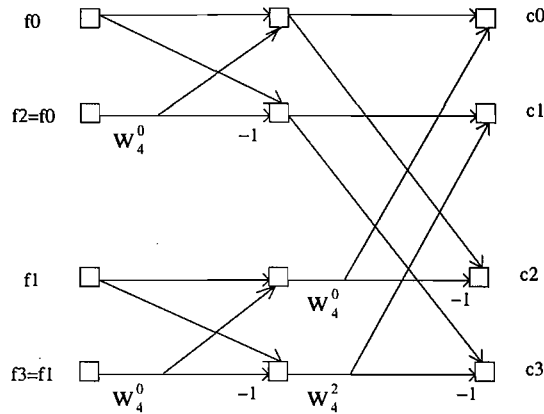


Figure 2.1: Butterfly algorithm of the Fast Fourier Transform.

2.2.2 Homogeneous directions

Given the values of a function $f(x)$ on the sequence of points $x_{-\frac{N}{2}}, x_{-\frac{N}{2}-1} \dots x_0 \dots x_{+\frac{N}{2}-1}$ such that $x_{-\frac{N}{2}} = 0$ and $x_{+\frac{N}{2}-1} = L = (N - 1)h$ the discrete Fourier transform of the sequence $\{f_i\}$ is defined as:

$$c_k = \frac{1}{N} \sum_{i=-\frac{N}{2}}^{\frac{N}{2}-1} f_i e^{-I2\pi \frac{ki}{N}} \quad k = -\frac{N}{2} \dots \frac{N}{2} - 1 \quad (2.20)$$

where I denotes the imaginary unit. The inverse transform of (2.20) gives the $\{f_i\}$ as a function of the spectral coefficients:

$$f_i = \sum_{k=-\frac{N}{2}}^{\frac{N}{2}-1} c_k e^{I2\pi \frac{ik}{N}} \quad i = -\frac{N}{2} \dots \frac{N}{2} - 1. \quad (2.21)$$

Values of derivatives can then be evaluated from (2.21) as

$$f_i^{(j)} = \sum_{k=-\frac{N}{2}}^{\frac{N}{2}-1} z_k^{(j)} e^{I2\pi \frac{ik}{N}} \quad i = -\frac{N}{2} \dots \frac{N}{2} - 1 \quad (2.22)$$

with

$$z_k^{(1)} = \frac{Ik2\pi}{Nh} c_k \quad z_k^{(2)} = -\left(\frac{k2\pi}{Nh}\right)^2 c_k.$$

The procedure is therefore straightforward: we first evaluate the spectral coefficients c_k according to (2.20), then we calculate the coefficients $z_k^{(j)}$ and finally we derive $f_i^{(j)}$ from (2.22). The transformation operations is made by a base 2 FFT algorithm reducing the number of operations from $O(N^2)$ to $O(N \log_2 N)$.

The use of the spectral technique has proven to be essential throughout this study. First of all, as detailed later (cfr. §2.3) it provides the opportunity to calibrate easily the spectral accuracy of the calculation during run-time. Another advantage is its straightforward application as a diagnostic tool for stability analysis. Even more interestingly, although the code is not spectral/pseudospectral where specific modes can be deliberately excited or removed (see, for instance, an interesting application given by Sandberg [91] for stability analysis of supersonic wakes), due to the special symmetry of the butterfly algorithm we can maintain a similar benefit: it is possible to introduce disturbances confined in a specific range of frequencies. We clarify this last point in more detail.

In order to render any calculation effectively three-dimensional, the use of the spectral differentiation requires the introduction of an initial disturbance exciting some of the azimuthal wavenumbers. In the absence of any perturbation, if the initial flow field is perfectly axisymmetric (either defined analytical or resulting from a previous axisymmetric run) the 3D calculation will continue to produce axisymmetric results. One possibility is the introduction of a small perturbation on every meridional plane at the same location (r_0, z_0) , that is, a random signal $f = f(r_0, \theta = 0 \dots 2\pi, z_0)$ is superimposed on one of the flow variables. In the attempt to detect self-sustained dynamics, this operation must be performed just for the first iteration and has to be distinguished from the application of continuous forcing.

As discussed in the introductory chapter, swirling flows are characterised by the existence of self-excited global modes. According to most of the existing studies, these are generally bending modes $m = 1$, associated with the rotation of the vortex tube around its axis. Our interest is however mainly focused on the examination of superimposed dynamics driven by self-sustained modes with higher azimuthal wavenumber. When the disturbances are small, the assumption of linearity holds, and each mode can be thought to evolve independently. Conversely, when these modes reach a large amplitude, nonlinearity produces a transfer of energy from low to high wavenumbers which continues until the growth of the global modes is fully compensated (saturation). This mechanism renders problematic the identification of the “long-term” behaviour of higher modes, because it’s not possible to discriminate between linear and nonlinear effects.

The nonlinear interactions are described by algebraic identities of the form

$$\sin p + \sin q = \frac{1}{2} \sin \frac{p+q}{2} \cos \frac{p-q}{2} .$$

According to the above formula, the nonlinear interaction of two modes, say m_1 and m_2 , produces wavenumbers $p = m_1 + m_2$ and $q = m_1 - m_2$. It turns out that if m_1 and m_2 are both multiples of a certain integer, the nonlinearly generated wavenumbers are multiples of the same integer.

In figure 2.1 it is reported a schematic of the butterfly algorithm working on a sequence of 4 points. In the diagram it has been indicated $W_N^k = \exp(i2\pi k/N)$. To remain in the context of our applications, the sequence can be thought as the perturbation introduced at (r_0, z_0) during a calculation performed with $n_\theta = 4$ meridional planes. Consider a signal obtained by duplication: $\{f_0, f_1, f_2 = f_0, f_3 = f_1\}$; now, due to the duplication in the physical space, the corresponding Fourier coefficients will be zero for $k = 1$ and $k = 3$. If performed by FFT, these values will result exactly zero at whatever precision one may work. Indeed, after the binary reversal swap [18] has been performed, the samples are stored according to the first line on the left side of the butterfly. Following the diagram, the computed value for the coefficients c_1 and c_3 will be:

$$\begin{aligned} c_1 &= (f_0 - W_4^0 f_0) + W_4^2 (f_1 - W_4^0 f_1) , \\ c_3 &= (f_0 - W_4^0 f_0) - W_4^2 (f_1 - W_4^0 f_1) . \end{aligned}$$

These values will be *exactly* zero, independently of the machine precision, because the operations that need to be performed (the evaluation of $W_4^0 = 1$ and the algebraic summation $x - x = 0$) are not subjected to round-off error. When used for a higher number of samples, the result remains unchanged, because the binary reversal swap orders the sequence in such a way that equal samples are always coupled to form an elementary unit of the butterfly (this actually represents an efficient and easy way to implement the binary reversal algorithm [18]).

The importance of these considerations relies on the fact that exciting an axisymmetric flow with a small perturbation obtained by duplication of a random signal, one ensures that all the azimuthal odd modes are filtered out during the calculation: nonlinearity does not modify this condition, since the product of two signals obtained by duplication is still a duplicated signal with all the odd modes *exactly* zero. Following the same reasoning, if the original signal is made by a quadruplication, during the calculation the only excited modes will remain multiples of $m = 4$. We have deliberately used this idea in order to isolate the growth of unstable modes with azimuthal wavenumber $m = 2, 4$ and to discriminate their evolution from that of the bending mode.

2.3 Time advancement

In the code two different techniques of time integration have been implemented: an explicit Runge-Kutta scheme, and a Dual Time Stepping method. The latter was introduced to circumvent the difficulty of the time step restriction, which becomes particularly severe in the DNS at high Reynolds numbers ($Re \geq 800$).

2.3.1 Explicit method

The explicit time integration is performed using the classic explicit 4th order Runge-Kutta method. After the discretisation of the spatial operators, we write eq. (2.3) in the compact notation:

$$\frac{d\mathbf{W}}{dt} = \mathbf{R}(\mathbf{W}) . \quad (2.23)$$

The form of the scheme implemented to update from temporal level n to $n + 1$ is

$$\begin{aligned} \mathbf{W}^{(1)} &= \mathbf{W}^n \\ \mathbf{W}^{(2)} &= \mathbf{W}^n + \Delta t \alpha_2 \mathbf{R}(\mathbf{W}^{(1)}) \\ \mathbf{W}^{(3)} &= \mathbf{W}^n + \Delta t \alpha_3 \mathbf{R}(\mathbf{W}^{(2)}) \\ \mathbf{W}^{(4)} &= \mathbf{W}^n + \Delta t \alpha_4 \mathbf{R}(\mathbf{W}^{(3)}) \\ \mathbf{W}^{n+1} &= \mathbf{W}^n + \Delta t \sum_{j=1}^4 \beta_j \mathbf{R}(\mathbf{W}^{(j)}) , \end{aligned} \quad (2.24)$$

where the coefficients are:

$$\begin{aligned} \alpha_2 &= \frac{1}{2} & \alpha_3 &= \frac{1}{2} & \alpha_4 &= 1 , \\ \beta_1 &= \frac{1}{6} & \beta_2 &= \beta_3 &= \frac{1}{3} & \beta &= \frac{1}{6} . \end{aligned}$$

In the linear case of a scalar model problem we have $R(W) = \Omega W$ with Ω complex. A recursive substitution in (2.24) gives

$$\begin{aligned} W^{(2)} &= \left(1 + \frac{1}{2}\Omega\Delta t\right) W^n , \\ W^{(3)} &= \left[1 + \frac{1}{2}\Omega\Delta t + \frac{1}{4}(\Omega\Delta t)^2\right] W^n , \\ W^{(4)} &= \left[1 + \Omega\Delta t + \frac{1}{2}(\Omega\Delta t)^2 + \frac{1}{4}(\Omega\Delta t)^3\right] W^n \end{aligned}$$

and

$$W^{n+1} = z W^n = \left[1 + \Omega\Delta t + \frac{(\Omega\Delta t)^2}{2} + \frac{(\Omega\Delta t)^3}{6} + \frac{(\Omega\Delta t)^4}{24}\right] W^n , \quad (2.25)$$

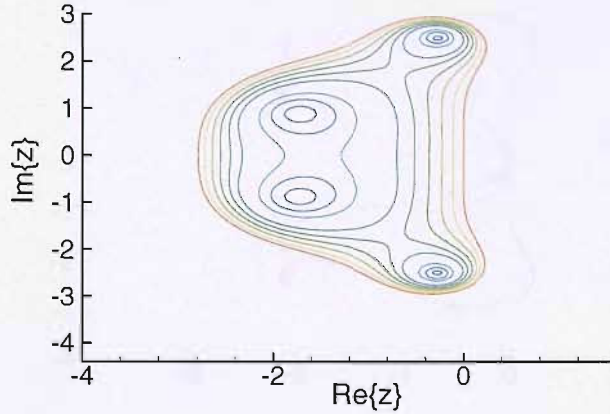


Figure 2.2: Stability region of the Runge-Kutta 4-th order scheme, visualised by isocontour of the amplification factor $|z|$ for $|z| = 1, 2, \dots, 10$. Blue regions are the most damped. Red regions are the less damped.

where $z = z(\Omega\Delta t)$ is the root of the characteristic polynomial (also known as the amplification factor) providing the main information about the numerical scheme. In particular, the formula is fourth-order accurate, since z is the Taylor expansion of the exact amplification $e^{(\Omega\Delta t)}$ up to the fourth order. Furthermore, the linear stability condition requires $|z| \leq 1$, defining a stability region \mathfrak{R}_A in the complex plane shown in fig. 2.2.

In order to study the stability condition for the scheme applied to (2.3), we assume a scalar linear equation model of the form:

$$\frac{\partial w}{\partial t} + a \left[\frac{\partial}{\partial z} + \frac{\partial}{\partial r} + \frac{1}{r} \frac{\partial}{\partial \theta} \right] w = \nu \left[\frac{\partial^2}{\partial z^2} + \frac{\partial^2}{\partial r^2} + \frac{1}{r^2} \frac{\partial^2}{\partial \theta^2} \right] w. \quad (2.26)$$

According to Von Neumann theory, the overall stability will be guaranteed if the spectrum of the spatial discretisation operators is contained within the stability region \mathfrak{R}_A . If the periodic direction θ is discretised by a spectral method, then the eigenvalues associated with θ differentiation can be straightforwardly derived from (2.22):

$$\begin{aligned} \{w'_i\}_k &= \frac{Ik2\pi}{N\Delta\theta} c_k e^{I2\pi\frac{ik}{N}} = \frac{I\Phi_k}{\Delta\theta} \{w_i\}_k, \\ \{w''_i\}_k &= -\left(\frac{k2\pi}{N\Delta\theta}\right)^2 c_k e^{I2\pi\frac{ik}{N}} = -\frac{\Phi_k^2}{\Delta\theta^2} \{w_i\}_k, \end{aligned} \quad (2.27)$$

with the phase $\Phi_k = \frac{2\pi k}{N}$ varying from $-\pi$ to π since the Discrete Fourier Transform accounts for wavenumbers k in the range $-N/2 \dots N/2$.

For the z and r directions, supposing they are discretised by compact schemes, eigenvalues can be obtained introducing the usual *shift* operator E

$$E_{\pm x} \{w_i\}_k = \{w_{i\pm 1}\}_k$$

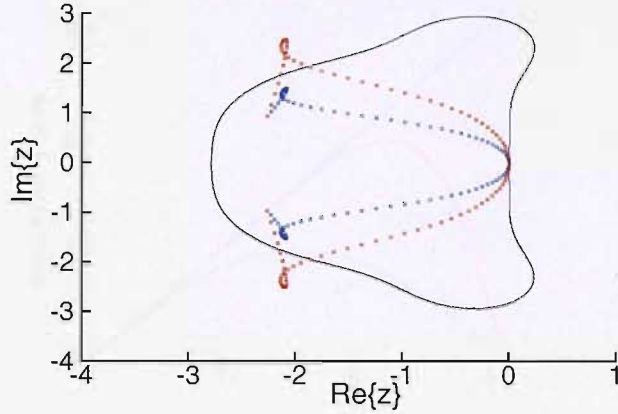


Figure 2.3: Fourier symbol obtained keeping constant the values $CFL_{zr}^{(2)} = 0.3$, $CFL_{\theta}^{(1)} = 0.4$, $CFL_{\theta}^{(2)} = 0.1$, and increasing the $CFL_{zr}^{(1)}$ from 0.4 (blue curve) to 0.9 (red curve). The linear stability is lost because some frequencies lie outside the stability region of the Runge Kutta 4-th order.

and recalling its property to have eigenvalues of the form $e^{I\Phi_k}$ with corresponding eigenfunctions $e^{Ii\Phi_k}$. Substituting into the standard formula giving the first and second compact derivatives for internal points (2.16)-(2.19), we get:

$$\begin{aligned} \{w'_i\}_k &= \frac{I \left[\frac{1}{18} \sin(2\Phi_k) + \frac{14}{9} \sin(\Phi_k) \right]}{h \left[1 + \frac{2}{3} \cos(\Phi_k) \right]} \{w_i\}_k, \\ \{w''_i\}_k &= \frac{\frac{3}{22} [\cos(2\Phi_k) - 1] + \frac{24}{11} (\cos \Phi_k - 1)}{h^2 \left[1 + \frac{4}{11} \cos(2\Phi_k) \right]} \{w_i\}_k. \end{aligned} \quad (2.28)$$

We can therefore write eq. (2.26) for a single mode k on the node i as

$$\Delta t \frac{dw}{dt} = \left[\dot{z}^{(1)} + \dot{z}^{(2)} \right] w, \quad (2.29)$$

with the Fourier symbols $\dot{z}^{(1)}$, $\dot{z}^{(2)}$ given by

$$\begin{aligned} \dot{z}^{(1)} &= -CFL_{\theta}^{(1)} I \Phi - CFL_{zr}^{(1)} I \frac{\frac{1}{18} \sin(2\Phi) + \frac{14}{9} \sin(\Phi)}{1 + \frac{2}{3} \cos(\Phi)}, \\ \dot{z}^{(2)} &= -CFL_{\theta}^{(2)} \Phi^2 + CFL_{zr}^{(2)} \frac{\frac{3}{22} [\cos(2\Phi) - 1] + \frac{24}{11} (\cos \Phi - 1)}{1 + \frac{4}{11} \cos(2\Phi)} \end{aligned} \quad (2.30)$$

and

$$\begin{aligned} CFL_{\theta}^{(1)} &= \frac{a \Delta t}{r \Delta \theta} & CFL_{zr}^{(1)} &= a \left[\frac{1}{\Delta z} + \frac{1}{\Delta r} \right] \Delta t, \\ CFL_{\theta}^{(2)} &= \frac{\nu \Delta t}{r^2 \Delta \theta^2} & CFL_{zr}^{(2)} &= \nu \left[\frac{1}{\Delta z^2} + \frac{1}{\Delta r^2} \right] \Delta t. \end{aligned} \quad (2.31)$$

The Fourier symbol associated with the right hand side of (2.29) depends on the four CFL parameters and different combinations of these parameters can be used to preserve the sta-

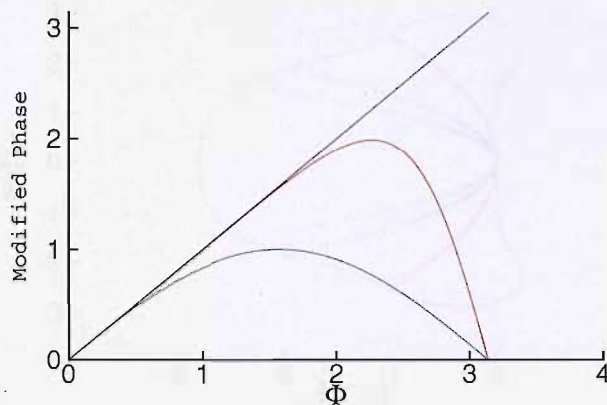


Figure 2.4: Plot of the modified phase vs the real phase for first derivatives approximations: spectral method (black curve), sixth-order compact method (red curve) and second-order central differences (blue curve).

bility. For example, figure 2.3 shows how the stability is lost when $\text{CFL}_{z_r}^{(1)}$ is increased keeping constant the others. In (2.30) the coefficients multiplying the four CFL parameters are a function of the phase Φ . They measure how good the numerical scheme approximates the spatial derivative. They are called modified phases or modified (scaled) wavenumbers. For the spectral differentiation, real and modified phase coincide, *i.e.* when working within the range $\Phi = -\pi \dots \pi$ the only error generated by spectral differentiation is given by round-off. For finite difference schemes, the modified phase is a more complicated function of Φ . Figure 2.4 shows the modified phase for the sixth-order compact scheme used here, and, for comparison, the modified phase of the classic explicit central second-order scheme. As the modified phase deviates from the true one, the dispersive error of the scheme is produced.

As a consequence of the higher spectral accuracy offered by the spectral differentiation, it can be verified that the two terms which multiply $\text{CFL}_{z_r}^{(1)}$ and $\text{CFL}_{z_r}^{(2)}$ in (2.30) are in magnitude always smaller than π and π^2 . Therefore, in order to strengthen the stability of the scheme and to reduce the control parameters within the code, we can adopt a more stringent condition assuming in our analysis that all the derivatives are performed spectrally². In this case, the Fourier symbols of the modal equation (2.29) become

$$\begin{aligned} \dot{z}^{(1)} &= -\text{CFL}^{(1)} I \Phi, \\ \dot{z}^{(2)} &= -\text{CFL}^{(2)} \Phi^2, \end{aligned}$$

²Observe that in spite of these considerations the discussion about whether or not a higher accuracy discretisation scheme should be *a priori* preferred is not trivial at all.

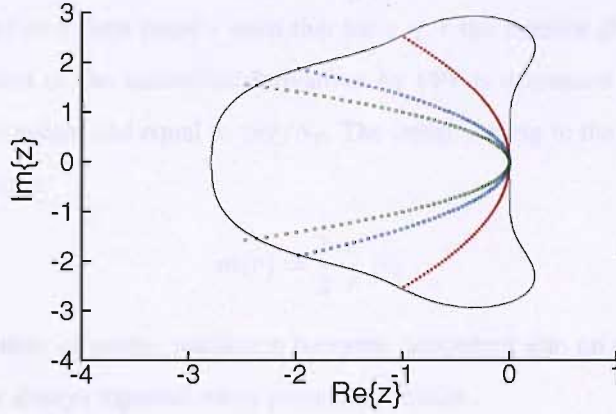


Figure 2.5: Fourier symbol $|z^{(1)} + z^{(2)}|$ calculated for $\text{CFL}^{(1)} = 0.5, \text{CFL}^{(2)} = 0.05$ (green curve), $\text{CFL}^{(1)} = 0.6, \text{CFL}^{(2)} = 0.1$ (blue curve) and $\text{CFL}^{(1)} = 0.8, \text{CFL}^{(2)} = 0.2$ (red curve).

with

$$\begin{aligned} \text{CFL}^{(1)} &= a \left[\frac{1}{\Delta z} + \frac{1}{\Delta r} + \frac{1}{r} \frac{1}{\Delta \theta} \right] \Delta t, \\ \text{CFL}^{(2)} &= \nu \left[\frac{1}{\Delta z^2} + \frac{1}{\Delta r^2} + \frac{1}{r^2} \frac{1}{\Delta \theta^2} \right] \Delta t. \end{aligned}$$

Figure 2.5 shows that adopting for example the value $\text{CFL}^{(1)} = 0.8$ and $\text{CFL}^{(2)} = 0.2$ the spectrum of the spatial operator lies completely within the stability region of the Runge-Kutta \mathfrak{R}_A , *i.e.* linear stability is ensured. Therefore the time step has to be calculated as

$$\Delta t = \min \left\{ \frac{\text{CFL}^{(1)}}{a} \left[\frac{1}{\Delta z} + \frac{1}{\Delta r} + \frac{1}{r} \frac{1}{\Delta \theta} \right]^{-1}; \frac{\text{CFL}^{(2)}}{\nu} \left[\frac{1}{\Delta z^2} + \frac{1}{\Delta r^2} + \frac{1}{r^2} \frac{1}{\Delta \theta^2} \right]^{-1} \right\} \quad (2.32)$$

Application of the criterion to the full set of equation (2.3) is not direct. In that case, a is not uniquely defined because the acoustic wave propagation is not isotropic. The spectral radii of the Jacobian matrices associated with the Eulerian fluxes, namely $|V_z + c|$, $|V_r + c|$ and $|V_\theta + c|$ have to replace a and be divided by the grid size of the corresponding direction in the definitions of the two CFL parameters. The value to choose for ν is problem dependent. Assuming $\nu = \frac{\mu}{(\gamma-1)M^2 \text{Re}Pr}$, the most stringent limitation in the subsonic regime would be given by viscous diffusion. However, this is not always the case, since unless there are sources of energy and strong thermal effects, the stiffness of system (2.3) is represented by the acoustic wave propagation. Numerical tests have confirmed this conclusion, thus the value selected in this study is $\nu = \frac{\mu}{\text{Re}}$.

Time step restriction imposed by (2.32) is too severe in the three-dimensional simulations because of the dependence on r and r^2 . A widely adopted procedure [10, 81, 87, 91]

to alleviate this condition is to drop the number of azimuthal modes when approaching the axis. We define a limit point \bar{r} such that for $r \leq \bar{r}$ the number of modes accounted in the reconstruction of the azimuthal derivatives by FFT is decreased keeping the quantity $\Delta s = 2\pi r/N_\theta$ constant and equal to $2\pi\bar{r}/N_\theta$. The linear scaling in the number of azimuthal modes is therefore:

$$m(r) = \frac{1}{2} \frac{r}{\bar{r}} N_\theta .$$

For a given number of points, resolution becomes dependent also on the choice of \bar{r} whose value should be always reported when presenting results.

In spite of these considerations, in the code we assume, as a natural extension in the definition of the two CFL parameters, the following expressions

$$\begin{aligned} \text{CFL}^{(1)} &= \left[\frac{|V_z + c|}{\Delta z} + \frac{|V_r + c|}{\Delta r} + \frac{m(r)}{r} |V_\theta + c| \right] \Delta t = \text{dc}_1 \Delta t , \\ \text{CFL}^{(2)} &= \frac{\mu}{\text{Re}} \left[\frac{1}{\Delta z^2} + \frac{1}{\Delta r^2} + \frac{m^2(r)}{r^2} \right] \Delta t = \text{dc}_2 \Delta t , \end{aligned}$$

and the time step is calculated as

$$\Delta t = \min \left[\frac{\text{CFL}^{(1)}}{\text{dc}_1}, \frac{\text{CFL}^{(2)}}{\text{dc}_2} \right] . \quad (2.33)$$

The great advantage offered by the technique of dropping the number of modes is the possibility to modify the resolution during run-time. As discussed in the introduction, the main elements characterising swirling flows are vortex breakdown and vortex stability. At least at low Reynolds number, we will show that there exists a causal relation between them, *i.e.* the loss of stability occurs as a consequence of the vortex breakdown. Since the vortex breakdown itself represents a pure axisymmetric phenomenon developing on time scales relatively long, the use of a high resolution in the azimuthal direction (here measured by a small value of \bar{r}), is not necessary. By monitoring the growth of azimuthal unstable modes, one can calibrate \bar{r} , reducing its values if necessary.

The technique has proved to be robust and efficient for low Reynolds number cases. For high Reynolds numbers ($\text{Re} \geq 800$), resolution requirements have forced us to maintain the number of modes nearly constant when moving along the radius. For these specific cases, therefore, to circumvent the difficulty of the time step restriction, a dual time stepping approach was introduced.

2.3.2 Dual Time Stepping

In a dual time step approach the base idea is to introduce a temporal discretisation of eq. (2.23) using an A-stable integration scheme, where for A-stable we mean an integration formula whose stability region \mathfrak{R}_A coincides with the entire negative complex plane [43]. Among all the A-stable formulae, the most accurate is the trapezoidal, but it's well documented [37] that it can generate spurious oscillations in the solution. For our applications, a second order backward scheme is preferred. Equation (2.23) is discretised as follows:

$$\frac{3}{2\Delta t}\mathbf{W}_{n+1} - \frac{2}{\Delta t}\mathbf{W}_n + \frac{1}{2\Delta t}\mathbf{W}_{n-1} = \mathbf{R}(\mathbf{W}_{n+1}). \quad (2.34)$$

The scheme is implicit, since the rhs is a function of the unknown variables, and as a consequence of the A-stability, the time step Δt becomes an user-input parameter to be chosen based *only* on accuracy constraints. To solve the nonlinear equation (2.34), solution \mathbf{W}^{n+1} is computed as the *steady* solution of the initial value problem:

$$\begin{aligned} \frac{d}{d\tau}\mathbf{W} &= \mathbf{R}^*(\mathbf{W}) \\ \mathbf{W}(\tau = 0) &= \mathbf{W}_0, \end{aligned} \quad (2.35)$$

where τ is a non-physical variable *ad hoc* introduced, \mathbf{W}_0 is an arbitrary solution of first guess, and the $\mathbf{R}^*(\mathbf{W})$ is the so-called *unsteady* residual, given by:

$$\mathbf{R}^*(\mathbf{W}) = -\frac{3}{2\Delta t}\mathbf{W} + \mathbf{R}(\mathbf{W}) + \mathbf{Q}(\mathbf{W}_n, \mathbf{W}_{n-1}) \quad (2.36)$$

with

$$\mathbf{Q}(\mathbf{W}_n, \mathbf{W}_{n-1}) = \frac{2}{\Delta t}\mathbf{W}_n - \frac{1}{2\Delta t}\mathbf{W}_{n-1}. \quad (2.37)$$

A steady solution of (2.35) is also the desired physical solution \mathbf{W}_{n+1} in the (2.34). In practice, to update the physical solution from level n to level $n + 1$ equation (2.35) has to be integrated in the dual variable τ , until a steady solution is reached. The integration in the dual variable can be performed using the Runge-Kutta described in previous subsection, and will be similarly subjected to stability constraints. The great difference is that now the integration represents a pure iterative process, thus one may use techniques which reduce the accuracy of the transient solution but accelerate the convergence toward a steady state. Among these, the simplest one, but very likely the most efficient, is the Local Time Stepping: the stability restriction imposed on the time step becomes local and the solution on any

grid point is updated according to a local integration time step. Formally, it's like solving instead of (2.35) the following equation:

$$\frac{1}{\alpha(r, \theta, z)} \frac{d}{d\tau} \mathbf{W} = \mathbf{R}^*(\mathbf{W}) . \quad (2.38)$$

It's obvious that (2.35) and (2.38) have the same steady solution.

With regard to the stability condition of the dual integration, one has to follow the analysis of previous subsection applied to the linear scalar form of (2.35). The term \mathbf{Q} can be omitted because it represents a constant during the integration. The modal equation (2.29) is modified in:

$$\Delta\tau \frac{dw}{dt} = \left[-\frac{3\Delta\tau}{2\Delta t} + \dot{z}^{(1)} + \dot{z}^{(2)} \right] w . \quad (2.39)$$

The Fourier symbol of the unsteady residual is made of two contributions, one is defined by (2.30) and corresponds to the steady counterpart of (2.36); the additional term is a constant, real, negative value, so that the whole Fourier symbol is shifted on the left (ref. to fig. 2.5) in the complex plane. This may create numerical instability if the time step is evaluated according to (2.32) without further restrictions. To overcome this difficulty, a possible solution is to treat implicitly the unsteady term $-\frac{3\Delta\tau}{2\Delta t}w$. We first recast the integration scheme (2.24) applied to (2.35) in the form:

$$\begin{aligned} \mathbf{W}_{n+\frac{k}{m}} &= \mathbf{W}_n + \alpha_k \Delta\tau \mathbf{R}^*(\mathbf{W}_{n+\frac{k-1}{m}}) , \\ m &= 4 \quad k = 1 \dots 4 . \end{aligned} \quad (2.40)$$

Observe that the integration scheme (2.40) coincides with (2.24) if the new coefficients are:

$$\alpha_1 = \frac{1}{4} \quad \alpha_2 = \frac{1}{3} \quad \alpha_3 = \frac{1}{2} \quad \alpha_4 = 1 .$$

Then, following Melson *et al.* [76], the unsteady term contained into \mathbf{R}^* is evaluated at level $n + \frac{k}{m}$, obtaining:

$$\begin{aligned} \mathbf{W}_{n+\frac{k}{m}} &= \mathbf{W}_n - \alpha_k \frac{3\Delta\tau}{2\Delta t} \mathbf{W}_{n+\frac{k}{m}} + \alpha_k \Delta\tau \left[+\mathbf{R}(\mathbf{W}_{n+\frac{k-1}{m}}) + \mathbf{Q} \right] , \\ k &= 1 \dots m . \end{aligned} \quad (2.41)$$

Arranging for $\mathbf{W}_{n+\frac{k}{m}}$ on the left hand side, this gives:

$$\begin{aligned} \mathbf{W}_{n+\frac{k}{m}} &= \frac{1}{1 + \alpha_k \frac{3\Delta\tau}{2\Delta t}} \left\{ \mathbf{W}_n + \alpha_k \Delta\tau \left[+\mathbf{R}(\mathbf{W}_{n+\frac{k-1}{m}}) + \mathbf{Q} \right] \right\} , \\ k &= 1 \dots m . \end{aligned} \quad (2.42)$$

It can be easily shown [76] that the above modification leads to an adaptive enlargement of the stability region \mathfrak{R}_A , and the condition (2.32) can now be safely used within the dual time integration.

The great advantage offered by Dual Time Stepping is the simplicity of its implementation within a pre-existing code, its flexibility and robustness. Some concern is associated with the stopping criterion chosen for the dual time integration. The definition of steady solutions requires the introduction of a norm. Theoretical analysis can be done starting from the requirement that the difference between the converged solution \mathbf{W} of the dual solver and the exact steady solution \mathbf{W}_{es} should have second order accuracy, in order to preserve the order of the backward difference. It can be proved that a sufficient condition to achieve this is that a norm of the unsteady residual $\mathbf{R}^*(\mathbf{W})$ (easily computed after any step of integration) has to be of order Δt . Unfortunately the condition is not necessary, and is generally more severe than what is really needed. A general procedure adopted (Tukel, personal communication) is to fix a number of sub-iterations, and eventually calibrate it according to the dynamics of the flow, similarly to what was previously discussed about the radial scaling of the azimuthal wavenumbers used in the FFT.

2.4 Boundary conditions

The specification of boundary conditions for swirling flow is particularly challenging, due to the ability of this class of flow to support travelling waves. This renders the flow particularly sensitive to small perturbations which may eventually be introduced in the boundary condition treatment.

In a multi-dimensional domain, the number and type of conditions at a boundary depend on the eigenvalue spectrum of the Jacobian associated with the direction normal to the boundary. This defines local quasi one-dimensional propagation properties, which can be expressed by the characteristic variables, or equivalently, by the Riemann invariants [43]. To deal with a boundary normal to direction z , in compact form the so-called compatibility relations [43] for the characteristic variables are

$$\frac{\partial m_i}{\partial t} + \lambda_i \frac{\partial m_i}{\partial z} = S_i, \quad (2.43)$$

representing the transport of variables m_i along the characteristic curve $(\frac{dz}{dt})_i = \lambda_i$ plus the additional effect of a source term, accounting for Eulerian derivatives in the directions normal to z , for all the viscous derivatives, and for the source terms appearing in (2.3).

From eq. (2.43), when the sign of λ_i is such that the variable m_i is entering the domain, a *physical* boundary condition has to be imposed, whereas if m_i is leaving the domain then a *numerical* boundary condition is required. Most techniques used for the treatment of boundary conditions differ in the way in which the numerical boundary conditions are derived, but the above mentioned procedure is universally applied in the framework of the unsteady compressible Navier-Stokes equations.

The method we have implemented was first developed by Poinso and Lede [86], and we summarise here the main elements. Let \mathbf{W} and \mathbf{U} be the conservative and primitive variables vectors:

$$\mathbf{W} = [\rho, \rho V_r, \rho V_\theta, \rho V_z, \rho E]^T, \quad \mathbf{U} = [\rho, V_r, V_\theta, V_z, p]^T \quad (2.44)$$

and $\mathbf{R} = \frac{\partial \mathbf{W}}{\partial \mathbf{U}}$ the Jacobian associated with the transformation $\mathbf{U} \rightarrow \mathbf{W}$. Equation (2.3) can be written putting on the right hand side all the terms except the unsteady and the convective derivative normal to the boundary:

$$\frac{\partial \mathbf{W}}{\partial t} + \frac{\partial \mathbf{F}_z^{(e)}}{\partial z} = \text{rhs}; \quad (2.45)$$

then we can write

$$\frac{\partial \mathbf{W}}{\partial \mathbf{U}} \frac{\partial \mathbf{U}}{\partial t} + \frac{\partial \mathbf{F}_z^{(e)}}{\partial \mathbf{W}} \frac{\partial \mathbf{W}}{\partial \mathbf{U}} \frac{\partial \mathbf{U}}{\partial z} = \text{rhs} \quad (2.46)$$

and, with

$$\mathbf{B} = \mathbf{R}^{-1} \frac{\partial \mathbf{F}_z^{(e)}}{\partial \mathbf{W}} \mathbf{R}, \quad (2.47)$$

we derive

$$\frac{\partial \mathbf{U}}{\partial t} + \mathbf{B} \frac{\partial \mathbf{U}}{\partial z} = \mathbf{R}^{-1} \text{rhs}, \quad (2.48)$$

which represents the Navier-Stokes equations written for the primitive variables. Now, a matrix \mathbf{T} can be defined that will diagonalise the matrix \mathbf{B}

$$\mathbf{T}^{-1} \mathbf{A} \mathbf{T} = \mathbf{B};$$

therefore eq. (2.48) gives

$$\mathbf{T} \frac{\partial \mathbf{U}}{\partial t} + \mathbf{A} \mathbf{T} \frac{\partial \mathbf{U}}{\partial z} = \mathbf{T} \mathbf{R}^{-1} \text{rhs} \quad (2.49)$$

which coincides with (2.43) having assumed $dM = TdU$. A comparison between (2.49) and (2.45) gives:

$$\frac{\partial \mathbf{F}_z^{(e)}}{\partial z} = \mathbf{RT}^{-1} \mathbf{L} = \mathbf{RT}^{-1} \left[\mathbf{\Lambda T} \frac{\partial \mathbf{U}}{\partial z} \right]. \quad (2.50)$$

Thus we have obtained an expression relating the normal derivative of $\mathbf{F}_z^{(e)}$ to the normal derivative of the characteristic variables. Now, matrices $\mathbf{\Lambda}$ and \mathbf{T} are easily obtained by determining eigenvalues and corresponding eigenvectors of \mathbf{B} ; vector \mathbf{L} , defined by (2.50), can be written explicitly as:

$$\mathbf{L} = \begin{bmatrix} L_1 \\ L_2 \\ L_3 \\ L_4 \\ L_5 \end{bmatrix} = \begin{bmatrix} \left(\frac{\partial p}{\partial z} - \rho c \frac{\partial V_z}{\partial z} \right) (V_z - c) \\ \frac{\partial V_r}{\partial z} V_z \\ \frac{\partial V_\theta}{\partial z} V_z \\ \left(\frac{\partial p}{\partial z} - c^2 \frac{\partial \rho}{\partial z} \right) V_z \\ \left(\frac{\partial p}{\partial z} + \rho c \frac{\partial V_z}{\partial z} \right) (V_z + c) \end{bmatrix}. \quad (2.51)$$

The set of equations (2.51) can be inverted giving

$$\frac{\partial \mathbf{U}}{\partial z} = \frac{\partial}{\partial z} \begin{bmatrix} \rho \\ V_r \\ V_\theta \\ V_z \\ p \end{bmatrix} = \begin{bmatrix} \frac{1}{2c^2} \left(\frac{L_5}{V_z+c} + \frac{L_1}{V_z-c} \right) - \frac{L_4}{V_z c^2} \\ \frac{L_2}{V_z} \\ \frac{L_3}{V_z} \\ \frac{1}{2\rho c} \left(\frac{L_5}{V_z+c} - \frac{L_1}{V_z-c} \right) \\ \frac{1}{2} \left(\frac{L_5}{V_z+c} + \frac{L_1}{V_z-c} \right) \end{bmatrix} \quad (2.52)$$

and the relations obtained can be used to write physical boundary conditions in terms of L_i .

To clarify the procedure, we explicitly write the set (2.48) for the primitive variables:

$$\begin{aligned} \frac{\partial \rho}{\partial t} + V_z \frac{\partial \rho}{\partial z} + \rho \frac{\partial V_z}{\partial z} &= [\mathbf{R}^{-1} \text{rhs}]_1 \\ \frac{\partial V_r}{\partial t} + V_z \frac{\partial V_r}{\partial z} &= [\mathbf{R}^{-1} \text{rhs}]_2 \\ \frac{\partial V_\theta}{\partial t} + V_z \frac{\partial V_\theta}{\partial z} &= [\mathbf{R}^{-1} \text{rhs}]_3 \\ \frac{\partial V_z}{\partial t} + V_z \frac{\partial V_z}{\partial z} + \frac{1}{\rho} \frac{\partial p}{\partial z} &= [\mathbf{R}^{-1} \text{rhs}]_4 \\ \frac{\partial p}{\partial t} + V_z \frac{\partial p}{\partial z} + \rho c^2 \frac{\partial V_z}{\partial z} &= [\mathbf{R}^{-1} \text{rhs}]_5. \end{aligned} \quad (2.53)$$

Let's formulate the same equations using relations (2.52). We get:

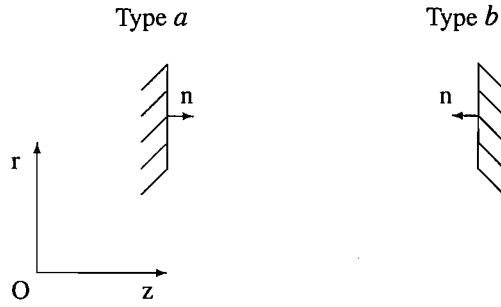


Figure 2.6: Boundary type definition.

$$\begin{aligned}
 \frac{\partial \rho}{\partial t} + \frac{1}{2c^2} (L_1 + L_5) - \frac{1}{c^2} L_4 &= [\mathbf{R}^{-1} \text{rhs}]_1 \\
 \frac{\partial V_r}{\partial t} + L_2 &= [\mathbf{R}^{-1} \text{rhs}]_2 \\
 \frac{\partial V_\theta}{\partial t} + L_3 &= [\mathbf{R}^{-1} \text{rhs}]_3 \\
 \frac{\partial V_z}{\partial t} + \frac{1}{2\rho c} (L_5 - L_1) &= [\mathbf{R}^{-1} \text{rhs}]_4 \\
 \frac{\partial p}{\partial t} + \frac{1}{2} (L_1 + L_5) &= [\mathbf{R}^{-1} \text{rhs}]_5 ,
 \end{aligned} \tag{2.54}$$

and it's now possible to exploit this set of equations to obtain relations that single components L_i have to satisfy in order to reflect the physical boundary condition required. Most of the results presented in this work have been obtained imposing subsonic inflow boundary conditions with constant mass rate and subsonic non-reflective conditions for the open boundaries. For the inflow boundary, the physical conditions to impose are:

$$V_r = 0 ; V_z = \text{const} ; V_\theta = \text{const} ; \rho = \text{const} . \tag{2.55}$$

From (2.51) L_1 [L_5] has to be calculated from the interior points on a boundary type a [b] because it is associated with an outgoing characteristic. The first [fifth] of (2.51) has to be used, with the derivatives given by a spatial discretisation scheme on the boundary points. Moreover, since the inflow velocity profile used is a steady solution of the Euler equations (cfr. §4.1), the rhs of (2.53) is zero if we neglect the contribution of viscosity. From (2.54), the physical conditions (2.55) then require that

$$\begin{aligned}
 L_1 + L_5 &= 2L_4 , \\
 L_2 &= 0 , \\
 L_3 &= 0 , \\
 L_1 &= L_5 .
 \end{aligned} \tag{2.56}$$

On a boundary type a , L_1 is known and L_2, L_3, L_4, L_5 are obtained by (2.56). On a boundary type b , L_5 is known and L_1, L_2, L_3, L_4 are analogously derived.

For a non reflective boundary condition, following Thompson [97], we impose that the amplitudes of the incoming waves are constant in time. On a boundary type b this leads to the following conditions:

$$\left(\mathbf{\Lambda T} \frac{\partial \mathbf{U}}{\partial z} \right)_i = (\mathbf{TR}^{-1} \text{rhs})_i, \quad (2.57)$$

with

$$\begin{aligned} i &= 1 & \text{if } V_z \geq 0, \\ i &= 1, 2, 3, 5 & \text{if } V_z < 0. \end{aligned}$$

In conclusion, the procedure can be summarised in the following steps:

- Calculate the rhs without the convective derivatives normal to boundary.
- Evaluate vector \mathbf{L} according to (2.51).
- Modify \mathbf{L} imposing the physical boundary conditions. Use (2.56) for an inflow, and (2.57) for a non-reflective boundary.
- Calculate the convective derivative normal to boundary as $\mathbf{RT}^{-1}\mathbf{L}$ and add to rhs.

The treatment has turned out to be very accurate and up to $\text{Re}=1200$ there was no need to supplement the physical domain with additional sponge layers or buffer zones to damp the amplitude of outgoing waves. Results presented in chapter 5 also indicate a clear absence of feedback instability, since the growth found is in many cases perfectly exponential. However, a buffer zone was found necessary for calculations at $\text{Re}=1200$. We followed the idea of Visbal and Gaitonde [100], coupling a grid coarsening in the axial direction with a numerical low-pass filter (in the same direction). In their analysis it is shown that propagation of a 1D pulse through a sudden mesh coarsening generates a wave packet of reflected energy propagating upstream. The reflected solution is characterised by spurious high-frequency modes which may eventually contaminate the genuine solution, and should therefore be removed by numerical filters. Furthermore, since the mesh is stretching rapidly in the buffer zone, the energy propagating downstream is also quickly dissipated by filtering, since the wavenumber range supported by the grid is narrowed. Note that for the numerical scheme used here, central differences with no artificial dissipation at the level of spatial discretisation, the use

of filtering is necessary to activate the damping in the buffer zone. The computational variable $0 \leq \xi \leq 1$ is mapped onto the physical one z by the following relations:

$$z(\xi) = \frac{(L_z - L_{buf})}{\xi^*} \xi \quad \forall \xi \leq \xi^* ,$$

$$z(\xi) = (L_z - L_{buf}) + b \left[e^{a(\xi - \xi^*)} - 1 \right] \quad \forall \xi > \xi^* ,$$

where L_z is the length of the whole computational domain in the axial direction, L_{buf} the length of the buffer zone; the coefficient a is a user-input parameter measuring the coarsening, ξ^* is the grid point where the buffer zone begins and b is:

$$b = \frac{L_{buf}}{e^{a(1 - \xi^*)} - 1} .$$

The filter used is given in [62] (formula (C.2.4) pag. 40), and is a compact filter fourth order accuracy, constructed imposing that the associated transfer function $T(\omega)$ has $T(\pi) = \frac{dT}{d\omega}(\pi) = 0$.

2.5 Axis treatment

The presence of terms containing factors $1/r$ in the set of equations (2.3) leads to singularities at the centerline of the cylindrical coordinate system. These singularities are a consequence of the coordinate mapping; since the flow field does not have any singularity, the axis has to be treated as a numerical boundary condition.

Different options exist to deal with the problem, and what appears immediately clear from the literature review is that a variety of methods exist, depending essentially on the kind of code used (finite difference/finite volume/spectral).

In the context of the finite difference codes, Jiang & Luo [38] and Griffin *et al.* [36] used the L'Hopital rule to write on the axis a new set of equations without singularities. Freund [28] and Boersma & Lele [10] in their studies on compressible jets introduce a Cartesian coordinate system for the points on the axis. The axis of the Cartesian system are arbitrarily chosen, and the multi-valued variables (V_r, V_θ) are then obtained by a simple rotation. Another possibility is the use of a staggered mesh, with a grid distribution in the radial direction spanning from $-L_r$ to $+L_r$ and the first two points off the axis located at $\pm \Delta r/2$. This is the method proposed by Mohseni and Colonius [78].

In our study, we decided to adapt a method initially introduced for spectral/pseudo spectral codes [83] and recently used in linear stability analysis by Sandberg [91]. The

main idea is to reconstruct the values on the axis using polynomial expansions in the radial directions for the coefficients of an azimuthal Fourier decomposition; these expansions are obtained by imposing special symmetry constraints which guarantee the solution to be well posed on the axis.

Consider a transformation between Cartesian coordinates (x, y, z) and cylindrical coordinates (r, θ, z) defined by:

$$\begin{aligned} x &= r \cos \theta , \\ y &= r \sin \theta . \end{aligned} \tag{2.58}$$

In what follows, z doesn't play any role and will be omitted in the notation. Transformation (2.58) is invariant under a change of variable $(r, \theta) \rightarrow (-r, \theta + \pi)$ meaning that these two cylindrical coordinates identify the same physical point in the Cartesian reference. In the rotating frame, we have to discriminate between single-valued and multiple-valued variables: single-valued variables (thermodynamic quantities and the axial velocity component) are those for which

$$\phi(r, \theta) = \phi(-r, \theta + \pi) , \tag{2.59}$$

that is, they are unique functions of points in the *Cartesian* system. Radial and azimuthal components of velocity are multiple-valued variables, since for them this uniqueness is lost. Formally we have:

$$\phi(r, \theta) = -\phi(-r, \theta + \pi) . \tag{2.60}$$

In the cylindrical frame of reference, consider the Fourier series representation with respect to θ :

$$\phi(r, \theta) = \sum_{m=-\infty}^{+\infty} a_m(r) e^{im\theta} . \tag{2.61}$$

For a single-valued variable, substitution of (2.61) in (2.59) readily leads to:

$$\sum_{m=-\infty}^{+\infty} a_m(r) e^{im\theta} = \sum_{m=-\infty}^{+\infty} (-1)^m a_m(-r) e^{im\theta} . \tag{2.62}$$

In the limit, when $r \rightarrow 0$, condition (2.62) written for a generic mode m means that if m is even, then $a_m(0^+) = a_m(0^-)$; conversely, if m is odd it has to be $a_m(0^+) = -a_m(0^-)$. In other words, the polynomial expansions $a_m(r)$ of a single-valued variable are even functions

for even modes and odd functions for odd modes. Following Lewis and Bellan [64], the dependence of a_m on r can be more rigorously formalised:

$$\phi(r, \theta) = \sum_{m=-\infty}^{+\infty} a_m(r) e^{im\theta} = \sum_{m=-\infty}^{+\infty} \frac{a_m(r)}{r^{|m|}} \left[r e^{\pm i\theta} \right]^{|m|} = \sum_{m=-\infty}^{+\infty} \frac{a_m(r)}{r^{|m|}} [x + iy]^{|m|} . \quad (2.63)$$

For a single-valued variable we can require the ϕ to be analytical at the origin (analytical means differentiable and with derivative independent on the path of differentiation). Now, the complex function $(x + iy)^{|m|}$ is analytical because it satisfies the Cauchy-Riemann conditions. In order to be $\phi(r, \theta)$ regular, $a_m(r)/r^{|m|}$ must not be singular in the origin. Therefore $a_m(r) \sim r^{|m|}$ when $r \rightarrow 0$. This leads to writing:

$$\begin{aligned} \phi & \quad \text{single - valued :} \\ \frac{da_m}{dr}(r = 0) & = 0 \quad \forall m \quad \text{even ,} \\ a_m(r = 0) & = 0 \quad \forall m \quad \text{odd .} \end{aligned} \quad (2.64)$$

For a multiple-valued variable, the parity of the above condition is swapped. Lewis and Bellan [64] give a rigorous proof of this, but for an intuitive explanation we can substitute again (2.61) into (2.60) obtaining:

$$\sum_{m=-\infty}^{+\infty} a_m(r) e^{im\theta} = - \sum_{m=\infty}^{+\infty} (-1)^m a_m(-r) e^{im\theta} . \quad (2.65)$$

For a single mode m , the new condition requires that if m is even, then $a_m(r)$ has to be odd, whereas if m is odd, then $a_m(r)$ has to be even. Schematically:

$$\begin{aligned} \phi & \quad \text{multiple - valued :} \\ \frac{da_m}{dr}(r = 0) & = 0 \quad \forall m \quad \text{odd ,} \\ a_m(r = 0) & = 0 \quad \forall m \quad \text{even .} \end{aligned} \quad (2.66)$$

Relations (2.64) and (2.66) represent the first constraints that need to be accounted in the reconstruction process of any variable on the centerline.

As previously mentioned, the single-valued variables are uniquely defined at the origin, thus, an additional constraint can be written as:

$$\frac{\partial \phi}{\partial \theta}(r = 0) = 0 . \quad (2.67)$$

Among the even modes, relation (2.67) is satisfied only by $m = 0$, thus, for a single-valued variable we have reached the conclusion that the non-zero mode on the axis is only the mean, which has to be calculated imposing the first of (2.64).

Condition (2.67) can no longer be used for a multiple-valued variable, but it can still be applied for a Cartesian velocity component (which is single-valued). So we consider the quantity:

$$V_y = V_r \sin \theta + V_\theta \cos \theta . \quad (2.68)$$

Imposing that the derivative with respect to θ is equal to zero, we can write:

$$\left[\frac{\partial V_r}{\partial \theta} - V_\theta \right]_{r=0} \sin \theta + \left[\frac{\partial V_\theta}{\partial \theta} + V_r \right]_{r=0} \cos \theta = 0 . \quad (2.69)$$

Since equation (2.69) holds for any θ , it has to be:

$$\begin{aligned} \frac{\partial V_r}{\partial \theta}(r=0) &= V_\theta(r=0) , \\ \frac{\partial V_\theta}{\partial \theta}(r=0) &= -V_r(r=0) . \end{aligned} \quad (2.70)$$

Denoting by \hat{V}_θ and \hat{V}_r the Fourier coefficients for a generic azimuthal mode m , this means:

$$\begin{aligned} im \hat{V}_r &= \hat{V}_\theta , \\ im \hat{V}_\theta &= -\hat{V}_r . \end{aligned} \quad (2.71)$$

Conditions (2.71) can be satisfied only by $m = \pm 1$. These two modes need to be calculated according to the first of (2.66). All the other modes have to be zeroed.

Summarising the method, once the solution is updated at all the points (except the axis), a Fourier decomposition in the azimuthal direction is performed in some points off the axis. The number of points depends on the stencil of the one-sided finite difference formula selected to discretise $da_m(r)/dr$. We used a fourth order accuracy requiring 5 points. Then, for the state variables which are single-valued, namely $\rho, \rho V_z$ and ρE , $a_0(r=0)$ has to be evaluated imposing $da_0/dr = 0$. This will provide readily the required values on the axis (there's no need of an inverse FFT). For the remaining state variables $\rho V_r, \rho V_\theta$, one has to calculate $a_{+1}(r=0)$ and $a_{-1}(r=0)$ imposing $da_{\pm 1}/dr = 0$ and then $\rho V_r, \rho V_\theta$ are reconstructed by inverse FFT.

The method has the advantage of not introducing any extra equation for the pole. For spectral/pseudo spectral codes, the method is widely used, eventually with some small variants; some authors report problems when using the method for finite difference codes (it

is a personal communication reported in reference [83], so it's not clear whether or not the azimuthal derivatives are performed spectrally) and we may advance the hypothesis of some numerical instability if the azimuthal differentiation were not performed spectrally. We did not experience any difficulty and the method was also validated against the technique (of easier implementation) of Mohseni and Colonius [78] which avoids placing points on the polar axis. In the test-case used for the comparison (linear stability calculation reported in chapter 3) the difference was negligible, but the polynomial expansion method seems to be closer to the nature of the spectral differentiation.

2.6 Coordinates transformation

In the final chapter we will present a few cases of vortex breakdown developing in a varying-section pipe with frictionless walls. For this purpose, the code was upgraded to handle simple but non trivial cylindrical geometries by means of a coordinate transformation.

A non-uniform, non-orthogonal region in the meridional plane (z, r) is transformed to a uniform rectangular grid in the computational space (ξ, η) by functional dependencies of the form:

$$\xi = \xi(z, r), \quad \eta = \eta(z, r). \quad (2.72)$$

Using the chain rule, it is possible to evaluate derivatives in the physical space after differentiation in the computational space:

$$\begin{aligned} \frac{\partial}{\partial z} &= \xi_z \frac{\partial}{\partial \xi} + \eta_z \frac{\partial}{\partial \eta}, \\ \frac{\partial}{\partial r} &= \xi_r \frac{\partial}{\partial \xi} + \eta_r \frac{\partial}{\partial \eta}. \end{aligned} \quad (2.73)$$

The basic set of equations (2.3) can then be recast in the form:

$$\frac{\partial \mathbf{W}}{\partial t} + \left[1 + \frac{\xi_r}{\xi_z} \right] \xi_z \frac{\partial \mathbf{F}_z}{\partial \xi} + \left[1 + \frac{\eta_z}{\eta_r} \right] \eta_r \frac{\partial \mathbf{F}_r}{\partial \eta} + \frac{1}{r} \frac{\partial \mathbf{F}_\theta}{\partial \theta} + \frac{\mathbf{S}}{r} = 0. \quad (2.74)$$

In practical computations one has to determine the metrics coefficients $\xi_z, \xi_r, \eta_z, \eta_r$, through the inverse relation of (2.72):

$$x = x(\xi, \eta), \quad y = y(\xi, \eta). \quad (2.75)$$

For complex geometries the functional dependencies in (2.75) are unknown, since the grids are obtained by grid generation algorithms. In that case, the metric coefficients are calcu-

lated as:

$$\begin{bmatrix} \xi_x & \xi_r \\ \eta_x & \eta_y \end{bmatrix} = \frac{1}{x_\xi y_\eta - x_\eta y_\xi} \begin{bmatrix} +y_\eta & -x_\eta \\ -y_\xi & +x_\xi \end{bmatrix}. \quad (2.76)$$

Note however that relation (2.76) is obtained by linearisation of (2.75), therefore it is of second order accuracy, and its application to higher order methods may be questionable. With the cylindrical coordinates, the geometries handled can generally be described analytically, and the use of (2.76) is not necessary. For example, in our work, following references [7, 41, 69], we have considered a pipe whose radius R varies with the axial coordinate according to a functional dependency (cfr. §5.5):

$$R = R(z) \quad 0 \leq z \leq L_z. \quad (2.77)$$

The grid used is algebraically defined by the simple scaling law

$$\begin{aligned} z &= \xi L, \\ r &= \eta R(z), \end{aligned}$$

and the metrics can be analytically calculated.

The derivatives of the inviscid fluxes are obtained calculating the value of the fluxes at each node, and differentiating by compact schemes. For the viscous fluxes, one may choose to store the viscous stress tensor, and calculate its divergence by successive application of the first derivatives. In curvilinear coordinates, this approach would be cheaper than employing directly the second derivatives, but it's well known that in this way the representation of high wavenumbers is much less accurate [92]. In the code, we adopted the second strategy, so all the viscous terms requiring evaluation of successive derivatives, for example the term

$$\frac{\partial}{\partial r} \left[\mu \frac{\partial V_r}{\partial r} \right],$$

have been expanded and evaluated as:

$$\frac{\partial \mu}{\partial r} \frac{\partial V_r}{\partial r} + \mu \frac{\partial^2 V_r}{\partial r^2}.$$

When the grid transformation is active, formulae for the second derivatives similar to (2.73) are used. These are defined as

$$\frac{\partial^2}{\partial x_i \partial x_j} = +\xi_{x_i} \xi_{x_j} \frac{\partial^2}{\partial \xi^2} + \xi_{x_i x_j} \frac{\partial}{\partial \xi} + (\xi_{x_i} \eta_{x_j} + \xi_{x_j} + \eta_{x_i}) \frac{\partial^2}{\partial \xi \partial \eta} + \eta_{x_i x_j} \frac{\partial}{\partial \eta} + \eta_{x_i} \eta_{x_j} \frac{\partial^2}{\partial \eta^2},$$

with $i, j = 1, 2$ and $x_i = z, x_j = r$.

Some care needs to be taken to extend the boundary condition treatment discussed in §2.4, because the grid obtained algebraically does not preserve the orthogonality between the radial and axial directions. We have seen that the key-point of the Poinot-Lele method is the evaluation of Eulerian derivatives normal to the boundary after the imposition of physical constraints through relations of the form

$$\frac{\partial \mathbf{F}_n}{\partial n} = \mathbf{R}\mathbf{T}^{-1} \left[\mathbf{\Lambda}\mathbf{T} \frac{\partial \mathbf{U}}{\partial n} \right], \quad (2.78)$$

where n indicates a generic direction identified in the orthogonal reference (r, z) by the unit vector $\hat{i}_n = \hat{i}_z n_z + \hat{i}_r n_r$. Consider the inviscid counterpart of equation (2.3); the derivatives in the azimuthal direction do not play any role, and can be omitted in what follows:

$$\frac{\partial \mathbf{W}}{\partial t} + \frac{\partial \mathbf{F}_z}{\partial z} + \frac{\partial \mathbf{F}_r}{\partial r} + \frac{\mathbf{S}}{r} = 0. \quad (2.79)$$

The above formulation is weakly-conservative, since the source term \mathbf{S}/r accounts also for the decomposition of $\frac{1}{r} \frac{\partial(r\mathbf{F}_r)}{\partial r}$. In this way, the meridional plane (r, z) , where the boundary conditions have to be imposed, can be considered as purely two-dimensional, and we may write

$$\frac{\partial \mathbf{W}}{\partial t} + \underline{\nabla} \cdot \mathbf{F} = -\frac{\mathbf{S}}{r}, \quad (2.80)$$

with

$$\underline{\nabla} = \hat{i}_r \frac{\partial}{\partial r} + \hat{i}_z \frac{\partial}{\partial z} \quad (2.81)$$

and \mathbf{F} a second order tensor defined in in the (r, z) plane as:

$$\mathbf{F} = \hat{i}_r \mathbf{F}_r + \hat{i}_z \mathbf{F}_z. \quad (2.82)$$

We need to express the normal derivative $\frac{\partial \mathbf{F}_n}{\partial n}$ in terms of $\frac{\partial \mathbf{F}_z}{\partial z}$ and $\frac{\partial \mathbf{F}_r}{\partial r}$. In the weakly-conservative formulation adopted, this is immediate. Indeed we have:

$$\frac{\partial \mathbf{F}_n}{\partial n} = (\underline{\nabla} \mathbf{F}_n) \cdot \hat{i}_n = \left(\hat{i}_r \frac{\partial \mathbf{F}_n}{\partial r} + \hat{i}_z \frac{\partial \mathbf{F}_n}{\partial z} \right) \cdot \left(\hat{i}_r n_r + \hat{i}_z n_z \right) = n_r \frac{\partial \mathbf{F}_n}{\partial r} + n_z \frac{\partial \mathbf{F}_n}{\partial z}. \quad (2.83)$$

Applying the chain rule (2.73), this leads to:

$$\frac{\partial \mathbf{F}_n}{\partial n} = \left[n_z + n_r \left(\frac{\xi_r}{\xi_z} \right) \right] \left(\xi_z \frac{\partial \mathbf{F}_n}{\partial \xi} \right) + \left[n_r + n_z \left(\frac{\eta_z}{\eta_r} \right) \right] \left(\eta_r \frac{\partial \mathbf{F}_n}{\partial \eta} \right). \quad (2.84)$$

The final step is to write \mathbf{F}_n in terms of \mathbf{F}_r and \mathbf{F}_z . Since it is

$$\mathbf{F}_n = \mathbf{F} \cdot \hat{i}_n = n_r \mathbf{F}_r + n_z \mathbf{F}_z, \quad (2.85)$$

substituting (2.85) into (2.84), after a few elementary manipulations one obtains:

$$\begin{aligned} \frac{\partial \mathbf{F}_n}{\partial n} = & + \left[n_z + n_r \left(\frac{\xi_r}{\xi_z} \right) \right] \left[n_z \left(\xi_z \frac{\partial \mathbf{F}_z}{\partial \xi} \right) + n_r \left(\xi_z \frac{\partial \mathbf{F}_r}{\partial \xi} \right) \right] \\ & + \left[n_r + n_z \left(\frac{\eta_z}{\eta_r} \right) \right] \left[n_z \left(\eta_y \frac{\partial \mathbf{F}_z}{\partial \eta} \right) + n_r \left(\eta_r \frac{\partial \mathbf{F}_r}{\partial \eta} \right) \right] \\ & + \left[n_z + n_r \left(\frac{\xi_r}{\xi_z} \right) \right] \left[\mathbf{F}_z \left(\xi_z \frac{\partial n_z}{\partial \xi} \right) + \mathbf{F}_r \left(\xi_z \frac{\partial n_r}{\partial \xi} \right) \right]. \end{aligned} \quad (2.86)$$

The rhs of (2.86) is now completely computable and has to be subtracted from the entire rhs on the boundary points. After this operation has been performed, one has to reconstruct the normal Eulerian derivatives using the rhs of (2.78) where it is understood that vector $\mathbf{L} = \mathbf{A} \mathbf{T} \frac{\partial \mathbf{U}}{\partial n}$ is given by (2.51) replacing z with n (normal direction to the boundary) and r with t (tangential direction to the boundary).

In the calculations presented here, the radial boundary $R(z)$ is treated as a stream surface. From (2.51), the condition

$$L_2 = L_3 = L_4 = 0 \quad (2.87)$$

guarantees the impermeability condition $V_n = 0$. L_5 is associated with the only outgoing characteristic and has to be calculated from the interior as

$$L_5 = \left(\frac{\partial p}{\partial t} + \rho c \frac{\partial V_n}{\partial n} \right) (V_n + c).$$

Calculation of L_1 requires a further physical condition. We have considered a constant temperature wall, for which

$$\frac{\partial T}{\partial t} = 0 \quad \Leftrightarrow \quad \frac{\partial p}{\partial t} - \frac{c^2}{\gamma} \frac{\partial \rho}{\partial t} = 0. \quad (2.88)$$

Substitution of (2.54) into (2.88) leads quickly to writing the final condition:

$$L_1 = \frac{2}{1 - \gamma} L_4 - L_5.$$

Chapter 3

Vortex core dynamics

3.1 The Batchelor vortex

The objective of this section is to understand the effect of the swirl on the stability characteristics of jets and wakes at low Mach numbers. For the sake of this, we analyse the three-dimensional response of a parallel swirling flow induced by a localised small perturbation. It will be shown how the underlying dynamics of a free shear-layer is significantly modified by the addition of the swirl. The base flow considered here is the Batchelor vortex, for which a large amount of analytical and numerical studies has been produced [21, 48, 61, 63]. Comparison with existing results will provide a validation of the linear code developed. This velocity profile, sometimes referred to as a q-vortex, was first introduced to describe aircraft trailing vortices and it is often used to model experimental jets, for its well known capability to capture features common to many swirling flows.

3.1.1 Formulation and diagnostic tools

In a cylindrical frame of reference (r, θ, z) , the dimensional Batchelor vortex is defined as follows:

$$\begin{aligned} V_z(r) &= V_\infty + (V_c - V_\infty)e^{-\left(\frac{r}{\delta}\right)^2} \\ V_r(r) &= 0 \\ V_\theta(r) &= \Omega\delta\frac{1 - e^{-\left(\frac{r}{\delta}\right)^2}}{(r/\delta)}, \end{aligned} \tag{3.1}$$

where V_∞ is the free-stream axial velocity, V_c is the centerline axial velocity and δ is the vortex core edge. In the limit $r \rightarrow 0$ one has $V_\theta(r) \sim \Omega r$, then Ω is the angular velocity of the solid body rotation for this limit. Non-dimensionalisation can be obtained assuming δ

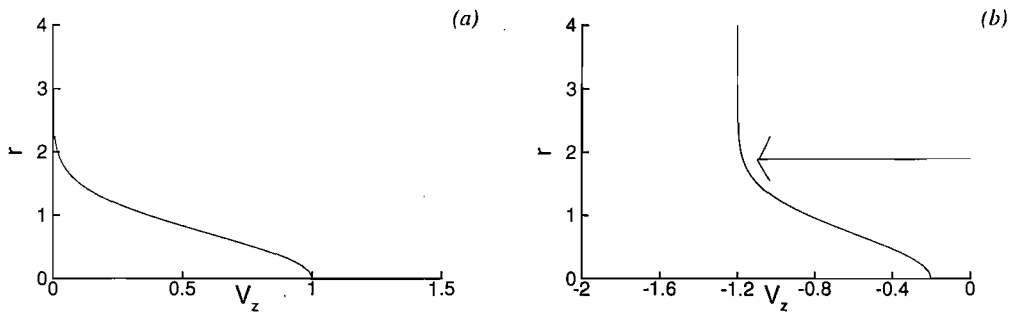


Figure 3.1: Axial velocity profile of the Batchelor vortex, corresponding to equation (3.2) with (a): $a = 0$ (jet) and (b): $a = -1.2$ (wake).

and $V_c - V_\infty$ as length and velocity scale, respectively. Therefore, one easily obtains

$$\begin{aligned} V_z(r) &= a + e^{-r^2} \\ V_r(r) &= 0 \\ V_\theta(r) &= q \frac{1 - e^{-r^2}}{r}, \end{aligned} \quad (3.2)$$

with

$$\begin{aligned} a &= \frac{V_\infty}{V_z - V_\infty}, \\ q &= \frac{\Omega \delta}{V_c - V_\infty}. \end{aligned}$$

The two parameters a and q identify fully the Batchelor vortex: q is the swirl number¹ and a describes the external flow. We will focus on the condition of a jet without external flow, $a = 0$ (see fig. 3.1-a), and on a full wake at $a = -1.2$. Note however, that when $a < -1$, the axial velocity V_z is a wake pointing to the negative axial direction (see fig. 3.1-b) and consequently misaligned with the axial unit vector \hat{i}_z . This means that any result of the spectral analysis should be evaluated by symmetry in order to recover the conventional alignment. To avoid any possible source of confusion, we preferred to study the wake type profile $a = -1.2$ implementing the first of (3.2) with opposite sign.

The linearised code described in section 2.1.2 has been used to study the evolution of the Batchelor vortex after the introduction of a small perturbation. Linear temporal simulations (LTS) have been conducted using periodic boundary conditions in both streamwise and azimuthal directions. The use of the periodic boundary conditions in the axial direction converts any physical problem to a closed system, where the perturbation cannot leave the

¹Throughout this thesis, we will often make reference to a swirl number defined differently (for example cfr. §4.1) and denoted by S . Here we comply with the literature.

domain. As a consequence, convective instabilities, which in spatial simulations would be expelled from the computational domain under the advection of the base flow, in the temporal approach remain in the system and the possibility of monitoring their growth is offered. Axial modal decomposition can then be strictly applied to perform a rigorous stability analysis.

L_z	L_r	n_z	n_r	n_θ	\bar{r}	b_r
20	7	128	120	32	0	0.6

Table 3.1: Numerical parameters used for linear calculations LTS on the Batchelor vortex.

Numerical parameters used for LTS are given in table 3.1. The computational domain is $L_z \times L_r \times 2\pi$ discretised by $n_z \times n_r \times n_\theta$. A coordinate transformation is adopted to stretch radially the region near the axis. The transformation adopted is

$$r(\eta) = \frac{L_r}{e^{b_r} - 1} \left(e^{b_r \eta} - 1 \right) \quad 0 \leq \eta \leq 1$$

with b_r user-input parameter. It is convenient to maintain $b_r < 1$ in order to preserve a smooth stretching. Since stability test-cases require particular precision, we put $\bar{r} = 0$, that is the radial dropping of azimuthal modes was not applied. This leads to very small integration time steps, a condition which however doesn't represent a big problem for this specific study, as the non-dimensional time to simulate is quite limited. We point out that the length of the box L_z gives the resolution in the axial wavenumber dk , while the grid resolution n_z fixes k_{co} giving the cut-off frequency. For the parameters reported in table 3.1, we have $dk = 2\pi/L_z = 0.31$ and $k_{co} = (n_z/2 - 1)dk = 19.5$.

Following Delbende *et al.* [21], the stability analysis was conducted on the axial velocity component $V_z(r, \theta, z, t)$ of the perturbation. First, we consider its corresponding analytical representation obtained by convolution:

$$\tilde{V}_z(r, \theta, z, t) = \left[\delta(z) + \frac{i}{\pi z} \right] * V_z(r, \theta, z, t). \quad (3.3)$$

In (3.3), $\delta(z)$ is the Dirac function, i the imaginary unit and the term

$$\frac{1}{\pi z} * V_z(r, \theta, z, t)$$

is the Hilbert transform [18] in the z direction of the signal V_z , whose fundamental property is to shift by -90 degrees all the positive frequencies, and by +90 degrees all the negative

ones. In the frequency space, this means

$$FT \left[\frac{1}{\pi z} * V_z \right] = G(k) = -i \cdot \text{sgn}(k) FT [V_z] ,$$

where FT designates the linear operator of Fourier transformation. For the analytical representation one has:

$$FT [\tilde{V}_z] = FT [V_z] + i G(k) = FT [V_z] + \{\text{sgn}(k) \cdot FT [V_z]\} . \quad (3.4)$$

According to (3.4), the demodulated signal \tilde{V}_z has zeroed all the negative k -modes. In this way, one recovers the usual notation of temporal stability analysis [45], where the wavenumber k is assumed real and positive. Then, a double Fourier transform in the azimuthal and axial direction gives

$$\hat{\tilde{V}}_z(r, m, k, t) = \int_{-\infty}^{+\infty} \int_0^{2\pi} \tilde{V}_z(r, \theta, z, t) e^{-i(m\theta + kz)} d\theta dz . \quad (3.5)$$

The amplitude of each Fourier component pair (m, k) is measured by an appropriate integral along the radial direction r

$$A(m, k, t) = \left(\int_0^{\bar{r}} |\hat{\tilde{V}}_z(r, m, k, t)|^2 r dr \right)^{1/2} , \quad (3.6)$$

where \bar{r} is a radial station to be taken outside the vortex core where the whole dynamics is expected to develop. On the other side, the phase associated with the Fourier pair is given by:

$$\phi(m, k, t) = \arg \left[\hat{\tilde{V}}_z(r_0, m, k, t) \right] . \quad (3.7)$$

In the last expression r_0 is the radial position where the initial disturbance is introduced. We decided to initiate the perturbed flow field assigning small random values to the azimuthal velocity component at $z_0 = 2, r_0 = 0.3$ and for $\theta = 0 \dots 2\pi$. The temporal stability properties of each pair (m, k) are described by the growth rate (the imaginary part of ω in a normal mode decomposition, cfr. §1.4) and by the temporal frequency (the real part of ω). In our analysis, these quantities are evaluated as follows:

$$\begin{aligned} \omega_i(m, k) &= \frac{\partial}{\partial t} \ln A(m, k, t) \simeq \frac{\ln [A(m, k, t_2)/A(m, k, t_1)]}{t_2 - t_1} , \\ \omega_r(m, k) &= -\frac{\partial}{\partial t} \phi_m(m, k, t) \simeq -\frac{\phi_m(m, k, t_4) - \phi_m(m, k, t_3)}{t_4 - t_3} . \end{aligned} \quad (3.8)$$

The values of t_1, t_2, t_3 and t_4 in (3.8) have to be chosen with some care. If t_1, t_2 are too small, different modes may not achieve their asymptotic behaviour, and non-physical contamination due to Gibbs phenomenon [18] may be present. In practice t_1, t_2 have to be large

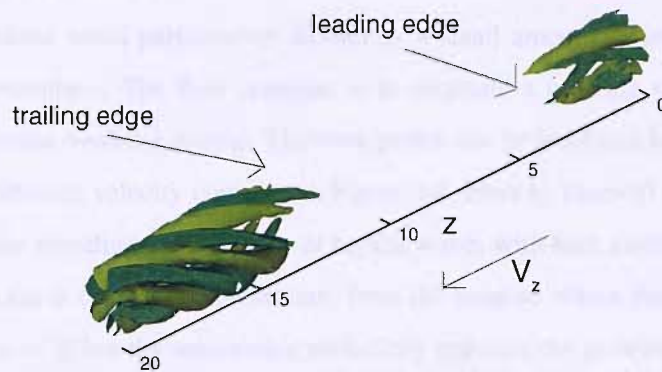


Figure 3.2: Response of the perturbed Batchelor vortex at $Re=667$, $q = 0.8$, $a = 0$. Isosurfaces of radial velocity component at $Time=30$. $V_r = \pm 0.0002$. The arrow V_z indicates the direction of the base flow.

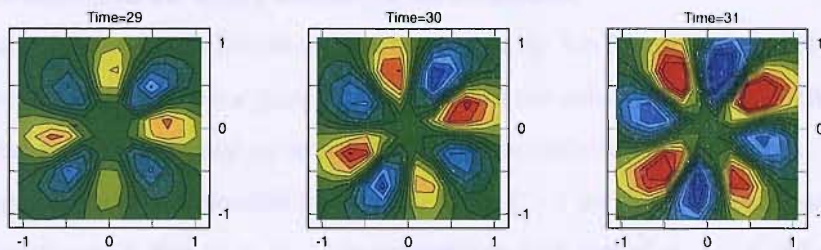


Figure 3.3: Response of the perturbed Batchelor vortex at $Re=667$, $q = 0.8$, $a = 0$. Cross sectional contours of radial velocity component at $z = 19$ and different times. Contours levels are in the range $[-0.0008, +0.0007]$.

enough to guarantee that an initial transient is ended. On the other hand, t_3 and t_4 for the phase calculation have to be close because the phase function has a typical saw-tooth shape due to its intrinsic discontinuity at 2π . The time instants selected have to be confined within a range where the jump is not occurring. This range is different depending on the pair (m, k) considered. Therefore, for the growth rate we have assumed the values $t_1 = 25$ and $t_2 = 30$, while the values t_3, t_4 for the phase were not uniquely fixed.

3.1.2 Validation: results at $Re=667$, $q=0.8$

With a Mach number $M = 0.3$ we expected results to be very similar to the incompressible ones of Delbende *et al.* [21], obtained with identical technique². In light of the inviscid study of Khorrami [49], the effect of compressibility at this Mach number is negligible. The Reynolds number is $Re=667$, and we consider the case with swirl $q = 0.8$ and $a = 0$. The non-dimensional time simulated is $Time=30$; the whole calculation lasted 20 hours running

²The specification of the initial thermodynamic field, leading to a precise definition of the Mach number is detailed in §4.1.

on 32 CPUs of a PC cluster.

The localised small perturbation introduces a small amount of energy in all the azimuthal wavenumbers. The flow response is to originate a growing wave packet with a spatial distribution evolving in time. The wave packet can be identified by the isosurfaces of a single perturbation velocity component. Figure 3.2 refers to Time=30 and shows a multi-armed structure revealing the existence of helical waves with high azimuthal wavenumber. The wave packet is convected downstream from the location where the initial disturbance was placed ($z_0 = 2$) but the streamwise periodicity prevents the growing disturbance leaving the computational domain. Of course, what in the figure are labelled as leading and trailing edges provide just a qualitative indication of the packet ends, which at this level of description depend on the values selected for the isosurfaces.

Results of the spectral analysis are summarised in fig. 3.4: for each azimuthal mode m , we plot the computed temporal growth rate ω_i against the axial wavenumber k (fig. 3.4-*a*), and the real part of frequency ω_r over the range of unstable wavenumbers (fig. 3.4-*b*). A broad range of negative azimuthal modes $-12 \leq m \leq -1$ are found to be unstable. The highest growth rate is that of $m = -4$ in competition with that of $m = -3$ and $m = -5$. Due to its exponential growth, mode $m = -4$ seems to dominate the response at Time=30, as clearly shown in figure 3.3, where the cross sectional contours reveal 4 pairs of peaks with alternating signs. The axisymmetric mode $m = 0$ and all the positive modes $m > 0$ are stable. As an example, figure 3.5 shows the temporal evolution of the amplitude $A(m, k, t)$ defined by (3.6) for the azimuthal modes $m = \pm 3$ and several values of k . The positive modes are damped whereas the negative ones grow exponentially. Note also that the slope of the different curves remains constant, ensuring that a calculation over 30 temporal units is sufficient for our analysis and that the computed values of ω_i do not depend on the two instant times t_1 and t_2 chosen in (3.8).

Convergence and domain independence have been evaluated performing a higher resolution case, doubling the length of the box, $L_z = 40$, and with $n_z = 512, n_y = 160, n_\theta = 64$ grid points. Figure 3.6-*a* shows the perfect agreement between the two solutions: the higher resolution case produces smoother curves due to the halved value of dk , but the computed ω_i match over all the axial wavenumbers. In addition, the present test-case has been used to compare two strategies for the axis treatment: the default method based on the spectral reconstruction of the value in the centre (cfr. §2.6) against the method of Mohseni and Colonius [78], which avoids placing grid points on the axis. The comparison, reported in

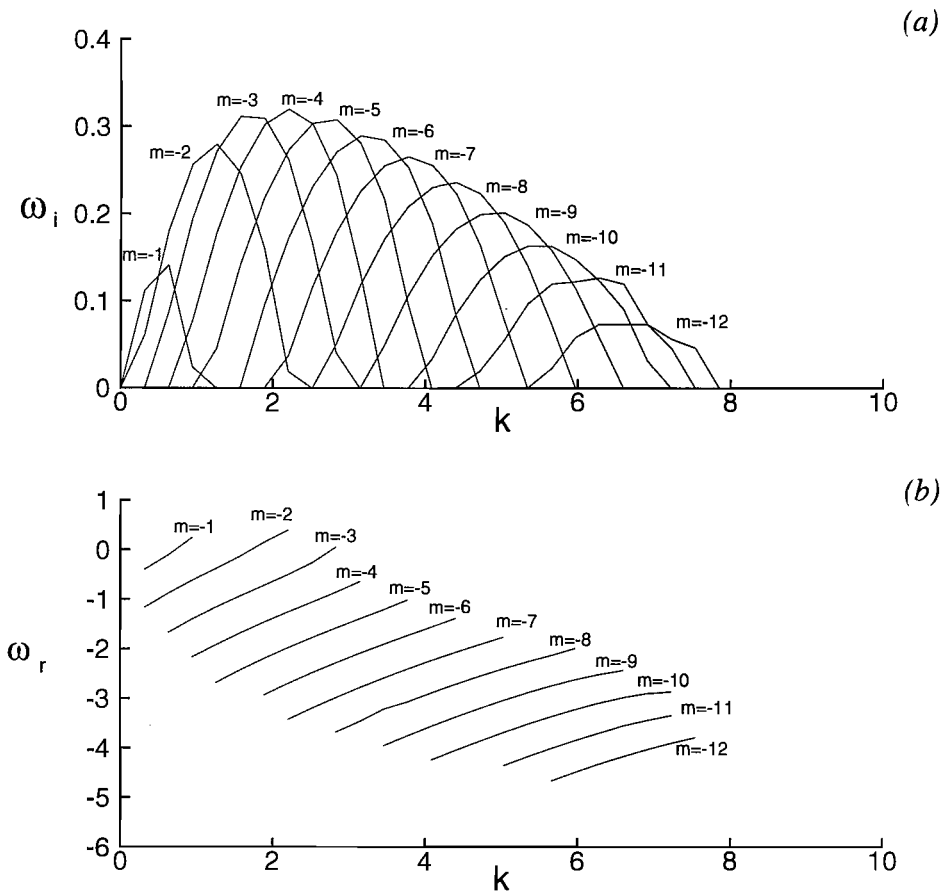


Figure 3.4: Temporal stability properties of the Batchelor vortex at $Re=667$, $q = 0.8$, $a = 0$, retrieved by LTS. (a): Temporal growth rate $\omega_i(k)$. (b): Real part of the frequency $\omega_r(k)$.

fig. 3.6-b, shows a good agreement for the most unstable azimuthal modes, while some difference is noticed for the less unstable $m = -12$. The method of Mohseni and Colonius yields a higher growth rate for $m = -12$ which is also localised on a narrower range of axial wavenumbers: although we believe that the difference is negligible, as the energy level of the $m = -12$ mode is very small, the results of Delbende *et al.* suggest that the technique of the spectral reconstruction is slightly more precise. Their results were obtained by direct numerical simulation of the linearised incompressible Navier-Stokes with a solver in Cartesian coordinates. The comparison is reported in table 3.2: the growth rate of the most amplified wavenumber is in a very good agreement. In the same table are reported the inviscid results of Lessen *et al.* [63], obtained by numerical solution of the Howard-Gupta equation [44]. The viscous calculations provide slightly smaller values than the inviscid counterparts of Lessen *et al.*. As in the current study, these authors have found that each unstable mode

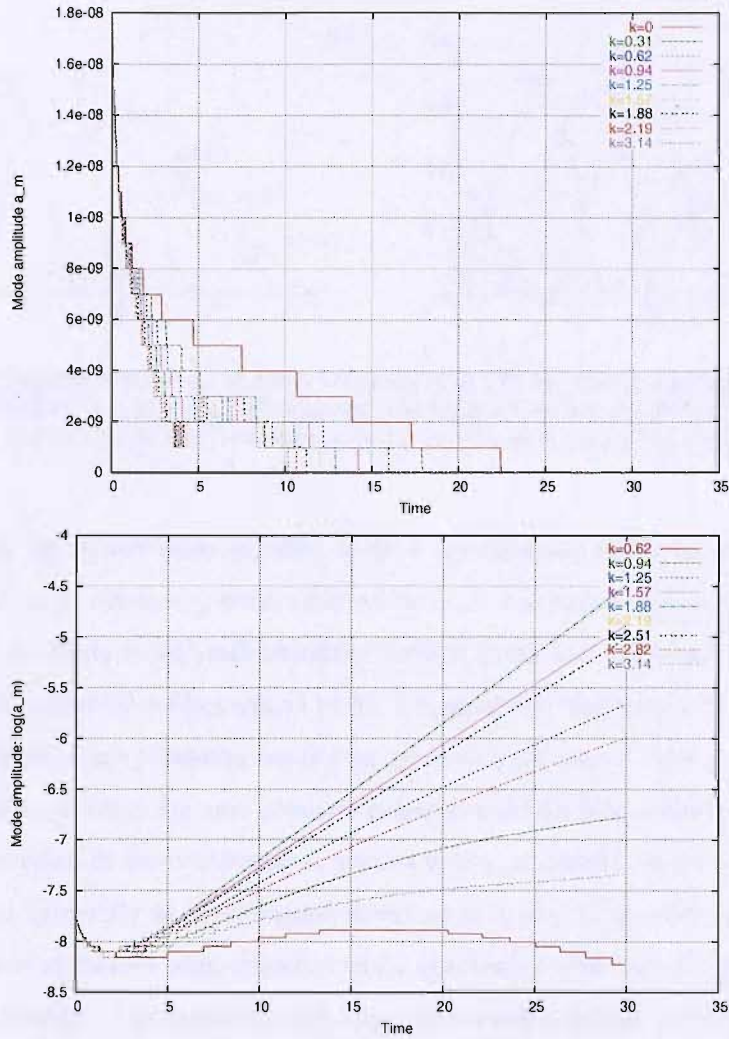


Figure 3.5: Response of the perturbed Batchelor vortex at $Re=667$, $q = 0.8$, $a = 0$. Time evolution of the amplitude A associated with different Fourier pairs (m, k) . Top: $m = +3$. Bottom: $m = -3$.

remains amplified in a range of axial wavenumbers whose limits increase with m . The main difference between these viscous and inviscid studies is that in the latter case the maximum growth rate over all axial wavenumbers increases with m : the asymptotic analysis of Leibovich and Stewartson [61] developed on the same Batchelor vortex predicts that in the inviscid case $\{\omega_i\}_{max}$ approaches a limiting value as $m \rightarrow \infty$.

To proceed with the discussion of the real frequency ω_r , it is convenient to describe in detail the sign convention adopted here. The temporal stability characteristics obtained following the procedure described in §3.1.1 are complying with the classic normal mode decomposition. Consequently, results have to be evaluated with reference to a wave form $\exp\{i(kz + m\theta - \omega_r t)\}$ with $k > 0$. In this context, the sign of the azimuthal wavenumbers

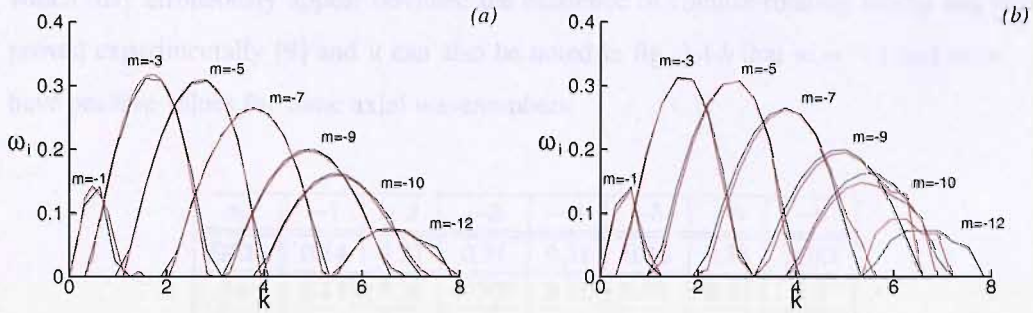


Figure 3.6: Numerical comparisons of growth rate measured by LTS. (a): Grid convergence: the default resolution (black) of table 3.1 vs the higher resolution case (red) reported in the text. (b): Different axis treatments: default method based on the spectral reconstruction on the axis (black) vs the method using a staggered grid (red).

m is given by the Fourier decomposition in the θ direction and defines the winding sense of the helical wave: when $m < 0$ the wave vector $k\hat{i}_z + m\hat{i}_\theta$ points clockwise if seen from downstream; the wave front, mathematically defined as the line with constant phase and graphically identified by the isosurfaces of fig. 3.2, represents therefore a helix which rolls counterclockwise when extending toward the positive z direction. These modes are said to be *cowinding*, whereas the term *counterwinding* is used for helical modes with $m > 0$. The waves revealed in our computations are cowinding, as clearly shown in figure 3.2. It often happens (generally in experimental works or in spatial DNS) that such cowinding modes are defined positive with reference to the observation that they are spirals winding in the same direction of the base flow; this may create some confusion in comparing results with those described here: in our convention, positive (negative) modes are counterwinding (cowinding).

The real frequency provides information about how these unstable modes move in time. Now, the wave form $\exp\{i(kz + m\theta - \omega_r t)\}$ propagates in the z direction according to the sign of the product $k\omega_r$. When it is positive, the single Fourier pair (k, m) moves in the positive axial direction, *i.e.* downstream. Note however that, by dispersion, propagation of the wave packet follows the sign of the group velocity $d\omega_r/dk$ and can be different. Following the same reasoning, the sense of rotation in a cross sectional plane is given by the sign of the product $\omega_r m$. When it is positive, the wave rotates in the positive direction, *i.e.* counterclockwise. In our study, the dominant modes are negative and have negative frequency for all the range of unstable k . These waves are said to be *corotating*, in the sense that their temporal rotation is in the same direction of the base swirling flow, a circumstance

which may erroneously appear obvious: the existence of counter-rotating modes has been proved experimentally [9] and it can also be noted in fig. 3.4-*b* that $m = -1$ and $m = -2$ have positive values for some axial wavenumbers.

m	-1	-2	-3	-4	-5	-6	-9
DCH	0.14	0.27	0.31	0.31	0.30	0.28	$\simeq 0.7$
AL	0.14	0.28	0.305	0.31	0.30	0.29	0.7
LSP	0.17	0.31	0.36	0.37	0.39	0.40	-

m	-1	-2	3	-4	-5	-6	-9
DCH	0.54	1.18	1.68	2.17	2.68	3.22	$\simeq 7$
AL	0.62	1.25	1.72	2.19	2.67	3.29	6.78
LSP	0.61	1.22	1.66	2.14	2.65	3.20	-

Table 3.2: Comparison of growth rates with previous computations. DCH: Delbende *et al.*, AL: current study, LSP: Lessen *et al.*. Top table reports the maximum growth rate $\{\omega_i\}_{max}$. Bottom table reports the most amplified axial wavenumber k_{max} .

3.1.3 Effect of the swirl

The validation based on the reference case $Re=667$, $q = 0.8$, $a = 0$ provides confidence in the code developed and offers the possibility to conduct a parametric study to evaluate the effect of the swirl on the stability characteristics of a pure jet. For this purpose, we consider LTS in the range of the swirl number $0 \leq q \leq 1.6$.

Figure 3.7 reports the temporal growth rates found. At $q = 0$, the base flow reduces to a fully developed jet and presents only two unstable modes $m = \pm 1$ with identical characteristics. Higher azimuthal modes $|m| \geq 2$ as well as the axisymmetric mode $m = 0$ remain stable for all the axial wavenumbers. Velocity profiles with a shear layer thickness smaller than that of (3.1) may present a competition between the bending modes and the axisymmetric one, or even the destabilisation of $m = \pm 2$. An example of this condition is found in the calculations of Gallaire and Chomaz [29], or in that of Michalke [77]. It is however recognised as a well established result that an axisymmetric nonrotating jet is dominated by unstable disturbances with azimuthal wavenumber $m = -1, 0, 1$.

The radial distribution of azimuthal velocity given by the third of (3.2) defines a pure rotational flow. According to the Rayleigh criterion for centrifugal instability [24], the vortex flow will be unstable to axisymmetric small perturbations if and only if the square of

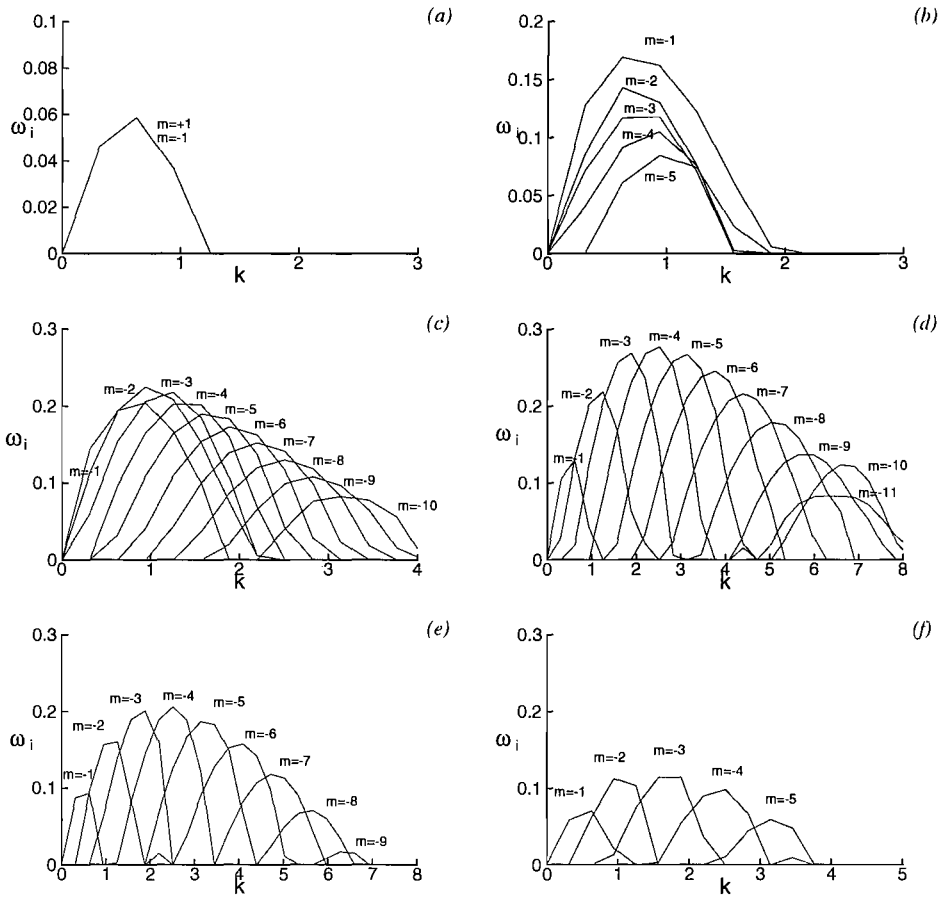


Figure 3.7: Temporal growth rate ω_i retrieved by LTS for the Batchelor vortex at $Re=667$, $a = 0$ and different swirl levels. (a): Non-rotating jet $q = 0$ (b): $q = 0.2$ (c): $q = 0.4$ (d): $q = 1$ (e): $q = 1.2$ (f): $q = 1.4$

the circulation has negative radial gradient anywhere. Similarly, the generalisation of the two-dimensional inflection criterion (also known as Rayleigh criterion) to circular geometries ensures that a necessary condition for instability to pure two-dimensional disturbances with $k = 0$ (*i.e.*, those existing in a cross sectional plane and associated with the azimuthal shear), is that the axial vorticity presents a local extremum. It can be easily verified that our rotational flow $(0, V_\theta(r), 0)$ is stable to both centrifugal and shear instabilities: the present study will therefore highlight what is the result of combining a vortex flow which is rotationally stable on a shear flow unstable by itself to modes $m = \pm 1$.

As soon as a small amount of swirl is introduced, $q = 0.2$, we have an immediate stabilisation of the positive mode, accompanied by a destabilisation of the negative modes $-5 \leq m \leq -1$. This result is again consistent with the inviscid analysis of Lessen *et al.* [63],

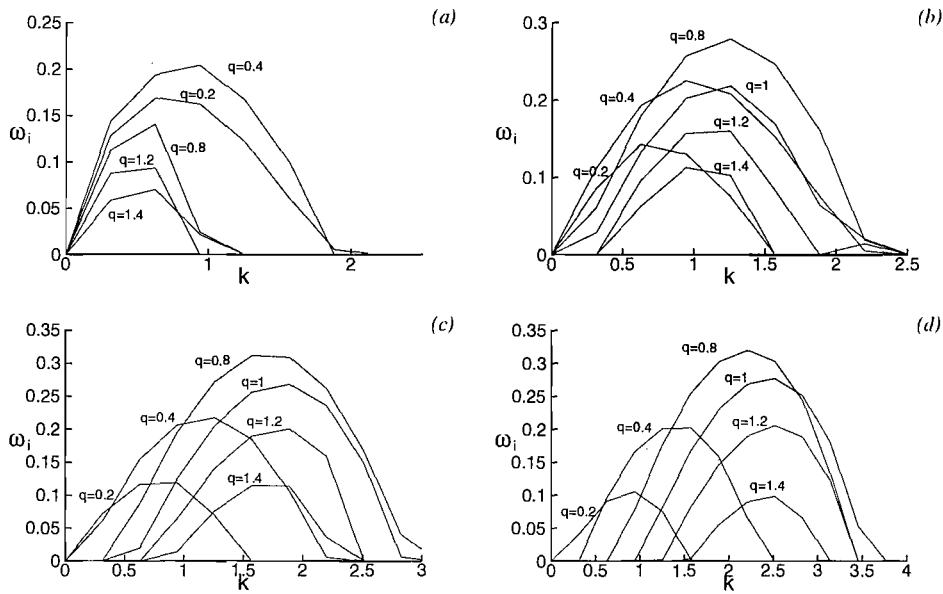


Figure 3.8: Effect of the swirl on the temporal growth rate ω_i of negative azimuthal modes. (a): $m = -1$ (b): $m = -2$ (c): $m = -3$ (d): $m = -4$.

showing that a full stabilisation of positive modes occurs at $q = 0.08$. At this small level of swirl the bending mode is dominant but a further increase to $q = 0.4$ leads to a competition between $m = -2$ and $m = -3$. For each azimuthal mode, the range of unstable axial wavenumbers is gradually enlarged. The reference case studied in the previous subsection has shown the most unstable response: at $q = 1$ the azimuthal wavenumber $m = -12$ is stabilised, and the maximum growth rate is always below the value 0.3. The stabilisation process becomes more evident at $q = 1.2$ and $q = 1.4$. At $q = 1.6$ the Batchelor vortex becomes totally stable. The same results are reproduced in fig. 3.8 in a form which synthetically highlights the effect of the swirl on each single mode m . For the higher modes $m = -2, -3, -4$, the curves modify in such a way that a common behaviour can be identified: during the stabilisation occurring for $q > 0.8$, the most amplified wavenumber remains approximately constant. The process appears to be less evident for the bending mode, which on the other hand begins to stabilise for $q > 0.4$. The asymptotic analysis $|m| \gg 1$ of Leibovich and Stewartson [61] shows that the most unstable of the axial wavenumbers has to satisfy the relation

$$\frac{1}{2}q < \frac{k_{max}}{m} < \frac{1}{q},$$

determining as condition for the instability of the incompressible Batchelor vortex that

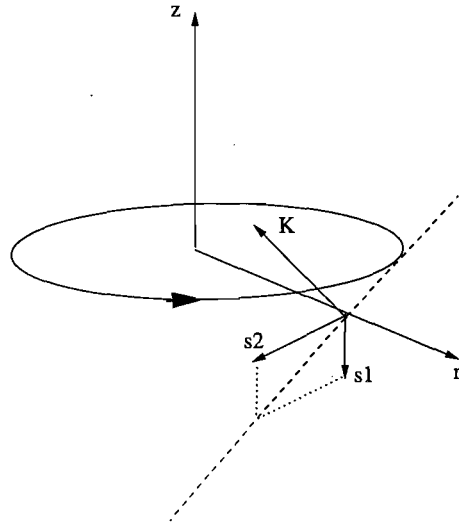


Figure 3.9: Representation of the sloped plane where the centrifugal instability occurs for the Batchelor vortex in jet configuration. \mathbf{k} is the wave vector.

$q < \sqrt{2}$. In addition, the above relation indicates that when $q \rightarrow \sqrt{2}$, it has to be $k_{max} \rightarrow \sqrt{2}m$. Although the computed values to which k_{max} converge are a bit smaller than those predicted by Leibovich and Stewartson, the overall behaviour of k_{max} converging for $q \rightarrow \sqrt{2}$ is captured by our viscous computations. These authors suggest that this class of modes are centrifugal, that is of the same kind as those for which the Rayleigh criterion guarantees stability with respect to axisymmetric perturbations. The works of Pedley [84] and Emanuel [25] corroborate this view showing that the same mechanism can indeed be responsible of instability but in the sloped frame of reference which locally contains all the shear components. When the azimuthal velocity is positive everywhere, as for the Batchelor vortex, the Rayleigh condition for centrifugal instability reduces to the existence of a radial position where the axial vorticity is negative. In the cylindrical frame of reference (r, θ, z) , the local components of the shear for a swirling flow $(0, V_\theta(r), V_z(r))$ are (cfr. §2.1.1) $s_1 = \frac{\partial V_z}{\partial r}$ and $s_2 = r \frac{\partial}{\partial r} \left(\frac{V_\theta}{r} \right)$. Then, a new frame of reference (r, θ', z') can be obtained rotating the original around the radial direction of an angle (see fig. 3.9)

$$\alpha = \arctg \frac{s_1}{s_2} .$$

In the new frame, the angular velocity has a vertical component to the plane (r, θ') which contains all the shear. Emanuel [25] shows that instability arises if the vorticity component perpendicular to this plane becomes locally negative, which is the equivalent of the cylindrical Rayleigh criterion for the particular case $V_\theta > 0$. If this condition is fulfilled, there

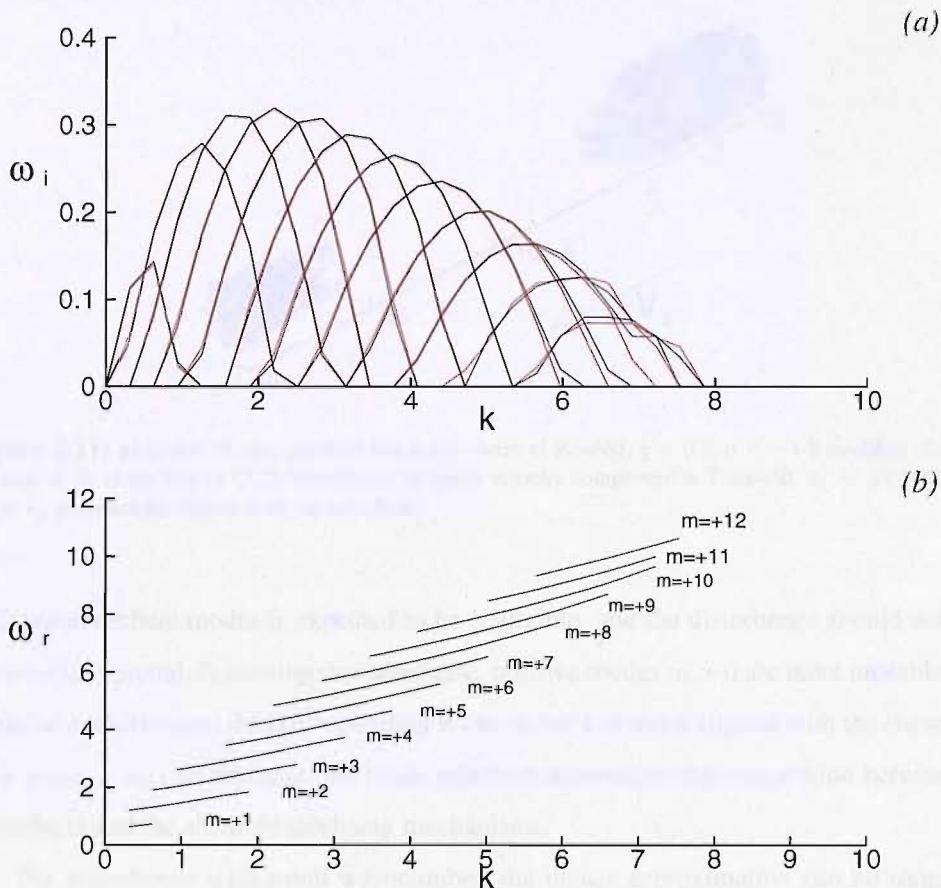


Figure 3.10: Temporal stability characteristics of the Batchelor vortex at $Re=667$, $q = 0.8$, $a = -1.2$ modified changing the sign of V_z in the first of (3.2). (a): Temporal growth rate $\omega_i(k)$ of positive azimuthal modes (black curve). For comparison, the red curve is the one of fig. 3.4, pertaining to the negative modes for the jet-like profile with $a = 0$. (b): Real part of the frequency $\omega_r(k)$.

exist unstable modes with wave vector directed along z' . From these considerations one may deduce the sign of the unstable azimuthal modes according to the sign of the two shear components. For the Batchelor vortex (see fig. 3.9) both s_1, s_2 are negative (s_2 is generally negative for any swirling flow driven by a vortex core in a solid body rotation), therefore for $k > 0$ it has to be $m < 0$ and this provides the explanation for the winding sense of these helical waves.

Note however that if those modes were of Kelvin-Helmholtz type, rather than centrifugal, the situation may *not* be necessarily different. As described by the 'tilting shear model' of Gallaire and Chomaz [30], for a high wavenumber disturbance with wave vector $\mathbf{k} = k\hat{i}_z + m\hat{i}_\theta$, shear instabilities would lead to a growth rate $\frac{1}{2} |\mathbf{k} \cdot \mathbf{s}|$ (Kelvin-Helmholtz instability of a plane vortex sheet) because the effect of the curvature of the vortex sheet on

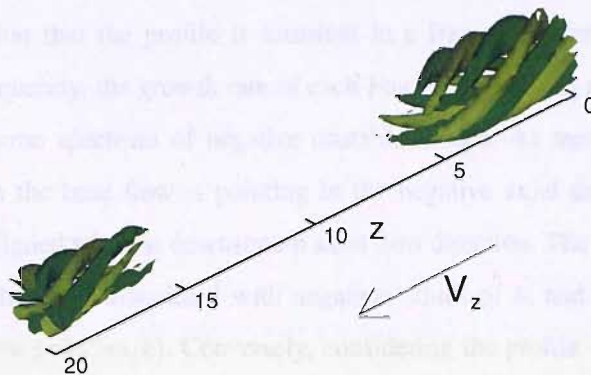


Figure 3.11: Response of the perturbed Batchelor vortex at $Re=667$, $q = 0.8$, $a = -1.2$ modified changing the sign of V_z in the first of (3.2). Isosurfaces of radial velocity component at Time=30. $V_r = \pm 0.0002$. The arrow V_z indicates the direction of the base flow.

high wavenumbers modes is expected to be negligible, and the disturbance should develop as two-dimensional. Following this reasoning, positive modes $m > 0$ are more unstable than negative ones, because the corresponding wave vector \mathbf{k} is more aligned with the shear vector $\mathbf{s} = s_1 \hat{i}_z + s_2 \hat{i}_\theta$. In this case, the mode selection depends on the competition between the centrifugal and the shear destabilising mechanisms.

For disturbance with small wavenumber, the planar approximation can no longer be considered valid, and the effect of the swirl on the development of the shear instabilities is controlled by a more sophisticated mechanism. The important results of Loiseleux *et al.* [67], revisited in section 3.3, suggest that under the effect of the rotation, the Kelvin-Helmholtz waves can interact with the neutral Kelvin waves discussed in the introduction and detailed in §3.2. This interaction leads to a damping effect, which is generally more intense with the positive modes. As a results, negative modes would be more unstable than their positive counterparts. In terms of mode selection, in this case the generalised centrifugal instabilities would be combined with the Kelvin-Helmholtz instabilities. For the Batchelor vortex, both axial and azimuthal shear are very weak, as suggested by the observation that at $q = 0$ the axisymmetric mode $m = 0$ is stable, and that whatever swirl is applied the wavenumber $k = 0$ is never destabilised. We can therefore assume with some confidence that the main destabilising mechanism is the generalised centrifugal effect.

To conclude this section, it is of interest to examine results of the Batchelor vortex when changing the axial velocity distribution from a jet-like into a wake-like profile. This can be achieved by letting $a < -1$ in (3.2). Theoretically, the temporal stability properties

of the new profile can be recovered by simple frequency shift $\omega_r \rightarrow \omega_r - ak$, associated with the consideration that the profile is invariant in a frame of reference moving with velocity $a \hat{i}_z$. Consequently, the growth rate of each Fourier pair (m, k) remains unchanged and preserves the same spectrum of negative unstable modes. As mentioned previously, under this condition the base flow is pointing in the negative axial direction, that is the swirl is negatively aligned with the downstream axial flow direction. The negative azimuthal modes $m < 0$ are therefore associated with negative values of k , and by symmetry they correspond to positive pairs (m, k) . Conversely, considering the profile $-V_z(r)$ with $a < 1$, that is changing the sign in the first of (3.2), one recovers a swirl which is positively aligned with the axial flow. The magnitude of the two shear components is invariant under this modification, thus the growth rate has to be unaffected. We decided to run this case as a further internal check about the validity of the whole method. Results are reported in fig. 3.10 for the set of parameters $q = 0.8, a = -1.2$. The unstable modes are all positive and their growth rate is identical to those pertaining to the negative ones for the reference case $a = 0$. Their temporal frequencies are positive (note that due to the modification introduced, the values of ω_r cannot be deduced by frequency shift); according to the sign of m and ω_r , these waves are corotating and counterwinding. The wave front has to be a spiral rolling in the opposite direction to the base flow, a circumstance which is confirmed by the isosurfaces in fig. 3.11.

3.2 Kelvin waves

There is no unanimous consensus on the idea that Kelvin waves are those responsible for the breakdown of slender vortices. In the attempt to give an autonomous interpretation, in this section we review some results obtained on parallel flows. A linear stability analysis is rigorously conducted on a base flow consisting of the Rankine vortex. For the sake of simplicity, the analysis considers an incompressible fluid. A clear advantage of the Rankine vortex is that the dispersion relation can be obtained analytically in terms of transcendental functions. This will render it possible to identify fundamental properties associated with the core and common to all swirling flows. Simple experiments using DNS are presented and comparisons are discussed. The same analytical model will be later completed to account for the introduction of the axial shear.

3.2.1 Linear analysis

In the cylindrical frame of reference (r, θ, z) , the Rankine vortex is defined by:

$$\begin{aligned} V_\theta &= \begin{cases} \Omega r & 0 \leq r \leq \delta \\ \frac{\Omega}{r} \delta^2 & r \geq \delta \end{cases} \\ V_r &= 0 \\ V_z &= 0, \end{aligned} \quad (3.9)$$

with Ω the angular velocity of the solid body rotation and δ the vortex core radius. The base flow can therefore be described as a plug profile for the axial vorticity ξ_z assuming the constant value $\xi_z = 2\Omega$ for $r < \delta$ and $\xi_z = 0$ for $r > \delta$.

The evolution of small perturbations (v_r, v_θ, v_z, p) is studied linearising around the base flow the Euler equations within the vortex core, and considering the Laplace equation for the outer region, where the flow is potential. Thus, for $r < \delta$, the linearised equations of the disturbance are:

$$\begin{aligned} \left[\frac{\partial}{\partial t} + \Omega \frac{\partial}{\partial \theta} \right] v_r &= -\frac{1}{\rho} \frac{\partial p}{\partial r} + 2\Omega v_\theta \\ \left[\frac{\partial}{\partial t} + \Omega \frac{\partial}{\partial \theta} \right] v_\theta &= -\frac{1}{\rho r} \frac{\partial p}{\partial \theta} - 2\Omega v_r \\ \left[\frac{\partial}{\partial t} + \Omega \frac{\partial}{\partial \theta} \right] v_z &= -\frac{1}{\rho} \frac{\partial p}{\partial z} \\ \underline{\nabla} \cdot \mathbf{v} &= 0. \end{aligned} \quad (3.10)$$

Following the standard procedure described in chapter 1, a normal mode decomposition is performed. A generic variable of perturbation ϕ is represented by:

$$\phi(r, \theta, z, t) = \frac{1}{(2\pi)^3} \int \int \int_{-\infty}^{+\infty} \hat{\phi}(r) e^{i(kz+m\theta-\omega t)} dk dm d\omega. \quad (3.11)$$

The equation for a single mode is readily obtained from (3.10)-(3.11):

$$D\hat{v}_r = -\frac{1}{\rho} \frac{d\hat{p}}{dr} + 2\Omega\hat{v}_\theta \quad (3.12)$$

$$D\hat{v}_\theta = -\frac{im}{\rho r} \hat{p} - 2\Omega\hat{v}_r \quad (3.13)$$

$$D\hat{v}_z = -\frac{ik}{\rho} \hat{p} \quad (3.14)$$

$$\frac{d\hat{v}_r}{dr} + \frac{\hat{v}_r}{r} + \frac{im}{r} \hat{v}_\theta + ik\hat{v}_z = 0, \quad (3.15)$$

where $D = \frac{\partial}{\partial t} + im\Omega$. The linear set of equations (3.12)-(3.15) govern the modal evolution of a small perturbation introduced into the given base flow. Some algebraic manipulations are

now required to reduce the system to a single equation. Differentiating (3.14) with respect to r and comparing with the radial pressure derivative in (3.12) gives:

$$\frac{1}{ik} D \frac{d\hat{v}_z}{dr} = D\hat{v}_r - 2\Omega\hat{v}_\theta . \quad (3.16)$$

Now, applying the operator D to (3.16), replacing $D\hat{v}_\theta$ by (3.13) and afterwards the pressure with its expression in (3.14), one obtains:

$$D^2\hat{v}_r + 4\Omega^2\hat{v}_r = \frac{1}{ik} D^2 \frac{d\hat{v}_z}{dr} + \frac{2\Omega m}{kr} D\hat{v}_z . \quad (3.17)$$

The above equation has the form $A\hat{v}_r = B\hat{v}_z$ with the linear operator given by the differentials. We need to write something similar between \hat{v}_θ and \hat{v}_z . Comparison between (3.13) and (3.14) leads to:

$$\frac{m}{kr} D\hat{v}_z = D\hat{v}_\theta + 2\Omega\hat{v}_r . \quad (3.18)$$

Again, applying D to (3.18) and replacing $D\hat{v}_r$ with the expression given by (3.12), it comes out:

$$\frac{m}{kr} D^2\hat{v}_z = D^2\hat{v}_\theta - \frac{2\Omega}{\rho} \frac{d\hat{p}}{dr} + 4\Omega^2\hat{v}_\theta . \quad (3.19)$$

Now, differentiating (3.14) with respect to r and substituting the resulting expression for pressure into (3.19), one gets

$$D^2\hat{v}_\theta + 4\Omega^2\hat{v}_\theta = \frac{m}{kr} D^2\hat{v}_z - \frac{2\Omega}{ik} D \frac{d\hat{v}_z}{dr} , \quad (3.20)$$

which is another relation of the form $A\hat{v}_\theta = B\hat{v}_z$. We can now exploit the continuity equation (3.15) to get from (3.17) and (3.20) one single equation for \hat{v}_z . Indeed (3.15), (3.17) and (3.20) are a set of equations in which the pressure is not appearing. Applying $(D^2 + 4\Omega^2)$ to the continuity equation, an expression for $(D^2 + 4\Omega^2)\hat{v}_\theta$ is obtained; this can be introduced in (3.20) giving:

$$-\frac{1}{im} \frac{d}{dr} [(D^2 + 4\Omega^2)(r\hat{v}_r)] - \frac{kr}{m} (D^2 + 4\Omega^2)\hat{v}_z = \frac{m}{kr} D^2\hat{v}_z - \frac{2\Omega}{ik} D \frac{d\hat{v}_z}{dr} . \quad (3.21)$$

Finally, using (3.17) for $(D^2 + 4\Omega^2)(r\hat{v}_r)$, after some elementary manipulations one obtains

$$D^2 \left[\frac{d^2}{dr^2} + \frac{1}{r} \frac{d}{dr} - k^2 - \frac{m^2}{r^2} \right] \hat{v}_z = 4k^2\Omega^2\hat{v}_z . \quad (3.22)$$

Since we are looking for solutions harmonic in time, we write

$$\begin{aligned} D &= -i\omega + im\Omega \\ D^2 &= -(\omega - m\Omega)^2 , \end{aligned}$$

and (3.22) explicitly reads

$$\frac{d^2}{dr^2} \hat{v}_z + \frac{1}{r} \frac{d}{dr} \hat{v}_z + \left[\gamma^2 - \frac{m^2}{r^2} \right] \hat{v}_z = 0 \quad (3.23)$$

with

$$\gamma^2 = k^2 \left[\frac{4\Omega^2}{(\omega - m\Omega)^2} - 1 \right], \quad (3.24)$$

representing the eigenvalue problem for the internal flow field. Equation (3.23) is widely studied since it often describes wave propagation within cylindrical geometries. A general solution [102] is $C_1 J_m(\gamma r) + C_2 Y_m(\gamma r)$, where J_m and Y_m are the ordinary Bessel functions of first and second kind of order m . Since Y_m is singular at $r = 0$, it follows that $C_2 = 0$, and a particular solution of (3.12)-(3.15) is recovered:

$$v_z(r, \theta, z, t) = C_1 J_m(\gamma r) e^{i(kz + m\theta - \omega t)} \quad (3.25)$$

with $J_m(r)$ identifying the eigenfunction corresponding to the m -th azimuthal mode of the perturbation v_z . The other components of perturbation are quickly obtained by (3.12)-(3.15).

In particular, the eigenfunctions are:

$$\begin{aligned} \hat{p}(r) &= -\frac{\rho}{k} (m\Omega - \omega) C_1 J_m(\gamma r) = A J_m(\gamma r) \\ \hat{v}(r) &= \frac{ik^2 A}{\gamma \rho (\omega - m\Omega)} \left[J'_m(\gamma r) - \frac{2\Omega m}{r\gamma (\omega - m\Omega)} J_m(\gamma r) \right] \\ \hat{v}_\theta(r) &= \frac{m}{r\rho} \frac{A}{(\omega - m\Omega)} J_m(\gamma r) + \frac{2\Omega k^2 A}{\gamma \rho (\omega - m\Omega)^2} \left[J'_m(\gamma r) - \frac{2\Omega m}{r\gamma (\omega - m\Omega)} J_m(\gamma r) \right]. \end{aligned} \quad (3.26)$$

For the external field, the potential of perturbation $\Phi = \Phi(r, \theta, z, t)$ has to satisfy the Laplace equation:

$$\left(\frac{\partial^2}{\partial r^2} + \frac{1}{r} \frac{\partial}{\partial r} + \frac{1}{r^2} \frac{\partial^2}{\partial \theta^2} + \frac{\partial^2}{\partial z^2} \right) \Phi = 0. \quad (3.27)$$

As before, the normal mode decomposition gives the modal equation

$$\frac{d^2}{dr^2} \hat{\Phi} + \frac{1}{r} \frac{\partial}{\partial r} \hat{\Phi} - \left[k^2 + \frac{m^2}{r^2} \right] \hat{\Phi} = 0 \quad (3.28)$$

which is a modified Bessel equation whose general solution is $CI_m(kr) + BK_m(kr)$ and I_m , K_m are the first and second modified Bessel functions. Since I_m is singular for $r \rightarrow +\infty$, imposing the perturbation to be evanescent in the far-field requires that $C = 0$, and a particular solution of (3.28) is:

$$\Phi = BK_m(kr) e^{i(kz + m\theta - \omega t)}. \quad (3.29)$$

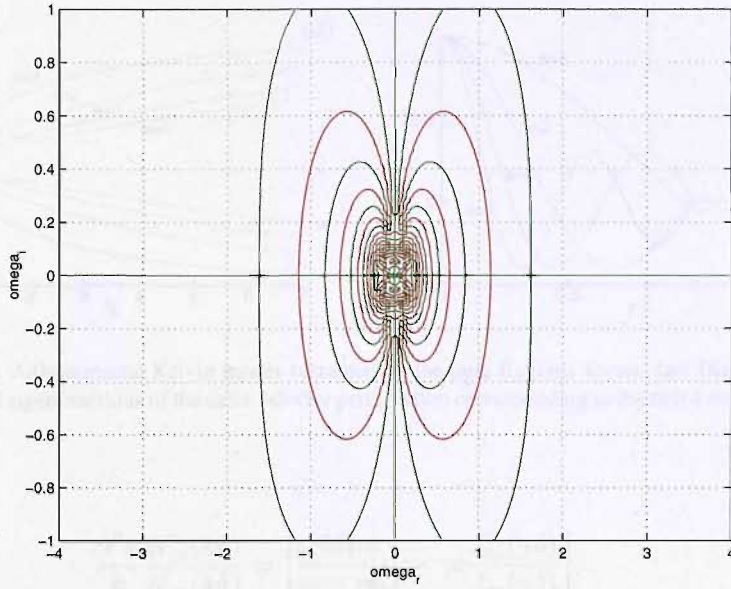


Figure 3.12: Complex frequency plane: line intersections between red and green curves represent solutions of the dispersion relation (3.34) with $k = 2$, $m = 0$.

The velocity is calculated by $\mathbf{v} = \nabla\Phi$ giving the following expressions for the eigenfunctions

$$\begin{aligned}\hat{v}_r(r) &= BkK'_m(r) \\ \hat{v}_\theta(r) &= \frac{im}{r}BK_m(kr) \\ \hat{v}_z(r) &= ikBK_m(kr),\end{aligned}\tag{3.30}$$

while the pressure is obtained by the linearised Bernoulli theorem:

$$\hat{p} = \rho \left[-\mathbf{v} \cdot \mathbf{V} - \frac{\partial\Phi}{\partial t} \right] = i\rho \left[\omega - \frac{\Omega\delta^2}{r^2}m \right] BK_m(kr).\tag{3.31}$$

The existence of such modes, and the evaluation of their nature (stable/unstable) can now be investigated by enforcing a second boundary condition at the vortex core edge δ . The general dynamic condition requires the balance of pressure at the interface, whereas the kinematic condition (at leading order) imposes the equality of the radial velocity perturbation. Using (3.26), (3.30) and (3.31) this leads to

$$\begin{aligned}AJ_m(\gamma\delta) &= i\rho(\omega - \Omega m)BK_m(k\delta) \\ \frac{ik^2A}{\gamma\rho(\omega - m\Omega)} \left[J'_m(\gamma\delta) - \frac{2\Omega m}{\gamma\delta(\omega - m\Omega)}J_m(\gamma\delta) \right] &= kBK'_m(k\delta),\end{aligned}\tag{3.32}$$

consisting in an algebraic system in the unknowns A and B . There will exist non-trivial solutions if and only if the matrix of coefficients has zero determinant. The condition requires

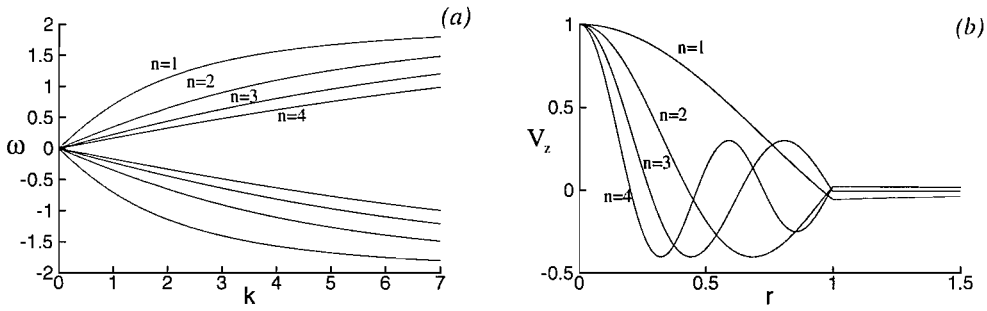


Figure 3.13: Axisymmetric Kelvin modes sustained by the pure Rankine vortex. (a): Dispersion diagram. (b): Normalised eigenfunctions of the axial velocity perturbation corresponding to the first 4 modes, at $k = 3/2$.

that:

$$\frac{\gamma^2 \delta K'_m(k\delta)}{k K_m(k\delta)} = \left[\frac{2\Omega m}{\omega - m\Omega} - \gamma \delta \frac{J'_m(\gamma\delta)}{J_m(\gamma\delta)} \right]. \quad (3.33)$$

Equation (3.33) is the dispersion relation $F(k, m, \omega) = 0$ providing information about the stability of the pure Rankine vortex. In a temporal framework, the wavenumbers (k, m) are assumed real and complex eigenfrequencies ω are looked for. Much analytical work has been done in seeking solutions of (3.33) (see for instance the asymptotic analysis of Saffman [90] or that of Le Dizès & Lacaze [56]). Here we study (3.33) numerically, calculating the values of $F(k, m, \omega)$ at each point of a mesh in the complex plane $\Re(\omega), \Im(\omega)$. The intersections of the curves $\Re(F) = 0$ and $\Im(F) = 0$ give the solutions of (3.33). The use of the standard MATLAB routines renders the operations very simple.

3.2.2 The bulging mode

For the current study it is convenient to non-dimensionalise using the vortex core radius δ as reference length and $\Omega\delta$ as reference velocity. The dispersion relation becomes

$$\frac{\gamma^2 K'_m(k)}{k K_m(k)} = \left[\frac{2m}{\omega - m} - \gamma \frac{J'_m(\gamma)}{J_m(\gamma)} \right] \quad (3.34)$$

with

$$\gamma^2 = k^2 \left[\frac{4}{(\omega - m)^2} - 1 \right].$$

In this section we focus on the axisymmetric (bulging) mode $m = 0$. Following the numerical procedure in the complex plane, it is found that only real values of ω exist: they are associated with neutral inertial modes (the Kelvin waves) propagating longitudinally. For example, fig. 3.12 shows in the complex plane the isolines $\Re(F) = 0$ and $\Im(F) = 0$ for

$k = 2$. Note that due to the oscillatory character of the Bessel functions, the detection of the intersections points becomes problematic especially for $\omega_r \rightarrow 0$ and much depends on the resolution used to discretise the complex plane. We have checked by a direct solver of (3.34) that in this limit solutions yielding a non-zero value of ω_i are false. The results are shown in fig. 3.13-*a*: for a given real wavenumber k , there is a countable sequence $\{\omega(k)\}_n$ of infinite neutral waves with temporal eigenfrequencies $-2 < \{\omega(k)\}_n < +2$. Figure 3.13-*a* shows the dispersion curve for the first 4 modes of the sequence $\{\omega\}_n$. Each mode has a corresponding eigenfunction (fig. 3.13-*b*) given by

$$\{\hat{v}_z\}_n(r) = \begin{cases} \{\hat{v}_z\}_n(0) J_0(\gamma_n r) & r \leq 1 \\ \{\hat{v}_z\}_n(0) \frac{J_0(\gamma_n)}{K_0(\gamma_n)} K_0(\gamma_n r) & r \geq 1, \end{cases} \quad (3.35)$$

where it is understood that n refers to the dependence on the n -th mode of the sequence. Note that the cut-off on the frequency can easily be checked noting that when $m = 0, \omega > 2$, from the second of (3.34) γ^2 is negative and the perturbation (3.35) is purely imaginary. In other words, the axisymmetric Kelvin waves have a specific range $[-2, 2]$ of temporal frequencies.

Inspired by the numerical calculation of Melander and Hussain [75], we have performed direct numerical simulations of the perturbed Rankine vortex. Note that Melander and Hussain do not discuss the possible relation of their results with Kelvin waves. The results of the current study should be evaluated with some care: first, the base flow presents a discontinuity in the axial vorticity at $r = 1$ which renders the test-case not very suitable for a direct numerical simulation; in addition, the difficulty in matching analytical results when dealing with marginal stability is well known. Despite of these considerations, we believe that the case is worth being presented, because it will help to interpret on a physical ground the critical state of Benjamin [6], very relevant in the theoretical studies on vortex breakdown, and because it will provide the opportunity to develop interesting vorticity considerations.

We consider a vortex defined by the non-dimensional form of (3.9) extending on a computational domain of size $L_z = 25, L_r = 10$; conditions at infinity are simulated using the non-reflective techniques discussed in the previous chapter, while the axis treatment implicitly provides conditions of symmetry at $r = 0$ when the calculation runs axisymmetric. The perturbation introduced is easily expressed in terms of axial vorticity:

$$\xi_z^{(p)} = \epsilon \sin[k(z - z_c)] \quad (3.36)$$

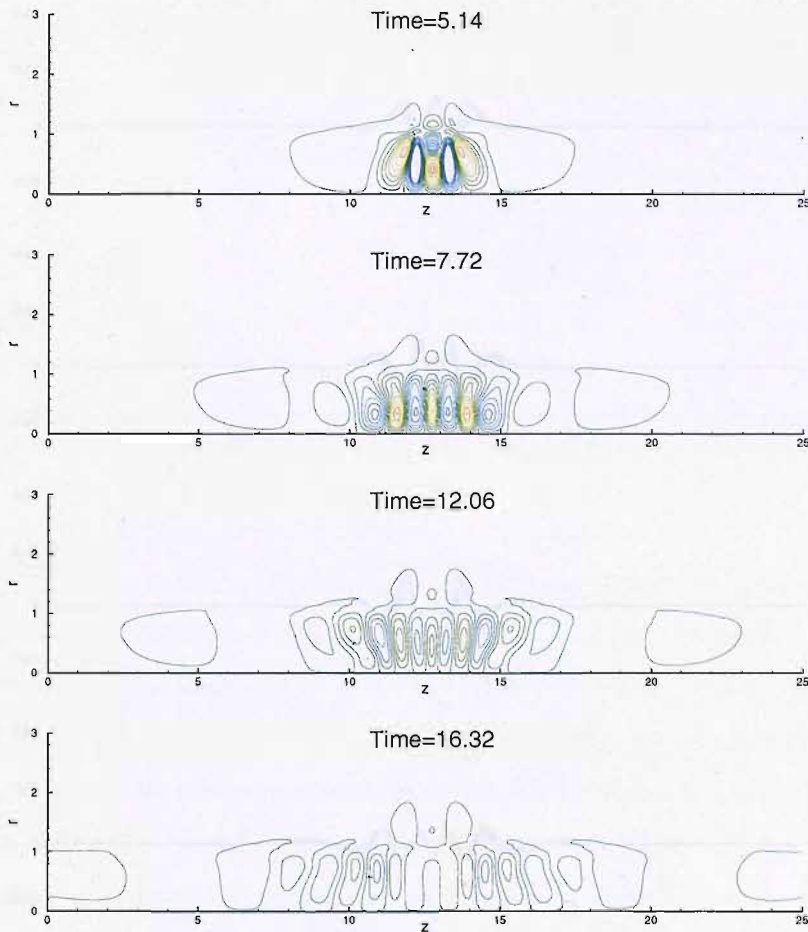


Figure 3.14: Response of the perturbed Rankine vortex at $Re=500$, excited by an axisymmetric perturbation with wavenumber $k = 2\pi$. Contours of azimuthal vorticity revealing the propagation of waves within the vortex core.

$$z \in \left[z_c - \frac{\lambda_k}{2}; z_c + \frac{\lambda_k}{2} \right]$$

$$r \in [0; 1],$$

where ϵ is a small amplitude parameter $\epsilon = 0.01$, z_c is the center of the vortex tube and λ_k is the wavelength associated with the wavenumber k of the linear theory by the simple relation $k = \frac{2\pi}{\lambda_k}$. In words, the perturbation consists of a narrow region localised around the center, where the local angular velocity varies sinusoidally. Since we expected a globally stable response, for the current case there was no need to use the linearised code, which would have required some modifications of the base flow to account for the discontinuity at the core radius. We used the nonlinear code but suppressed the base diffusion: in the absence of radial velocity and with the pressure distribution which balances the centrifugal force, the

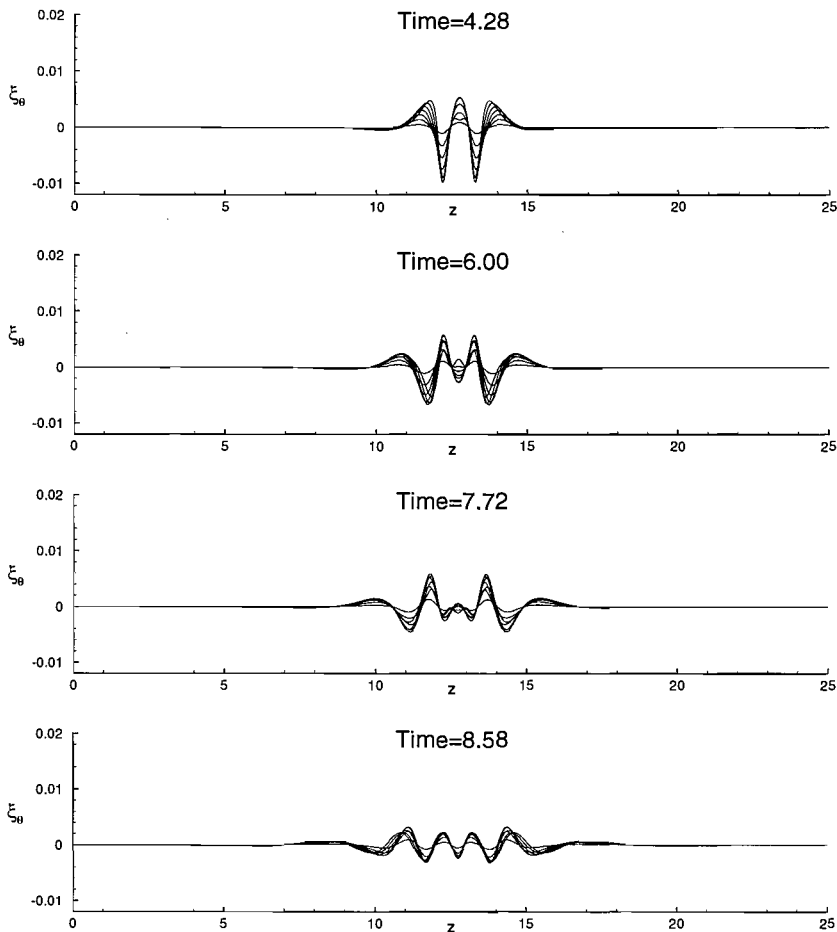


Figure 3.15: Response of the perturbed Rankine vortex at $Re=500$, excited by an axisymmetric perturbation with wavenumber $k = 2\pi$. Evolution of the axial distribution of azimuthal vorticity at different radial locations within the vortex core.

governing Navier-Stokes equations reduce to a pure diffusion equation for (ρV_θ) and (ρV_z) . By adding a body force to the rhs of the governing equations one can compensate for the viscous diffusion and avoid significant changes in time of the base flow, a procedure which has been already adopted for stability analysis [71]. When the perturbation remains small, there's no difference between this approach and the use of the linearised Navier-Stokes.

Figure 3.14 shows the temporal evolution of the azimuthal vorticity ξ_θ for the vortex at $Re=500$, excited by a perturbation with wavenumber $k = 2\pi$. The Mach number is $M = 0.3$ thus the effect of compressibility can be considered nearly negligible. The unperturbed vortex has zero azimuthal vorticity, since there's no axial shear in the initial flow field. After the perturbation has been introduced, a periodic oscillation in the centre induces a symmetrical wave propagation in both the directions. As the wave train moves away from

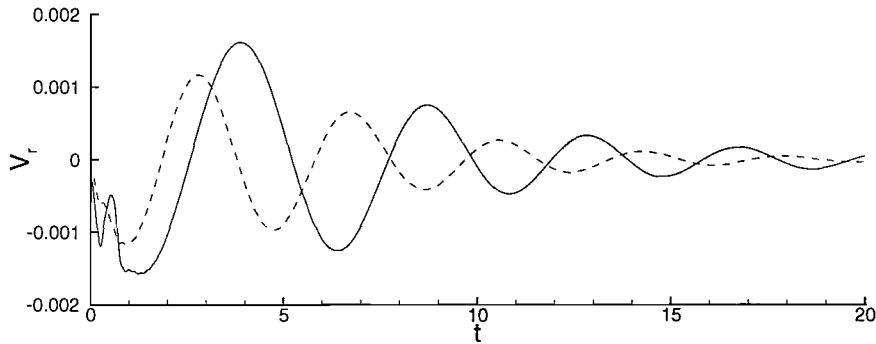


Figure 3.16: Response of the perturbed Rankine vortex at $Re=500$, excited by an axisymmetric perturbation with wavenumber $k = 2\pi$ (dash) and $k = \pi$ (solid). Radial velocity registered in the center of the vortex tube at $r = 0.3$.

the source in z_c , the amplitude of the oscillation in the center gradually reduces until all the energy of the initial disturbance is partially dissipated by viscosity, and partially transferred to the wave train. The value of $k = 2\pi$ was chosen on purpose in order to give graphic evidence that as the time goes on, the oscillation in the center of the tube preserves a $k = 2\pi$ structure (corresponding to a unit wavelength). This is even better evaluated in figure 3.15, where the axial evolution of ξ_θ is plotted at different radial positions within the core. The figure highlights the peculiar formation of the wave train and indicates that its axial structure remains nearly unchanged at z_c . In some sense, this circumstance renders the current case suitable for a stability analysis in a temporal framework, because k is given by the initial perturbation, while ω is looked for.

The frequency ω was then measured monitoring the radial velocity component at z_c and $r = 0.3$. Figure 3.16 reveals a period $\Delta T = 3.8$ corresponding to an angular frequency $\omega = 1.65$. The dispersion diagram (see fig. 3.13-a) shows that the value obtained is close to the predicted frequency for $k = 2\pi$ and $n = 1$ (the precise value by linear theory is 1.76). In the same figure 3.16 it is reported the analogous curve obtained introducing an initial disturbance with $k = \pi$: the angular frequency found is again in good agreement with that of the first mode in 3.13-a (1.45 vs 1.48 of the theory); in the latter case, however, the period of oscillation tends to reduce with time, a behaviour that we found to become more and more evident as $k \rightarrow 0$. The result is somehow elusive, because on the one hand it confirms the low-pass filtering of the core $-2 < \omega < 2$, on the other the computed eigenfrequencies do not seem to account for the higher cylindrical modes.

As mentioned earlier, the signal was registered in the center of the tube z_c : moving

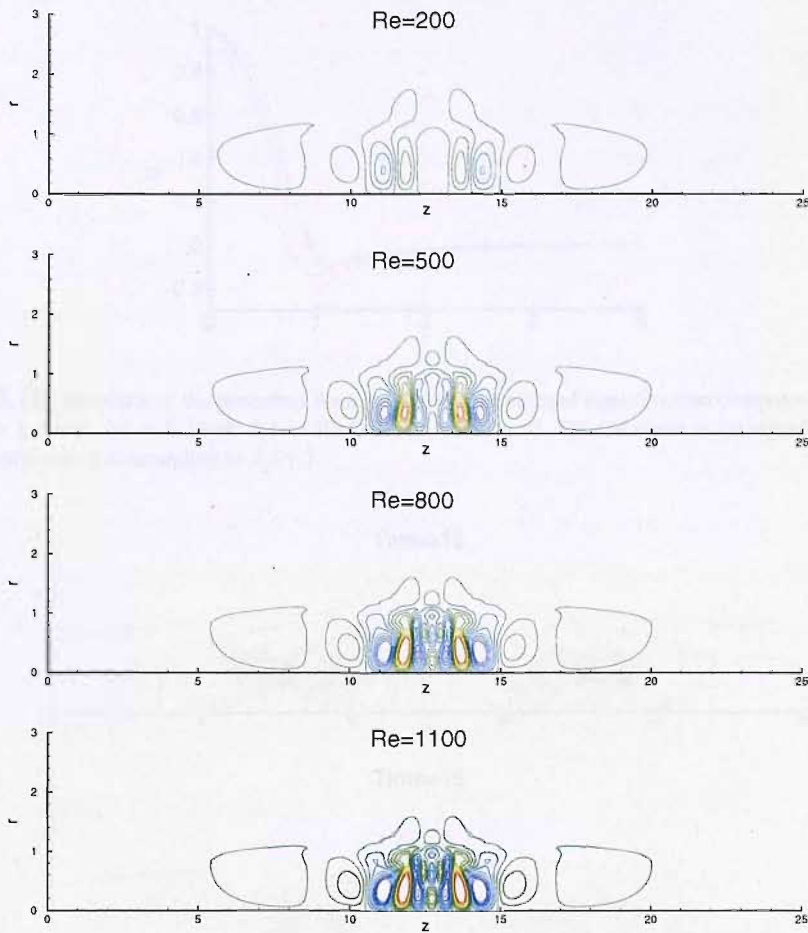


Figure 3.17: Effect of the Reynolds number on the response of the Rankine vortex excited by an axisymmetric perturbation with wavenumber $k = 2\pi$. Contours of azimuthal vorticity at Time=7.76

away from z_c the period of oscillation decreases, consistently with the observation that the spatial structure of the wave train undergoes an axial stretching, clearly visible from fig. 3.14. A non-negligible contribution to this deformation is surely provided by viscosity, but the analytical work of Arendt *et al.* [3] based on the purely inviscid model (3.34) shows a similar behaviour, and they suggest that it is the result of a dispersion mechanism which can be recognised by the diagram of fig. 3.13. It is argued that since for a fixed wavenumber k there exist infinite modes, each of them travelling with a different phase velocity ω/k , the propagation at different speeds rapidly leads the wave to stretch. The resulting wave packet will then move with a velocity which is given by the group velocity $d\omega/dk$: the dispersion diagram reveals that the group velocity at lower k is bigger than that at higher k . It turns out that as the packet is formed, it has to propagate faster leaving the slower modes behind, a

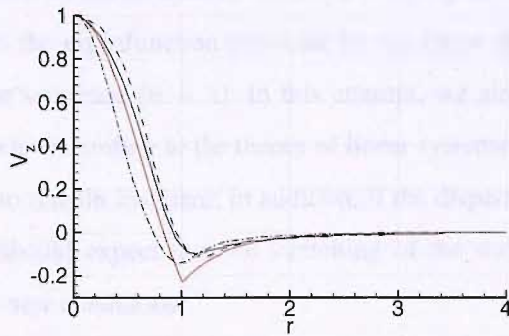


Figure 3.18: Response of the perturbed Rankine vortex. Normalised eigenfunction computed along the ray $\Delta z/\Delta t = 1$. Solid: $\Delta t = 5$. Dash: $\Delta t = 10$. Dash-dots: $\Delta t = 15$. The red curve is the eigenfunction of the initial disturbance, corresponding to $J_0(\gamma_1)$.

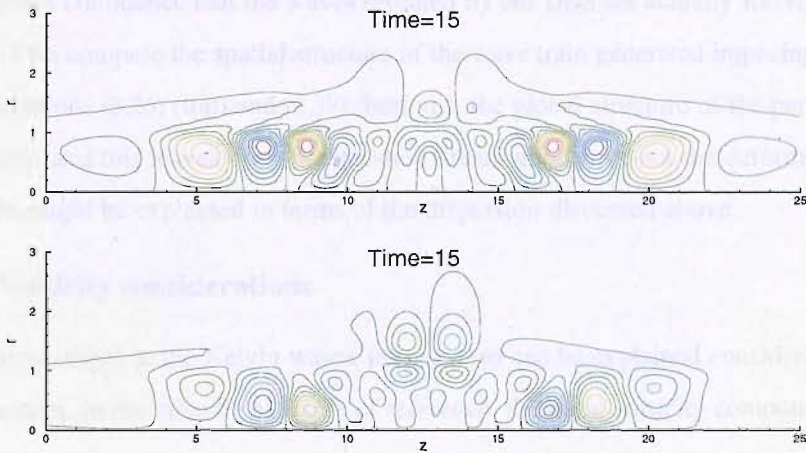


Figure 3.19: Effect of the initial perturbation on the response of the perturbed Rankine vortex. Top: Perturbation defined by (3.36). Bottom: Perturbation defined by (3.37). In both cases the excited wavenumber is $k = 2$

behaviour which seems quite evident in fig. 3.14.

To evaluate the role of viscosity in this specific context, in figure 3.17 we compare responses obtained at different Reynolds numbers. The contour levels are left unchanged, and the damping effect on the amplitude appears evident. However, the spatial distribution of the wave train doesn't seem to be modified and this supports the idea of Arendt *et al.*. Inspired by this consideration, we were prompted to carry on another experiment: in the initial disturbance we replaced expression (3.36) with the following

$$V_z^{(p)} = \{\hat{v}_z\}_1(r) \sin[k(z - z_c)] \tag{3.37}$$

$$z \in \left[z_c - \frac{\lambda_k}{2}; z_c + \frac{\lambda_k}{2} \right],$$

where $\{\hat{v}_z\}_1(r)$ is given by (3.35). That is, we are now giving as input a perturbation having as radial distribution the eigenfunction provided by the linear theory and associated with the first mode of the sequence ($n = 1$). In this attempt, we aimed to isolate as much as possible a single mode: according to the theory of linear systems [18], the eigenfunction of the disturbance has to remain invariant; in addition, if the dispersion mechanism discussed above is valid, we should expect that the stretching of the wave train would be largely reduced under these new conditions.

Figure 3.18 reports the computed normalised eigenfunctions along the spatio-temporal ray $\Delta z/\Delta t = 1$: considering that the analytical solution is based on an inviscid model, the result is satisfactory, as the shape of the perturbation deviates from the initial one just a little. This provides confidence that the waves revealed by our DNS are actually Kelvin modes. In figure 3.19 we compare the spatial structure of the wave train generated imposing the different perturbations (3.36) (top) and (3.37) (bottom): the global structure of the perturbation is very similar, and this leaves open the question about whether or not the deformation of the wave train might be explained in terms of the dispersion discussed above.

3.2.3 Vorticity considerations

The physical origin of the Kelvin waves' propagation can be explained considering the vorticity equation. In the cylindrical frame of reference, the three vorticity components are

$$\begin{aligned}\xi_r &= -\frac{\partial V_\theta}{\partial z} \\ \xi_\theta &= \frac{\partial V_r}{\partial z} - \frac{\partial V_z}{\partial r} \\ \xi_z &= \frac{1}{r} \frac{\partial(rV_\theta)}{\partial r},\end{aligned}\tag{3.38}$$

where it is understood that axisymmetric conditions have been assumed. By taking the curl of the momentum equation in the incompressible Euler equations, the evolution of the vorticity components reads [4]:

$$\begin{aligned}\frac{D\xi_r}{Dt} &= \xi_r \frac{\partial V_r}{\partial r} + \xi_z \frac{\partial V_r}{\partial z} \\ \frac{D\xi_\theta}{Dt} &= \xi_r \frac{\partial V_\theta}{\partial r} + \xi_z \frac{\partial V_\theta}{\partial z} - \frac{V_\theta \xi_r}{r} + \frac{V_r \xi_\theta}{r} \\ \frac{D\xi_z}{Dt} &= \xi_r \frac{\partial V_z}{\partial r} + \xi_z \frac{\partial V_z}{\partial z}.\end{aligned}\tag{3.39}$$

Terms on the right hand side of (3.39) can be denoted as ‘‘tilting’’ or ‘‘stretching’’. The stretching terms are those for which a component remains produced (in magnitude) by the effect of

the flow field on itself, namely $\xi_r \frac{\partial V_r}{\partial r}$, $\frac{V_r \xi_\theta}{r}$ and $\xi_z \frac{\partial V_z}{\partial r}$ in the first, second and third of (3.39) respectively. The structure of the term $\frac{V_r \xi_\theta}{r}$ is different and its physical interpretation may be less recognisable. It derives from the use of the cylindrical coordinates and shows that if positive (negative) azimuthal vorticity is present, a positive (negative) feedback exists due to the radial flow divergence ($V_r > 0$). All the other terms on the rhs of (3.39) are tilting, and they are associated with a gyroscopic effect: rotation around two axes produces vorticity on the third axis.

Let's now analyse in detail the early evolution of the perturbed Rankine vortex in light of (3.39). We consider the case where the initial disturbance is defined by (3.36) with $k = 2$, consisting of a sinusoidal variation of ξ_z (see the first of figure 3.20 showing the axial vorticity distribution of perturbation). In terms of velocity, the disturbance is simply a differential rotation V_θ imposed upon the centre of the vortex tube. Now, differential rotation means a gradient of azimuthal velocity; integrating the third of (3.38) leads to

$$V_\theta(r, z) = \frac{1}{2} \xi_z(z) r$$

thus, the sign of $\frac{\partial V_\theta}{\partial z}$ follows that of $\frac{\partial \xi_z}{\partial z}$.

In the azimuthal vorticity equation, the second of (3.39), the stretching term is initially zero; note also that all the tilting terms can be made compact using the expressions given by (3.38), obtaining

$$\left(\frac{D\xi_\theta}{Dt} \right)_{\text{tilt}} = \frac{\partial}{\partial z} \left(\frac{L^2}{r^3} \right) \quad (3.40)$$

where $L = rV_\theta$ represents the circulation. Equation (3.40) highlights that the axial gradient of V_θ generates azimuthal vorticity by vortex tilting. The ξ_θ produced will be positive where $\frac{\partial V_\theta}{\partial z} > 0$ (that is where $\frac{\partial \xi_z}{\partial z} > 0$) and negative where $\frac{\partial V_\theta}{\partial z} < 0$. The second of fig. 3.20 is consistent with these observations: the curves refer to different radial positions in the core, with the amplitude growing in modulus from the axis toward the edge. The tilting effect generates an axial distribution of ξ_θ which advances in phase by $\lambda_k/4$ that of ξ_z . The axial velocity induced by ξ_θ (the third of fig. 3.20) has an axial distribution which is in phase with that of ξ_θ , therefore advancing ξ_z of $\lambda_k/4$: it turns out that $\frac{\partial V_z}{\partial z}$ will be counter phase with respect to ξ_z . At this point the stretching term $\xi_z \frac{\partial V_z}{\partial z}$ in the third of (3.39) becomes important, but due to the established phase delay the axial vorticity will be reduced where it was initially bigger, while it will be increased where it was initially smaller. In other words, where ξ_z is negative in the first of fig. 3.20 (recall that it is the axial vorticity

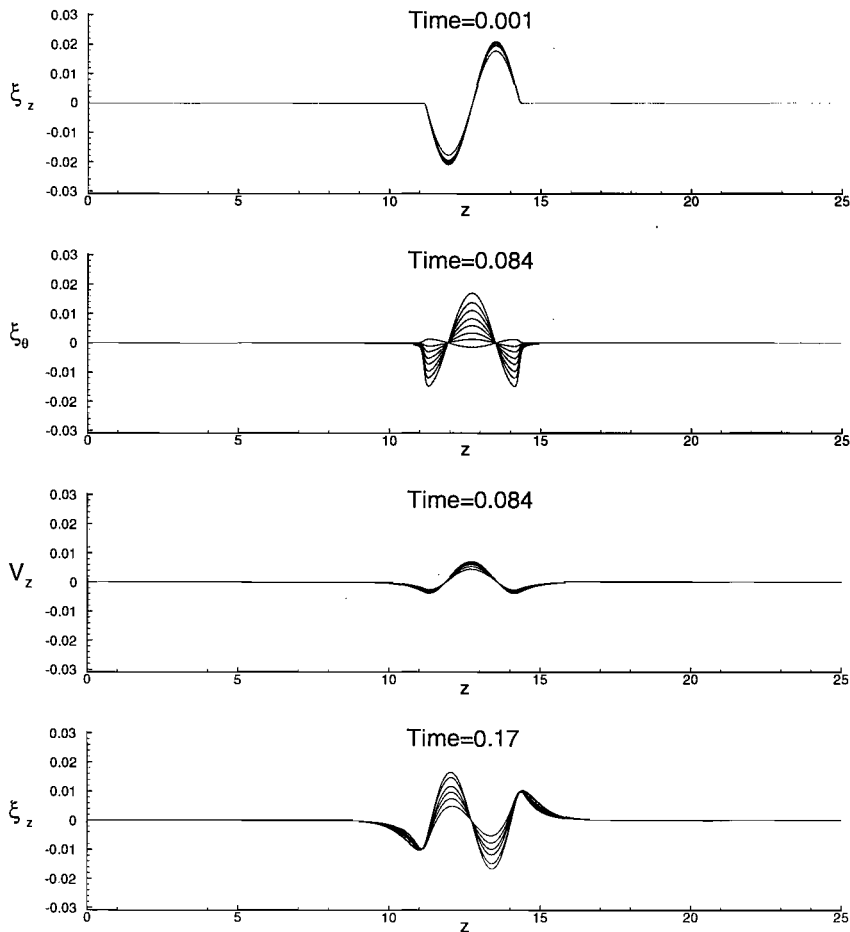


Figure 3.20: Early evolution of the perturbed Rankine vortex; axial distribution of different perturbation quantities within the core. For the azimuthal vorticity, the maximum amplitude is reached at vortex edge; for the axial vorticity (bottom), the maximum amplitude is near the axis.

of the perturbation, to be added to the constant value 2 to get the axial vorticity of the total flow field) the axial velocity accelerates (the third of 3.20) and the total axial vorticity has to increase by stretching. Exactly the opposite occurs where ξ_z is initially positive: by stretching, the total axial vorticity has to reduce. A restoring mechanism is therefore created due to the coupling between the tilting and the stretching. This acts on the vortex tube as a sort of radial elasticity which causes the propagation of the axisymmetric Kelvin modes. It's important to point out that the wave propagation described is due to pure inertial effects, and it would be completely absent without axial vorticity.

3.2.4 The critical state

Let's consider the superimposition of the pure Rankine vortex with a uniform flow field $\hat{i}_z V_z$ oriented along the axis. In a frame of reference $(r', \theta', z') = (r, \theta, z - V_z t)$ moving with $\hat{i}_z V_z$, the base flow will appear as a pure vortex, and a single perturbation component $\hat{\phi}(r') e^{i(kz' + m\theta' - \omega t)}$ will exist if the dispersion relation (3.33) admits non-trivial solutions. The observer in the laboratory frame, will see the perturbation as

$$\hat{\phi}(r) e^{i(kz + m\theta - \omega t)} = \hat{\phi}(r') e^{i(kz' + kV_z t + m\theta' - \omega t)} = \hat{\phi}(r') e^{i(kz' + m\theta' - (\omega - kV_z)t)},$$

which is the same as in the moving frame, but with frequency $\omega - kV_z$. It turns out that the addition of the base flow corresponds to a frequency shift $\omega \rightarrow \omega - kV_z$. The dispersion relation will still be given by (3.33) provided that ω is replaced by $\omega - kV_z$:

$$\begin{aligned} \frac{\gamma^2 \delta}{k} \frac{K'_m(k\delta)}{K_m(k\delta)} &= \left[\frac{2\Omega m}{\omega - kV_z - m\Omega} - \gamma \delta \frac{J'_m(\gamma\delta)}{J_m(\gamma\delta)} \right] \\ \gamma^2 &= k^2 \left[\frac{4\Omega^2}{(\omega - kV_z - m\Omega)^2} - 1 \right]. \end{aligned} \quad (3.41)$$

In order to introduce the swirl number, it is convenient to non-dimensionalise assuming now δ as reference length, and V_z as reference velocity. The resulting relation is:

$$\frac{\gamma^2}{k} \frac{K'_m(k)}{K_m(k)} = \left[\frac{2mS}{\omega - k - mS} - \gamma \frac{J'_m(\gamma)}{J_m(\gamma)} \right] \quad (3.42)$$

with

$$\begin{aligned} S &= \frac{\Omega \delta}{V_z} \\ \gamma^2 &= k^2 \left[\frac{4S^2}{(\omega - k - mS)^2} - 1 \right]. \end{aligned} \quad (3.43)$$

It can be noticed that when $S = 1$, (3.42) reduces to (3.34) with $\omega - k$ replacing ω . We arrive at the (maybe trivial) conclusion that in the case $S = 1$ the dispersion diagram corresponding to (3.42) is given by that of (3.34) rotated by $\pi/4$. For the bulging mode $m = 0$, the first branches of the infinite sequence are reported in figure 3.21. The other branches (not shown) lie between these lower and upper curves. Under these conditions, the sign of the group velocity, given by the slope of these curves, is everywhere positive, meaning that upstream propagation of energy is not possible: any perturbation introduced will be convected downstream from the base flow. In this case the flow is said to be *supercritical*.

For lower level of swirl, the lower branch of the dispersion diagram may have a range of axial wavenumbers (close to zero) where the group velocity is negative. In this case the

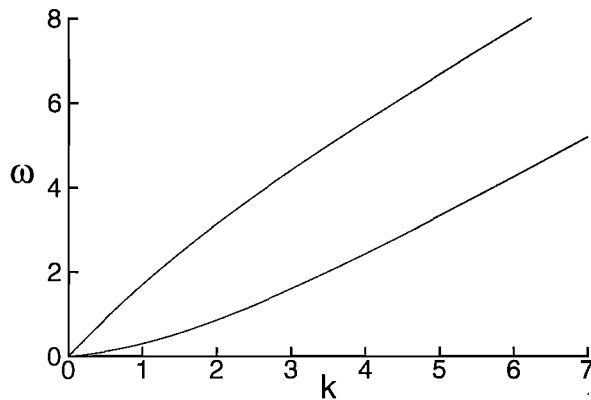


Figure 3.21: Axisymmetric Kelvin modes sustained by a swirling flow defined by a Rankine vortex superimposed on an uniform axial flow field. $S = 1$.

flow is said to be *subcritical* and Kelvin waves can propagate upstream. The critical case marks the interface between the two states: the group velocity is zero for $k \rightarrow 0$ and an infinitesimal standing wave with infinite wavelength can be sustained by the base flow. The corresponding value of the swirl ratio S represents the critical swirl number first introduced by Squire [96] and Benjamin [6]. Criticality represents therefore a pure theoretical concept based on a local analysis in which the flow is assumed infinitely long and parallel.

Squire [96] was the first to associate the onset of vortex breakdown to the concept of criticality. In his view, when inhomogeneities are introduced, a critical state can be locally reached somewhere and eventually divide a supercritical flow from a subcritical one. In that case, an unstable global mode would be constructed as a superposition of waves propagating upstream. The section where the critical conditions are reached would then act as a barrier where disturbances grow to large amplitude. The linear analysis does not model this process, and one should rather refer to the nonlinear theory of Leibovich [57, 58, 59] discussed in the introduction. It's interesting to note that Benjamin [6] started from a completely different perspective than Squire, although he finally reached the same definition of criticality. In his analysis he shows that supercritical flows (those which do not sustain waves) are characterised by an excess of flow force, defined as

$$\int_S (p + \rho V_z^2) ds$$

and representing an integral measure of the axial momentum flux. A transition from supercritical to subcritical should be accompanied by a reduction of flow force and Benjamin

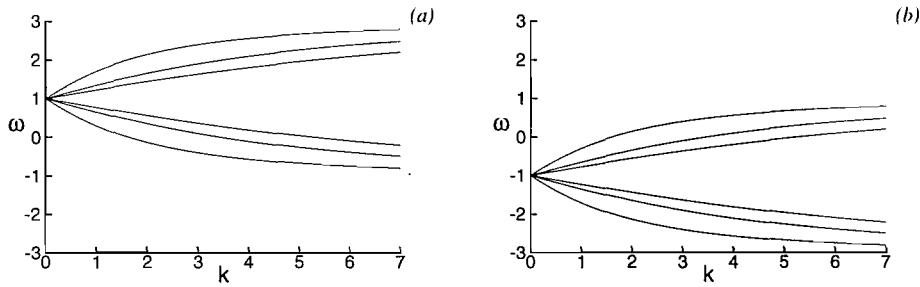


Figure 3.22: Bending Kelvin modes sustained by the pure Rankine vortex. Dispersion diagram for (a): $m = +1$ and (b): $m = -1$.

identifies the vortex breakdown as the formation of a wave train which accounts for such a reduction of flow force [6].

3.2.5 The bending modes

Figure 3.22 shows the computed dispersion diagram corresponding to relation (3.34) with $m = +1$ and $m = -1$. According to these results, the symmetry between lower and upper branches is no longer valid for the bending modes. In particular, the positive bending modes $m = +1$ increase their frequency of $\simeq +1$ while the negative bending mode $m = -1$ are seen to reduce their frequency of $\simeq -1$. As for the bulging mode, the cut-off on the frequency can be again recovered from the expression for γ in (3.34): when $|\omega - m| > 2$, γ is negative and the eigenfunctions become purely imaginary. Saffman [90] suggests classifying the bending modes according to the sign of the frequency $\omega - m$ observed in a frame moving with the vortex core. *Cograde* modes are those for which $\omega - m > 0$ (the upper branches in fig. 3.22) while *retrograde* modes have $\omega - m < 0$ (the lower branches).

In analogy to the previous study of the bulging mode, DNS was used to evaluate the response of the Rankine vortex to a bending perturbation defined as:

$$\begin{aligned} \xi_z^{(p)} &= \epsilon \sin [k(z - z_c) + m\theta] \\ z &\in \left[z_c - \frac{\lambda_k}{2}; z_c + \frac{\lambda_k}{2} \right] \\ r &\in [0; 1] . \end{aligned} \quad (3.44)$$

The axial wavenumber excited is $k = 2\pi$. Fig. 3.23-3.24 show results relative to an initial perturbation with $m = +1$ and with $m = -1$. Consistent with the dispersion diagrams, in each case the wave propagation is no longer symmetric. On the other hand, the flow field generated by an initial disturbance with $m = -1$ is symmetric to that generated by a disturbance with $m = +1$. A perturbation with $m = -1$ corresponds to a cowinding spiral, a

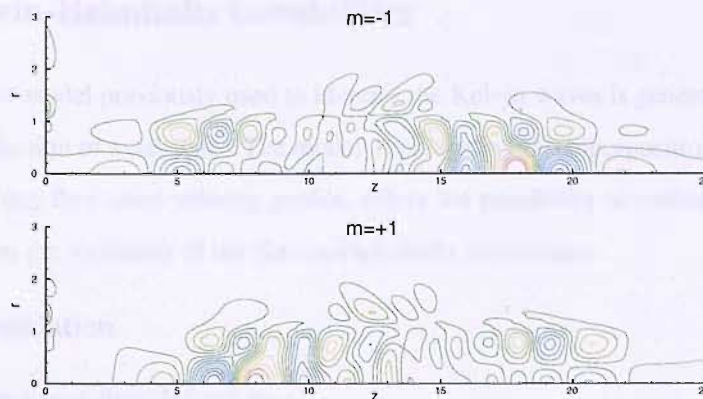


Figure 3.23: Response of the perturbed Rankine vortex, excited by a wavenumbers pair $(m, k) = (1, 2\pi)$. Azimuthal vorticity contours on the meridional plane $\theta = 0$ at Time=20.



Figure 3.24: Response of the perturbed Rankine vortex, excited by a wavenumbers pair $(m, k) = (1, 2\pi)$. Iso-surfaces of radial velocity component: $V_r = \pm 0.0004$. Time=20.

spiral twisting counterclockwise if advancing along z . In a frame of reference moving with the base flow, such an initial perturbation will appear axisymmetric: the flow response to the initial perturbation has to be a wave train of the same kind as that produced by an axisymmetric perturbation $m = 0$, but moving along a helical path. This is clearly confirmed in figure 3.24 which shows the iso-surface of the radial velocity component. Note that the helix is extending in both directions, but the energy level of the packet propagating upstream is smaller, and it cannot be seen in the figure. According to the indications of fig. 3.22, for $m = -1$, the lower branches correspond to waves propagating upstream $\omega < 0$ and have higher frequency (in magnitude) than those moving downstream. This means that their energy level has to be smaller, because the wave train, whose formation absorbs energy from the disturbance, develops on a faster scale. For an initial disturbance $m = +1$ everything is swapped; the Kelvin modes propagate on a counterwinding helix, and due to their higher frequency, waves propagating downstream are attenuated faster.

3.3 Kelvin-Helmholtz instabilities

The analytical model previously used to identify the Kelvin waves is generalised to account for the introduction of axial shear. The model, representing the superposition of the Rankine vortex on a plug flow axial velocity profile, offers the possibility to evaluate the effect of the swirl on the evolution of the Kelvin-Helmholtz instabilities.

3.3.1 Formulation

Let's consider a base flow defined as:

$$\begin{aligned} V_\theta &= \begin{cases} \Omega r & 0 \leq r < \delta \\ \frac{\Omega}{r} \delta^2 & r > \delta \end{cases} \\ V_r &= 0 \\ V_z &= \begin{cases} V_\infty & 0 \leq r < \delta \\ 0 & r > \delta \end{cases} \end{aligned} \quad (3.45)$$

In the present model the axial shear is generated at the interface between the vortex core and the external potential flow. The linear analysis has to be conducted following the same steps undertaken in §3.2.1, with the external and internal flow field studied separately, and a dispersion relation obtained imposing an appropriate interface condition. Compared to the pure Rankine vortex, the external flow field remains unchanged, therefore the eigenfunctions of perturbations are still given by (3.30)-(3.31).

For the internal flow field, linearisation of the base equations and subsequent modal decompositions lead to a set of equations preserving the same formal structure of (3.12)-(3.15) provided that the differential operator D is now given by

$$D = \frac{\partial}{\partial t} + im\Omega + ikV_\infty. \quad (3.46)$$

Hence, all the manipulations performed to reduce the set (3.12)-(3.15) to the single equation for \hat{v}_z remain unaffected, and one has again

$$D^2 \left[\frac{d^2}{dr^2} + \frac{1}{r} \frac{d}{dr} - k^2 - \frac{m^2}{r^2} \right] \hat{v}_z = 4k^2 \Omega^2 \hat{v}_z, \quad (3.47)$$

with

$$D^2 = (-i\omega + im\Omega + ikV_\infty)^2 = -(\omega_j - m\Omega)^2$$

and $\omega_j = \omega - kV_\infty$. The eigenvalue problem for solutions harmonic in time is

$$\begin{aligned} \frac{d^2}{dr^2} \hat{v}_z + \frac{1}{r} \frac{d}{dr} \hat{v}_z + \left[\gamma^2 - \frac{m^2}{r^2} \right] \hat{v}_z &= 0 \\ \gamma^2 &= k^2 \left[\frac{4\Omega^2}{(\omega_j - m\Omega)^2} - 1 \right]. \end{aligned} \quad (3.48)$$

Consequently, the eigenfunctions are those defined by (3.25)-(3.26) but with ω_j replacing ω . For the boundary conditions at the interface, one has to consider the surface $\eta = \eta(\theta, z, t)$ defining the cylindrical vortex sheet. After the introduction of the disturbance, the sheet will move with velocity given by its material derivative:

$$\frac{D\eta}{Dt} = \frac{\partial\eta}{\partial t} + \mathbf{V} \cdot \nabla\eta = \frac{\partial\eta}{\partial t} + V_r \frac{\partial\eta}{\partial r} + \frac{V_\theta}{r} \frac{\partial\eta}{\partial\theta} + V_z \frac{\partial\eta}{\partial z}. \quad (3.49)$$

For the external and internal field respectively, (3.49) is evaluated at the interface neglecting the products of linear terms:

$$\begin{aligned} \frac{D\eta}{Dt} &= \frac{\partial\eta}{\partial t} + \Omega \frac{\partial\eta}{\partial\theta} \\ \frac{D\eta}{Dt} &= \frac{\partial\eta}{\partial t} + \Omega \frac{\partial\eta}{\partial\theta} + V_\infty \frac{\partial\eta}{\partial z}. \end{aligned} \quad (3.50)$$

Following the analogy of Drazin [24] for the planar vortex sheet, we suppose that a local displacement of the sheet occurs with velocity given by v_r . That is:

$$\begin{aligned} v_r^{(e)} &= \frac{\partial\eta}{\partial t} + \Omega \frac{\partial\eta}{\partial\theta} \\ v_r^{(i)} &= \frac{\partial\eta}{\partial t} + \Omega \frac{\partial\eta}{\partial\theta} + V_\infty \frac{\partial\eta}{\partial z}. \end{aligned} \quad (3.51)$$

Assuming now a Fourier decomposition for η

$$\eta(r, \theta, z) = \hat{\eta} e^{i(kz + m\theta - \omega t)},$$

the two equations (3.51) are used to explicitly determine the amplitude $\hat{\eta}$:

$$\begin{aligned} \hat{v}_r^{(e)} &= (m\Omega - \omega) i \hat{\eta} \\ \hat{v}_r^{(i)} &= (m\Omega + kV_\infty - \omega) i \hat{\eta}. \end{aligned} \quad (3.52)$$

Continuity of the particle displacement finally implies that

$$\frac{\hat{v}_r^{(e)}}{\omega - m\Omega} = \frac{\hat{v}_r^{(i)}}{\omega - m\Omega - kV_\infty}, \quad (3.53)$$

which reduces to the equality of the two radial components in the case of the pure Rankine vortex. As before, the constraint on the balance of pressure together with (3.53), consist of a system of two homogeneous equations whose solvability condition gives the desired dispersion relation:

$$\gamma^2 \delta k \frac{K'_m(k\delta)}{K_m(k\delta)} = \frac{(\omega - m\Omega)^2}{(\omega - kV_\infty - m\Omega)^2} \left[\frac{2\Omega m}{\omega - m\Omega - kV_\infty} - \gamma \delta \frac{J'_m(\gamma\delta)}{J_m(\gamma\delta)} \right]. \quad (3.54)$$

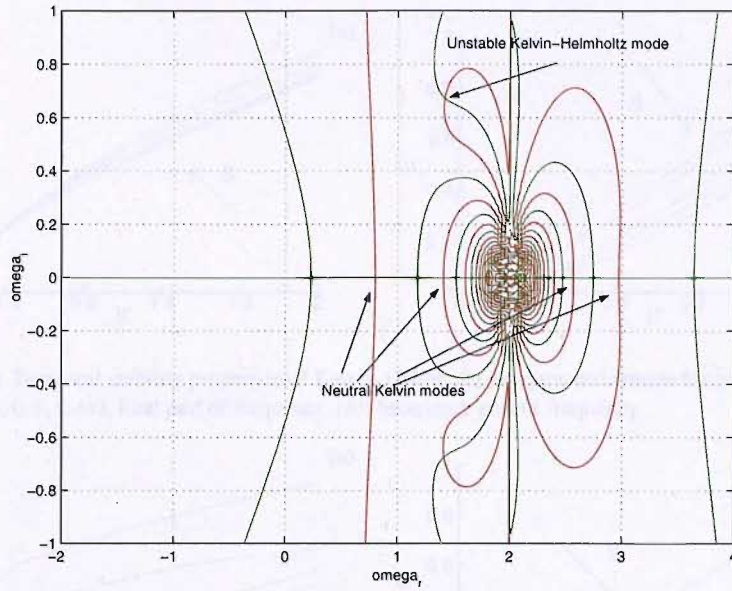


Figure 3.25: Complex frequency plane: line intersections between red and green curves represent solutions of the dispersion relation (3.55) with $S = 1$, $k = 2$, $m = 0$.

Then, following the usual lines, the swirl ratio S is introduced by non-dimensionalisation using δ and V_∞ as reference quantities. The final dispersion relation that needs to be studied in the complex plane is written:

$$\frac{\gamma^2}{k} \frac{K'_m(k)}{K_m(k)} = \frac{(\omega - mS)^2}{(\omega - k - mS)^2} \left[\frac{2mS}{\omega - k - mS} - \gamma \frac{J'_m(\gamma)}{J_m(\gamma)} \right] \quad (3.55)$$

$$\gamma^2 = k^2 \left[\frac{4S^2}{(\omega - k - mS)^2} - 1 \right].$$

3.3.2 Analytical results

As mentioned earlier, the effect of the curvature at $r = \delta$ may be considered negligible for axisymmetric perturbations with high wavenumber k . For such disturbances, we can therefore estimate that the evolution is that of a pure two-dimensional planar shear developing in a meridional plane, with growth rate [24]:

$$\omega_i = \frac{1}{2} k V_\infty. \quad (3.56)$$

Figure 3.25 shows in the complex plane the solutions of the dispersion relation (3.55) found at $S = 1$, $k = 2$, $m = 0$. As for the isolated Rankine vortex, there are infinite solutions on the real axis representing the extension of the inertial Kelvin modes to the current swirling jet.

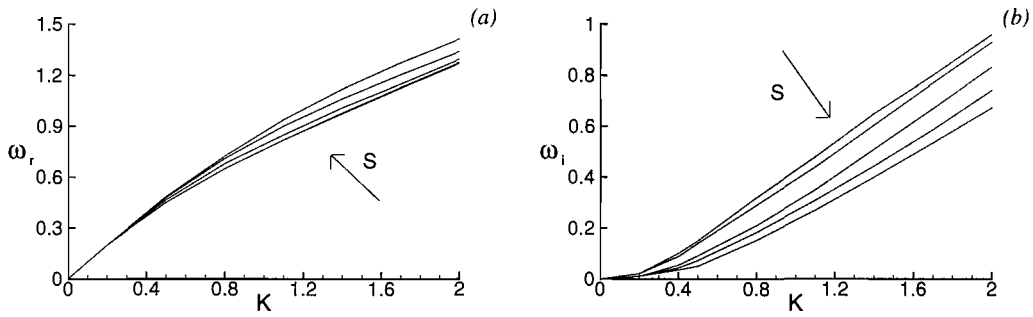


Figure 3.26: Temporal stability properties of Kelvin-Helmholtz axisymmetric mode for levels of swirl ratio $S = 0, 0.2, 0.6, 0.8, 1$. (a): Real part of frequency. (b): Imaginary part of frequency.

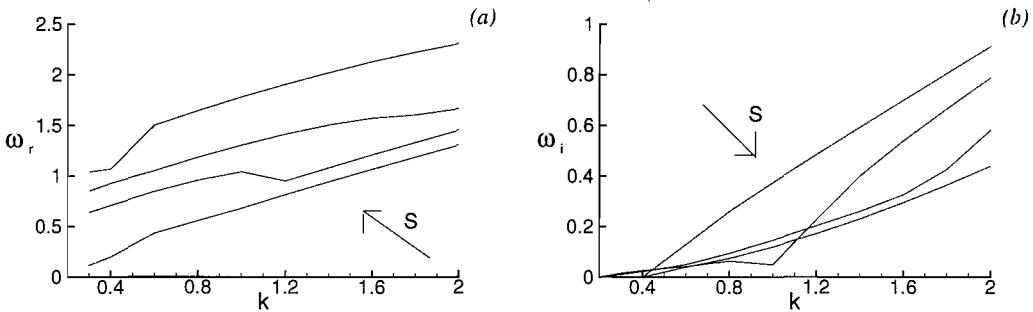


Figure 3.27: Temporal stability properties of Kelvin-Helmholtz bending mode $m = +1$ for levels of swirl ratio $S = 0.2, 0.4, 0.6, 1$. (a): Real part of frequency. (b): Imaginary part of frequency.

The novelty here is the existence of a single unstable mode which has to be associated with the additional presence of the axial shear at the core edge.

The temporal stability properties of this unstable axisymmetric mode are reported in figure 3.26 for different values of the swirl ratio. At $S = 0$ (pure cylindrical jet), the imaginary part is seen to have a constant slope for wavenumbers higher than $k \simeq 0.6$. Its value at $k = 2$ is $\omega_i(k = 2) = 0.96$, in agreement with the value predicted by the non-dimensional form of (3.56); increasing the swirl, any axial wavenumber remains unstable, but the growth rate is reduced, so the effect of the swirl on the development of the axisymmetric Kelvin-Helmholtz mode is clearly *stabilising*. At higher wavenumbers all the curves tend to become parallel and to increase linearly in accordance with the planar approximation (3.56). The value of k above which the slope remains constant increases with S , that is, the higher is the swirl applied, the wider is the range of low wavenumbers sensitive to the rotation.

Results relative to the negative bending mode $m = -1$ are reported in figures 3.28 and 3.29. There exist two ranges of swirl with different behaviours. A first one, $S \leq 0.4$, in which the effect of the swirl is stabilising at low axial wavenumbers and slightly destabilising at

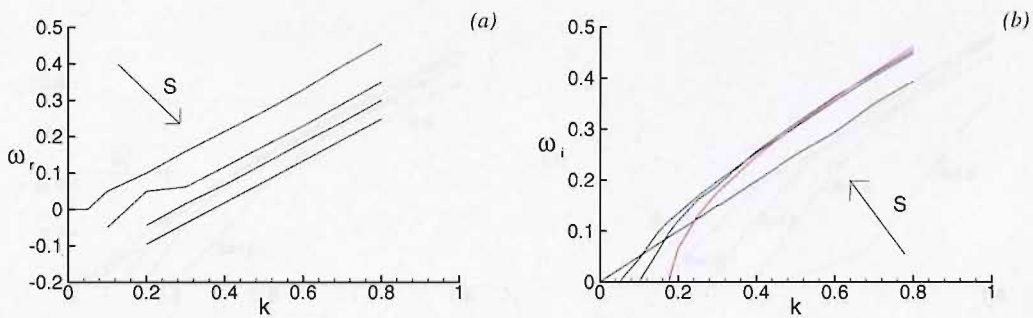


Figure 3.28: Temporal stability properties of Kelvin-Helmholtz bending mode $m = -1$ for levels of swirl $S = 0, 0.2, 0.3, 0.4$. (a): Real part of frequency. (b): Imaginary part of frequency.

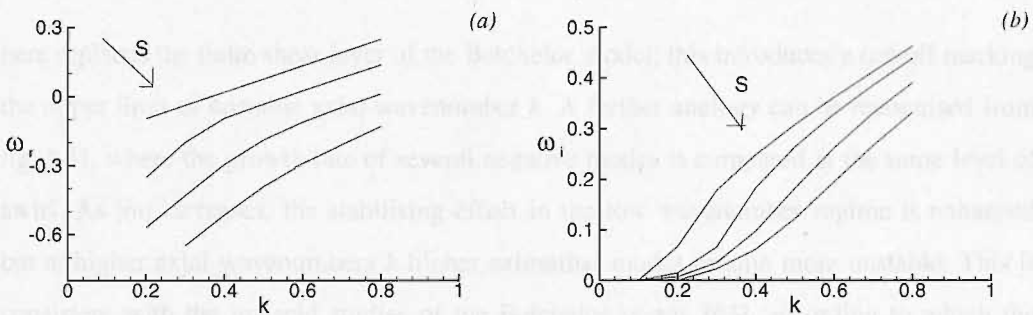


Figure 3.29: Temporal stability properties of Kelvin-Helmholtz bending mode $m = -1$ for levels of swirl $S = 0.4, 0.6, 0.8, 1$. (a): Real part of frequency. (b): Imaginary part of frequency.

higher wavenumbers (see fig. 3.28-*b*). Outside this range, $S > 0.4$, increasing the swirl decreases the temporal growth rate at all the axial wavenumbers (fig. 3.29-*b*). At low swirl the real frequency is positive for all wavenumbers (fig. 3.28-*a*). Increasing gradually the swirl, ω_r reduces and a range of low wavenumbers k with negative frequency appears visible. For $S > 0.6$, ω_r becomes negative for all the range of unstable wavenumbers (fig. 3.29-*a*). These negative modes consist therefore of winding corotating spirals. With regard to the positive bending mode $m = +1$, fig. 3.27 shows that the swirl has a stabilising influence qualitatively similar to that encountered for the negative mode in the range $S > 0.4$. Note, however, that the reduction in the growth rate due to the swirl is enhanced, leading to the important conclusion that the positive bending modes are less unstable than the negative ones.

A similar behaviour occurs for higher modes $m < -1$ (see fig. 3.30), the difference being that as $|m|$ increases, the value of S beyond which the swirl begins having a stabilising effect, becomes bigger. This result is strongly reminiscent of the behaviour revealed in the study of the Batchelor vortex, and one may consider the diagrams of fig. 3.30 as the equivalent of fig. 3.8 adapted to the current model; the discontinuity in the velocity profile studied

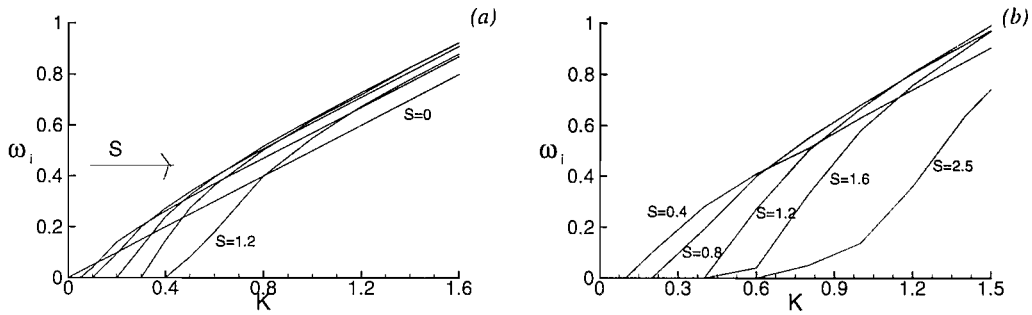


Figure 3.30: Temporal growth rate of Kelvin-Helmholtz modes (a) $m = -2$ and (b) $m = -5$ for different levels of swirl.

here replaces the finite shear layer of the Batchelor model; this introduces a cut-off marking the upper limit of unstable axial wavenumber k . A further analogy can be recognised from fig. 3.31, where the growth rate of several negative modes is compared at the same level of swirl. As $|m|$ increases, the stabilising effect in the low wavenumber regime is enhanced but at higher axial wavenumbers k higher azimuthal modes remain more unstable. This is consistent with the inviscid studies of the Batchelor vortex [63], according to which the maximum growth rate over all the axial wavenumbers increases with $|m|$.

Thus, some properties of the Batchelor vortex are captured by the current model: in particular, the mode selection follows the same trend, with negative waves dominating and presenting an opposite behavior in two ranges of swirl. In both cases these waves are corotating and cowinding, and the frequency increases with k . The main difference is observed in the absence of swirl. The present model reveals instability of all the azimuthal modes. These have to be necessarily shear instabilities, which come gradually modified when moderate swirl is introduced. The stabilisation of the shear layers modes due to the swirl has been found in several circumstances by different authors [48, 74] but a systematic study aiming to elucidate the interaction between axial shear and the core effect is relatively recent. In particular, Loseleux *et al.* [67] have pointed out that the stabilising role of the swirl occurs through a coupling between the Kelvin waves and the axial Kelvin-Helmholtz modes. They show that in the low wavenumber range (where full stabilisation takes place) the existence of direct resonance between the unstable Kelvin-Helmholtz modes and the neutral inertial modes. The same reasoning can be used to explain why negative modes are more unstable than the positive: we have noticed that the real frequency of the helical Kelvin-Helmholtz modes has always positive slope. A comparison with the frequency of the neutral bending modes sustained by the pure vortex (fig. 3.22) suggests that the interaction can affect pos-

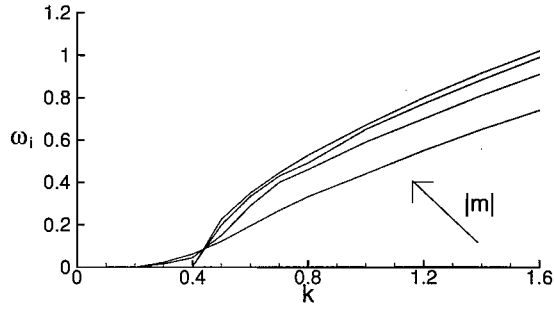


Figure 3.31: Growth rate of Kelvin-Helmholtz modes $m = -1, -2, -3, -4$ at the level of swirl $S = 1$.

itive modes more than negative. The damping effect of this coupling may therefore render the negative modes more unstable.

3.3.3 Numerical results

The analytical model discussed has provided some indications about the role of the swirl on the development of shear instabilities. In particular, the study suggests that axisymmetric Kelvin-Helmholtz modes, *i.e.* those responsible for the generation of the classic vortex rings in jets, appear to be stabilised by the addition of the rotation. The analysis on the Batchelor vortex could not highlight this mechanism, since at $q = 0$, we found unstable only the azimuthal modes $m = \pm 1$, and with a very small value of ω_i . It appears natural, therefore, to extend the Batchelor model to a velocity profile with smaller shear layer thickness, in order to evaluate the applicability of the results of previous subsection to a continuous model.

For this purpose, we present here the stability analysis obtained by LTS performed on the following swirling flow:

$$\begin{aligned}
 V_z(r) &= \frac{1}{1 + (\exp(r^2 \ln(2)) - 1)^3} \\
 V_r(r) &= 0 \\
 V_\theta(r) &= q \frac{1 - e^{-r^2}}{r} .
 \end{aligned} \tag{3.57}$$

The azimuthal velocity profile is the same as the Batchelor vortex, whereas the new axial velocity distribution (introduced by Billant [9] to model his experimental jet) presents a reduced value of the shear layer thickness:

$$\Theta = \int_0^\infty V_z(r) [1 - V_z(r)] dr = 0.13 .$$

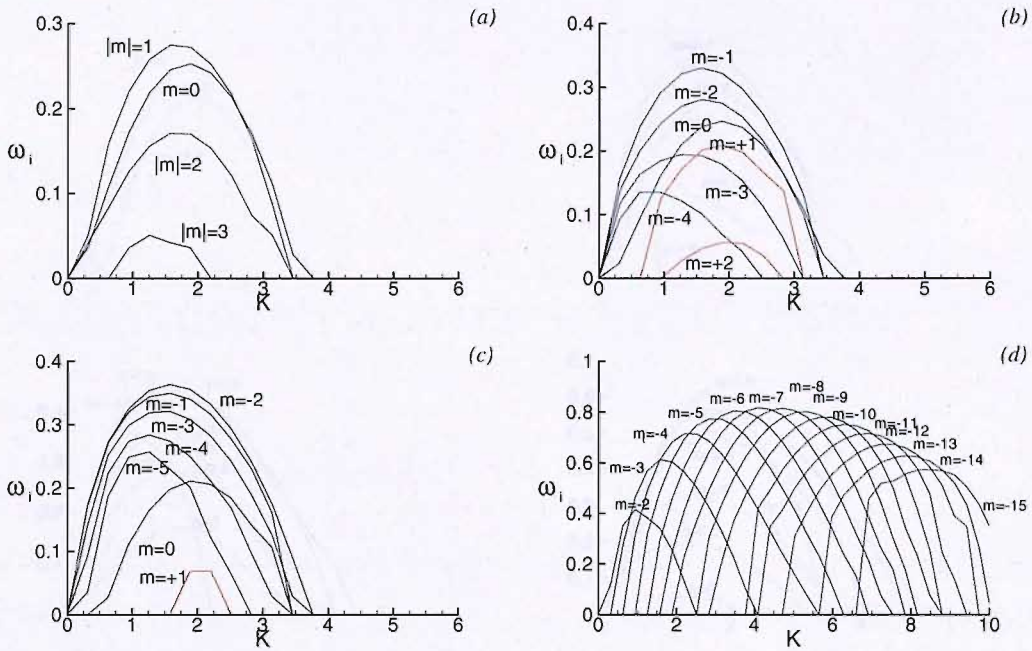


Figure 3.32: Temporal growth rate ω_i retrieved by LTS for the model (3.57) (a): Non-rotating jet $q = 0$ (b): $q = 0.2$ (c): $q = 0.4$ (d): $q = 2$.

The Reynolds and Mach numbers are set equal to $Re=667$, and $M = 0.3$. The range of swirl under investigation is $0 \leq q \leq 2.4$.

As expected, in the absence of rotation, (see fig. 3.32-a) the axisymmetric mode is unstable, together with the azimuthal mode $m = \pm 1$, $m = \pm 2$, $m = \pm 3$ (for the non swirling case positive and helical modes have the same growth rate). The stability analysis of Michalke [77], on the model $V_z(r) = \frac{1}{2} [1 + \tanh((\frac{1}{r} - r)/4\Theta)]$ shows that for $\Theta \geq 0.2$ the most unstable mode is $m = \pm 1$, replaced by $m = 0$ for $\Theta \leq 0.1$. In the range $0.1 \leq \Theta \leq 0.2$ Michalke's results reveal a close competition between $m = 0$ and $m = 1$, consistent with the current study.

The symmetry between positive and negative helical modes is broken when the swirl is introduced; positive modes reduce their growth rate but $m = +1$ remains unstable up to $q = 0.4$. This is in contrast to the Batchelor vortex, where the positive bending mode are subjected to an immediate stabilisation. Conversely, higher negative modes become unstable and, when a high level of swirl is applied, $q = 2$, the curve resembles the ones obtained for the Batchelor vortex, with the two limits of the unstable axial wavenumber range increasing with m .

The effect of the swirl on each single mode is better illustrated in fig. 3.33. Beside

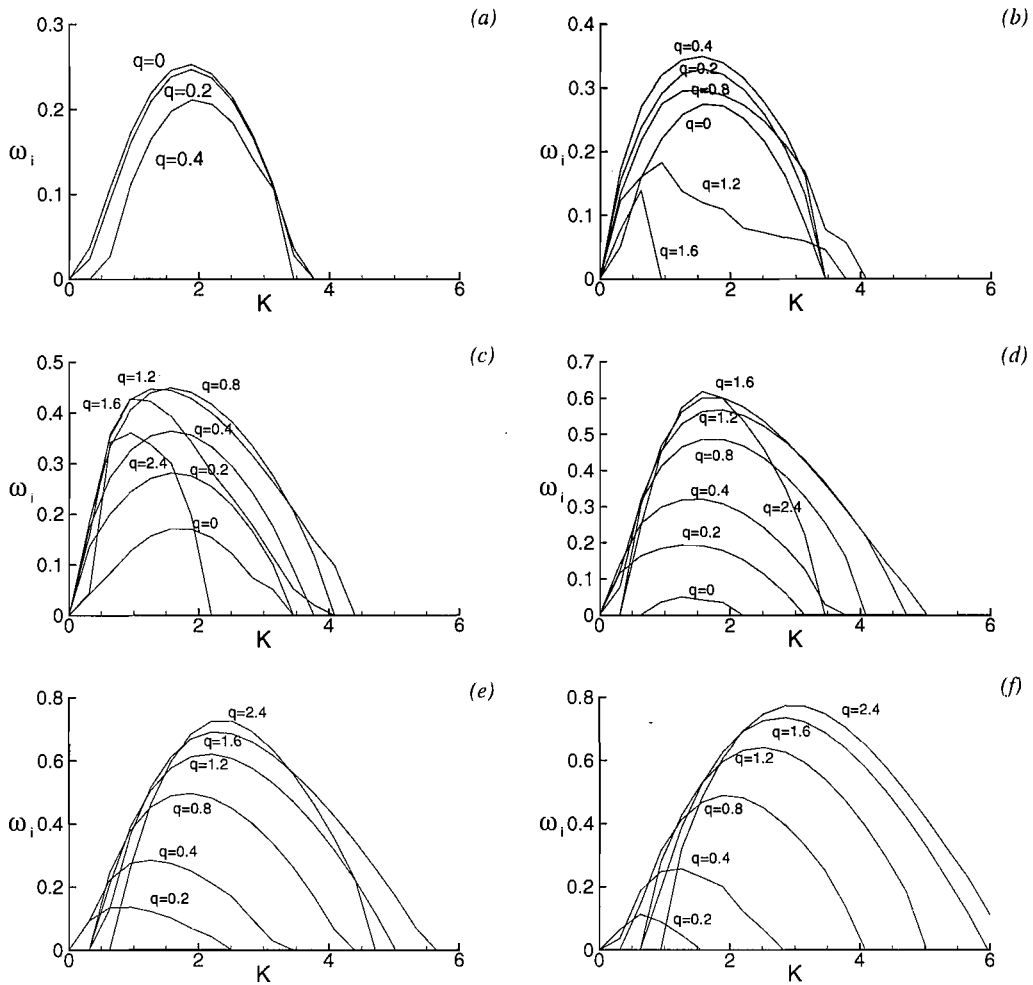


Figure 3.33: Effect of the swirl on the temporal growth rate ω_i of negative azimuthal modes for the model (3.57). (a): Axisymmetric mode $m = 0$ (b): $m = -1$ (c): $m = -2$ (d): $m = -3$ (e): $m = -4$ (f): $m = -5$.

the stabilisation of the axisymmetric mode, the LTS results also confirm that for the lower modes $m \leq 3$, it is possible to identify the existence of two ranges of swirl with opposite behaviour. The transition occurs at a value of swirl which increases with $|m|$. Higher modes do not stabilise, but the reason seems to be the limited extent of the range of swirl under investigation. Following this trend, we should expect a full stabilisation taking place for some value of q far beyond the value $q = 2.4$, in analogy with the Batchelor vortex.

Chapter 4

Axisymmetric vortex breakdown

4.1 Problem formulation

The assumption of parallel flow, which has permitted the study of the general instability mechanisms arising in a swirling flow, is relaxed in the present chapter. The base flow is allowed to develop axial gradients under the effect of viscous diffusion. When the swirl applied is particularly intense, the flow is seen to evolve into vortex breakdown. This evolution is analysed in the present chapter under the hypothesis of axisymmetry, *i.e.* based on a model which is unable to capture helical instabilities. It is important to recall the general theoretical view [26, 57, 59, 60] according to which vortex breakdown is essentially axisymmetric, but many of its manifested features may be eventually modified or even overwhelmed by secondary asymmetries. The axisymmetric assumption must not be considered as a limitation, but as the proper tool for the current investigation.

We discuss the evolution of a swirling flow initially one-dimensional and exhibiting a zero radial velocity everywhere. The axial and azimuthal velocity components are defined piecewise for the regions inside and outside a characteristic radius \tilde{R} , respectively. Hereafter dimensional quantities are indicated by a tilde. Assuming as reference length the core radius \tilde{R} and as reference velocity the free-stream axial velocity $\tilde{V}_{z,\infty}$, the non-dimensional velocity profiles have the following analytical expressions:

$$\begin{aligned} V_\theta &= \begin{cases} Sr(2-r^2) & 0 \leq r \leq 1 \\ S/r & r \geq 1 \end{cases} \\ V_r &= 0 \\ V_z &= \begin{cases} \alpha + (1-\alpha)r^2(6-8r+3r^2) & 0 \leq r \leq 1 \\ 1 & r \geq 1, \end{cases} \end{aligned} \quad (4.1)$$

where the swirl number S and the coflow parameter α are defined as:

$$S = \frac{\tilde{V}_\theta(\tilde{r} = \tilde{R})}{\tilde{V}_{z,\infty}},$$

$$\alpha = \frac{\tilde{V}_z(\tilde{r} = 0)}{\tilde{V}_{z,\infty}}.$$

The swirl number, which is different from the q parameter of the Batchelor vortex, represents the ratio between the azimuthal velocity at the edge of the vortex core and the axial free-stream velocity. The coflow parameter is the ratio between the axial velocity at the axis and the axial free stream velocity. Properties of these profiles are shown in figure 4.1: basically the first of (4.1) describes a vortex core embedded into an irrotational flow with the swirl number S representing a measure of the vortex strength. Setting α greater or less than one in the third of (4.1), one obtains a jet-like or a wake-like behaviour for the axial velocity support. Same velocity profiles have been first investigated by Grabowski and Berger [35] and more recently by Ruith *et al.* [88] for incompressible flows. As discussed in the introduction, our choice was motivated by the interest in a further investigation into some of the results obtained by Ruith *et al.* [88].

For our compressible code, we need to specify two thermodynamic initial conditions. We assume density constant in all the domain and pressure is fixed to satisfy the radial momentum equation. The reference density is the constant density $\bar{\rho}$, the reference pressure is twice the free-stream dynamic pressure $\bar{\rho}\tilde{V}_\infty^2$ and the reference temperature is the temperature on the axis. Thus, exploiting the state equation (2.4), the thermodynamic conditions initially assigned are

$$\begin{aligned} \rho &= 1 \\ T(r) &= 1 + \gamma M^2 \int_0^r \frac{V_\theta^2}{s} ds \\ p(r) &= \frac{T(r)}{\gamma M^2}, \end{aligned} \tag{4.2}$$

where M is the Mach number on the axis. In all the cases presented, the Mach number is kept constant in all the simulations and equal to $M = 0.5$. The chosen value represents a good compromise to get a relatively small integration time step remaining well below the transonic regime.

Direct Numerical Simulations of axisymmetric, highly swirling flows are widely available in the literature, but the Reynolds numbers studied are always quite moderate ($Re \leq 5000$). In addition, most of the computational studies refer to swirling flows in inviscid pipes and nozzle, where geometrical constraints and flow divergence strongly affect the development of vortex breakdown [1, 7, 19, 41, 69]. Fewer results analyse the phenomenon in the absence of an externally-imposed pressure gradient, where the breakdown results from

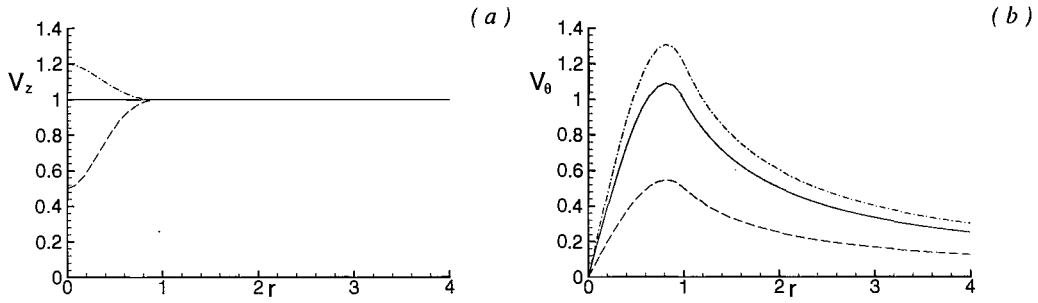


Figure 4.1: Velocity profiles corresponding to (4.1). (a): Axial velocity component for $\alpha = 0.5$ (dash) $\alpha = 1$ (solid) $\alpha = 1.2$ (dash dot). (b): Azimuthal velocity component for $S = 0.5$ (dash) $S = 1$ (solid) $S = 1.2$ (dash dot)

the diffusion and convection of vorticity away from the vortex core. In our study, we mainly focus on open jets and wakes, as we believe it's a better way to detect the fundamental mechanism, and in particular to show properly wave characteristics which otherways would be less recognisable [59].

Following reference [88], the computational domain has been chosen with streamwise and radial extent $L_z = 20$ and $L_r = 10$, respectively. To reflect the physical situation of a jet in an open domain, density and velocity are kept constant at the inflow boundary according to (4.1) and the first of (4.2); non-reflective conditions are applied at the open sides and a symmetric boundary is imposed on the axis. In agreement with what was reported by Lopez [69], we have found that the level of resolution required drastically increases when, for a fixed Reynolds number, the flow evolves into breakdown. The region of reversed flow manifests large gradients in both axial and streamwise directions, which may not be fully resolved, as often evidenced by the presence of “wiggles” in the flow field. Table 4.1 reports the number of grid points adopted for different Reynolds number cases.

The adopted resolution is higher than that employed in previous studies, and it has been found more than sufficient to guarantee a good grid convergence.

Re	n_z	n_r	b_r
200-400	256	95	0.8
800-1600	320	170	0.8

Table 4.1: Grid resolution used for spatial axisymmetric DNS at different Reynolds numbers.

4.2 Physical observations

In this section we present results related to $M = 0.5$, $\text{Re}=200$, $S = 0.95$ and $\alpha = 1$. This case will be later used as a reference for successive parametric studies. The axisymmetric columnar initial conditions described by (4.1)-(4.2) are a solution of the steady Euler equations. The initial evolution of the flow is therefore triggered by viscous diffusion, which reduces the axial vorticity producing a negative axial gradient of azimuthal velocity close to the inflow, where all the velocity components are kept constant (see fig. 4.2-*a*). This is the mechanism breaking the one-dimensionality. In these preliminary stages the axial gradients are much less than the radial, thus the interaction between pressure and swirl can still be examined considering the balance of the centrifugal acceleration and the restraining pressure force [39]:

$$\frac{\partial p}{\partial r} = \frac{\rho V_\theta^2}{r}. \quad (4.3)$$

The pressure is constant in the far-field, hence, differentiating along z , integrating from $r = 0$ to $r = L_r$, and neglecting the compressibility effects, we find:

$$\left(\frac{\partial p}{\partial z}\right)_{r=0} = -\rho \int_{r=0}^{r=L_r} \frac{1}{r} \frac{\partial V_\theta^2}{\partial z} dr = -\rho \int_{r=0}^{r=L_r} \frac{\partial}{\partial z} \left(\frac{L^2}{r^3}\right) dr. \quad (4.4)$$

An adverse pressure gradient must therefore be established on the axis near the inflow (fig. 4.2-*b*) due to negative gradient of circulation $L = rV_\theta$. As a consequence, the axial velocity has to decay, and this is clearly shown in fig. 4.2-*c*. Note that the term $\frac{\partial}{\partial z} \frac{L^2}{r^3}$ in (4.4) represents the production of azimuthal vorticity by vortex tilting (cfr. equation (3.40) of previous chapter).

Figure 4.3 shows the temporal evolution of the azimuthal vorticity ξ_θ . Since $\alpha = 1$, the initial columnar vortex doesn't exhibit azimuthal vorticity. At Time=2 localised negative vorticity appears near the inflow and grows in magnitude as the calculation goes on. This negative vorticity has to be associated with the established gradient of circulation and accounts for the same gyroscopic effect discussed when we have studied the response of the perturbed Rankine vortex (cfr. §3.2.3). In that case, the subsequent decay of axial velocity was found to offset the initial circulation gradient by mean of vortex stretching and the resulting balance gave rise to a periodic oscillation in the center of the tube. Here this mechanism cannot take place because the inlet conditions preserve the initial circulation and the

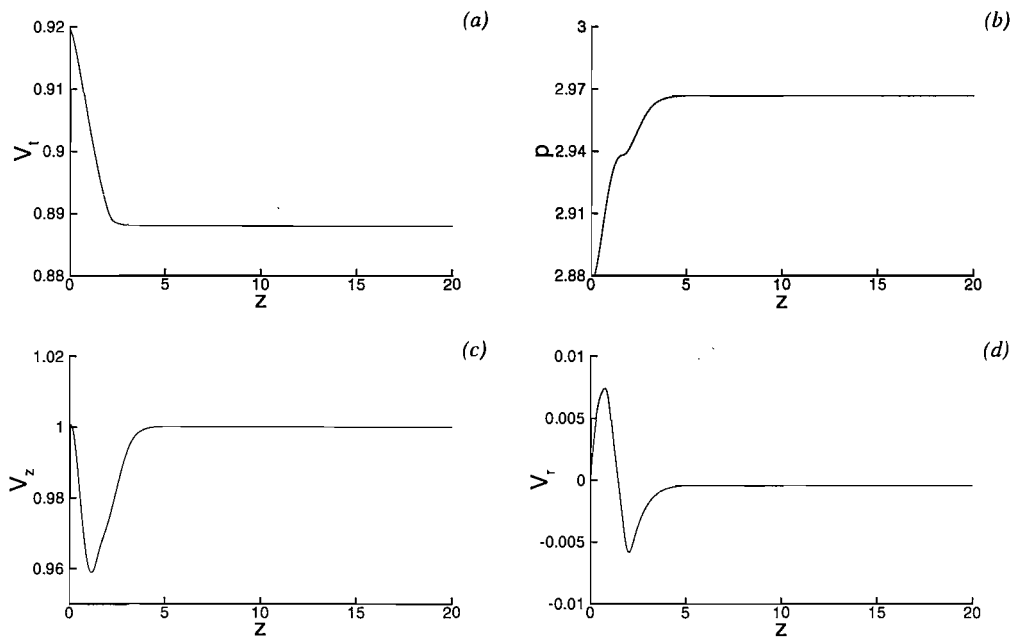


Figure 4.2: Early evolution of the $Re=200$ $S = 0.95$ case. Streamwise evolution at Time=2 of (a): azimuthal velocity near the axis, (b): pressure on the axis, (c): axial velocity on the axis, (d): radial velocity near the axis.

wave motion is inhibited. Conversely, the production of negative azimuthal vorticity causes the core to expand locally. To satisfy mass conservation, a significant amount of radial flow has to develop (fig. 4.2-d). Following the “positive feedback” discussed in Brown and Lopez [12], the local expansion reinforces the whole process, because fluid with less circulation is carried to larger r , producing a larger negative gradient of V_θ . In the vorticity equation, this process is modelled by the stretching term $\frac{V_r \xi_\theta}{r}$.

In addition, the viscous diffusion becomes effective for a larger axial extent, producing an extended distribution of negative vorticity ξ_θ throughout the domain (see fig. 4.3). When sufficient ξ_θ has been produced, the upstream velocity induced becomes so strong that a stagnation point appears on the axis. The flow separates and a region with recirculating fluid is formed. Figure 4.4 shows the instantaneous streamlines computed at different times: at Time=20, the small amount of negative vorticity produces a negligible expansion of the core, so that the stream surfaces appear essentially cylindrical. At Time=60 the flow is nearly stagnating and a pronounced bulge is visible between $z = 2$ and $z = 5$. In order to establish a precise criterion, the breakdown is identified by the existence of a stagnation point, and under this condition the flow is said to be globally subcritical, where the term “globally” is used to indicate the difference from Benjamin’s critical state which represents

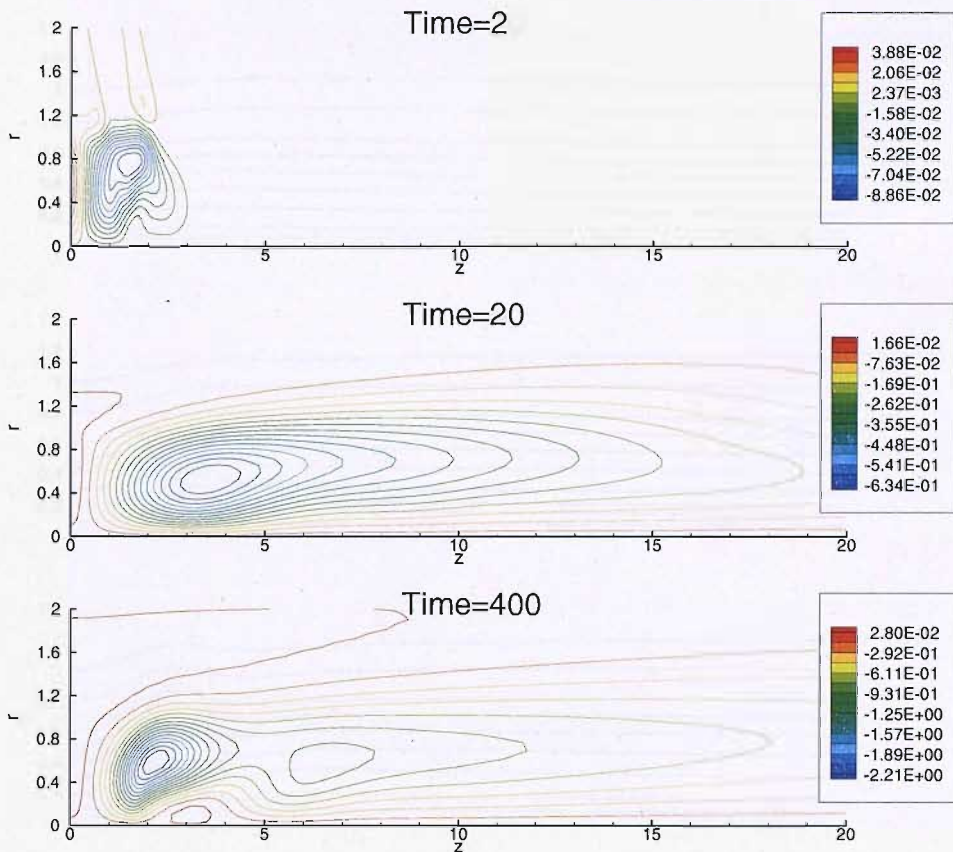


Figure 4.3: $Re=200$ $S = 0.95$ case. Time evolution of azimuthal vorticity. Time=400 corresponds to the final steady solution.

a local concept (§3.2.4). Once the breakdown has occurred, the recirculating region grows in size and undergoes a small upstream excursion. The flow slowly evolves toward a steady solution, with the vortex bubble anchoring its position at some distance from the inlet.

It is now of interest to analyse in more detail the flow field corresponding to the final steady solution reached. Figure 4.5 reports the streamwise evolution of the velocity components and pressure. The circumferential velocity is very low within the vortex bubble. This low level of circulation is a consequence of the large radial outflow. The local reduction of swirl is associated with a local peak of pressure on the axis. It can be noted, however, that the adverse pressure gradient in the recirculating region is very small. Therefore, due to their inertia, particles which move over the bubble are subjected to an inward motion (see the negative radial velocity between $z = 3$ and $z = 5$). In order to preserve angular momentum, this inward motion must be associated with a local increase of azimuthal velocity, and, to satisfy continuity, with an axial acceleration. The whole process tends to restore in the wake

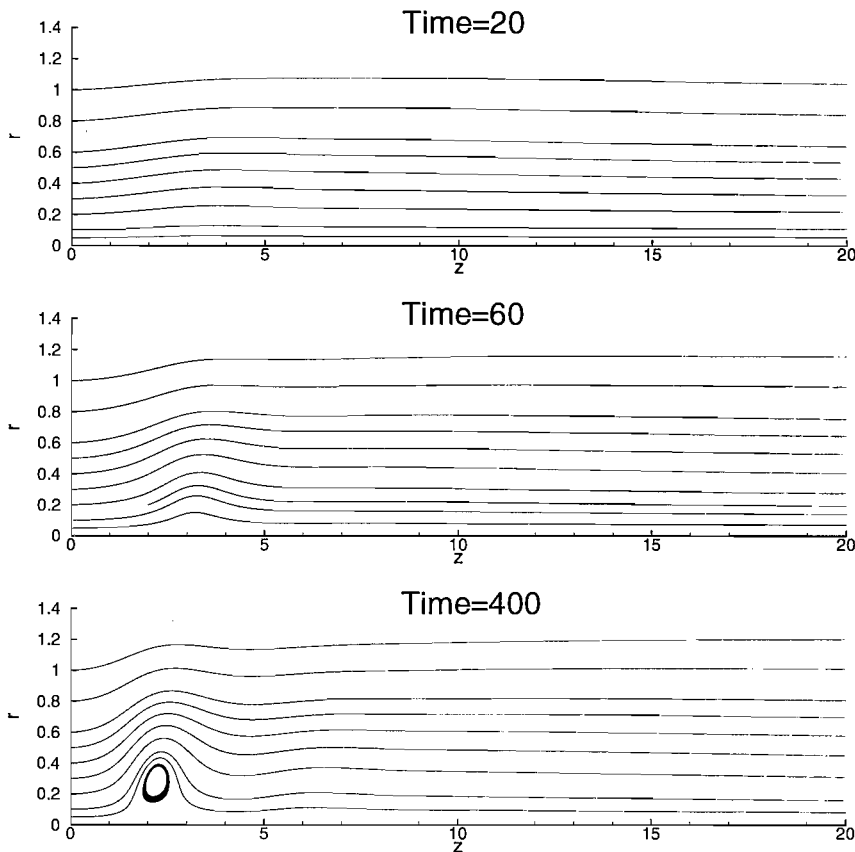


Figure 4.4: $Re=200$ $S = 0.95$ case. Time evolution of instantaneous streamlines. Time=400 corresponds to the final steady solution.

of the bubble conditions similar to those ahead of the bubble. Indeed, starting from $z \simeq 5$, viscous diffusion of axial vorticity again becomes important; an adverse pressure gradient is established, enhancing axial decay with subsequent outward motion. This should account for the concentrated positive vorticity located under the vortex bubble and revealed in the third of fig. 4.3. In some sense, the phenomenon tends to repeat itself on a smaller scale. The key-point is that, although viscous diffusion represents the driving force responsible for the pressure gradient, the basic mechanism is inviscid and related to pure inertial effects. It is then expected that increasing the Reynolds number or the swirl number would lead to possible wave trains, with the existence of more than one region of recirculating flow. In all these observations, it is remarkable that basic concepts of vorticity can be used to get a qualitatively phenomenological description, in accordance with what previously done for the linear Kelvin waves.

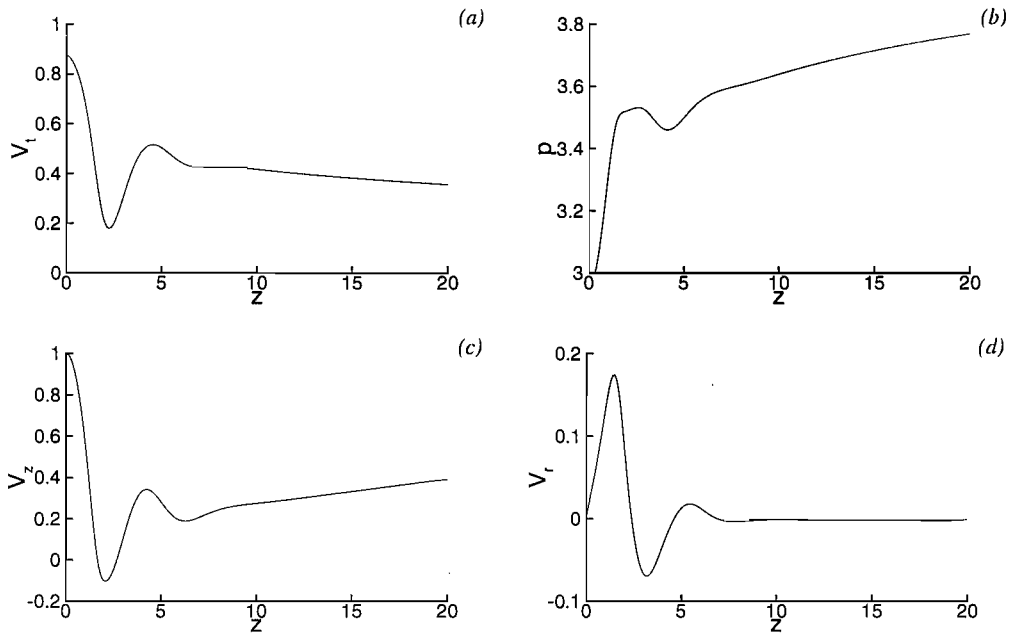


Figure 4.5: $Re=200$ $S = 0.95$ case. Steady solution: streamwise evolution of (a): azimuthal velocity at $r = 0.5$, (b): pressure on the axis, (c): axial velocity on the axis, (d): radial velocity at $r = 0.5$.

4.3 Effect of the swirl

A first parametric study was conducted in order to elucidate the effect of the swirl. A series of calculations was performed increasing the swirl number in the initial solution (4.1)-(4.2) up to $S = 1.9$. The other parameters were held constant and equal to those prescribed in previous section for the case $S = 0.95$. We remark that the initial flow field assumed for any calculation is described by (4.1). The response to a sequential increase of the swirl ratio will be discussed in section 4.5.

All the computations have reached a final steady solution; convergence was checked monitoring the rms, a global measure for the right hand side of the continuity equation, defined as

$$\text{rms} = \sqrt{\frac{1}{N} \sum \left(\frac{\partial \rho}{\partial t} \right)^2} \quad (4.5)$$

where the summation is extended to all the grid points N . The rms is the Holder mean value of the L_2 norm. Although it does not strictly represent a norm, it is generally preferred since it is monotonically decreasing with the number of points. In addition, the minimum axial velocity reached in the flow field was also considered to measure the unsteadiness of the flow. Figure 4.6 reports the convergence histories of rms and $(V_z)_{min}$ for some of the cases

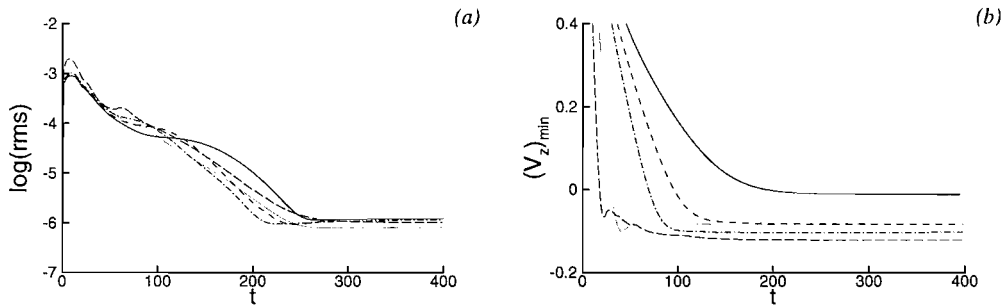


Figure 4.6: Convergence histories at $S = 0.89$ (solid), $S = 0.92$ (dash), $S = 0.95$ (dash-dots), $S = 1.1$ (dots) and $S = 1.3$ (long dash). (a): Time history of rms, (b): Time history of the minimum axial velocity in the flow field.

studied.

The flow field of the corresponding final steady solutions are reported in figure 4.7. The critical value for the flow to stagnate has been found $S = 0.88$. Under this condition, however, negative axial velocity is reached only on the centerline, and no counterflow is found (not shown). The recirculating region appears visible at $S = 0.89$ when the breakdown is manifested in its weakest form.

As the swirl increases to $S = 0.92$, the recirculating region is enlarged and moves upstream. The process is continued by further increasing to $S = 0.95$ first and then to $S = 1.1$: vortex breakdown becomes more intense (note also the minimum axial velocity which slightly decreases in fig. 4.6) and its upstream location moves closer to the inflow; unable to move further upstream, the vortex bubble starts to shift radially, a behaviour which becomes even more evident at $S = 1.3$. In the latter case, it can also be noted how the flow blows in the negative axial direction below the bubble. According to Spall *et al.* [94], the inlet boundary conditions force the vortex breakdown which in physical situations would continue to propagate upstream, emphasising the fact that the inflow conditions may be already highly subcritical at this level of swirl. We agree on this point, but it's worth mentioning that the experiments reported by Sarpkaya [93] show a similar behaviour, with the fluid that does not enter in the front of the bubble but moves over it before entering from the back. The inflow boundary does not permit upstream wave propagation, but as also pointed out in [88], the need for prescribing inflow conditions is not a prerogative of numerical simulations only.

Convergence histories reported in figure 4.6 reveal the different time scales on which the phenomenon takes place when varying the swirl. In all the cases studied, a satisfactory

steadiness is reached after 200 non-dimensional time units (fig. 4.6 -a), a result consistent with a simple non-dimensional analysis based on characteristic quantities: the time necessary for the viscous effects to be active on a length scale δ is $t_d = O(\frac{\delta^2}{\nu})$, whereas a characteristic time scale for convection is $t_c = O(\frac{\delta}{V})$; the ratio between these two quantities gives $\frac{t_d}{t_c} = O(\frac{\delta V}{\nu} = Re_\delta)$. As pointed out by Leibovich [60], the characteristic viscous length appropriate to any swirling flow is the vortex radius (note indeed that the inlet conditions defined by (4.1) are close to describing an axial vorticity distribution with a plug profile) so that $t_c = O(1)$. It turns out that in order to let viscous diffusion develop fully, it has to be $t_d = O(Re_\delta)$.

On the other side, the breakdown process occurs on a time scale which depends on the swirl (fig. 4.6-b). Increasing the swirl produces a much more rapid burst of the vortex core. At $S = 1.1$ and $S = 1.3$ the flow stagnates before Time=50, and the minimum axial velocity quickly settles on a constant value. The remaining unsteadiness is therefore associated with the diffusion of the vortex tube, and not with the vortex breakdown phenomenon. Conversely, for the critical case $S = 0.89$, breakdown and diffusion occur on the same temporal scale, a result which highlights how, even working with the simpler axisymmetric model, detection of the critical level becomes quite demanding at high Reynolds numbers unless other factors are introduced to support viscous diffusion in its role. This can be achieved for example by imposing a free-stream adverse pressure gradient. In that case the total axial pressure gradient would be the sum of a vortex tilting contribution and the free-stream contribution; equation (4.4) has to be replaced by:

$$\left(\frac{\partial p}{\partial z}\right)_{r=0} = + \left(\frac{\partial p}{\partial z}\right)_{r=\infty} - \rho \int_{r=0}^{r=Lr} \frac{\partial}{\partial z} \left(\frac{L^2}{r^3}\right) dr . \quad (4.6)$$

In the absence of any additional driving force, if the inlet conditions are already *locally* subcritical in the sense of Benjamin, an arbitrarily small flow divergence induces localised negative azimuthal vorticity stagnating the flow. If the inlet conditions are *locally* supercritical, it's necessary to wait for the viscous diffusion to render the flow field locally critical somewhere, in order to get a *global* subcriticality. Considerations developed in the previous section regarding the inertial effects of the fluid assume particular relevance here. Together with a more intense breakdown, higher swirling cases present a second expansion of the stream surfaces. At $S = 1.3$, this leads to breakdown the flow again, generating another recirculating region, which however appears to be morphologically very different. In ad-

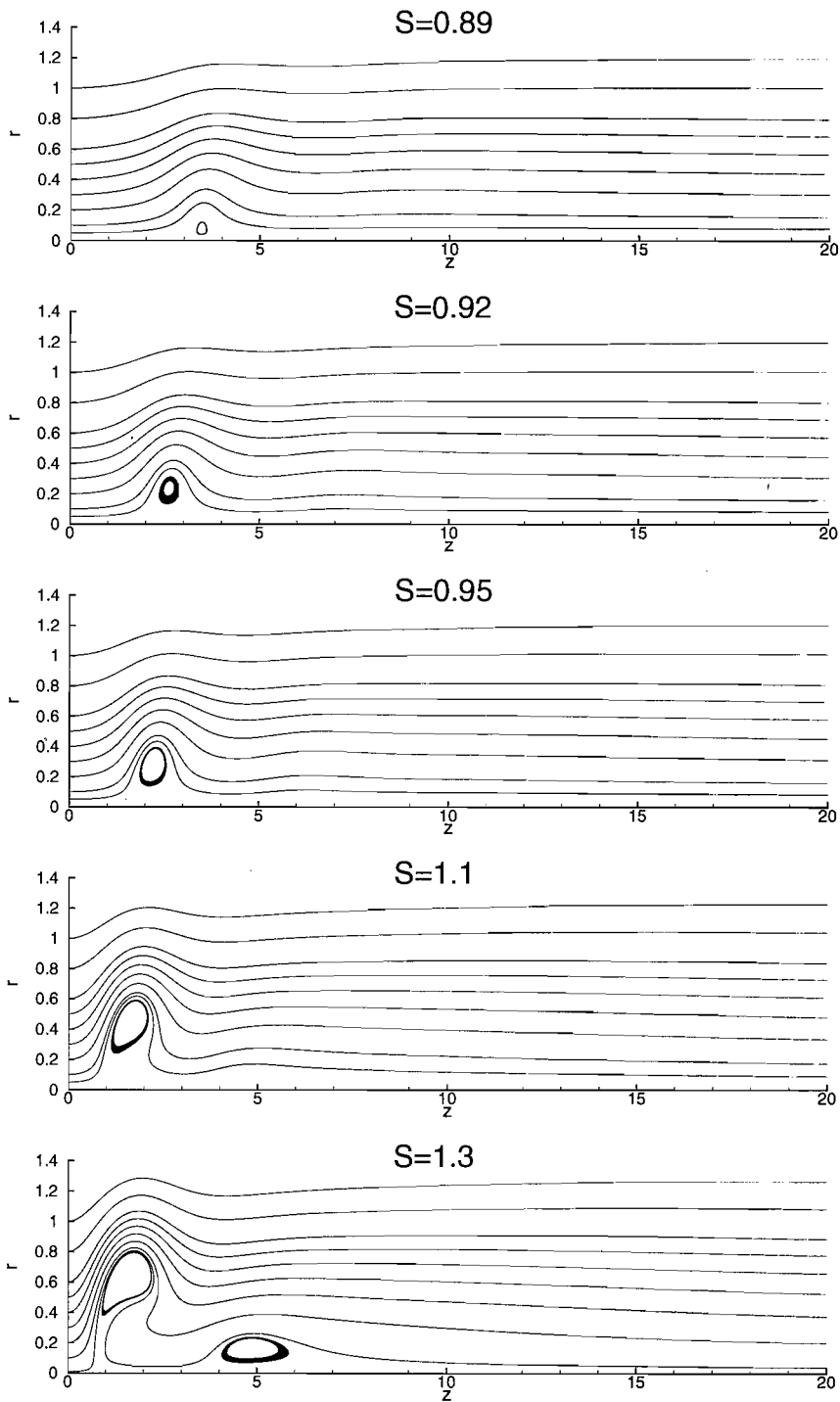


Figure 4.7: Steady solutions obtained at different swirl numbers. $Re=200$, $M = 0.5$, $\alpha = 1$.

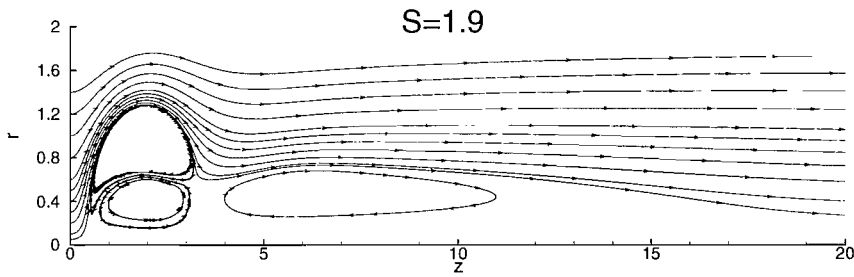


Figure 4.8: Steady solution obtained at $S = 1.9$ presenting multiple breakdown (two corotating vortices) with a double-celled structure (two counter-rotating vortices) of the first breakdown.

dition to the multiple breakdown configuration, *i.e.* the formation of corotating vortices, larger swirl may be characterised by vortex breakdown with a double cell structure. Figure 4.8 shows the steady state corresponding to $S = 1.9$: a counter-rotating vortex is formed below the first bubble at $z \simeq 2$. Double-celled structures have also been found numerically in references [88, 95], and in the experiment of Faler and Leibovich [27]. Ruith *et al.* [88] advance the hypothesis that it might be a manifestation of centrifugal instability, but they do not provide strong evidence for this. Application of the Rayleigh criterion based on the radial circulation distribution shows that instability should occur also at lower swirl levels. It is possible that it is merely a shear effect, also enhanced by the presence of the second vortex bubble, the one with bigger axial extent in fig. 4.8.

4.4 Effect of Reynolds number

Results of the present section need to be supplemented by those of §4.5, when the description of the bifurcation diagram will provide a more complete understanding about the dependence on the Reynolds number. Figure 4.9 shows steady solutions obtained at $S = 0.95, M = 0.5, \alpha = 1$ varying the Reynolds number. The results confirm the tendency of the swirling flow to burst in a series of bubbles sequentially smaller in size. The appearance of these bubbles corresponds to successive solutions bifurcating as the control parameter Re is increased. At $Re=50$, the final steady solution doesn't show any stagnation point; solution at $Re=200$, has been previously discussed and shows a well defined region of recirculating flow followed by a very light swelling in the lee. The swelling becomes a further breakdown at $Re=400$ while the first vortex bubble remains anchored at the same axial position $z \simeq 2$, but its morphology undergoes a light clockwise rotation together with a radial shift. The same characteristic with the flow starting to enter the bubble from the back, has been

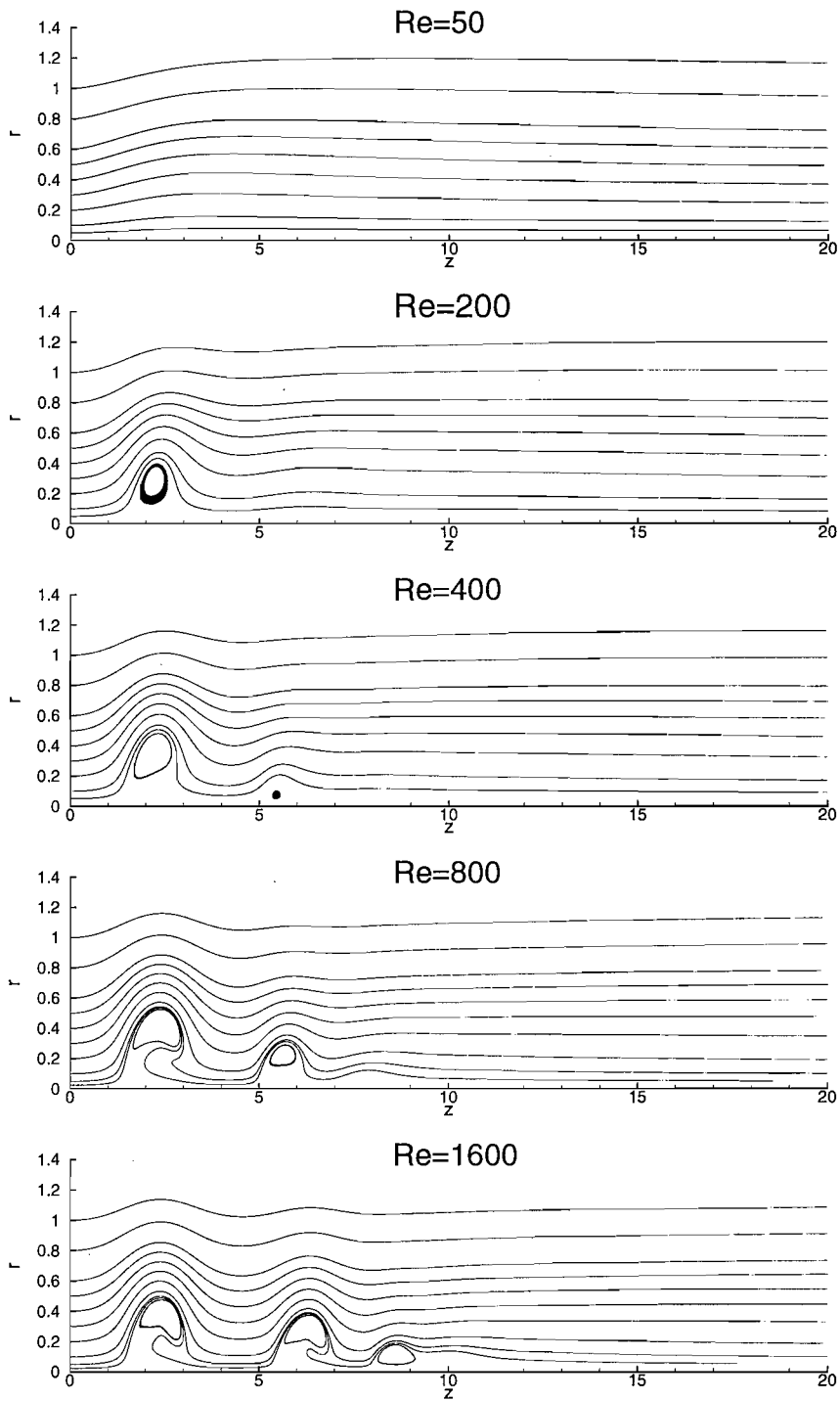


Figure 4.9: Steady solutions obtained at different Reynolds numbers. $S = 0.95$, $M = 0.5$, $\alpha = 1$.

previously when describing the effect of the swirl, but in that case it was enforced by the upstream motion of the bulge entering in competition with the inlet boundary conditions. Such a mechanism is absent here, and seems to be associated to the pressure gradient imposed by the second breakdown growing in the wake. Indeed it seems to repeat for the second bubble, as soon as a third bulge, already visible at $Re=800$, gives rise to a third recirculating region at $Re=1600$.

The non-dimensional time for each simulation was fixed $Time=Re$; the convergence was satisfactory for $Re < 800$ while in the higher Reynolds number cases the rms could be reduced by only two order of magnitude. Chen [15] reports temporal periodicity in his axisymmetric incompressible calculations at $Re=1000$. Up to $Re=800$ the convergence difficulties are deemed inherent to the use of DNS at these Reynolds numbers. However, some unsteadiness has been found at $Re=1600$, with the second and third recirculating regions unable to anchor completely their position, and experiencing small axial excursions.

Indications given by the present results are that in the inviscid limit, a possible solution of the axisymmetric Navier-Stokes equations consists in a wave train superimposed on the base flow. Experimental evidence of the existence of wave trains is quite problematic: we will see in the next chapter that as soon as the Reynolds number is increased, three-dimensional instabilities in the wake of the bubble start to develop on a time scale which is comparable, if not shorter, than that of breakdown. They can strongly modify the axisymmetric structure, so that, using the words of Sarpkaya [93], ‘only the rudiments of the wave train can be observed’. It is also of interest that these waves are sequentially smaller in size, and this recalls the dispersion mechanism which we have analysed for the linear Kelvin waves (cfr. §3.2.2). In that case we found that the fastest modes are those with less radial structure and a lower group velocity competes to higher wave-number k . An extension of this property to large amplitude waves, would provide a scenario where a bigger wave packet can propagate faster followed by slower, smaller packets. The major difficulty of this wave theory, originally proposed by Leibovich [59, 60], is the fact that the multiple breakdown does not develop as a single unified event, but is manifested as sequence of events associated with the evolution of the base flow. In other words, as will be shown in next section, each vortex breakdown appears to be created as a consequence of the structural change generated by the precursor breakdown state.

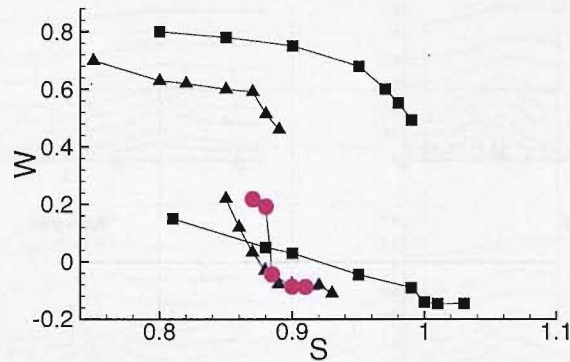


Figure 4.10: Computed bifurcation diagram at $Re=1000$ (squares), $Re=400$ (triangles) and $Re=200$ (circles).

4.5 Bifurcation diagram

Results presented so far have been obtained considering the evolution of a swirling flow which is initially columnar ($\frac{\partial}{\partial z} = 0$). During the study, we were mainly focused on analysing the conditions corresponding to the different steady solutions obtained by our computations. In the present section, we discuss the dynamical evolution of the flow subsequent to a *sequential* variation of the swirl ratio. Following Herrada *et al.* [41], this will serve to determine numerically the bifurcation diagram discussed in the introduction, and to find out whether or not possible hysteresis loops exist. In what follows we will make reference to fig. 1.2 of chapter 1: by S_1 we denote the level of swirl necessary to get breakdown (*i.e.* when the minimum axial velocity is negative); the critical point S_2 will denote the value of swirl when the flow “recovers” columnar conditions starting from a breakdown state. We discuss results relative to $Re=200$, $Re=400$ and $Re=1000$, as we consider these cases representative of the three different conditions in which breakdown may evolve. For each case treated, branch (I) of the bifurcation diagram is obtained by increasing the swirl number until a stagnation point appears. Branch (II) is then derived assuming the steady state reached at the critical level $S = S_1$ as initial condition for a new run with a slightly smaller value of S . The process is then iterated until the quasi columnar configuration is established again.

The computed bifurcation diagram is presented in figure 4.10. At $Re=200$, as the swirl is increased, the flow field presents a very gradual change with a localised perturbation which develops in the core. The stagnation point is reached at $S = 0.89$, and the corresponding flow field was found to match perfectly the one reported in the top of fig. 4.7. The situation is very different at $Re=400$, where the critical level S_1 assumes the meaning of threshold

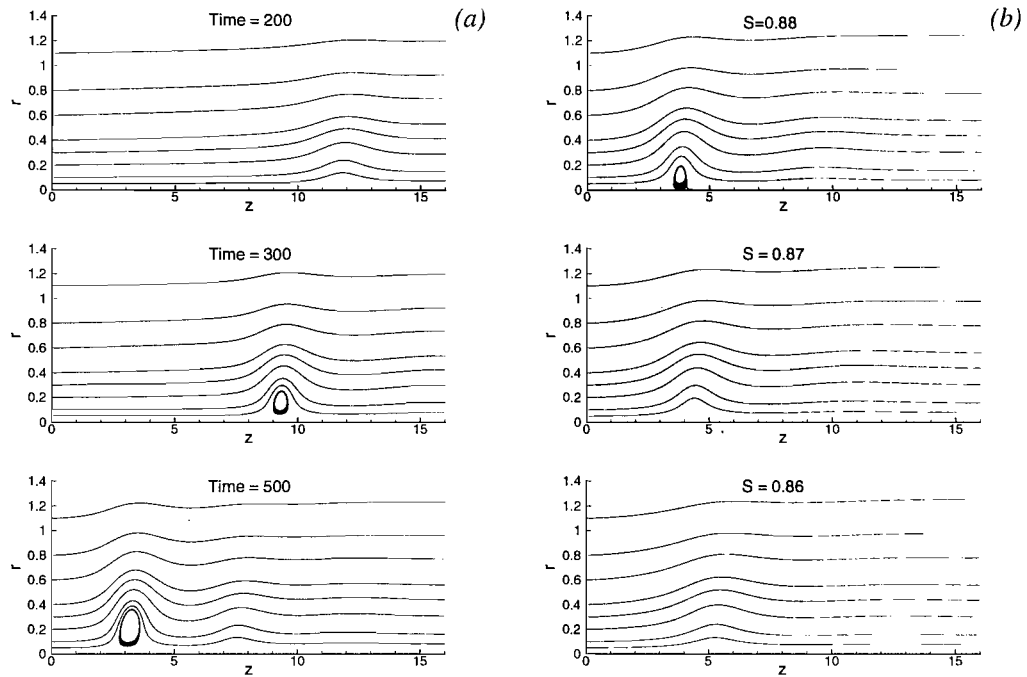


Figure 4.11: $Re=400$ case. (a): Evolution of instantaneous streamlines at $S = 0.9$. (b): Streamlines for steady solutions found on branch (II).

value between two completely different flows: for $S < S_1$ the flow is quasi-cylindrical with negligible axial gradients, while, for $S \geq S_1$ a drastic and sudden change in structure takes place. This is clearly highlighted in fig. 4.11-a, reporting the flow evolution when the value $S_1 = 0.9$ is reached: at Time=200 (here Time=0 is when the change of swirl from $S = 0.89$ to $S = 0.9$ has been applied at the inflow) a perturbation arises close to the outflow boundary, then it moves upstream growing in amplitude and leading to a region of separated flow at approximately Time=300. A final steady state is reached at Time=500 with the bubble located near the inflow and a swelling visible in the wake. A similar process develops at $Re=1000$ (fig. 4.12-a). Here, as the first wave moves upstream, another wave leads to a second breakdown: the final quasi-steady configuration presents the wave train.

In light of this behaviour, and also considering the results of section 4.4, we can deduce important conclusions. First, at high Reynolds numbers the breakdown always manifests itself as a wave train, independently of the fact that the swirl adopted is far from the critical level.

The critical point at $Re=1000$ is $S_1 = 1$ vs a value $S_1 = 0.9$ found at $Re=400$. On the other hand, the definition of the breakdown state employed here leads to the observation that $Re=400$ and $Re=200$ have approximately the same critical value. This evidence, which may

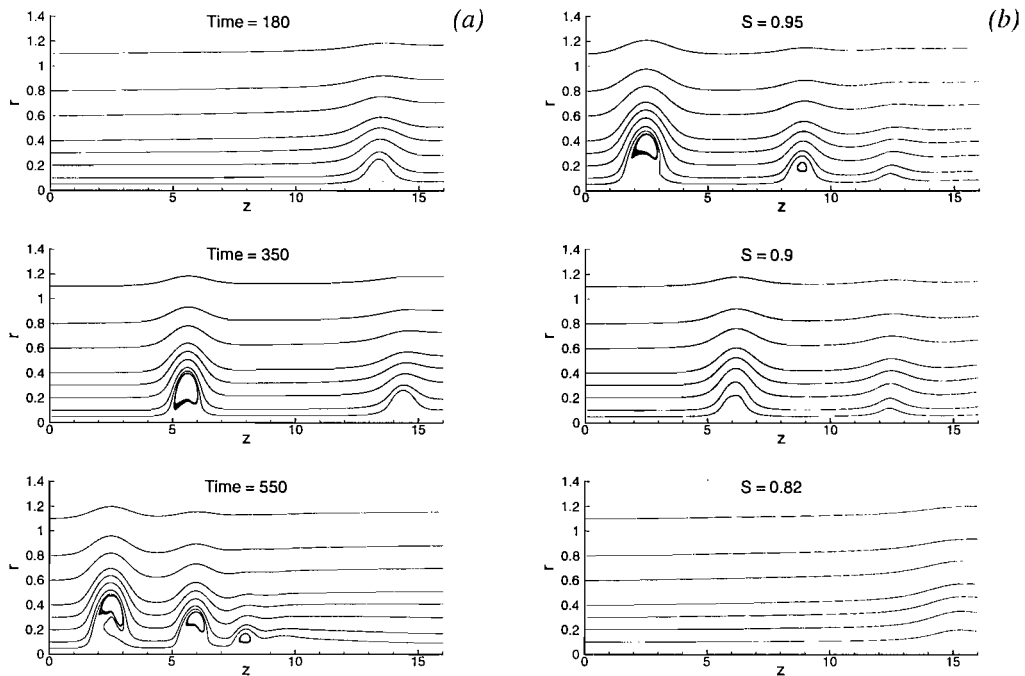


Figure 4.12: $Re=1000$ case. (a): Evolution of instantaneous streamlines at $S = 1$. (b): Streamlines for steady solutions found on branch (II).

appear as an inconsistency, is actually the consequence of a subtle role played by viscosity: if viscosity has to drive toward criticality, the expected trend should be that manifested at higher Reynolds, and the fact that the wave initially develops far downstream is a further confirmation of this. The key-issue is that at $Re=200$, S_1 does *not* represent a real threshold, but it's a just a definition. Localised disturbances are already present at $S < S_1$, as can be understood from the simple observation that the corresponding branch in fig. 4.10 goes to zero gradually. In practice, these results suggest that a perturbation which at high Reynolds number would grow and breakdown the flow, at low Reynolds number remains “trapped” by viscosity.

Now we investigate the flow behaviour when the swirl is sequentially decreased below the critical value. For the $Re=400$ case, (see fig. 4.11-*b*), the bubble becomes smaller and moves slightly upstream at $S = 0.88$. The region of reversed flow disappears at $S = 0.87$, however, a well pronounced swelling of the streamlines is still present, indicating that, although there's no breakdown, a wave of finite amplitude is still localised. The wave undergoes a small shift of its axial position before disappearing. The $Re=1000$ case is more interesting because it clearly shows the wave convected downstream from the main flow. When the second folding point $S = 0.82$ is reached, a light swelling is located exactly at the outlet,

thus the re-establishment of the columnar configuration is associated with the expulsion of the wave from the computational domain. We believe this case to be quite well representative of the inviscid limit analysed theoretically by Wang and Rusak [101]. When the swirl is decreased below the critical value S_1 , the main flow reduces its capability to sustain waves and the vortex bubble is pushed away weakened. In a process where the dissipative effects of viscosity are negligible, one expects the wave resulting from the downstream migration to be located where it was originated when the first point S_1 had been reached. Although not rigorously proved, this idea seems to be supported by the $Re=1000$ case: the instantaneous streamlines at $Time=180$ and $Time=350$ present an interesting resemblance with the steady streamlines at $S = 0.82$ and $S = 0.9$, respectively. The unsteady solutions are solitons growing in the main flow and moving upstream while the steady solutions represent waves of approximately the same amplitude standing at approximately the same position because of the reduced level of swirl. Viscosity renders the process irreversible: for intermediate Reynolds numbers ($Re=400$ case) the bubble can reach the inlet at $S = S_1$ but not the outlet at $S = S_2$ while at low Reynolds numbers ($Re=200$ case) the viscous diffusion is so high that the wave is trapped where it develops.

These differences are perfectly reflected in the way the bifurcation diagram is modified: the existence of multiple steady solutions presented by the bifurcation diagram in the range $S_2 < S < S_1$ is associated with the existence of developing solitons, and disappears when such dynamics are absent (low Reynolds). Different solutions on branch (II) represent a standing wave positioned at different axial positions. The meaning of S_1 is associated with the critical level first introduced by Benjamin [6] while numerical simulations identify S_2 as a critical point for finite amplitude waves.

4.6 Effect of the coflow

A further parametric study was conducted to analyse the effect of the coflow parameter α . In particular, two experiments were conducted, guided by the consideration that the coflow parameter measures the excess or defect of axial velocity inside the vortex core; hence, a wake-like profile is expected to enhance the capability of the base flow to sustain waves (*i.e.* driving a globally subcritical flow toward criticality), whereas a jet-like profile should activate the inverse tendency.

In the first experiment we considered a combination of parameters known to produce

a large recirculating region, namely $S = 1.1$, $Re=200$, $\alpha = 1$, and started to increase the coflow. Calculations were not performed sequentially, but results of section §4.5 guarantee the independence on the initial conditions at the Reynolds numbers employed here. Results are reported in figure 4.13. It appears evident that as the coflow is increased, the vortex bubble moves downstream and reduces in amplitude. A radial drift can also be observed at $\alpha = 1.4$ and $\alpha = 1.6$, a behaviour which is quite surprising, considering that this effect has been always associated with a strengthening of the vortex bubble. At $\alpha = 1.8$ the bubble is again near the axis, and positioned in the center of the computational domain. Finally, at $\alpha = 2$, the streamlines become slightly diverging but no stagnation point exists.

In the second experiment we carried out the opposite operation. We considered a case for which no breakdown was detected, namely $S = 0.84$, $Re=200$, $\alpha = 1$, $M = 0.5$ and evaluated the final steady solutions obtained reducing α . As expected, (see fig. 4.14), the defect of axial velocity leads to breakdown of the flow. Note however, that the size of the bubble remains very small, a result qualitatively consistent with the consideration that a non-uniform distribution of axial velocity renders the concept of criticality local *also* in the radial direction [59, 60]. Reducing α , the centerline axial velocity is decreased, but for the family of profiles used here the axial flow rapidly approaches the free-stream value within the vortex core. The base flow may be therefore susceptible to breakdown on a reduced radial scale.

4.7 Testing a simple criterion

There have been several attempts in the past to establish simple criteria for the onset of breakdown. In many cases, they aimed to determine critical values of the swirl ratio or even the helix angle of velocity (see the criteria of Spall *et al.* [94] based on the local Rossby number or the even simpler Mahesh's condition based on a 1D momentum equation [72]). Vortex breakdown appears to be a too complicated phenomenon and dependent on too many parameters to have a general criterion. In particular, the experimental and numerical profiles useful for any comparison are available only upstream and downstream of the breakdown. Ideally, one should require profiles that would have been at the breakdown region, had the breakdown not occurred, which is clearly something impossible to obtain. In addition, Lopez [69] remarks that the existence of multiple solutions in a specified range of swirl number renders the whole question meaningless, since the state of the vortex flow depends

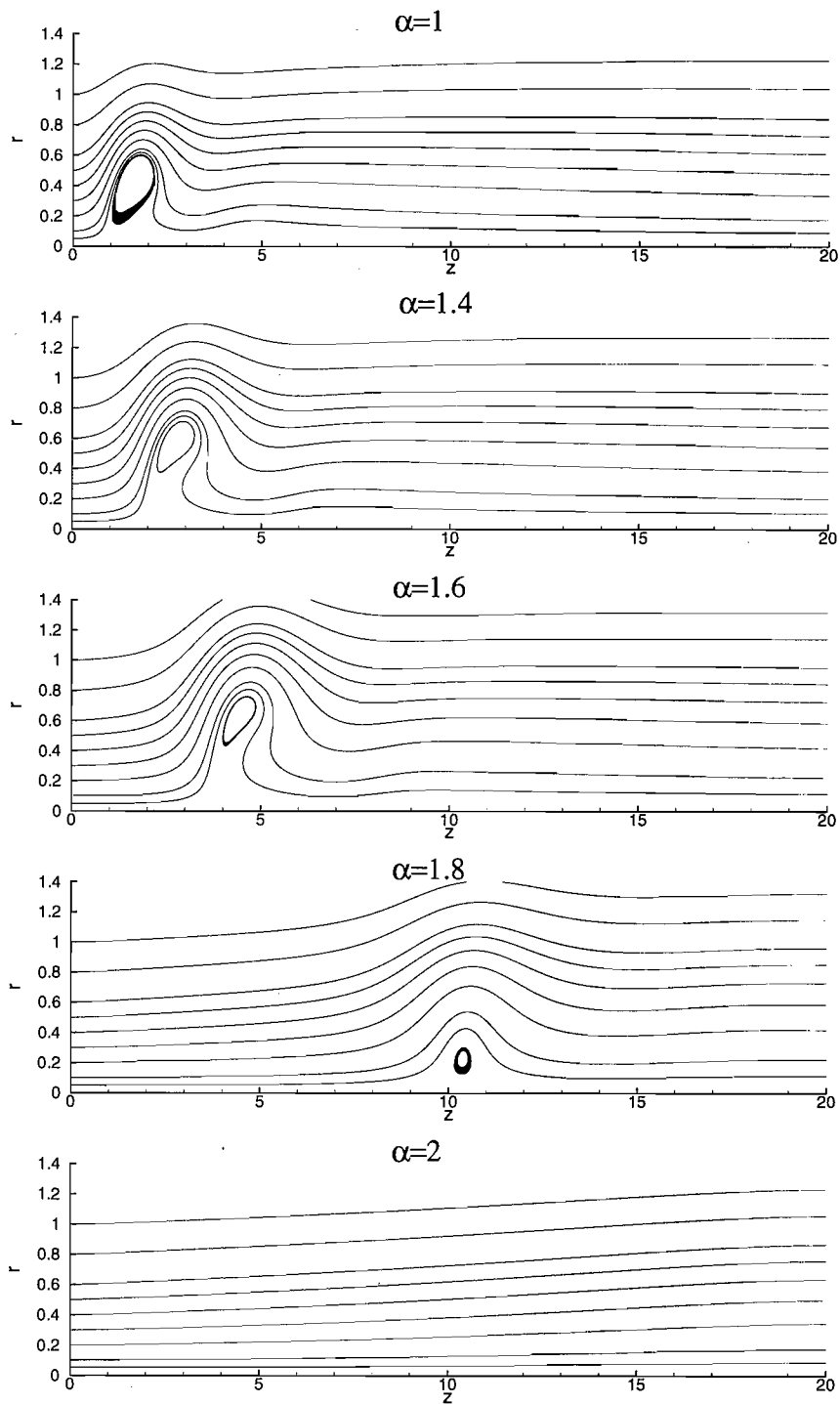


Figure 4.13: Steady solutions obtained at different coflow numbers. $Re=200$, $S = 1.1$, $M = 0.5$.

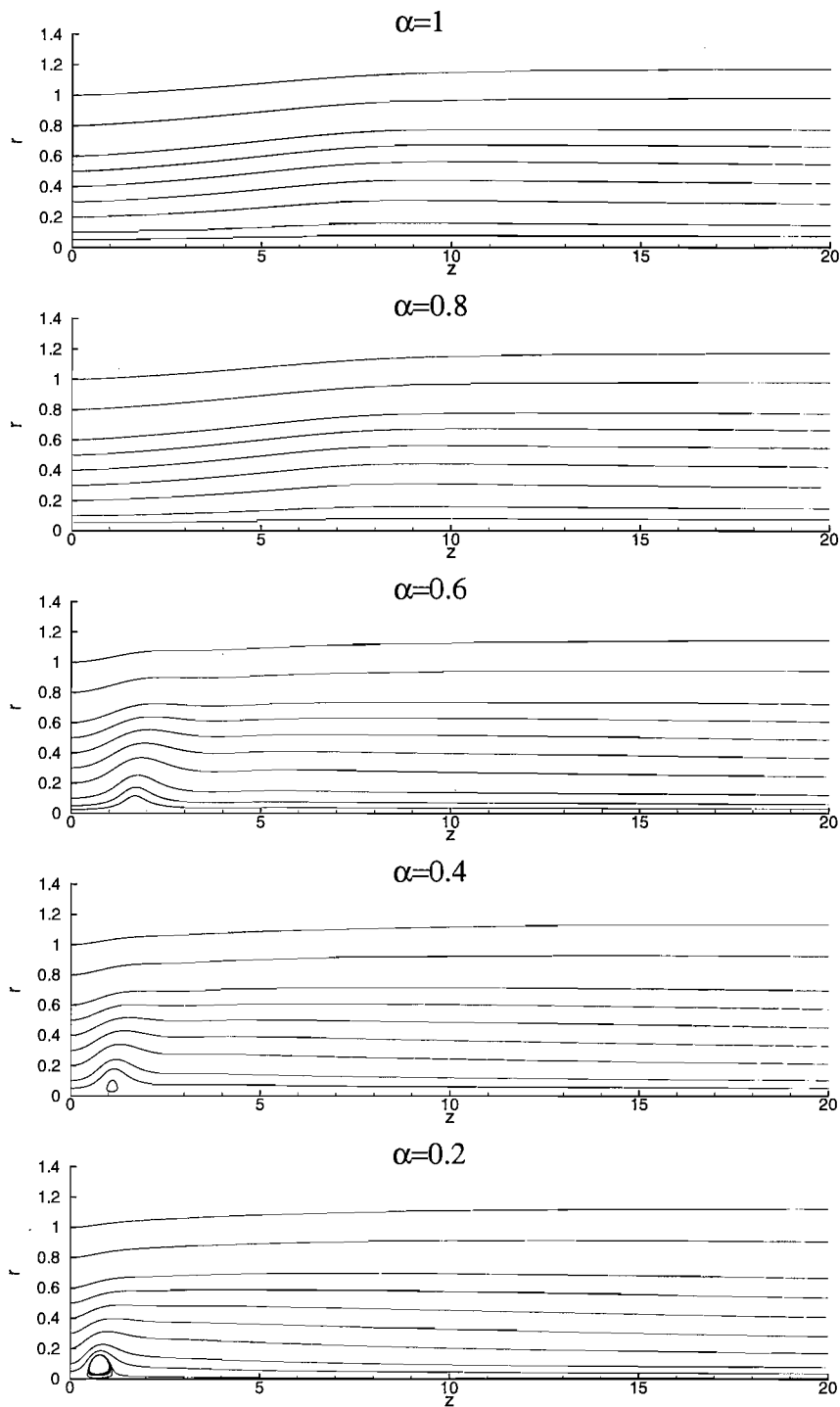


Figure 4.14: Steady solutions obtained at different coflow numbers. $Re=200$, $S = 0.84$, $M = 0.5$.

also on its history.

In the present analysis, we focus on the criterion first suggested by Jumper *et al.* [47]; the reason of this choice is two-fold. First, in some sense it appears to be more global, as the derived conditions require knowledge of the state of the flow upstream and downstream of the vortex flow; moreover, it is more inherent with what we believe to be the mechanism of an incipient breakdown: wave propagation associated with the twisting of the vortex tube. Jumper *et al.* consider a simple inviscid model made of a vortex tube defined by the Rankine velocity profile (cfr. §3.2.1) superimposed on a uniform distribution of axial velocity. The swirling flow evolves from an upstream vortex radius a to a downstream vortex radius b , with $b > a$. In the model, both the asymptotic conditions are described by the Rankine vortex with the same angular velocity Ω , the only difference being the edge of the core. Following the analysis of Batchelor [4], the divergence of the vortex tube leads the axial and the tangential velocity components to evolve as

$$\begin{aligned} \frac{V_z(r)}{V_z(z=0)} &= 1 + \left(\frac{a^2}{b^2} - 1 \right) kb \frac{J_0(kr)}{2J_1(kb)} \\ \frac{V_\theta(r)}{\Omega r} &= 1 + \left(\frac{a^2}{b^2} - 1 \right) \frac{b}{r} \frac{J_1(kr)}{J_1(kb)}, \end{aligned} \quad (4.7)$$

where $k = 2\Omega/V_z(z=0)$ and J_0, J_1 are Bessel functions. Vortex breakdown is postulated to occur when the centerline axial velocity approaches zero. This leads to write the following simple condition between the radius ratio b/a and the vortex strength (here measured by k):

$$\frac{a}{b} = \sqrt{1 - \frac{2J_1(kb)}{kb}}. \quad (4.8)$$

The above criterion has been tested *a posteriori* using the results of our DNS. Specifically, the inlet velocity profile at $z = 0$ is modelled as Rankine vortex assuming $\Omega = \frac{[V_\theta]_{max}}{r_{max}}$ where r_{max} represents the radial location where the azimuthal velocity achieves its maximum $[V_\theta]_{max}$ at the inlet (this corresponds to a in (4.7)). Similarly, b is evaluated as the radial position where V_θ is maximum at the outlet. All the terms in (4.7) can then be easily calculated.

Application of the criterion is reported in fig. 4.15 for a low Reynolds number $Re=200$ and for a high Reynolds number case $Re=1000$. Note that when no breakdown occurs, the ratio a/b in (4.8) exceeds the right hand side, hence the evaluation of the criterion requires that

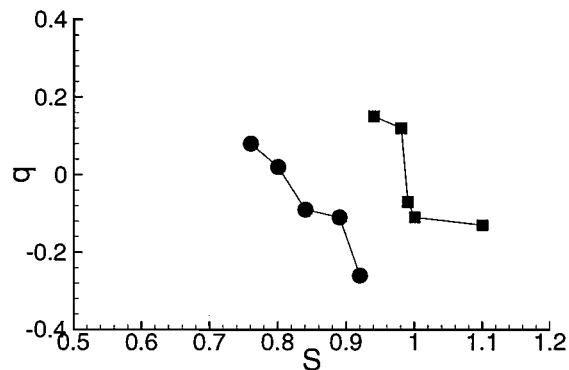


Figure 4.15: Application of the vortex breakdown criterion to the Re=1000 case (squares) and Re=200 case (circles).

their difference, hereafter named q becomes negative if criticality is reached when moving in the swirl number space. The result provides interesting information. For the high Reynolds number case q becomes negative at $S = 0.99$, while the DNS has found breakdown at $S = 1$: the difference can be considered very small, considering also that the velocity profiles used for simulations differ from the Rankine vortex. The comparison is much worse for the Re=200 case. Indeed, the value of q is already negative at $S = 0.84$ whereas computations have revealed the first appearance of the stagnation point at $S = 0.88$. The result, only partially satisfactory, can however offer a link with previous observations. The inviscid model used here accounts for the diffusion of the vortex tube by means of the two edges a, b , but it does *not* account for the effect of viscosity on the wave evolution. At higher Reynolds numbers, as soon as the threshold is reached, the wave evolves to generate breakdown. At lower Reynolds numbers, the wave is trapped, in accordance with the results discussed in 4.5. It turns out that the model of Jumper *et al.* may “read” the condition at $S=0.8$ as critical, because the trapping mechanism is completely invisible to it.

Lopez [69] appears one of the few who arose the question of a proper definition for breakdown. The appearance of a stagnation point may not be the best classification in spite of the elusive role of viscosity, which, if on the one hand drives toward criticality, on the other does not permit the vortex bubble to be fully manifest.

Chapter 5

Three-dimensional direct numerical simulations

5.1 Results at $Re=200$

We begin describing low Reynolds number cases, $Re=200$, for which other numerical results are available [88]. This will serve to validate the code and to illustrate the sequence of events characterising the whole process. The inflow velocity profile is still given by (4.1). If not specifically stated, the Mach number is kept constant and equal to $M = 0.5$, while the coflow parameter is $\alpha = 1$ corresponding to a uniform axial velocity profile without axial shear. Calculations were performed using the explicit time integration method with the numerical parameters reported in table 5.1.

5.1.1 Helical vortex breakdown

Figure 5.1 shows the temporal evolution of the flow field for the case $S = 1.1$. The flow field is visualised by means of streaklines obtained by releasing particles (without mass) from six positions located at the inflow boundary (left side), on a circle of radius $r = 0.1$. The particles are coloured according to their emission time. As synthetically illustrated in the bifurcation diagram of fig. 4.10, the amount of swirl introduced is far above the critical level, *i.e.* the inflow profile is already subcritical to axisymmetric perturbations. Consequently, the initial columnar swirling jet rapidly decelerates in the vortex core near the inflow and the vortex bubble is formed in quite a short time.

In order to render the computation effectively three-dimensional, a small random perturbation in the azimuthal component of velocity is superimposed on the initial conditions. The perturbation is located on a circle of radius $r_0 = 0.2$ in the cross sectional plane $z_0 = 0.5$ and feeds energy into all the azimuthal wavenumbers compatibly with the cut-off fixed by

L_z	L_r	n_z	n_r	n_θ	b_r	\bar{r}
20	10	256	95	64	0.8	0.3

Table 5.1: Numerical parameters used for spatial DNS at Re=200.

S	$\hat{\omega}_1$	$\hat{\omega}_2$	$\hat{\omega}_3$	$\hat{\omega}_4$
1.1	0.039	0.083	0.115	0.154
1.3	0.072	0.143	0.206	0.276

Table 5.2: Linear growth rates measured at $S = 1.1$ and $S = 1.3$. Note the dependence $\hat{\omega}_m \simeq m \hat{\omega}_1$.

the θ discretisation. Each component of perturbation does not exceed the value 10^{-4} .

The temporal evolution of streaklines (fig. 5.1) reveals that the flow remains axisymmetric until the breakdown has fully developed. Then, once the bubble has formed, a quasi-steady state is slowly reached before the wake behind the bubble becomes unstable to helical disturbances. Further confirmation of this is provided by the comparison of the rms history relative to the axisymmetric and the 3D calculations (fig. 5.4). For the case under investigation, $S = 1.1$, the two curves are approximately the same until Time=220 when the instability starts growing. Analogous diagrams are plotted for other swirl number cases. The effect of the swirl is clearly destabilising: At $S = 0.95$ the axisymmetric and 3D solutions are the same until Time=400; conversely, increasing the swirl to $S = 1.3$ anticipates the transition toward unsteadiness indicating a higher receptivity of the axisymmetric breakdown state.

The flow remains helically stable at $S = 0.89$: a snapshot of the streaklines at Time=800 is reported in fig. 5.2 and shows that the axisymmetric breakdown state remains unperturbed. Loss of stability has also been found at $S = 0.9$, although with an extremely small growth rate, so we have to assume that for this set of parameters (Re=200, $M = 0.5$, $\alpha = 1$) the critical point for three-dimensional instabilities to arise is in the range $0.89 < S < 0.9$. Ruith *et al.* [88] have found an identical result for the incompressible case. Above this value the flow field evolves toward a limit cycle represented by the saturated state; these global modes are self-sustained, *i.e.* obtained in the absence of external forcing. The limit cycle is therefore a manifestation of a HOPF bifurcation [24].

In the axisymmetric calculations the recirculating region was found at $S = 0.89$: this suggests a causal relation between the appearance of localised reversed flow and the origin of the global mode. Tromp and Beran [99] have found a similar behaviour at higher Reynolds numbers, when the axisymmetric bifurcation diagram is already composed of

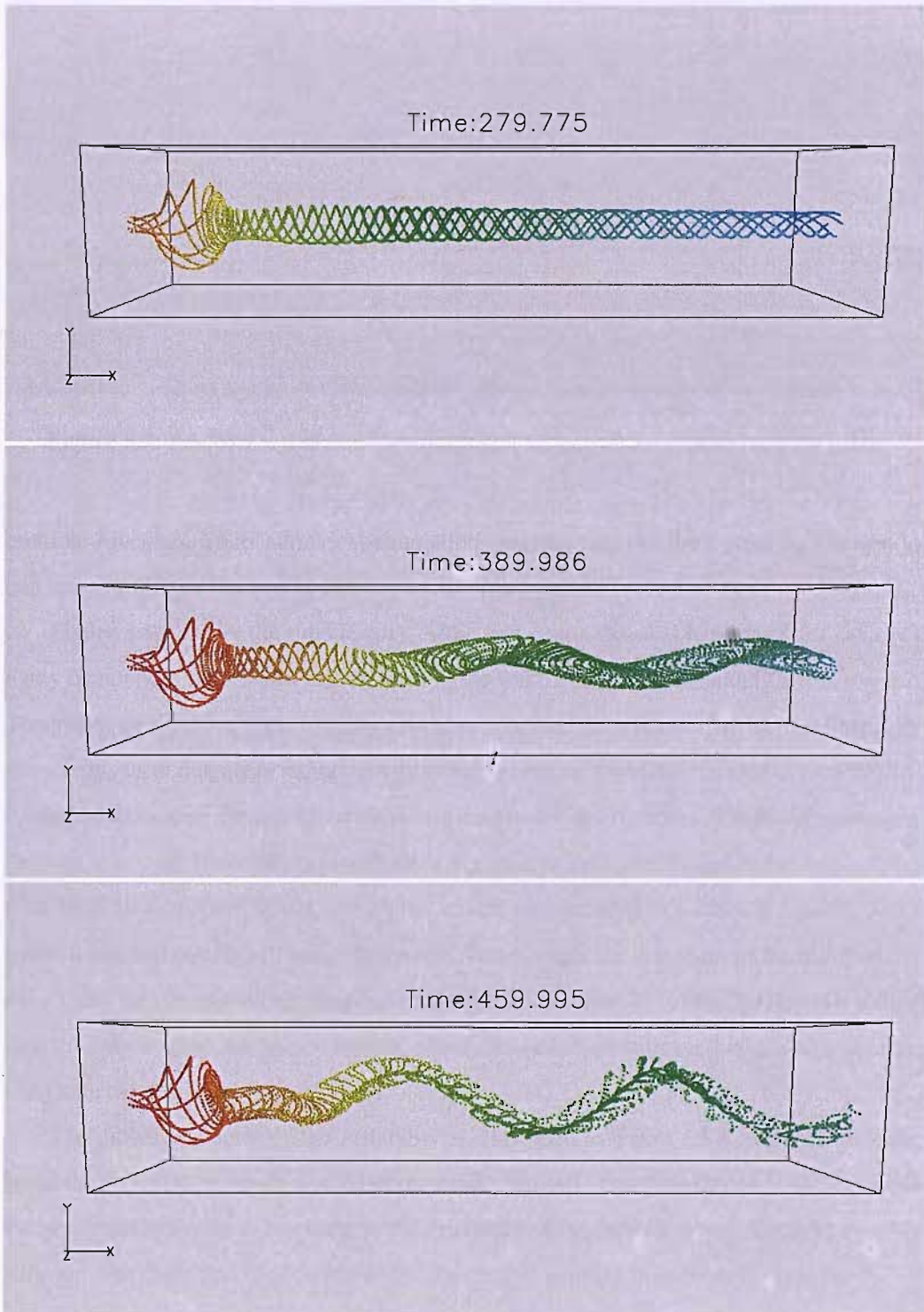


Figure 5.1: $Re=200$ $S = 1.1$ case. Evolution of the axisymmetric vortex breakdown toward a spiral breakdown state.

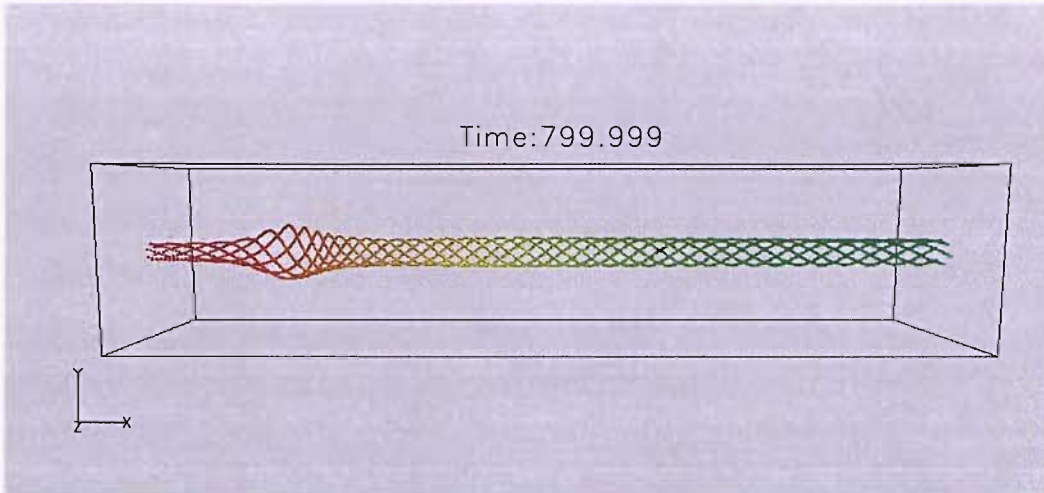


Figure 5.2: $Re=200$ $S = 0.89$ case. The axisymmetric vortex breakdown remains helically stable.

multiple branches. Their numerical simulations suggest that the limit point S_1 is close to that associated with the loss of stability to 3D disturbances.

Figure 5.5-*a* shows the time history of the first four azimuthal harmonics for each velocity component at a control station fixed in the wake of the bubble, namely $z = 5, r = 0.2$. The plot is on semi-log scale to highlight the exponential growth rate. We have deliberately chosen this local diagnosis rather than monitoring integral measures because it provides information to localise the axial position where the instability originates. The linearly unstable mode is $m = 1$; at Time=300 its amplitude is big enough to render the nonlinear interactions with itself no longer negligible, and higher modes start growing in a cascade process. Saturation is reached at approximately Time=420. At this stage, the dominant mode still remains $m = 1$ and the corresponding snapshot of the streaklines (the 3rd of fig. 5.1) reveals a flow field perturbed up to the vortex bubble, which, however, remains well confined within an axisymmetric region.

The global character of the instability is illustrated in figure 5.5-*b*, which shows the temporal evolution of mode 1 at different axial positions. The growth rate is identical but the perturbation seems to originate in the proximity of the bubble, where the axial shear is stronger. The definition of growth rate for the generic azimuthal mode m is given by

$$\hat{\omega}_m = \frac{1}{t_2 - t_1} \ln \frac{q_m(t_2)}{q_m(t_1)} \simeq \frac{\partial}{\partial t} \ln q_m(t),$$

where q_m is the generic m Fourier coefficient of any variable, while t_1 and t_2 are different times taken within the linear regime. For this specific case we have found $\hat{\omega}_1 = 3.9 \cdot 10^{-2}$.

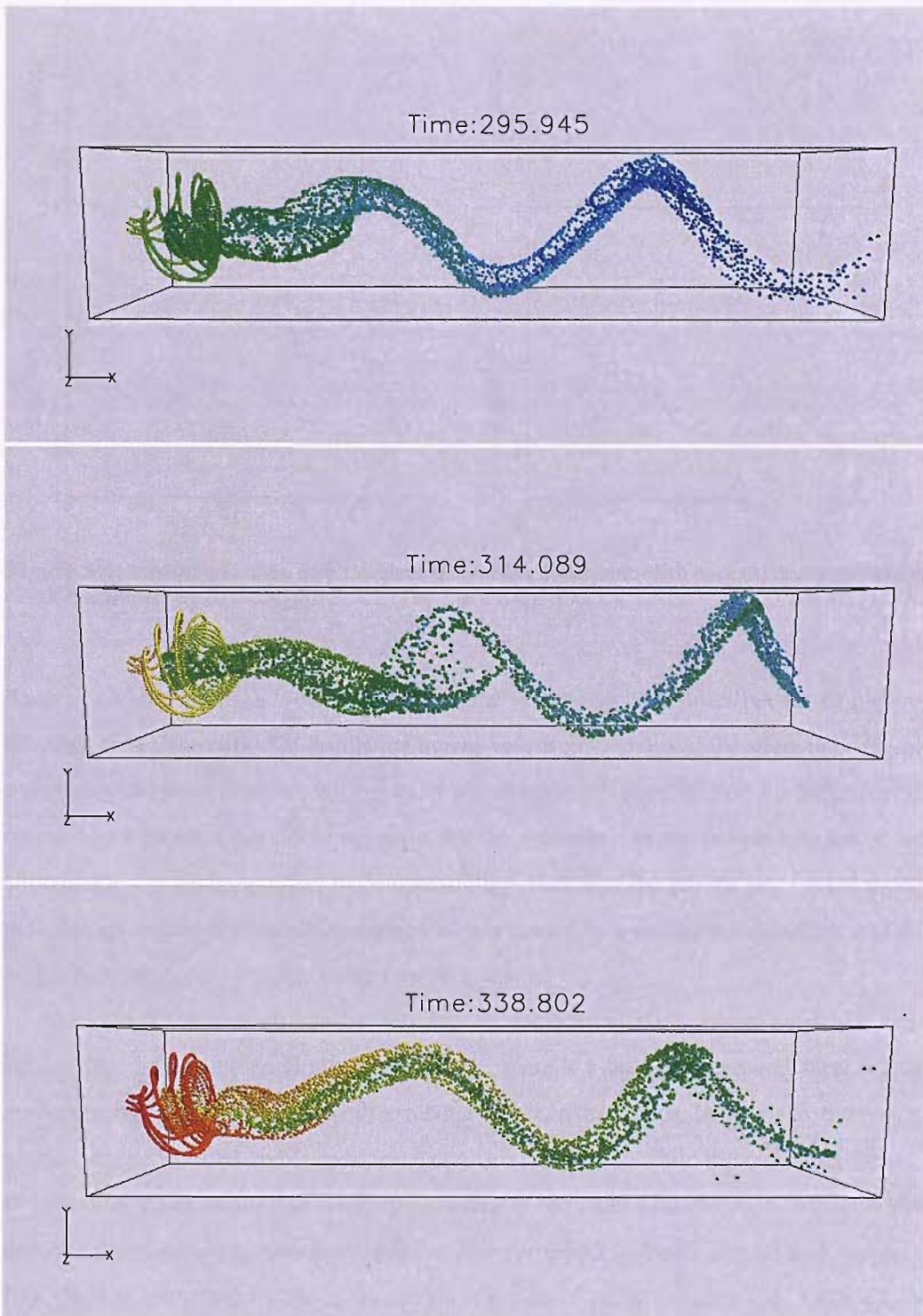


Figure 5.3: $Re=200$ $S = 1.3$ case. Spiral breakdown state with the appearance of double-helical structures.

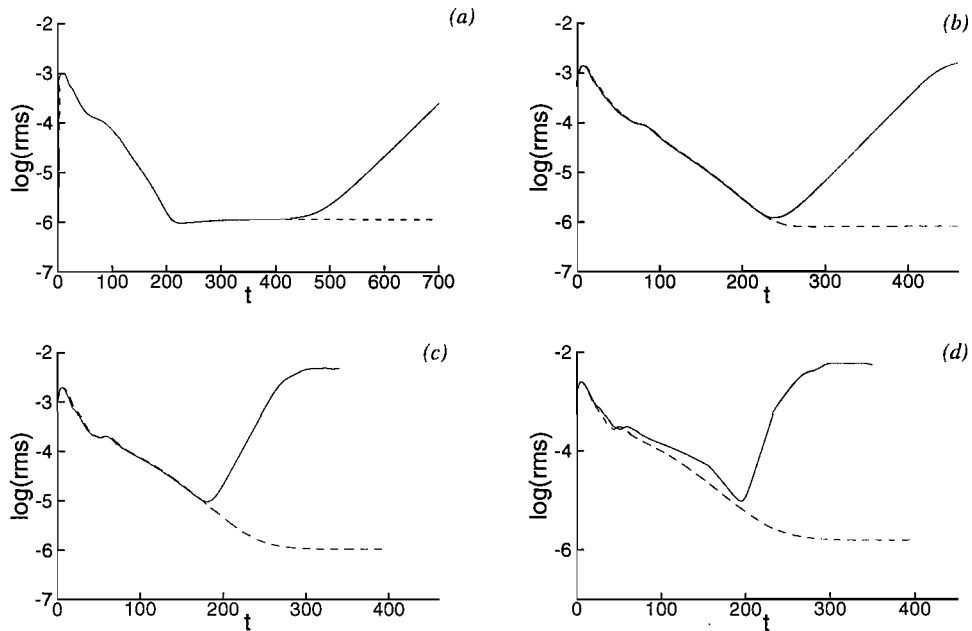


Figure 5.4: Unsteadiness of the flow. Comparison between axisymmetric (dash line) and three-dimensional (solid) simulations. (a): $S = 0.95$ (b): $S = 1.1$ (c): $S = 1.3$ (d): $S = 1.5$.

Ruith *et al.* [14] found $\hat{\omega}_1 = 6.63 \cdot 10^{-2}$ with the same velocity profiles but for an incompressible flow. The period of oscillation agrees very well, $T=5.5$, and the streaklines reveal a very similar spatial structure with an axial wavelength $\simeq 7$. A parametric study conducted on the Mach number (cfr. §5.6) suggests that the difference in the growth rate has to be attributed to the damping effect of compressibility. Note that the growth rate for the mode $m = 2$ is approximately double, ensuring that it is caused by a nonlinear interaction, and all higher harmonics $m > 1$ reach lower saturation levels.

Additional information can be retrieved by considering the vorticity amplitude iso-surface (fig. 5.7). In the proximity of the bubble, there is a strong background shear which renders problematic the detection of the tubular vortex in that region. In the wake, the vortex tube is better identified and is seen to revolve around its axis while the instability grows. If seen from downstream, the spiral is revolving in the clockwise direction, which is the opposite direction of the base flow. However, the perturbation rotates in time with the base flow. This is confirmed by the cross section contours of radial velocity (fig. 5.8), which clearly indicate an advection in the counterclockwise direction. The instability is therefore produced by corotating, counterwinding modes.

Increasing the swirl number to $S = 1.3$ leads to a higher growth rate (see fig. 5.6) but

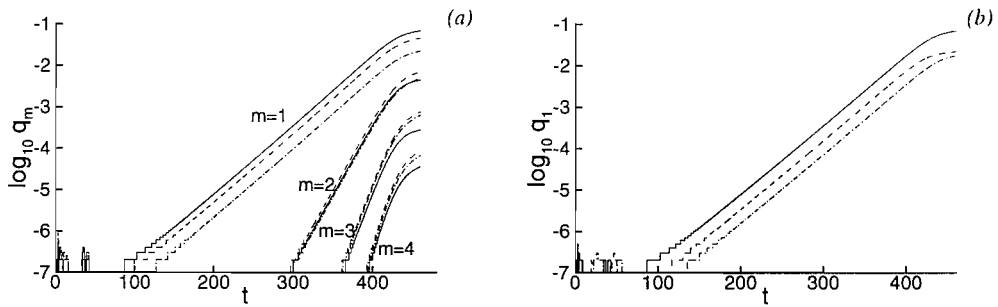


Figure 5.5: $Re=200$ $S = 1.1$ case. (a): Temporal evolution of azimuthal Fourier coefficients for axial velocity (solid), radial velocity (dash) and azimuthal velocity (dash-dots) at the probe $z = 5, r = 0.3$. (b): Temporal evolution of the first azimuthal mode $m = 1$ for the axial velocity measured at different axial positions: $z = 5$ (solid), $z = 10$ (dash), $z = 15$ (dash-dots).

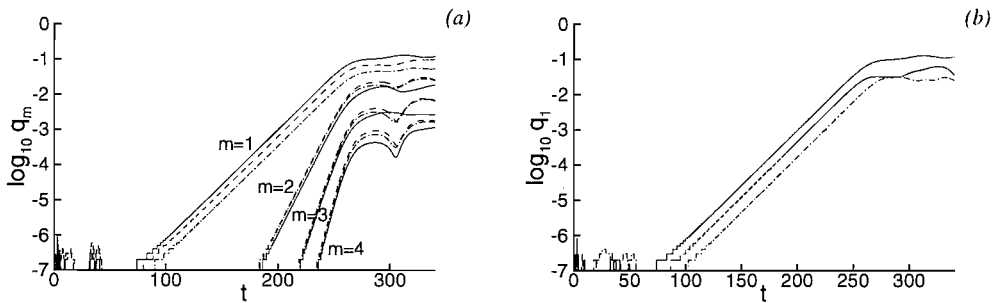


Figure 5.6: $Re=200$ $S = 1.3$ case. Refer to caption of fig. 5.5.

other significant differences have not been encountered: the bending mode is linearly unstable while higher modes are generated only due to nonlinear interaction. This conclusion is corroborated by the data reported in table 5.2: in both the circumstances ($S = 1.1$ and $S = 1.3$) the fundamental amplitude q_1 grows with a specific rate $\hat{\omega}_1$ while higher harmonics q_m are “slaved”, growing with $\hat{\omega}_m \simeq m \hat{\omega}_1$. The saturated state at $S = 1.3$ is however characterised by an increased energy level of higher harmonics, and the streaklines (see fig. 5.3) reveal the transient appearance of double-helical structures superimposed on a dominant helical mode.

5.1.2 Double-helical vortex breakdown

A substantial change in the three-dimensional response has been found at $S = 1.5$: the axisymmetric breakdown state evolves initially toward a spiral, but at later stage switches into a double-helical breakdown state (fig. 5.9). The vortex bubble becomes bigger in size

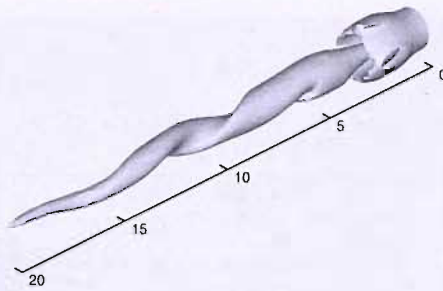


Figure 5.7: $Re=200$ $S = 1.1$ case. Iso-surface of vorticity magnitude. $|\xi| = 1.57$.

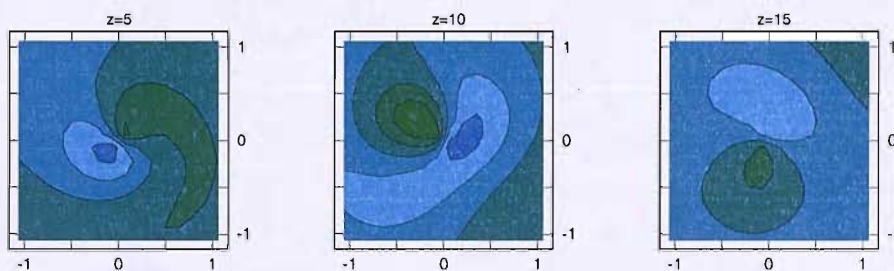


Figure 5.8: $Re=200$ $S = 1.1$ case. Cross sectional contour of the radial velocity component at different axial positions.

and the particles move in it before being ejected. At $S = 1.3$, the particles were already seen to enter the bubble from the back, but their behaviour appeared more regular.

The growth rates are reported in fig. 5.10: it can be noted that mode 1 grows regularly and smoothly while higher modes present a more complicated behaviour. Higher resolution has not changed this trend: the same calculation was conducted using all the parameters reported in table 5.1, with $\bar{r} = 0.15$ which corresponds almost to avoiding the fall of wavenumbers in computing the azimuthal derivatives, but no difference was detected.

Referring to both the $S = 1.1$ and $S = 1.3$ cases (fig. 5.5 and 5.6), it can be seen that the growth of $m = 2$ becomes visible in the scale adopted when the amplitude of mode 1 is approximately $q_1 = O(10^{-4})$, whereas $m = 3$ becomes visible when $q_1 = O(10^{-3})$ and $q_2 = O(10^{-5})$. The same mechanism seems to be reflected for the current case $S = 1.5$: the indications provided by fig. 5.10 are actually that modes 1 and 2 are those linearly unstable. At Time=210 we have $q_1 = O(10^{-3})$, $q_2 = O(10^{-5})$ and the growth of mode 3 begins. Modes 1 and 2 grow with approximately the same rate until Time=230, then the growth rate for $m = 2$ suddenly increases. This transition occurs because the nonlinear production of mode

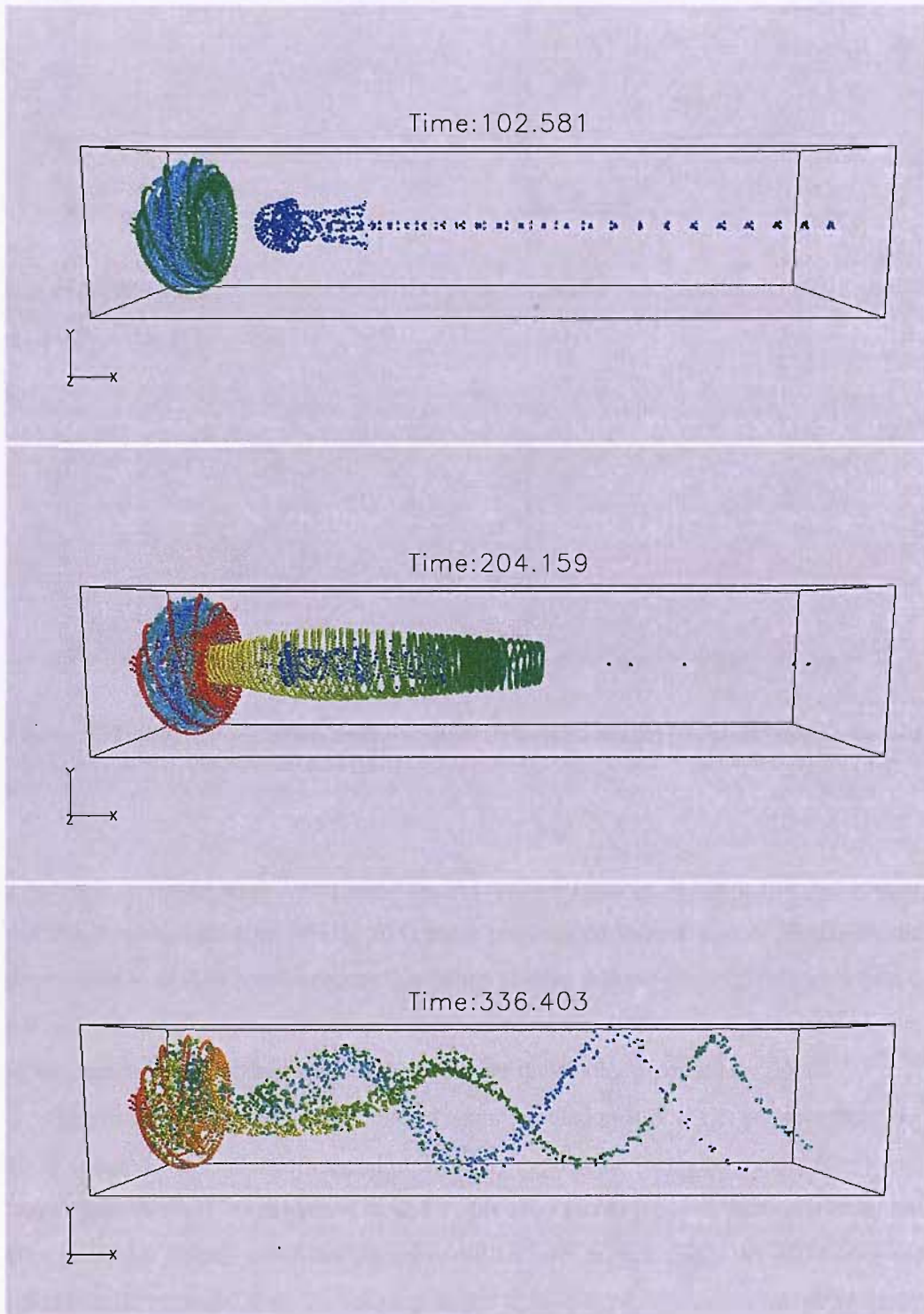


Figure 5.9: $Re=200$ $S = 1.5$ case. The axisymmetric breakdown ultimately evolves toward a double-helical breakdown mode.

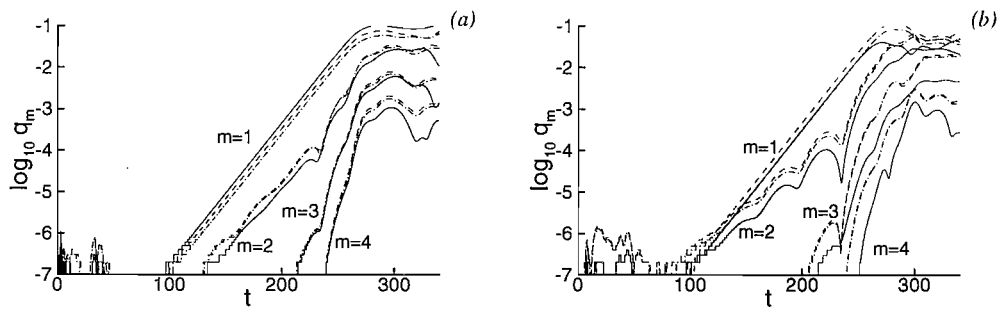


Figure 5.10: $Re=200$ $S = 1.5$ case. Temporal evolution of azimuthal Fourier coefficients for axial velocity (solid), radial velocity (dash) and azimuthal velocity (dash-dots) at different axial positions. (a): $z = 5$, $r = 0.3$. (b): $z = 10$, $r = 0.3$.

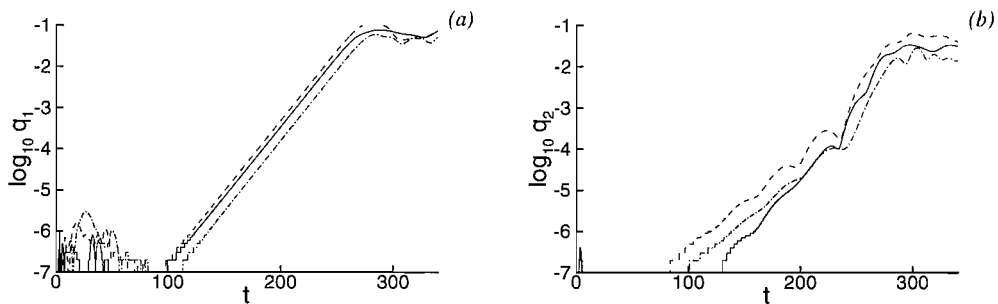


Figure 5.11: $Re=200$ $S = 1.5$ case. Temporal evolution of a single azimuthal Fourier coefficient for the axial velocity measured at different axial positions: $z = 5$ (solid), $z = 10$ (dash), $z = 15$ (dash-dots). (a): $m = 1$. (b): $m = 2$.

2 becomes dominant on its linear selection. A careful inspection of figure 5.10 also reveals that the irregular character at $z = 10$ is more pronounced than at $z = 5$. Moreover, the growth rate of mode 1 remains unchanged when moving downstream (fig. 5.11-a), whereas it is reduced and anticipated for mode 2 (fig. 5.11-b). In the author's view, this is a symptom of the coexistence of different dynamics rendering the whole response less global.

Surprised by this result, we conducted a new simulation at $S = 1.5$, but perturbing the initial condition with a random signal obtained by duplication (hereafter simply labelled as “even” perturbation). As explained in §2.2.2, this allows us to focus on the evolution of the even azimuthal modes, which are the only ones initially excited. Since the odd modes are automatically excluded from the calculation, the technique permits us to evaluate properly whether mode 2 is effectively linearly unstable. From the new run, we also expected indications of the irregular behaviour previously encountered: a possible competition between linear and nonlinear effects should now be absent. In addition, assuming as initial flow field

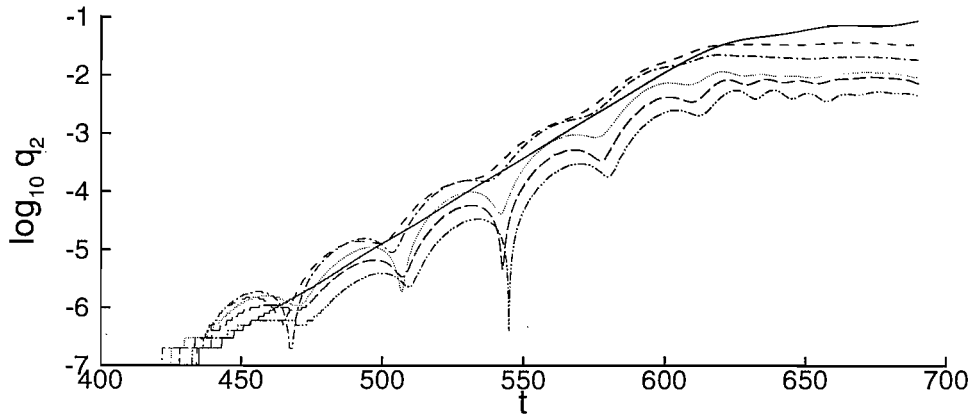


Figure 5.12: $Re=200$ $S = 1.5$ case excited by an “even” perturbation. Temporal evolution of the azimuthal Fourier coefficient $m = 2$ at different axial positions: $z = 4$ (solid), $z = 6$ (dash), $z = 8.5$ (dash-dot), $z = 11$ (dotted), $z = 14$ (long dash), $z = 16$ (dash-dot-dot).

the converged axisymmetric solution, we also exclude the possibility that some irregularity might be caused by the evolution of the base flow which gradually changes its stability properties.

Results are reported in fig. 5.12-5.13. A double-helix develops and contaminates the whole domain in the rear of the bubble. This confirms that the double-helix revealed in the previous computation, obtained exciting all the azimuthal modes, is a manifestation of a linear instability and not just caused by nonlinear interactions. Fig. 5.12 reports the growth rate of $m = 2$ measured at several axial stations. At $z = 4$ the growth is perfectly linear. As the probe location is shifted downstream, it is possible to recognise a sort of periodicity; each curve consists of different “lobes”, representative of transient periods during which the disturbance undergoes an amplification followed by a reduction. In this process, the envelope of the lobes seems to maintain a linear growth.

Also in light of results which will be presented later, we advance the hypothesis that this phenomenon results from the competition of two distinct global modes. There is a first instability mode whose behaviour is perfectly linear: it represents the natural extension of the global mode $m = 1$ examined at lower swirl levels. We will see that this global mode satisfies the theoretical prediction of Pier and Huerre [85], according to which it consists of a front located at the most upstream border of the absolutely unstable domain. In other words, there exists a specific section acting as wave-maker, *i.e.* giving the local absolute frequency to the global response. This section is the one which marks the transition from a

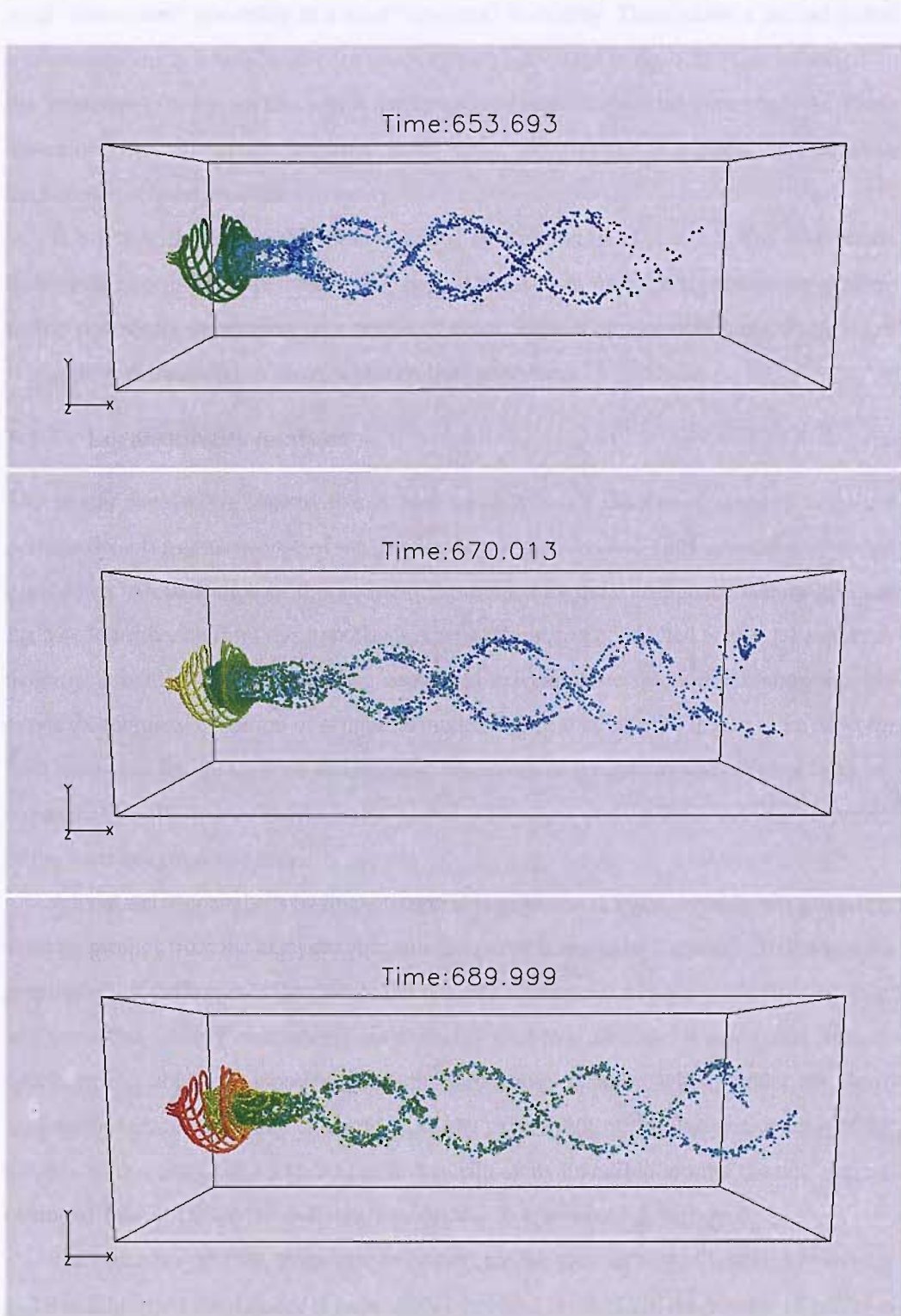


Figure 5.13: $Re=200$ $S = 1.5$ case perturbed by an “even” perturbation. A double-helical mode contaminates the whole domain.

local “convective” instability to a local “absolute” instability. There exists a second global mechanism which is responsible for the periodicity revealed in fig. 5.12. This is caused by the formation of wave packets which are irregularly sent out from the vortex bubble. These waves may be convectively amplified in the wake, and give rise to a global mode even in the absence of local absolute instability.

It is worth mentioning the result obtained by Ruith *et al.* at $S = 1.3$. The final breakdown state is defined as ‘pulsant double-helical breakdown mode’ and presents an axisymmetric periodicity developing on a period of about 100 non-dimensional units. Their result is somehow reminiscent of the mechanism discussed here.

5.1.3 Local stability analysis

The spatial simulations suggest that at least up to $S = 1.1$ the loss of stability to helical perturbations is a consequence of the structural change in the flow field generated by vortex breakdown. An indication of this scenario is provided by the convergence history given in fig. 5.4. To further confirm this hypothesis, a new 3D run was conducted at $S = 1.1$ assuming as initial condition the corresponding converged axisymmetric solution; a comparison between the temporal evolution of azimuthal modes reveals that the growth rate is the same for both cases (see fig. 5.14). With this premise, it remains of interest to find possible links between the global response shown by the spatial simulations and the local stability properties of the base axisymmetric flow.

A local stability analysis by linear temporal simulations (LTS) was conducted extracting velocity profiles from the axisymmetric solutions at different axial stations z . To enforce the assumption of strict parallelism the radial velocity is set equal to zero, while density, axial and azimuthal velocity components are explicitly read into the code. A new radial pressure distribution is obtained imposing the radial momentum balance, which, under the above assumptions, reduces simply to eq. (4.3). In the same spirit of the analysis conducted for the Batchelor vortex (cfr. §3.1), Navier-Stokes equations linearised around the new defined columnar flow are solved to evaluate the response to a localised perturbation.

The procedure and the diagnostic tools used are the same as those illustrated in chapter 3. Table 5.3 reports the numerical parameters employed for the LTS: the number of points in the streamwise and azimuthal directions were halved compared to the nonlinear counterpart; the radial scaling of azimuthal modes was not performed, and the radial discretisation was slightly increased to balance a reduction in the stretching factor b_r . The initial perturbation

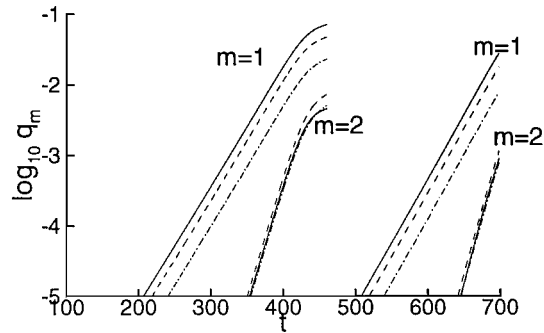


Figure 5.14: Independence on the initial condition for the $Re=200$ $S = 1.1$ case: temporal evolution of the azimuthal modes $m = 1$ and $m = 2$ for axial velocity (solid), radial velocity (dash) and azimuthal velocity (dash-dots). Solution starting from the axisymmetric base flow begins at Time=360.

is the same as used in the nonlinear spatial simulations and located at¹ $z_0 = 2, r_0 = 0.3$.

Details of the base flow under investigation are given in fig. 5.15-5.16. The radial distribution of axial vorticity presents local extrema at $z = 2, 3, 4$. This region may eventually show instability to two-dimensional disturbances of the form $e^{im\theta}$. Throughout the domain the circulation L increases outward, thus we expect the flow $V_\theta(r)$ to be centrifugally stable to axisymmetric perturbations everywhere. The recirculating flow is located between $z = 1$ and $z = 2.5$: in this region the flow rapidly accelerates on the centerline, so that the approaching wake-like profile $V_z(r)$ switches into a jet-like profile at $z = 2$, before recovering the wake character at $z = 3$. On the other hand, the circulation reaches its minimum between $z = 1$ and $z = 2$, thus this region is expected to be dominated by the axial shear, with eventually the generation of axisymmetric unstable modes via the classic vortex rings. In the lee of the bubble ($z > 4$), the wake is gradually attenuated and a slight reduction of the circulation accounts for the diffusion of the vortex tube.

As for the Batchelor vortex, the response of the flow to the localised perturbation consists in the formation of helical waves travelling within the vortex core. The spatial distribution of the wave packet can be appreciated in fig. 5.17, where are reported isocontours on the meridional plane $\theta = 0$ of the radial velocity perturbations. The figure refers to Time=30, when the wave packet has already crossed the right boundary and its leading edge is rapidly approaching the trailing edge.

The analysis relative to velocity profiles extracted at the sections $z = 4$ and $z = 8$

¹The homogeneous streamwise coordinate used in the local stability analysis must not be confused with its inhomogeneous counterpart of the spatial simulations.

L_z	L_r	n_z	n_r	n_θ	b_r	\bar{r}
20	10	128	120	32	0.4	0

Table 5.3: Numerical parameters used for linear calculations LTS on velocity profiles extracted by DNS.

reveals the development of similar structures and has to be considered representative of the general behaviour found for all the other stations far away from the bubble. For the profiles extracted at $z = 3.5$, the axial structure of the perturbation is enriched, while for those extracted at $z = 2$, even the radial structure appears to be modified, indicating a substantial change in the underlying dynamics.

The temporal stability properties $\omega_i = \omega_i(k)$ and $\omega_r = \omega_r(k)$ are evaluated according to (3.8) with the selected times t_1 and t_2 chosen appropriately to ensure that the unstable modes have been clearly selected after an initial transient period, and to circumvent the difficulty associated with the discontinuity of the phase function (cfr. §3.1.1). Figure 5.18 presents the growth rate ω_i of the unstable modes as a function of the axial wavenumber. The inflow profile, without axial shear, is found to be stable (not shown). In the recirculating region ($z = 2$), the first 4 modes are unstable. These are positive modes, sharing the most amplified axial wavenumber $k_{max} = 1.57$. The dominant mode is $m = 2$ with a maximum growth rate $\omega_i(k_{max}) = 0.405$. All the negative modes as well as the axisymmetric mode are found to be stable. In addition, all the modes are stable at $k = 0$. The curves obtained resemble qualitatively well those of the Batchelor vortex at $q = 0.2$ with the lower azimuthal modes dominant over the higher modes. Following this analogy, moving to $z = 3$ in the base flow, the swirl locally increases, and the growth rate of the bending mode is strongly reduced; mode 2 is also (slightly) reduced, and higher positive modes are destabilised. The dominant mode becomes $m = 3$ in close competition with $m = 2$ with a maximum growth rate $\omega_i(k_{max}) = 0.39$. The curves become similar to those relative to the Batchelor vortex for $q > 0.4$. In the latter case, however, we found destabilisation up to $|m| = 12$, but the Reynolds number was higher. The stability properties remain approximately unchanged for all the other sections downstream, consistent with the fact that the flow recovers the configurations of a quasi-columar vortex.

In the wake of the bubble the maximum growth rate always remains below the value 0.3, leading to the conclusion that the region with recirculating flow (where the effect of the swirl is less important) is the most unstable in a local analysis. This represents the major difference with the analysis conducted on the Batchelor vortex, where the effect of the swirl

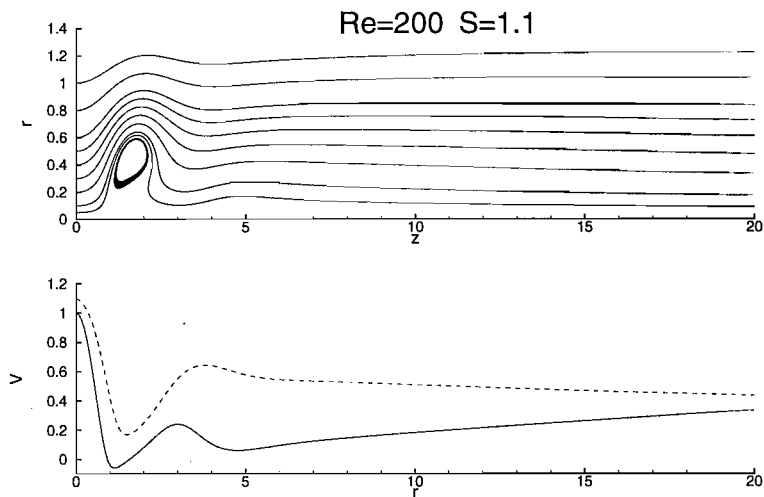


Figure 5.15: Base flow used for LTS. Top: streamlines. Bottom: centerline axial velocity (solid) and azimuthal velocity (dash) at $r = 0.5$.

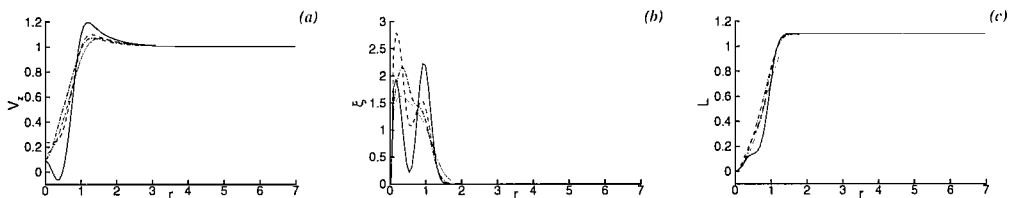


Figure 5.16: Base flow used for LTS: radial distribution of (a): axial velocity, (b): axial vorticity, (c): circulation, at different axial stations z . Solid: $z = 2$; dash: $z = 3$; dash-dot: $z = 4$; dotted: $z = 8$.

was found destabilising up to $q = 0.8$, and stabilising for $q > 0.8$. In that case, however, the axial shear was constant whereas in the current study it is more intense in the region of the bubble. This suggests that the centrifugal destabilising mechanism dominates the response in the wake of the bubble, while within the recirculating region there may be a higher contribution of Kelvin-Helmholtz instabilities enhanced by the stronger axial shear; this conclusion should also explain the differences revealed in the isocontours of fig. 5.17.

The question that now should be addressed is to understand the range of validity of the local analysis to our spatially developing swirling flow. Figure 5.19 shows the temporal frequency ω_r of the unstable modes for the sections $z = 2$ and $z = 4$. All the modes are positive and have a positive frequency, thus they rotate in time with the base flow but wind in space in the opposite direction. This is in agreement with the observations found in the spatial DNS. Conversely, a clear inconsistency is the evidence that the local linear analysis predicts higher modes $m > 1$ to be the most unstable at any station, whereas the helical

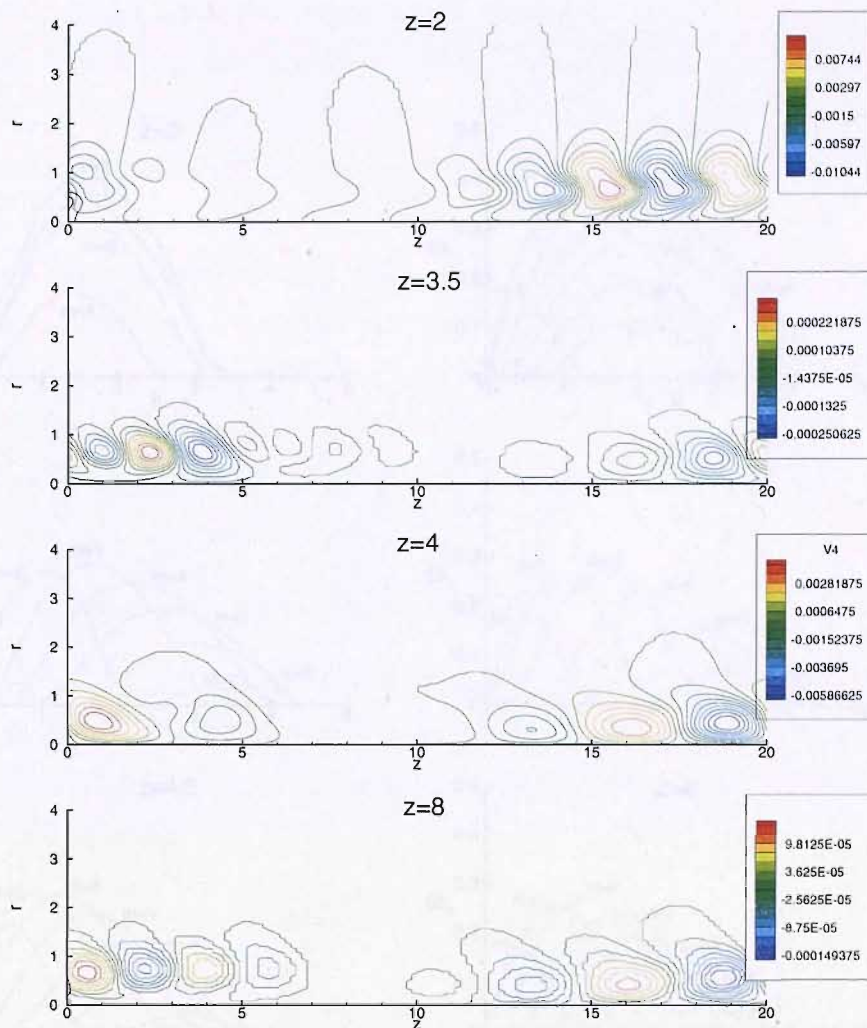


Figure 5.17: Response of the perturbed 1D swirling flows obtained extracting velocity profiles at different streamwise positions z from the converged DNS axisymmetric solution. Isocontours of radial velocity perturbation. Time=30.

breakdown found in the nonlinear spatial simulations has to be associated with a dominant bending mode. In other words, the local linear analysis, as currently performed, fails to account for a proper mode selection.

For slowly varying flows, the difference is generally explained in terms of the convective/absolute nature of the instability. As discussed in the introductory chapter, even if higher modes are subjected to a higher spatial amplification, they may be unable to trigger a global mode when they are only convectively unstable, since they require a continuous external forcing in order to remain in the region of interest. However, in our case the assumption of parallelism is strongly violated where the flow is recirculating, and we don't

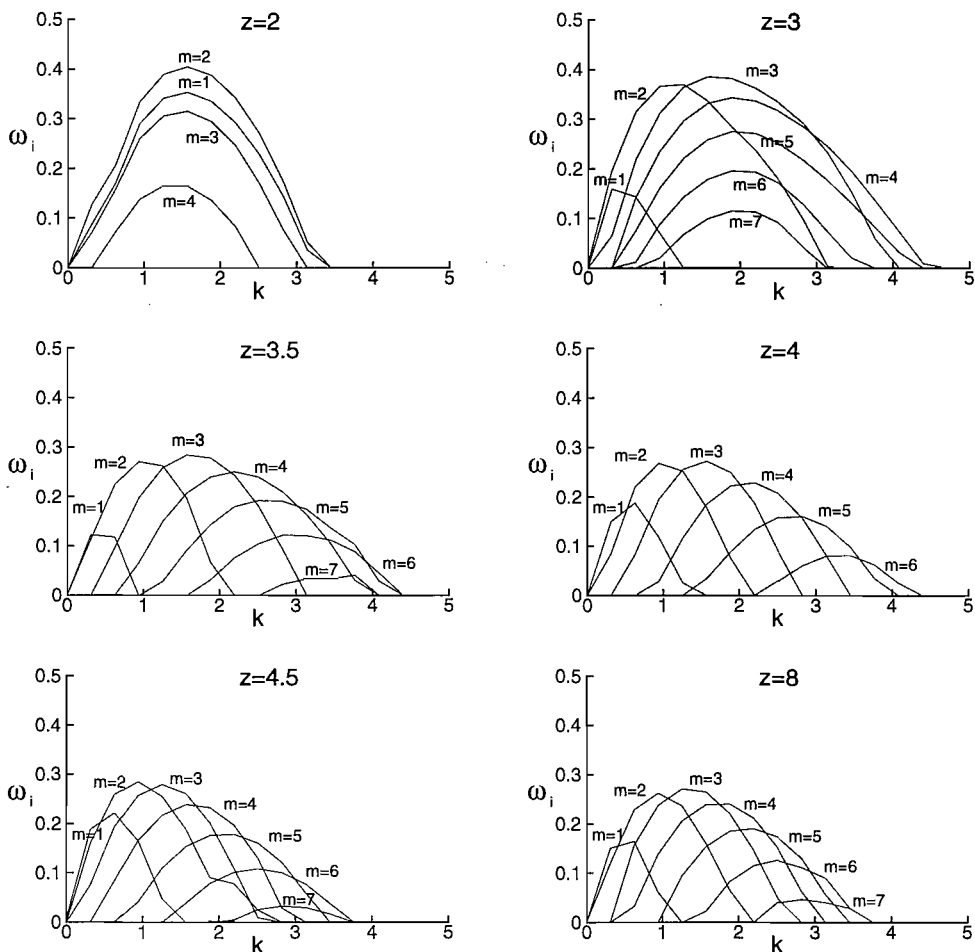


Figure 5.18: Temporal growth rate $\omega_i(k)$ of helical modes retrieved by LTS for velocity profiles extracted at different axial stations z .

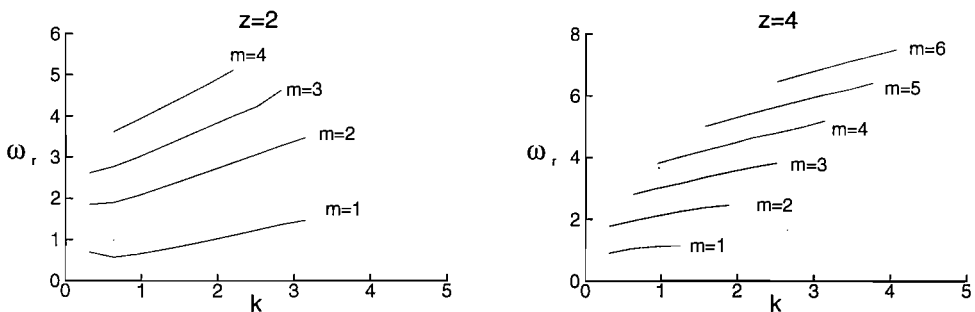


Figure 5.19: Real part of the frequency $\omega_r(k)$ of helical modes retrieved by LTS for velocity profiles extracted at different axial stations z .

know *a priori* to what extent these concepts can be applied.

In spite of these considerations, we proceeded as follow: results of figure 5.18 provide a quantitative indication of the convective amplification produced by the base flow for each azimuthal mode. By theoretical considerations [45] it can be shown that for each mode, the maximum growth rate over all the axial wavenumbers $\{\omega_i\}_{max}$ corresponds to the absolute growth σ_{max} “observed” along the spatio temporal ray $\frac{z}{t} = V_g$ where the amplification is highest. Therefore, we can use spatial DNS and perform experiments of convective amplification, measuring the spatial amplification produced on disturbances introduced at the inflow. We can compare these values with those obtained by the local linear analysis: if the two results show agreement, we gain confidence that the local analysis is actually suitable to describe the global response of our base flow.

5.1.4 Response to controlled perturbations

We evaluate here the global response of the base flow under investigation ($S = 1.1$) subjected to controlled perturbations applied at the inflow. The disturbance consists of small amplitude waves superimposed on the azimuthal velocity component. The analytical expression is the following:

$$V_{\theta}^{(p)}(r, \theta, t) = \epsilon V_{\theta}(r, z = 0) \sum_{m=1}^{\bar{m}} \sin(m\theta - \omega_m t) \quad (5.1)$$

The radial shape of the perturbation is somehow arbitrary since the streamwise inhomogeneity of the base flow does not permit identification of principal eigenfunctions. We preferred to express the perturbation as a percentage of the inflow profile by means of the amplitude parameter ϵ . A number of different cases were carried out by varying the number of modes excited in (5.1) and their corresponding frequency ω_m .

A first run was conducted assuming a nonlinear value for the amplitude ($\epsilon = 10^{-2}$). Based on the results of the linear temporal analysis the modes excited were chosen $m = 1...5$ with frequencies $\omega_m = m$. Results are shown in figure 5.20-5.21. Simulation restarts from the axisymmetric solution at Time=460 and runs until Time=500. From figure 5.17, we can estimate a speed of propagation of the perturbation applied at the inflow. Indeed, in the local analysis previously described, each velocity profile is initially disturbed at the axial location $z_0 = 2$, and the wave packet reaches the right boundary after $\simeq 30$ time units. We should therefore expect that the application of the continuous forcing at the inflow would generate after a time interval $\Delta T = 40$ a flow field fully perturbed and dominated by modes 2,3 in

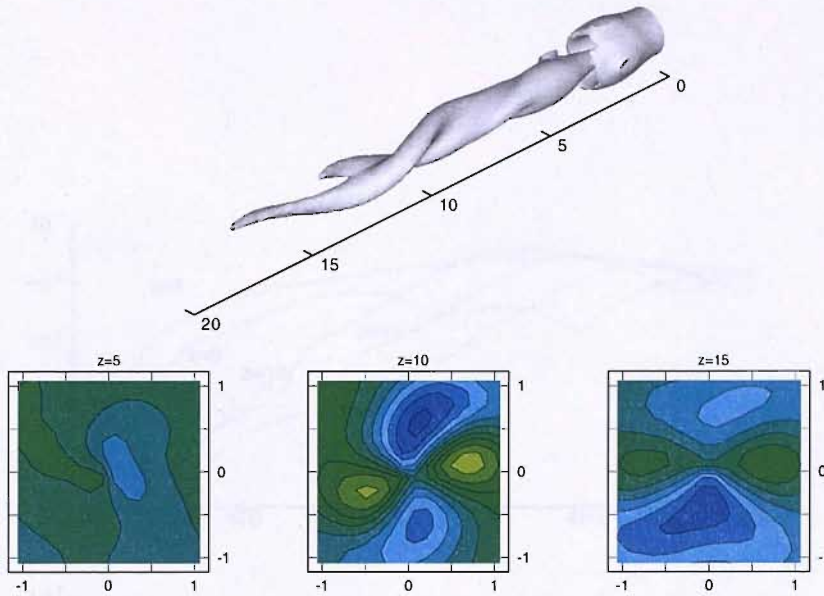


Figure 5.20: $Re=200$ $S = 1.1$ case subjected to nonlinear forcing ($\epsilon = 10^{-2}$), exciting modes $m = 1 \dots 5$ with frequency $\omega_m = m$. Time=500. Top: vorticity isosurface. Bottom: Cross sectional contours of radial velocity component at different axial positions.

competition. In this short time, the global mode $m = 1$, should not overwhelm the response because its growth $\omega_i = 3.9 \cdot 10^{-2}$ is too small compared to the absolute growth of the wave packets $m = 2, 3$.

Results however reveal a different scenario: the most amplified wavenumber is $m = 2$, followed by mode 1 and then mode 3 (see fig. 5.21). The indication given by the growth monitored along the axis, is that the amplitude of disturbance applied is too big; the wave packets quickly saturate, and no spatial amplification is recognised. Even this nonlinear effect however, does not explain the big amplification of modes 1 and 2.

To investigate further, we carried out a similar case imposing this time a linear perturbation ($\epsilon = 10^{-6}$). Adopting this value, the nonlinear code is expected to provide a linear response, with each mode evolving independently. In addition, with the purpose of running the calculation on a longer time, we removed from (5.1) mode 1, which in this way would be excited only by round-off error. We have monitored that its value never exceeded $O(10^{-6})$, and its effect can therefore be considered meaningless in the discussion. Results are reported in figure 5.22. The convective nature of mode 3 is now very well visible, since a steady state signal is everywhere left and the amplitude is seen to grow in space. The spatial amplification is reduced when moving downstream, and its order of magnitude compares well

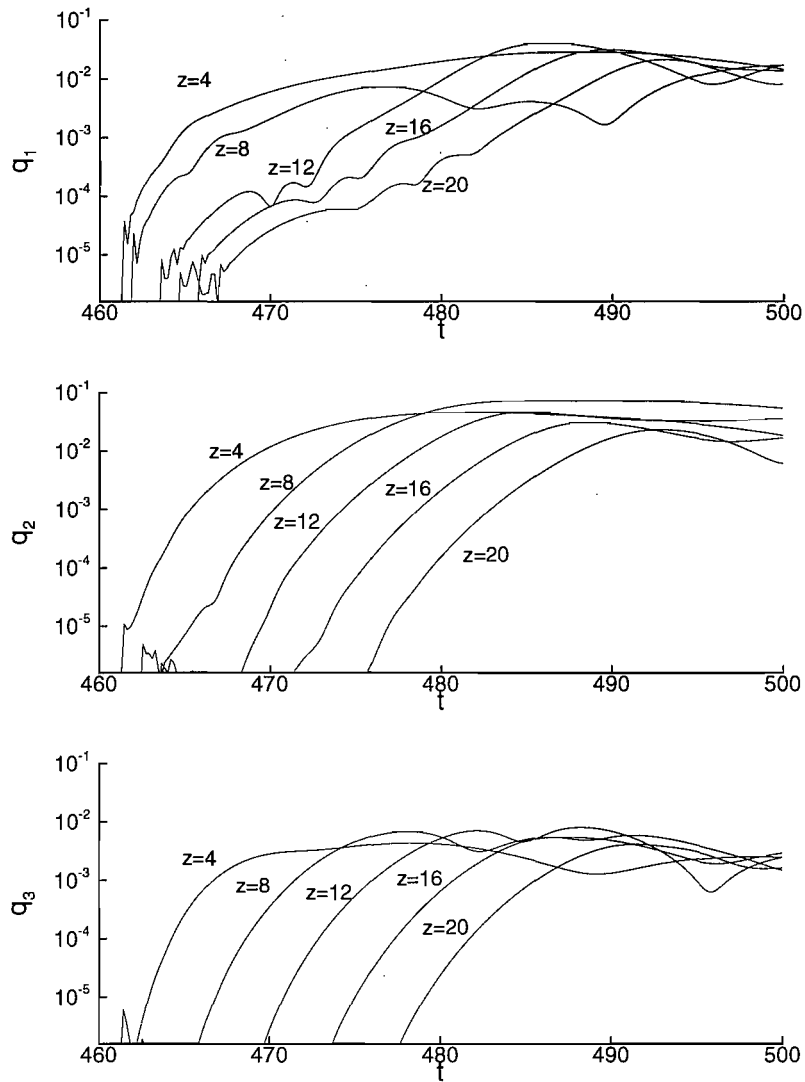


Figure 5.21: $Re=200$ $S = 1.1$ case subjected to nonlinear ($\epsilon = 10^{-2}$) forcing exciting modes $m = 1 \dots 5$ with frequency $\omega_m = m$. Time=500. Time history of modes $m = 1$ (top) $m = 2$ (center) and $m = 3$ (bottom) at different axial stations.

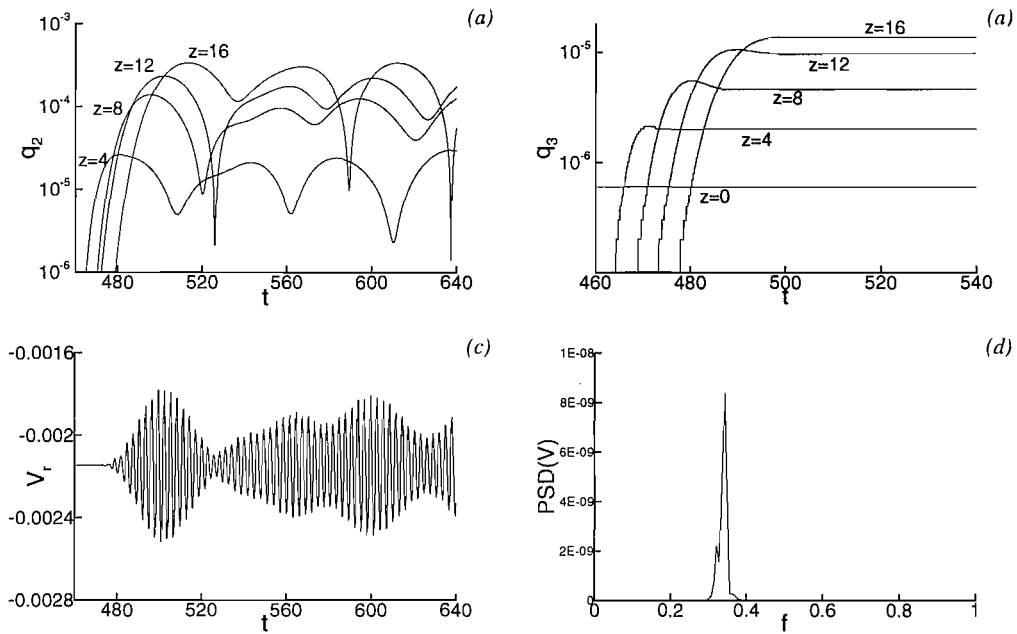


Figure 5.22: $Re=200$ $S = 1.1$ case perturbed by linear forcing ($\epsilon = 10^{-6}$) exciting modes $m = 2..5$ with frequency ($\omega_m = m$). (a): Time history of mode $m = 2$ at different streamwise positions. (b): Time history of mode $m = 3$ at different streamwise positions. (c): Radial velocity component recorded at $z = 10$, $r = 0.3$, $\theta = 0$. (d): Corresponding power spectrum density.

with the results of the local analysis: from 5.18 it can be noted that the maximum absolute growth rate relative to mode 3 remains almost constant for velocity profiles extracted between $z = 4$ and $z = 8$. In particular, its value is $\sigma_{max} \simeq 0.28$, thus the corresponding spatial amplification produced from the base flow on a disturbance with wavenumber $m = 3$ should be $e^{\sigma_{max} \Delta z} = 3.06$; in our DNS experiment the amplitude settles on $q_3(z = 8) = 4.9 \cdot 10^{-6}$ and $q_3(z = 4) = 1.9 \cdot 10^{-6}$ whose ratio is 2.57. In the recirculating region, the value of σ_{max} is more variable, so we may estimate the value at $z = 2$, namely $\sigma_{max} = 0.3$, leading to an amplification between $z = 0$ and $z = 4$ equal to 3.32. In the spatial simulation, the amplitude ratio calculated between these two locations is exactly 3. Therefore, a first interesting conclusion is that the evolution of mode $m = 3$ follows quite well the predictions provided by the local theory. We have also verified that similar results occur for mode $m = 4$, and we can confidently assume that this holds for all higher modes $m \geq 3$.

The behaviour of mode 2 is very different (see fig. 5.22-a): it still seems to be of convective nature, because it is spatially amplified, but at any axial station the amplitude undergoes strong variations. developing on a period of 50 time units. The ratio between the maximum value registered at $z = 8$ and that at $z = 4$ indicates an amplification of $\sigma_{max} = 0.34$,

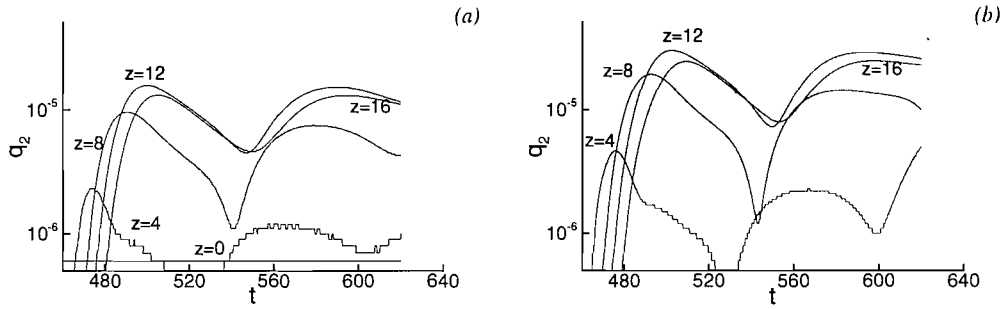


Figure 5.23: $Re=200$ $S = 1.1$ case. Temporal evolution of mode $m = 2$ at different streamwise positions. (a): Inflow perturbed by linear forcing $\epsilon = 10^{-6}$ exciting mode $m = 2$ with frequency $\omega_2 = 4$ and modes $m = 3..5$ with frequencies $\omega_m = m$. (b): Self-sustained case obtained by an initial “even” perturbation.

which is again in good agreement with the value estimated by the local theory ($\simeq 0.28$). The anomalous behaviour is between $z = 0$ and $z = 4$ (corresponding to the recirculating region), where mode 2 increases by almost two orders of magnitude rendering the global response completely dominated by mode 2. The radial velocity component registered at $z = 10, r = 0.3$ reveals a spectral peak at $f = 0.34$. Now, we conducted two other calculations: one was identical but obtained forcing mode 2 in (5.1) with a frequency $\omega_2 = 4$ (based on fig. 5.19 this value is out of the unstable range); another was performed removing the inflow forcing, and considering a self-sustained case initiated by superposing an “even” perturbation on the base flow. Time history of mode 2 is reported in figure 5.23: in both cases the behaviour is very similar, and again shows strong oscillations. The amplitude however, settles on values which are much smaller compared to the former case. Even more interestingly, the radial velocity component reveals a dominant frequency at the identical value $f = 0.34$. The result is very important, because it indicates a manifestation of an intrinsic dynamics: the value obtained has to be considered a natural frequency, and not associated with the external forcing.

The strong oscillations of mode 2 are reminiscent of the behaviour previously encountered when discussing the higher swirl case $S = 1.5$. In that situation, however, the amplitude was seen to increase “driven” by a global mode originating near the vortex bubble and growing linearly. Here, even if the global mode $m = 2$ is absent, wave packets beating at a specific internal frequency are irregularly generated and spatially amplified in the wake of the bubble. When left self-sustained, the amplitude of these waves oscillates around a value which remains small and grows in space in reasonable agreement with the results predicted by the local analysis. Conversely, if forced close to their natural rotation rate, the strong

oscillations are preserved but the amplitude rapidly increases in the recirculating region, following a mechanism which is invisible to the local analysis, and clearly associated with the presence of the vortex bubble. We suspect that this is the mechanism accounting for the “pulsant” breakdown state found by Ruith *et al.* [88]: their calculations are reported as self-sustained, but the possibility that some small source of error (even round-off) might produce the same effect of the inflow forcing applied here is not excluded.

We try now to summarise the considerations that need to be retained from the present discussion: according to the local linear theory higher modes are the most unstable in the wake of the bubble where the flow resembles well a parallel swirling flow. Lower modes are the most unstable in the recirculating region, where the swirl is less important. Therefore, the effect of non-parallelism is expected to be more important on lower modes. In the experiments reported here, we actually find that for higher modes ($m \geq 3$) the assumption of near parallelism can be considered valid *everywhere*, that is, the presence of recirculating region does not modify a behaviour which is pretty well explained in the parallel context. The reason why they do not appear in the spatial DNS must be their convective nature: in the absence of continuous forcing, they leave the computational domain.

For mode $m = 2$ the discussion is more complicated. The presence of the vortex bubble leads to the formation of self-sustained waves. These waves, which show a certain degree of irregularity, in the spatial DNS are unable to trigger a global mode and on a long time scale are completely overwhelmed by the bending mode $m = 1$. However, these waves do not play a completely passive role, because they remain spatially amplified downstream following the predictions of the local analysis. If the receptivity of the base flow is augmented, for example increasing the Reynolds number, we expect that the convective amplification produced on these wave packets may lead to a saturated state. In that case self-sustained structures of convective nature may become well visible: in section §5.3 we present spatial results at $Re=800$ which seem to match this scenario.

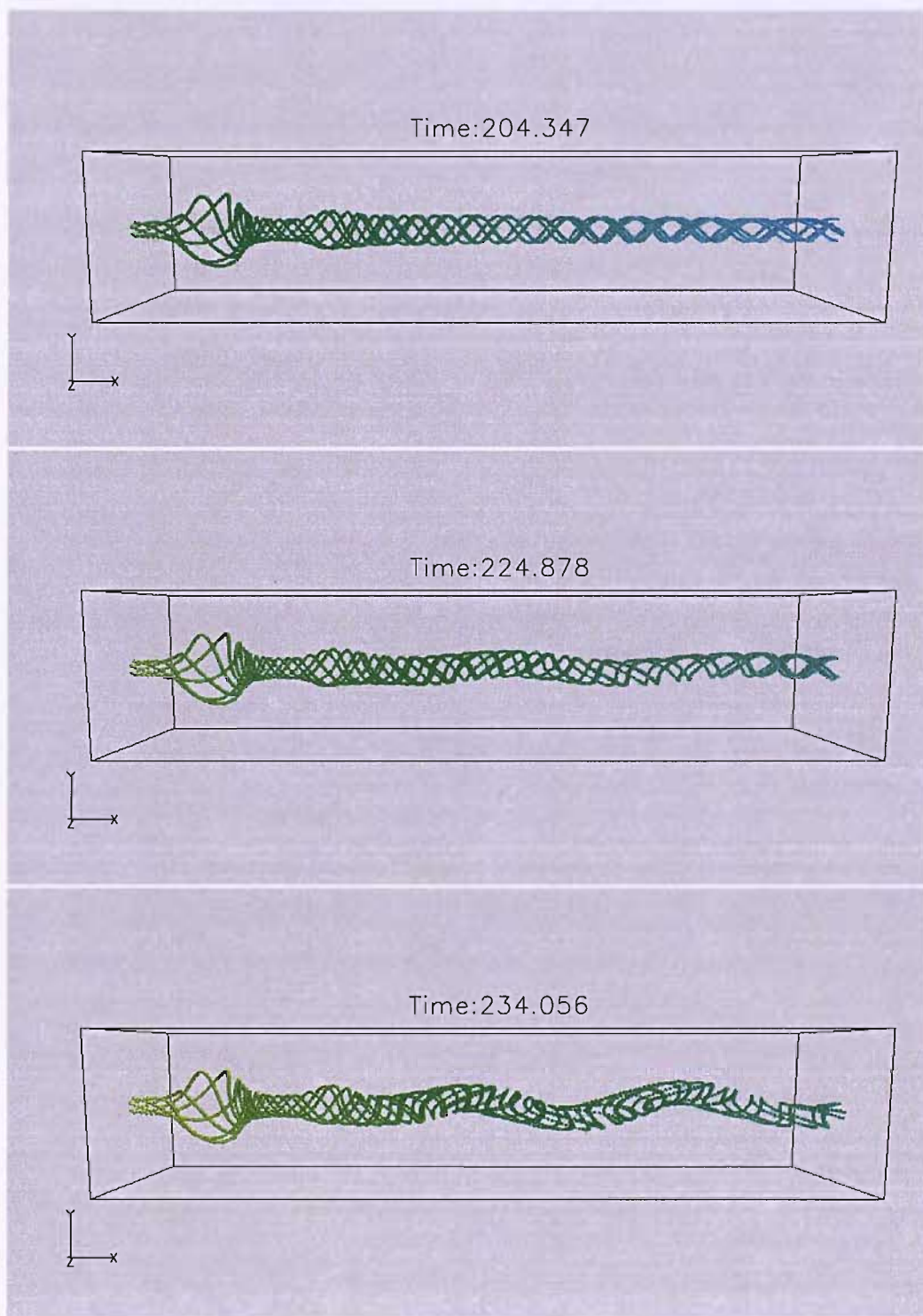
5.2 Results at $Re=400$

The aim of this section is to demonstrate that the spiral vortex breakdown is associated with the existence of local absolute instability for the bending mode $m = 1$. For reasons which will be clearer later, the analysis has been performed at $Re=400$, $S = 0.95$. For this set of parameters, axisymmetric results (cfr. fig. 4.9) reveal the existence of a second stagnation point formed in the wake of the first bubble. In what follows, we will first describe results of spatial DNS and later present the wave packet analysis as recently conducted by Gallaire *et al.* [33].

5.2.1 Spatial DNS

Direct numerical simulations were still performed using the numerical parameters of table 5.1. Figure 5.24 shows the evolution of the flow field. The sequence of events is not changed: the recirculating region is generated close to the inflow, then the flow slowly evolves toward a quasi-steady axisymmetric configuration which ultimately becomes helically unstable. Unlike the situation occurring at $Re=200$, the helical perturbation arising in the wake remains confined in the region downstream of a specific axial station for a considerably large time interval. At $Time=250$ the flow field reveals the existence of a front separating a nearly axisymmetric region upstream, from a fully three-dimensional region downstream. This configuration represents an axisymmetric vortex bubble followed by a spiral breakdown, and corresponds to the experimental breakdown state of Sarpkaya, reported in the introduction (fig. 1.1). At later time ($Time=280$), when the mean flow has been widely modified by the saturated perturbation, the instability contaminates the whole domain moving up to the first bubble.

According to the analysis of chapter 4, the second smaller breakdown is the result of the axial acceleration developed immediately after the bubble, responsible for the recovery of local supercritical conditions with respect to the marginal axisymmetric Kelvin modes. It is possible that a similar mechanism takes place with respect to the helical unstable modes. In other words, the negative radial velocity generated in the lee of the first bubble, well visualised by the inward motion of particles moving around it, locally increases axial and azimuthal velocity components. This can result in a local stabilisation of the flow with respect to the helical modes. Application of the local analysis should provide interesting information for this specific case, since the front of the wave is quite well identified and



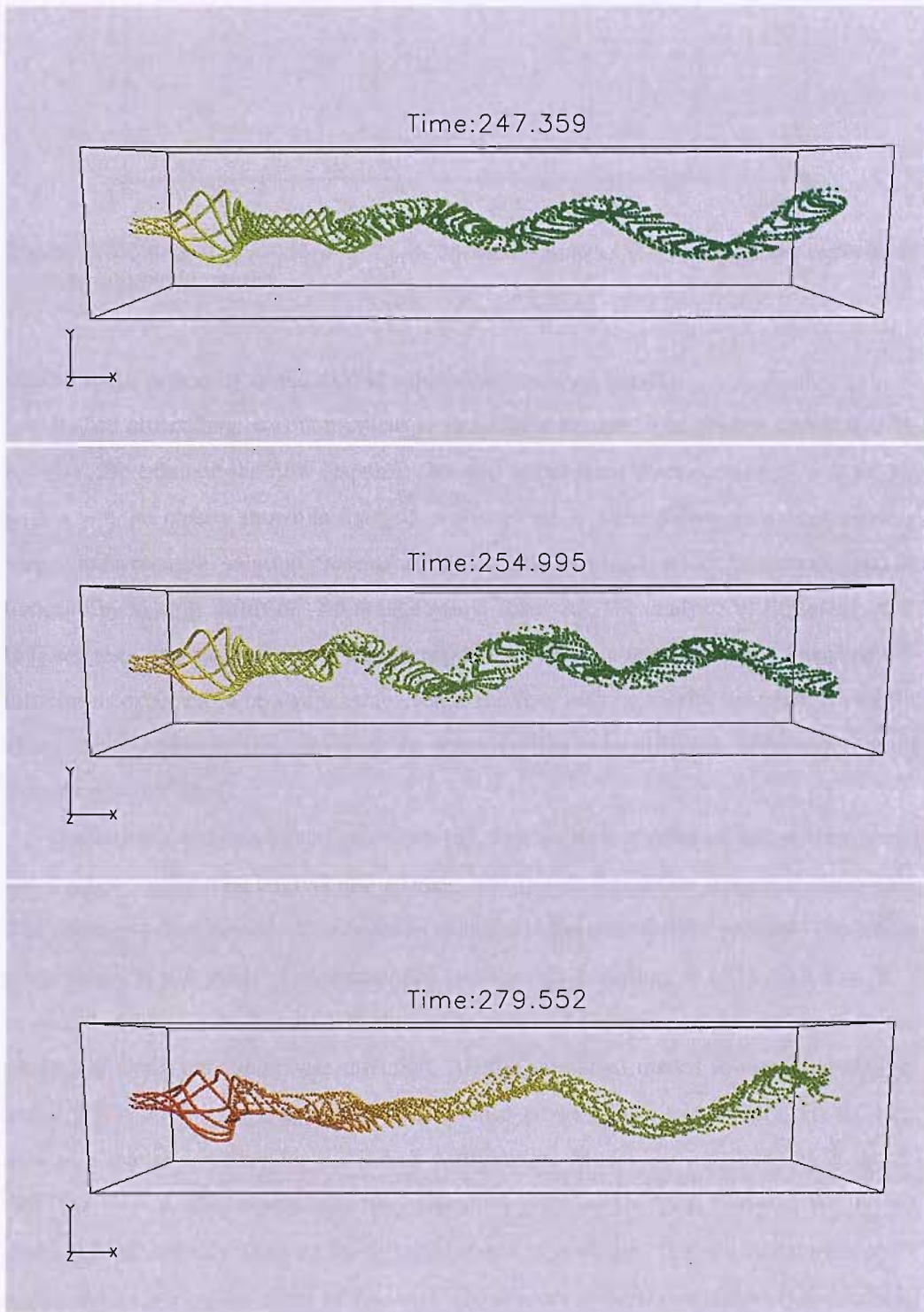


Figure 5.24: $Re=400$ $S = 0.95$ case. Axisymmetric vortex bubble followed by a spiral breakdown.

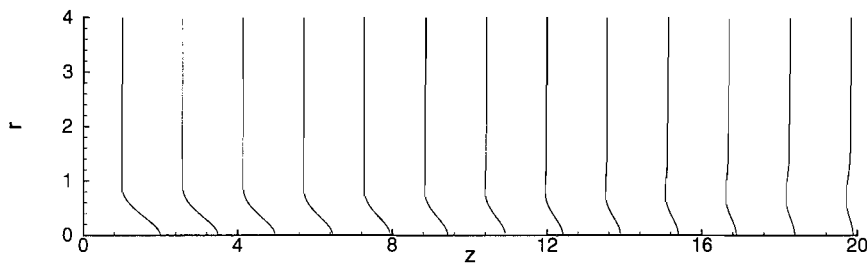


Figure 5.25: $Re=400$ $S = 0.95$, $\alpha = 2$ case. Streamwise evolution of the axial velocity profile in the converged axisymmetric solution.

located in the proximity of the second smaller recirculating region.

Before proceeding, it is convenient to illustrate an example of evident convective instability. We examine the flow response obtained at the same level of swirl, $S = 0.95$, but with $\alpha = 2$. As clearly shown in fig. 5.25, with this value of the coflow parameter the converged axisymmetric solution presents a jet inlet velocity profile which becomes gradually flattened by viscous diffusion. No breakdown is observed. The analysis of Loiseleux *et al.* [67] suggests that jet profiles are less susceptible to absolute instability; any localised disturbance is expected to be swept away even if the flow may be locally unstable. Under the effect of continuous forcing, however, the behaviour has to be different, as discussed in the introduction (cfr. §1.4).

Following a widely adopted procedure [85, 91], we have applied an inflow forcing and left it active for the time interval $400 < \text{Time} < 440$ (the 3D simulation restarts at $\text{Time}=400$). The forcing is then turned off in order to evaluate if the perturbation persists. The inflow perturbation is still made of superimposed small waves according to (5.1), with $\epsilon = 10^{-6}$, $m = 1.5$ and $\omega_m = m$. Figure 5.26 shows the temporal evolution of the first three modes monitored along the streamwise direction. All the azimuthal modes follow an analogous trend. While the forcing is active, the disturbance grows almost everywhere, *i.e.* the base flow is a spatial amplifier for the inflow perturbation. Modes $m = 2, 3$ are more amplified than $m = 1$, consistently with the indications given by the local analysis. We did not perform local stability analysis for this case, but it is now clear that the destabilisation of higher modes is a typical effect of the swirl. The absence of breakdown renders the stability characteristics well described by the curves obtained for the Batchelor vortex. It can also be noted that the amplitude of mode $m = 3$ experiences a spatial decrease starting by $z = 14$. A similar trend has been observed for all the higher modes $m = 3, 4, 5$, which therefore appear

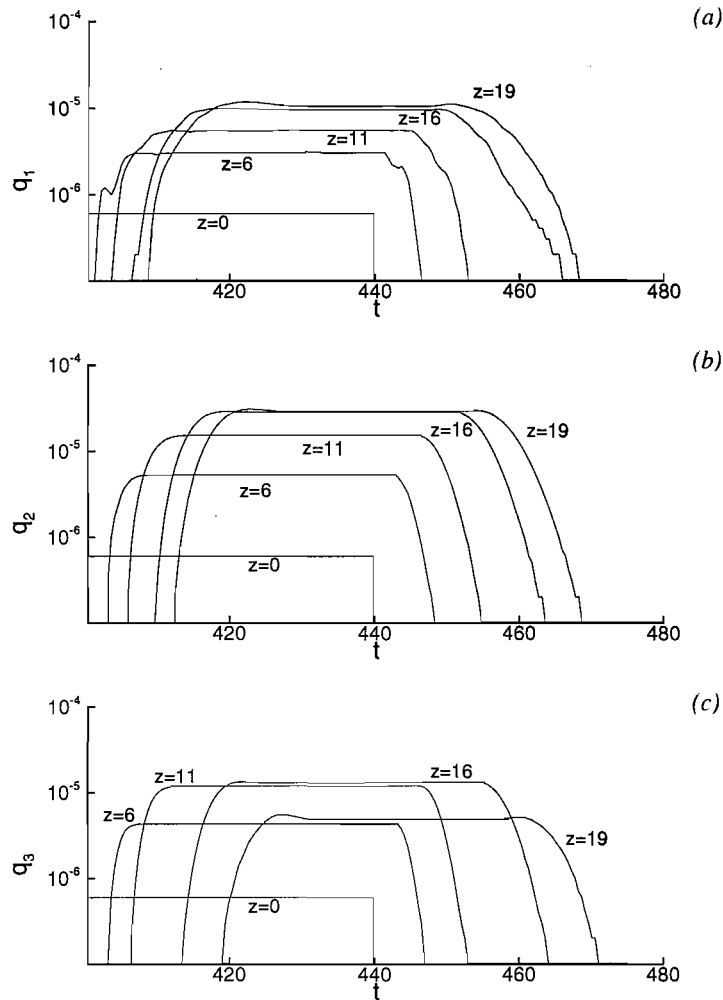


Figure 5.26: $Re=400$ $S = 0.95$, $\alpha = 2$ case subjected to a transient linear forcing ($\epsilon = 10^{-6}$), exciting modes $m = 1 \dots 5$ with frequency $\omega_m = m$. Temporal evolution of azimuthal Fourier coefficients for the axial velocity measured at different axial positions. (a): $m = 1$. (b): $m = 2$. (c): $m = 3$.

to be more sensitive to the reduction of circulation associated with the streamwise evolution of the base flow.

When the inflow forcing is turned off, all modes relax to zero, and self-sustained oscillations are not observed. What we wish to point out here is that the irregular behaviour found in the analogous forced experiment carried out at $Re=200$ $S = 1.1$ (cfr. §5.1.4) is in this case completely absent. This supports the conjecture that the phenomenon was associated with the presence of the recirculating region.

5.2.2 Wave packet analysis

The local analysis performed in §5.1.3 is repeated in a modified form for the azimuthal wavenumbers $m = 1, 2$. The objective is to detect the nature (convective or absolute) of these instability modes. Following the procedure of Gallaire *et al.* [33], the idea is to evaluate the growth rate of the wave packet “observed” along different spatio-temporal rays $\frac{z}{t} = V_g$. Similarly to what is described in §3.1.1, we consider the analytical representation of the axial velocity component $\tilde{V}_z = \tilde{V}_z(r, \theta, z, t)$ and perform a single Fourier transform in the azimuthal direction:

$$\hat{\tilde{V}}_z(r, m, z, t) = \int_0^{2\pi} \tilde{V}_z(r, \theta, z, t) e^{-im\theta} d\theta. \quad (5.2)$$

We define the amplitude associated with the wave packet m , and its corresponding phase functions as:

$$\begin{aligned} A_m(z, t) &= \left(\int_0^{\bar{r}} |\hat{\tilde{V}}_z(r, m, z, t)|^2 r dr \right)^{1/2}, \\ \Phi_m(z, t) &= \arg \left[\hat{\tilde{V}}_z(z, r_0, t) \right]. \end{aligned} \quad (5.3)$$

From the LTS, it is possible to measure the absolute growth rate and the corresponding frequency as a function of the group velocity according to the simple expressions:

$$\begin{aligned} \sigma_m(V_g) &= \frac{\partial}{\partial t} \ln A_m(V_g t, t) \simeq \frac{\ln [A_m(V_g t_2, t_2) - A_m(V_g t_1, t_1)]}{t_2 - t_1}, \\ \omega_{m0}(V_g) &= -\frac{\partial}{\partial t} \Phi_m(V_g t, t) \simeq -\frac{\Phi_m(V_g t_2, t_2) - \Phi_m(V_g t_1, t_1)}{t_2 - t_1}. \end{aligned} \quad (5.4)$$

These quantities are labelled as “absolute” [45] because their temporal evolution accounts for the dispersion mechanism which can make the disturbance grow in the same place where it is introduced. If the sign of σ_m at $V_g = 0$ is positive, the instability is absolute because the perturbation is able to withstand the advection due to the base flow. The corresponding local absolute frequency $\omega_{0,r} = \omega_{m0}(V_g = 0)$ is extremely important: following the theory of Pier and Huerre [85], for slowly varying flows the global response should beat at a frequency given by the value of $\omega_{0,r}$ computed where the flow locally switches from the condition of convective instability to that of absolute instability.

Although simple in principle, some of the operations to carry out are particularly subtle. In practice we need to determine the edges of the travelling wave packet as depicted in fig. 1.4. This corresponds to looking for the rays along which one has marginal stability. From the computational point of view, dealing with marginal stability is quite complicated,

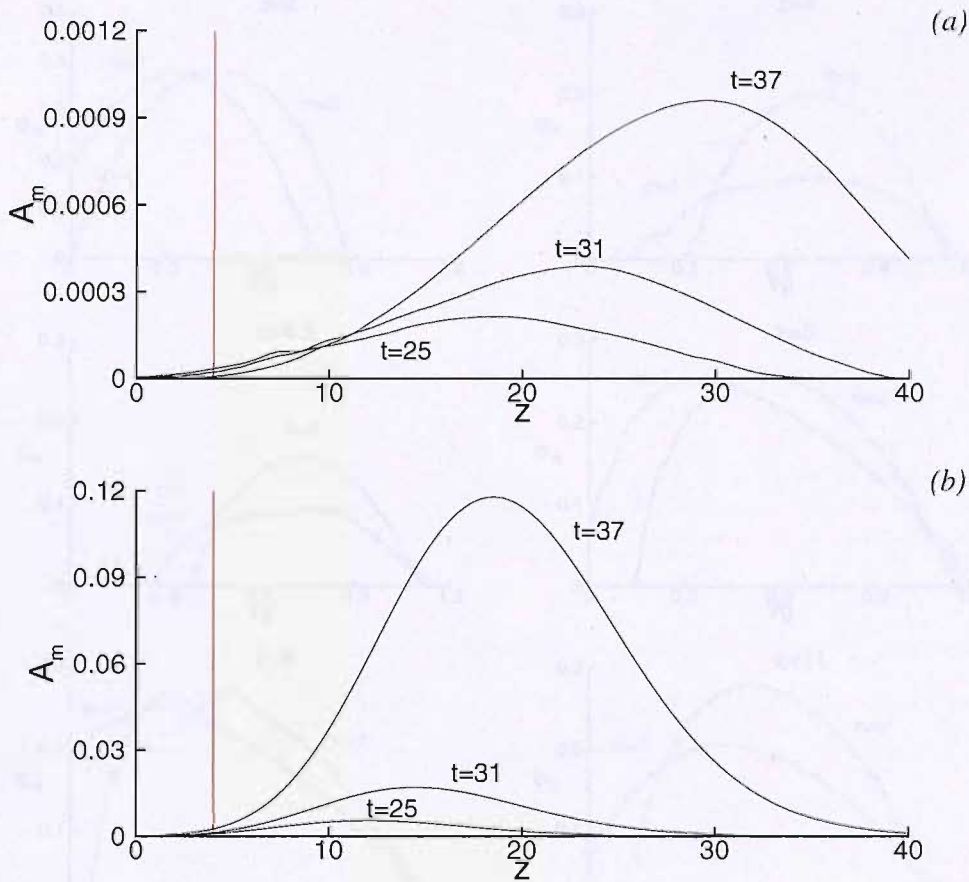


Figure 5.27: Streamwise distribution of the wave packet amplitude $A_1(z, t)$ as defined by (5.3). (a): LTS performed on velocity profiles extracted at (a): $z = 4$. (b): $z = 2$.

because the amount of energy that needs to be monitored is small, and easily subjected to background noise. It is therefore important to ensure that all the spurious oscillations initially given by the Gibbs phenomenon are well damped. Typically this has required $\simeq 20$ time units. It turns out the LTS results presented in §5.1.3, and relative to $Re=200$, are not suitable for this analysis. The computational domain is too small; after $Time=20$ the growth of the leading edge of the packet contaminates the growth at the trailing edge. To avoid this, we were obliged to adopt a box length $L_z = 80$ sampled by $n_z = 512$ points in the streamwise direction. Such discretisation did not allow a complete analysis for all the azimuthal modes, so we simply focused on $m = 1, 2$, fixing $n_\theta = 8$. The other parameters of table 5.3 were left unchanged.

Figure 5.27 illustrates the evolution of the amplitude $A_1(z, t)$ retrieved by LTS on the velocity profiles extracted at $z = 4$ and $z = 2$. The red vertical line marks the axial location

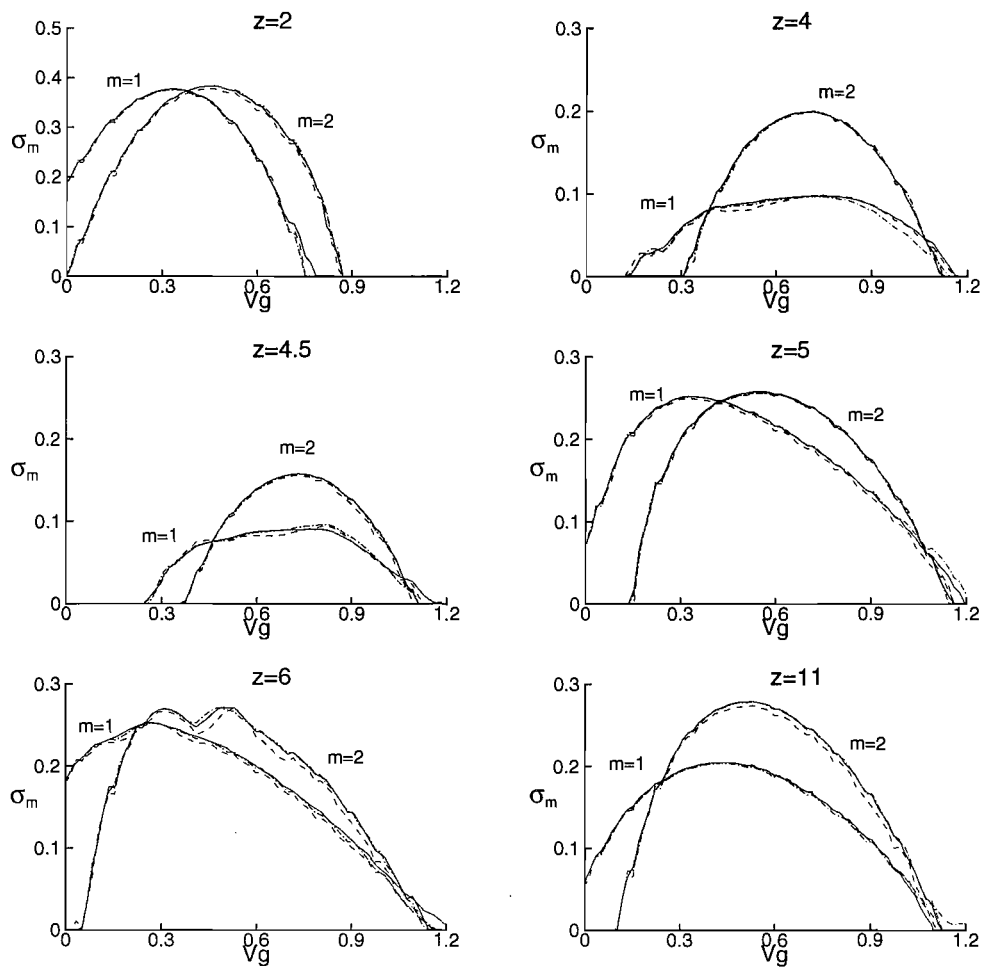


Figure 5.28: $Re=400$ $S = 0.95$ case. Absolute growth rate $\sigma(V_g)$ of helical modes $m = 1, 2$ retrieved by LTS for velocity profiles extracted at different axial stations z .

where the initial disturbance has been placed; in the first case (velocity profile extracted at $z = 4$) the instability is convective because the amplitude decreases at the location of the initial disturbance. Conversely, the velocity profile extracted at $z = 2$ exhibits an absolute instability since the amplitude is seen to increase at that location.

Figure 5.28 shows the absolute growth σ_m as a function of the group velocity computed for several velocity profiles. The first of (5.4) has been evaluated selecting $t_1 = 20$ and assuming for t_2 three different values $t_2 = 25, 30, 40$, in order to check the convergence of the whole procedure. The results show that mode $m = 2$ is only convectively unstable for most of the velocity profiles; at $z = 2$ it is $\sigma_2(0) \simeq 0$ so we can expect that there may exist some local stations where the instability is absolute. For the bending mode $m = 1$ we have a clear

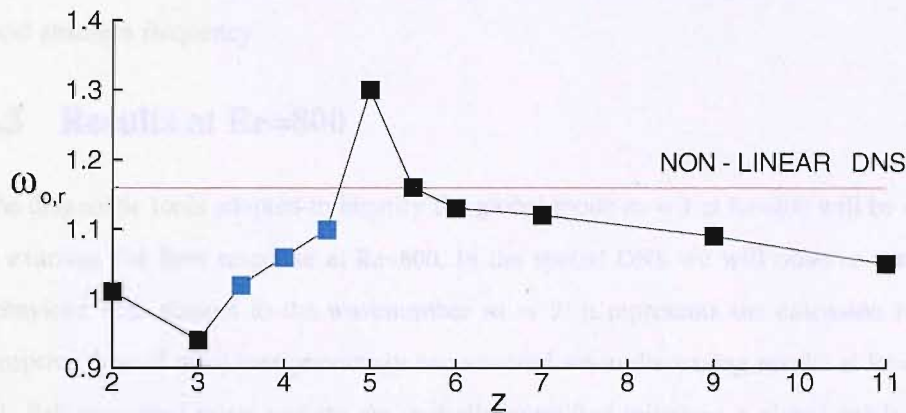


Figure 5.29: Streamwise evolution of the local absolute frequency $\omega_{0,r}$ of the helical mode $m = 1$ retrieved by LTS. Blue symbols are used for stations where the instability is convective. Black symbols where the instability is absolute. The horizontal red line represents the frequency measured in the spatial DNS.

absolute instability at ($z = 2$); then the instability becomes convective before recovering the absolute character at $z = 5$. A synthetic view of the overall behaviour for mode $m = 1$ is given in figure 5.29 where we display the streamwise evolution of the computed local absolute frequency. The blue symbols are adopted for the axial stations where the instability has been found convective, whereas the black ones identify local absolute instability. The horizontal red line corresponds to the frequency obtained in the spatial DNS; in the recirculating region, the flow is absolutely unstable but the local absolute frequency appears quite distant from the red horizontal line, and this suggests that the first vortex bubble doesn't play any role in the development of the global mode $m = 1$. This conclusion is consistent with the results of the spatial DNS, where the instability was seen to develop initially behind a front located downstream (see fig. 5.24). As suggested by Gallaire *et al.*, one possibility is that the absolutely unstable region is too small to be active, but any conclusion on this point has to be taken with some care, because of the strong non-parallelism of that region.

For $3 < z < 5$, that is between the first and the second bubble, the flow is seen to stabilise while a further transition from convective to absolute occurs for $4.5 < z < 5$. Absolutely unstable conditions are then preserved for all the other stations $z > 5$. The important result is that where this transition takes place, the local absolute frequency approaches the value of the global frequency measured in the spatial DNS. In other words, the current results show a good agreement with the steep front theory of Pier and Huerre [85]. The self-sustained global helical mode $m = 1$ is associated with the presence of a large region

of local absolute instability and is driven by a front which sends out waves beating at the local absolute frequency.

5.3 Results at Re=800

The diagnostic tools adopted to identify the global mode $m = 1$ at Re=400 will be now used to examine the flow response at Re=800. In the spatial DNS we will observe a surprising behaviour with respect to the wavenumber $m = 2$: it represents the extension to a more receptive flow of what was previously encountered when discussing results at Re=200, $S = 1.1$. Self-sustained wave packets are spatially amplified initiating a global mode which is essentially different from the global bending mode $m = 1$.

5.3.1 Evolution from a columnar vortex

The resolution adopted at $Re \geq 800$ is much higher compared to the lower Reynolds number cases. The number of grid points in the radial direction was nearly doubled while in the streamwise direction the grid increase was approximately of 20%. In the azimuthal direction the number of points was left unchanged but an increased resolution was obtained reducing the value of \bar{r} , the radial position from which the drop of azimuthal modes is applied in the FFT. The precise value for each numerical parameter is reported in table 5.4. The use of the Dual Time Stepping (DTS) method for the time advancement was necessary in order to overcome the difficulty of the CFL time step restriction, which otherwise would be too severe for the resolution adopted.

L_z	L_r	n_z	n_r	n_θ	b_r	\bar{r}	Δt	N_{sub}
20	10	320	170	64	1.3	0.1	0.02	38

Table 5.4: Numerical parameters used for spatial DNS at Re=800.

Three-dimensional direct numerical simulations of highly swirling flows are not many at this Reynolds number: Tromp and Beran [98, 99] have studied at Re=1000 the Batchelor vortex confined in an inviscid nozzle. The resolution reported in their work is of the same order as that used here. Recently Broadhurst [11] has extended the study of the Batchelor vortex to open domains. At Re=1000 his results show three-dimensional instabilities developing faster than vortex breakdown, that is the presence of axial shear in the velocity profile

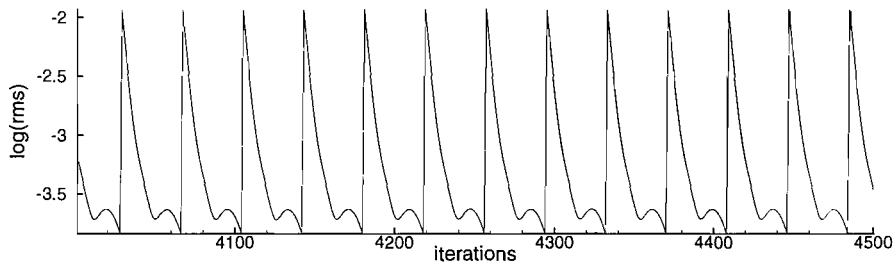


Figure 5.30: $Re=800$ $S = 0.95$ case. Convergence history within the Dual Time integration.

leads the flow to break into small scale turbulence. In the paper of Ruith *et al.* (2003), the maximum Reynolds number simulated is $Re=500$.

Using the DTS, the time step integration becomes an input parameter. For this specific case we chose $\Delta t = 0.02$ and the number of subiterations in the dual variable was fixed at $N_{sub} = 38$. This has guaranteed a reduction of the unsteady residual by almost two orders of magnitude (see fig. 5.30) during the iterative procedure in the dual variable. The result is assumed satisfactory, considering that in the corresponding axisymmetric calculations (obtained by marching explicitly in time) steadiness was reached with the same reduction of the residual.

Due to the increased computational cost, we couldn't perform a complete investigation in swirl number space, but we have focused on the $S = 0.95$ case. The value was chosen considering that according to our axisymmetric results, at this level of swirl simulations are expected to reveal the wave features of vortex breakdown, eventually modified by three-dimensional effects. This is an important point which has been generally underestimated in previous computational studies. Large eddy simulations of Muller and Kleiser [81], for example, are conducted at $Re=5000$. For this value, the wave propagation should be very well visible *if* the swirl employed is not too high. Conversely, by adopting a massive swirl the flow immediately stagnates near the inflow and helical disturbances grow so rapidly that they completely dominate the flow visualisation of the phenomenon.

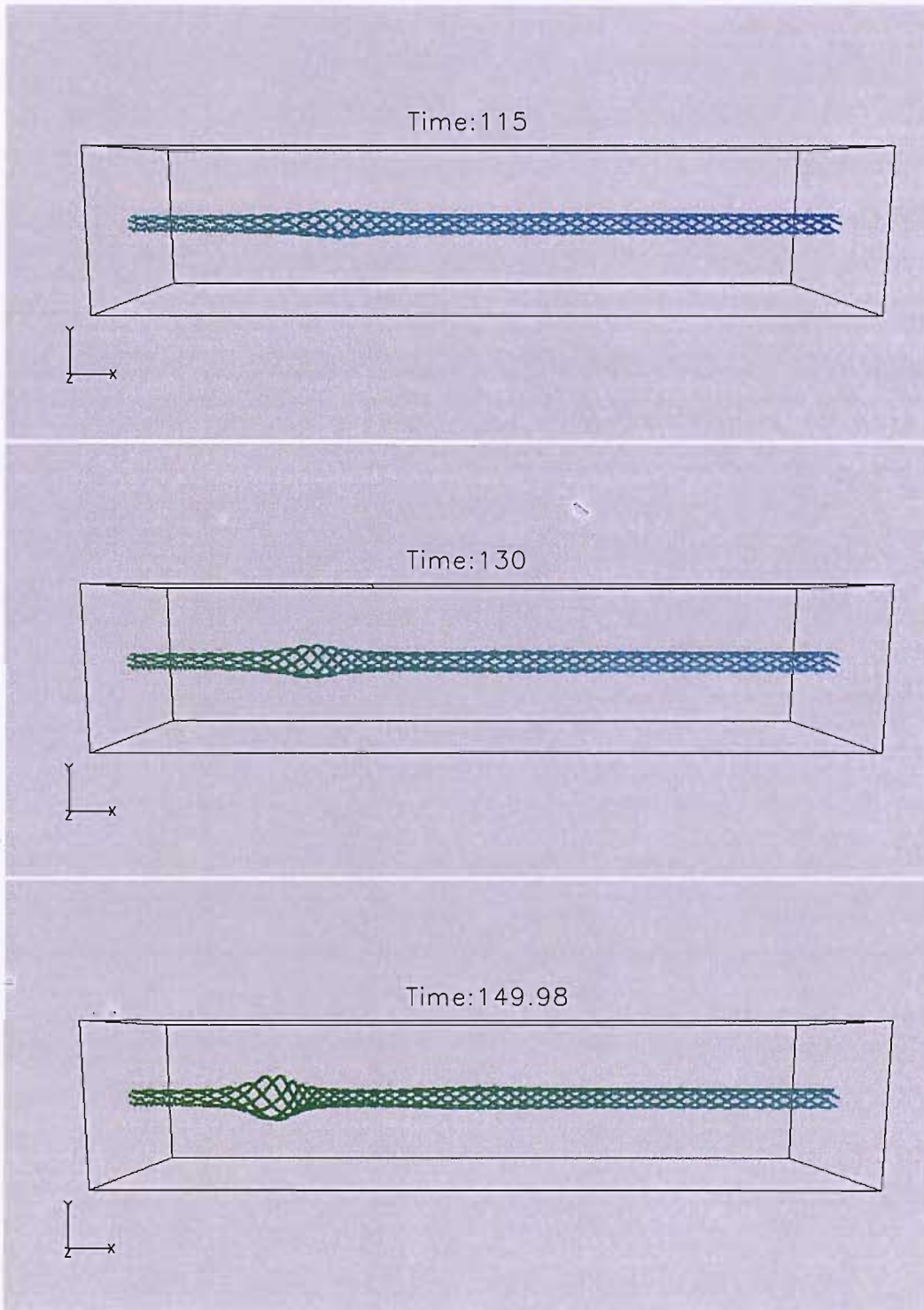
Figure 5.31 shows the temporal evolution of the streaklines. The figure is divided in three sequences highlighting the main points. Despite the higher Reynolds number employed, the flow remains axisymmetric during the breakdown process. From the first sequence a localised expansion of the vortex core accompanied by a large upstream excursion can be seen. According to Leibovich's theory [58, 59, 60] this is representative of the main features of vortex breakdown: an axisymmetric wave growing in amplitude and moving

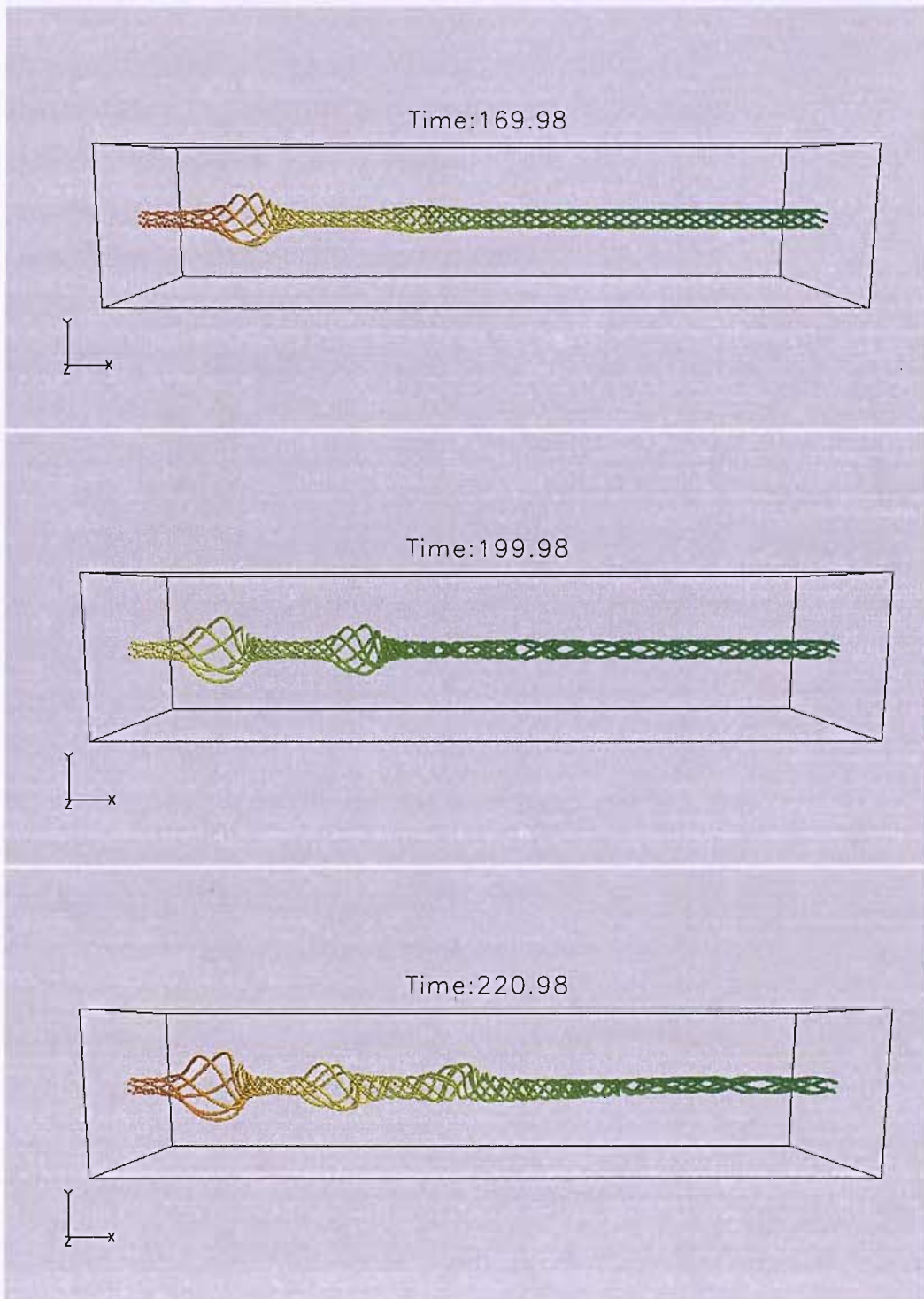
upstream. When the first bubble is formed (see the second sequence of fig. 5.31), the flow behind it undergoes an inward acceleration due to inertial effects, and, by continuity, the axial velocity increases, similarly to the $Re=400$ case discussed in the previous section. At this point a second wave starts growing and propagating upstream. The evidence that the second wave originates after the first one has reached a large amplitude, suggests that vortex breakdown in its basic nature is *not* multiple. The existence of more than a single recirculating region cannot be explained either in terms of the dispersion of Kelvin waves (cfr. §3.2.2) or considering Benjamin's conjecture [6] of a flow-force defect balanced by a wave train. It is more likely the consequence of the temporal evolution of the base flow which recovers in the rear of the bubble the same conditions existing ahead of it.

At Time=220, the streaklines begin to reveal three-dimensional instabilities located immediately behind the second vortex bubble. In the three-different probes considered to monitor the perturbation amplitude (see fig. 5.32), the behaviour is quite regular. The growth rate, however, is not perfectly uniform along the axis but is bigger at $z = 7.5$, closer to the second vortex bubble. It can also be noted a change in the slope of the curve relative to the bending mode at approximately Time=200. It is probably associated with the evolution of the base axisymmetric flow which is modifying its stability properties. The bending mode is linearly unstable while higher harmonics are excited at a later stage only by nonlinear effects. The measured growth rate for mode 1 at the axial station $z = 7.5$ is $\hat{\omega}_1 \simeq 2.9 \cdot 10^{-1}$ whereas that of mode 2 is $\hat{\omega}_2 \simeq 5.6 \cdot 10^{-1}$, thus the second harmonic grows as approximately the second power of the first one.

At Time=230 the flow field in the wake of the second bubble is fully perturbed by a helical structure with axial wavelength $\simeq 5$. According to the curves of fig. 5.32, the perturbation is now saturating, and although the energy level of higher harmonics is quite high, the dominant mode remains $m = 1$, as also revealed by the power spectral density of the registered azimuthal velocity component (fig. 5.33). The PSD has been computed over all the time interval simulated and it shows a dominant peak at $\omega = 1.19 (f = 0.18)$ corresponding to the angular frequency of mode 1.

It is worth noting the analogy with the $Re=400$ case: the second recirculating region delimits the upper border of the fully three-dimensional region. When the strong interaction with the helical waves takes place, the size of the second bubble is greatly reduced and a very interesting behaviour is highlighted in the last frame where it can be seen that the axial extent of the axisymmetric region is slightly increased. At this Reynolds number the





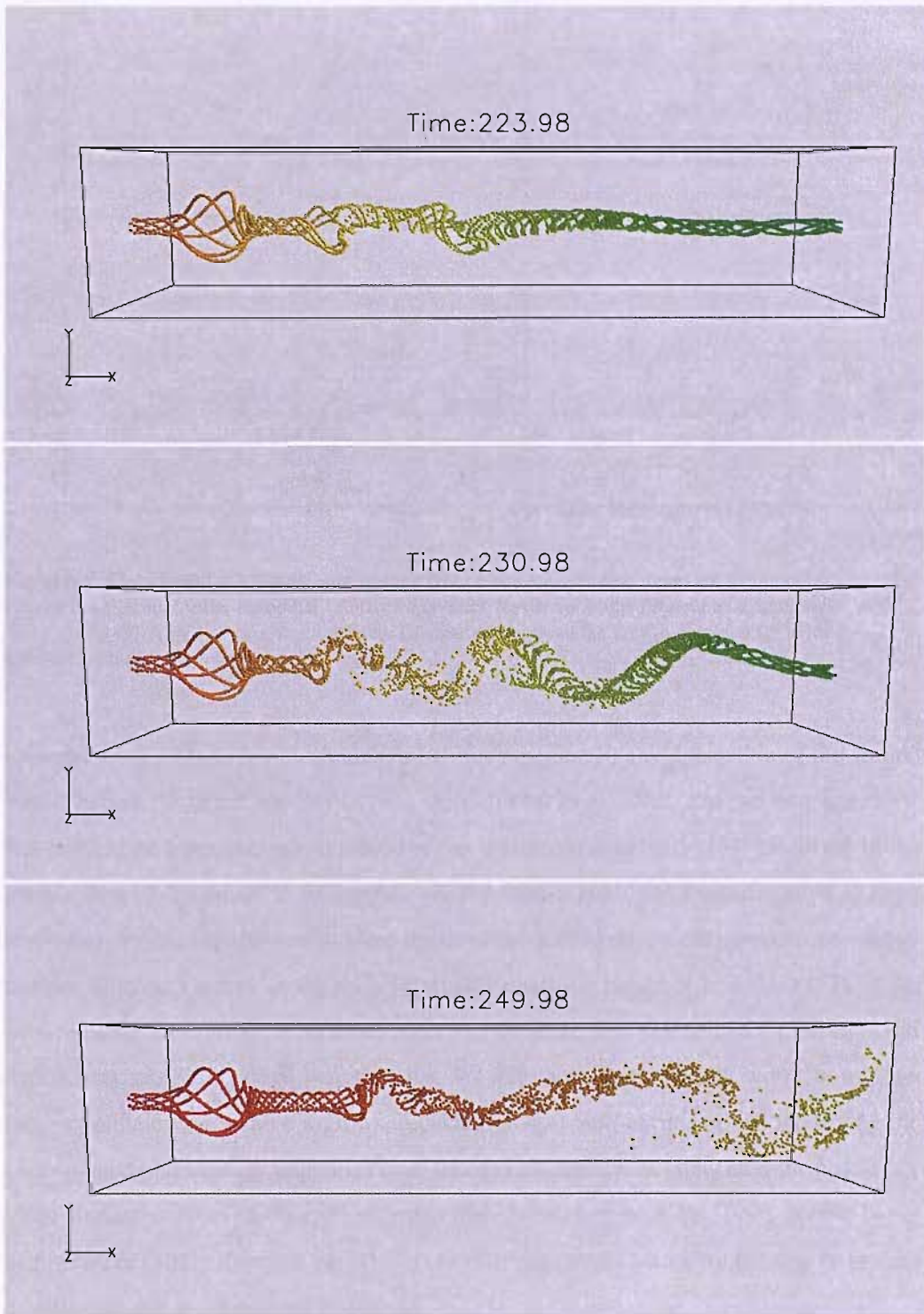


Figure 5.31: $Re=800$ $S = 0.95$ case starting from a columnar vortex. Formation of a double breakdown followed by helical instabilities.

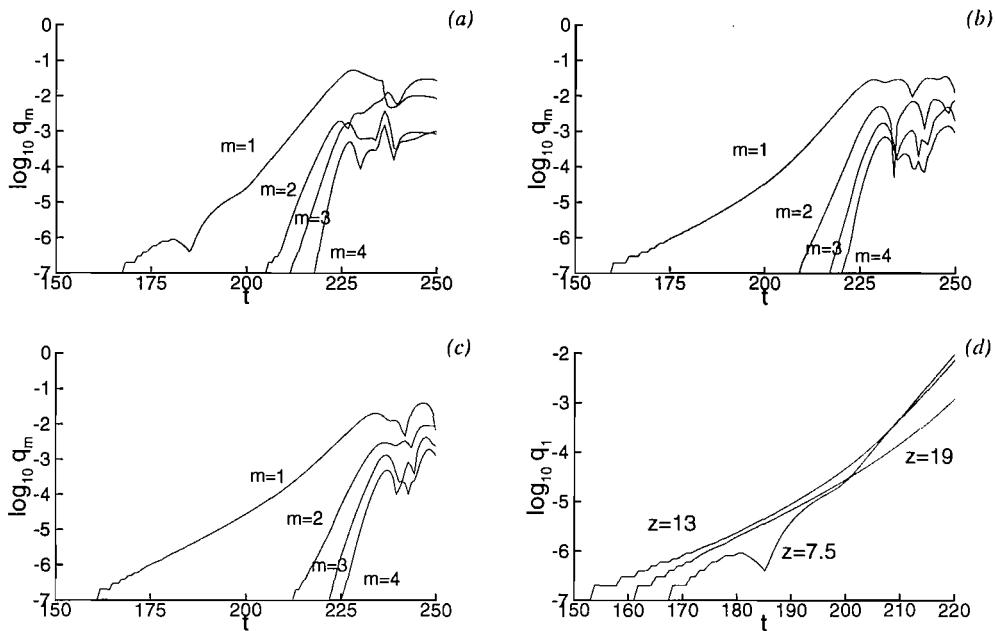


Figure 5.32: $Re=800$ $S = 0.95$ case starting from a columnar vortex. Temporal evolution of azimuthal Fourier coefficients for the azimuthal velocity component registered at the different axial stations ($r = 0.3$). (a): $z = 7.5$ (b): $z = 13$ (c): $z = 19$ and (d): Comparison between the growth observed for mode $m = 1$ at different axial stations.

corresponding axisymmetric calculation has not experienced any fluctuation of the second vortex bubble. It rather appears to be a three-dimensional effect, and we may speculate that it could be a possible consequence of the ‘positional instability’ [59] discussed in the introduction of this thesis. If we consider the breakdown bubble as a manifestation of finite amplitude waves, instabilities to three-dimensional perturbations can generate an energy transfer from such waves. In the inviscid, weakly nonlinear model of Leibovich [57], as the axisymmetric wave grows, it becomes faster and therefore able to penetrate the supercritical region, inaccessible to small perturbations. We have seen that viscosity works to trap the large amplitude wave where it grows, reducing its upstream excursion and modifying the corresponding bifurcation diagram. Three-dimensional instabilities may offer the possibility of an alternative form of dissipation; when their interaction with the vortex bubble is not negligible, as clearly shown in fig. 5.31 for the current case, the vortex bubble may be pushed downstream due to its reduced amplitude.

Now, the observation that following this downstream motion the flow seems to become less three-dimensional for some partial extent, may be a further indication of the existence of a front (the wave-maker) for the helical waves. This would be located in the proximity

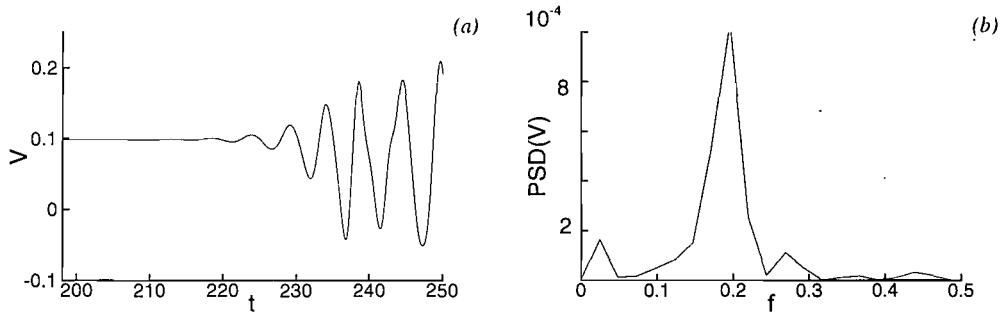


Figure 5.33: $Re=800$ $S = 0.95$ case starting from a columnar vortex. (a): Azimuthal velocity component registered at $z = 19$, $r = 0.3$, $\theta = 0$ and (b): Corresponding power spectrum density.

of the second bubble and sensitive to variations of the base flow caused by the interaction between vortex breakdown (axisymmetric) and helical instabilities (3D).

5.3.2 Evolution from the axisymmetric breakdown state

We now proceed to describe the three-dimensional response obtained by starting the 3D run from a steady axisymmetric solution. At $Re=200$ we didn't find any dependence on the initial conditions, whereas significant differences have been encountered for the current case.

Simulation restarts at $Time=360$, and the perturbation quickly contaminates the whole region behind the second vortex bubble (fig. 5.37). The streaklines reveal a different spatial structure: the axial wavelength is reduced, and the presence of a double helical structure is visible at $Time=425$. Note also the small downstream motion of the second vortex bubble, in accordance with what was described in previous subsection. The different character of the instability is better appreciated in fig. 5.34 which shows the azimuthal velocity component registered at the probe $z = 19$, $r = 0.3$, $\theta = 0$. The signal clearly reveals the development of more than one harmonic and the PSD presents two peaks corresponding to the angular frequencies $\omega = 1.44$ and $\omega = 2.38$.

Time evolution of different modes is reported in fig. 5.35. In the proximity of the second recirculating region ($z = 7.5$), the dominant mode is $m = 1$ but its growth widely deviates from a linear trend. Higher modes are characterised by a strong irregular behaviour. It can also be noted that a transition occurs at approximately $Time=410$ when modes 1 and 2 begin to saturate while modes 3 and 4 increase their rate. In the second axial station considered, $z = 19$, the behaviour is more regular and closer to be linear. Modes 1 and 2 grow with the same rate until saturation, while modes 3 and 4 show a clear transition, very likely

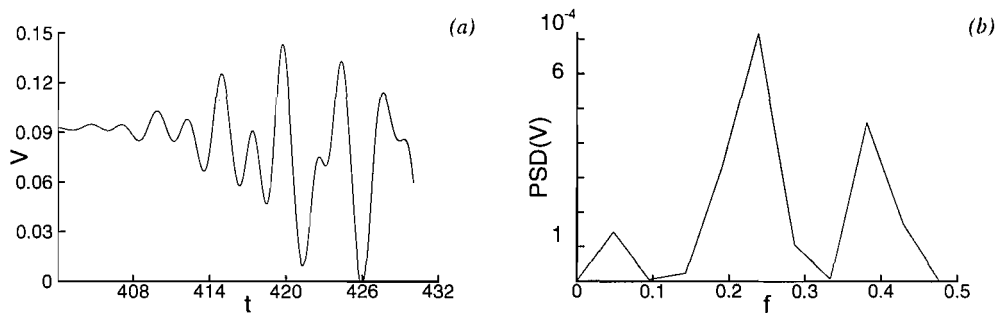


Figure 5.34: $Re=800$ $S = 0.95$ case starting from the axisymmetric converged solution at Time=360. (a): Azimuthal velocity component registered at $z = 19, r = 0.3, \theta = 0$ and (b): Corresponding power spectrum density.

associated with nonlinearity. Figure 5.36 displays on the same diagram the different evolutions of modes 1 and 2 along the axis. Regarding the bending mode, the instability seems to be initiated at $z = 7.5$ since the curves related to $z = 13$ and $z = 19$ show some delay. The comparison for mode 2 is more interesting: in this case the amplitude measured at $z = 7.5$ initially grows, then it temporarily settles on a constant value before growing again at Time=390. The amplitudes at $z = 13$ and $z = 19$ have a similar growth, but at $z = 13$ the curve seems to saturate first and on a smaller value. This represents an indication of convective instability for mode 2, and we believe that the behaviour reflected in fig. 5.35 is the result of a strong convective amplification of $m = 2$ which becomes gradually masked (due to nonlinearity) by the growth of the global mode $m = 1$. In other words, this context is characterised by the existence of the global mode $m = 1$ superimposed on wave packets with $m = 2$ which are convectively unstable.

A further indication of this is given in fig. 5.38-5.39 where the wave packets are better visualised by means of the radial velocity contours on a meridional plane (fig. 5.38), and on cross sectional planes (fig. 5.39). For clarity, the flow field related to the initial axisymmetric solution at Time=360 is also shown. This helps to identify the large amplitude axisymmetric waves in order to distinguish them from the helical instabilities. For the contour levels adopted, a first packet is visualised at Time=408 extending from the second vortex bubble up to $z \simeq 12$. In the wake, at approximately $z \simeq 18$, another perturbation is visible and seems to develop independently from the first. At Time=414, the first packet increases its amplitude and its spatial extent. Inspection of the cross sectional contours (see fig. 5.39) reveals that this is the bending mode, which, starting from the axial position where it has originated, is rapidly perturbing the whole domain behind the vortex bubbles.

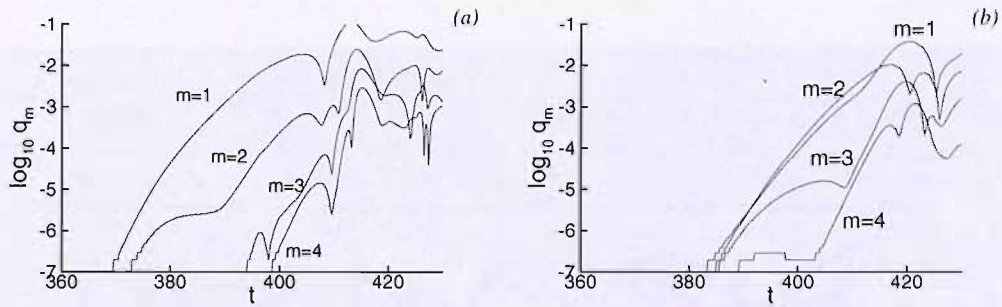


Figure 5.35: $Re=800$ $S = 0.95$ case starting from the axisymmetric converged solution at Time=360. Temporal evolution of azimuthal Fourier coefficients for the velocity component V_θ at (a): $z = 7.5, r = 0.3$ and (b): $z = 19, r = 0.3$.

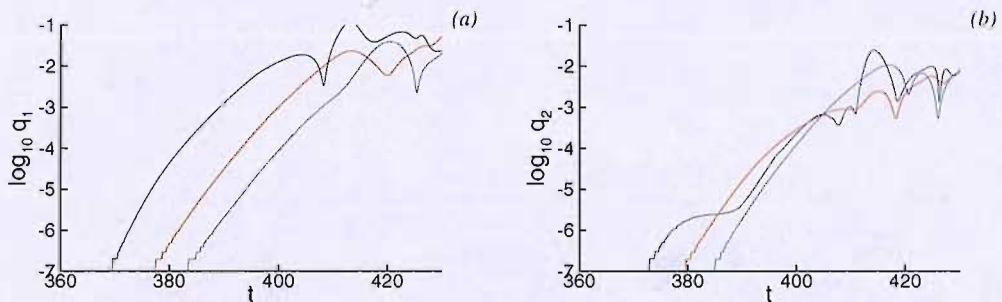


Figure 5.36: $Re=800$ $S = 0.95$ case starting from the axisymmetric converged solution at Time=360. Temporal evolution of the first (a) and second (b) azimuthal Fourier coefficients for the velocity component V_θ measured at different axial positions: $z = 7.5$ (black), $z = 13$ (red), $z = 19$ (blue).

Before this contamination has fully completed, the region close to the outflow (see the sectional iso-contours at $z = 19$) shows the presence of mode 2, thus the flow field at Time=414 is characterised by an incipient global mode $m = 1$ coexisting with the mode $m = 2$. The radial velocity contours highlight very well the difference of their nature: the former grows locally and spreads downstream (a manifestation of absolute instability), on the other hand $m = 2$ is convectively amplified (refer again to the spatial amplification provided by fig. 5.36-b), and consequently it appears visible in fig. 5.38 only close to the outflow boundary.

The question which now arises is whether or not mode 2 is self-sustained. Indeed, one possibility that we cannot *a priori* exclude is that this result is nothing else than a transient associated with the advection of the disturbance initially introduced. Running the calculation for longer would be pointless for this purpose, since the dynamics becomes rapidly dominated by the global bending mode. The easiest way to solve the problem is

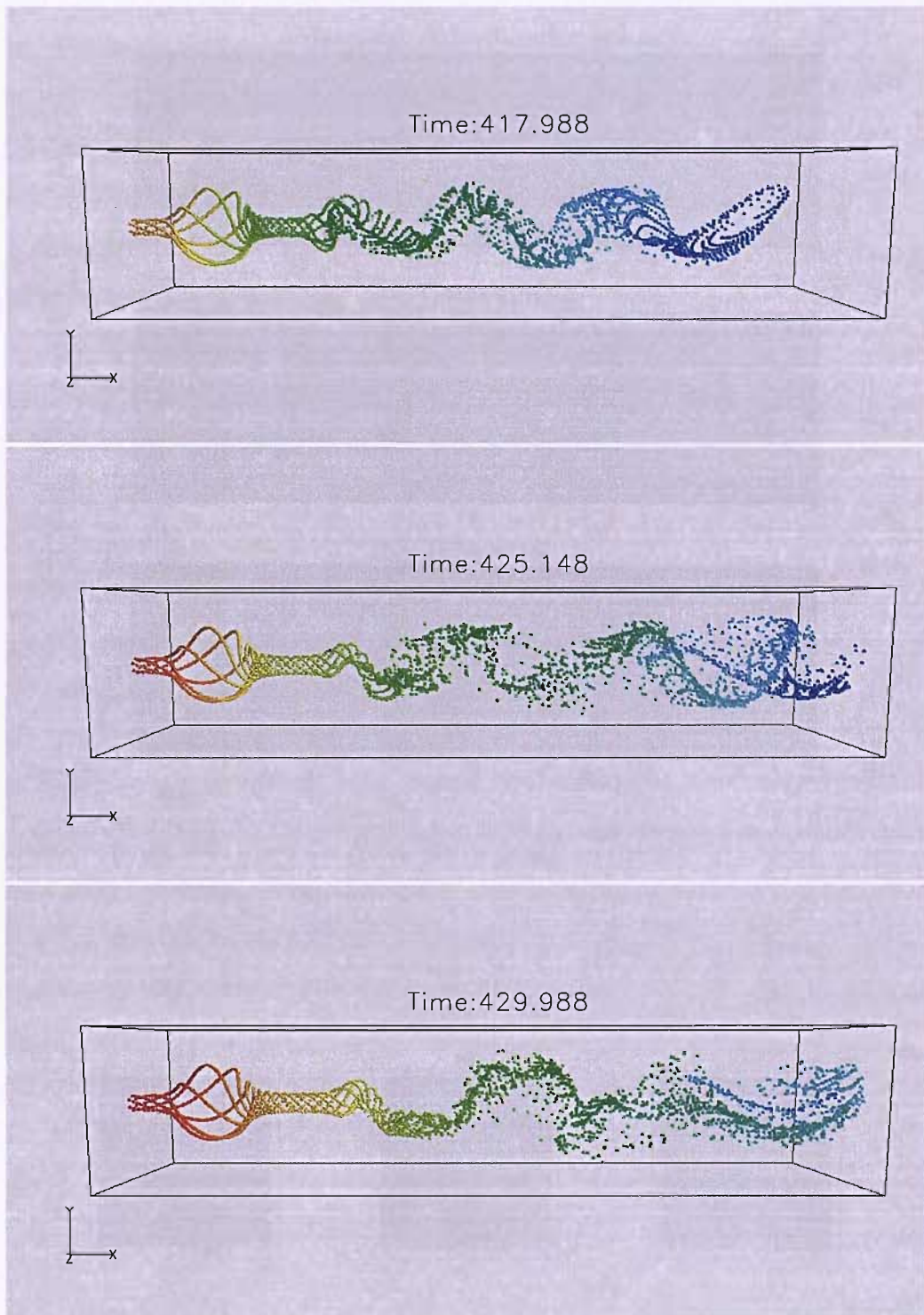


Figure 5.37: $Re=800$ $S = 0.95$ case starting from the axisymmetric converged solution.

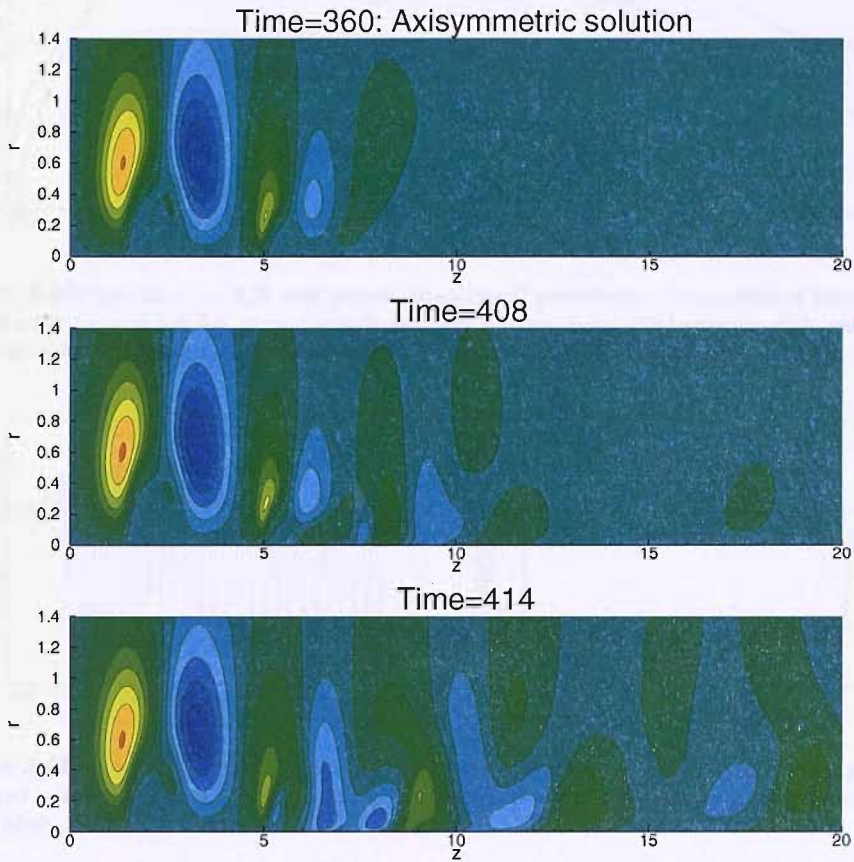


Figure 5.38: $Re=800$ $S = 0.95$ case starting from the axisymmetric converged solution. Radial velocity contours on the meridional plane $\theta = 0$. Contour levels in the range $[-0.13;0.27]$.

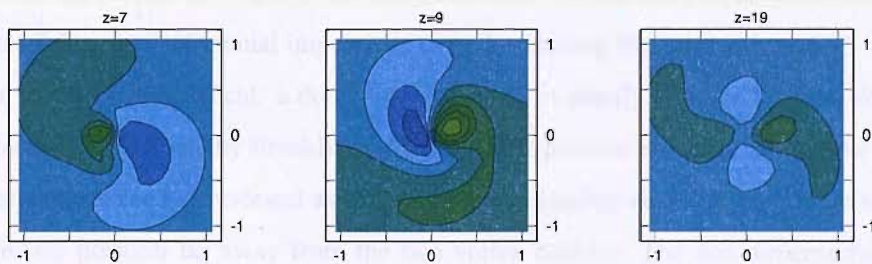


Figure 5.39: $Re=800$ $S = 0.95$ case starting from the axisymmetric converged solution. Time=414. Radial velocity contours on cross-sectional planes at different axial stations z .

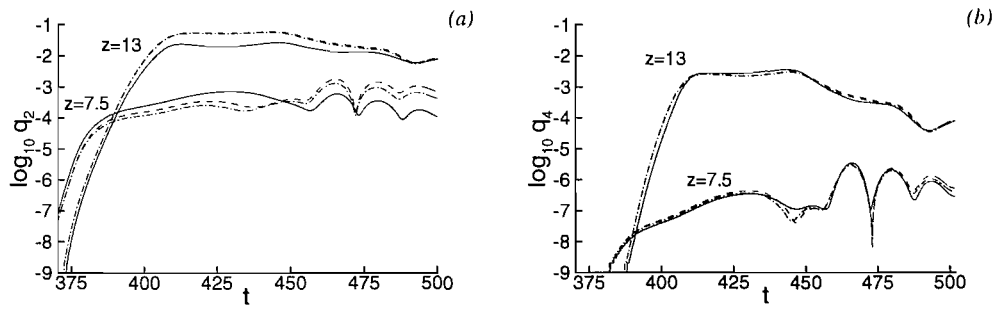


Figure 5.40: $Re=800$ $S = 0.95$ case excited by an “even” perturbation. Comparison of temporal growth of modes (a): $m = 2$ and (b): $m = 4$ at different axial stations. Solid: axial velocity; dash: radial velocity; dash-dots: azimuthal velocity.

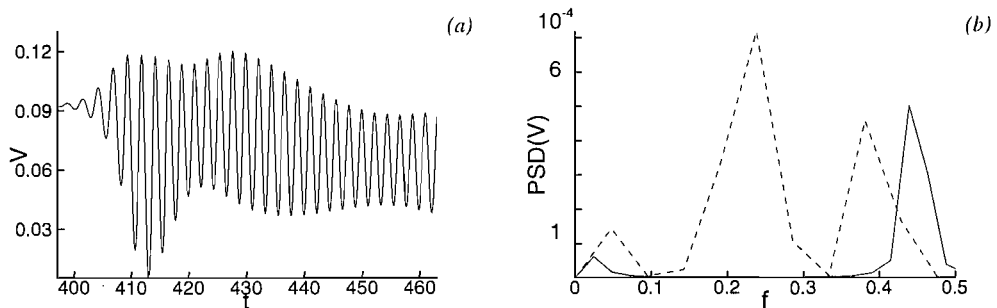


Figure 5.41: $Re=800$ $S = 0.95$ case excited by an “even” perturbation. (a): Azimuthal velocity component registered at $z = 19, r = 0.3, \theta=0$. (b): Corresponding power spectrum density (solid) and replication of fig. 5.34-b (dash).

to repeat the calculation perturbing the initial axisymmetric breakdown state by an “even” perturbation. Thus, as the calculation goes on, all the odd modes remain zero: the global bending mode is therefore suppressed and the instability of the even harmonics cannot be disguised by nonlinear effects. Since no external forcing is applied, if mode 2 is not self-sustained it has to relax to zero after the disturbance has left the computational domain. The outcome of this run is of crucial importance to understanding the nature of mode 2.

The result is unequivocal: a double-helical mode is clearly identified by the vorticity iso-surfaces (fig. 5.42) and by streaklines (fig. 5.43). The peculiar structure of multiple breakdown remains perfectly preserved as the three-dimensionality develops on a large scale at a streamwise position far away from the two vortex bubbles. The non-dimensional time simulated is $\Delta t = 152$, enough to guarantee that the response cannot be a transient effect. Conversely, a periodic quasi-steady state is left (see fig. 5.41), synchronized at the natural frequency $f = 0.44$ ($\omega = 2.76$). The value is slightly greater than what we have found for

$m = 2$ exciting all the modes, suggesting that the previous result was actually the competition of two self-sustained global modes. The first one develops downstream of a certain axial position (the wave-maker), and following the scenario depicted by Pier and Huerre [85] is associated with the presence of absolute instability. It is the same global mode which dominated the response at $Re=200$ and $Re=400$. The double-helical mode $m = 2$ is clearly of different nature: the growth measured locally (see 5.40) shows distinctly a spatial amplification representative of convective instability. What is important to notice is that although the large scale periodicity observed at $Re=200$, $S = 1.1$ is here absent, a certain level of irregularity is detected in fig 5.41. We therefore believe that the current case results from the same discussed mechanism associated with the presence of the recirculating region.

5.3.3 Wave packet analysis

To corroborate the conclusions developed in previous subsection, we show here the results of the wave packet analysis. We want to examine whether the differences revealed in the development of the two global modes $m = 1, 2$, are reflected in a local analysis. In particular, the spatial amplification exhibited by $m = 2$ is expected to correspond to a local convective instability, whereas the bending mode $m = 1$ should be a manifestation of absolute instability, as for the analogous case studied at $Re=400$.

The absolute growth was calculated according to the procedure discussed in §5.2.2. Results are reported in fig. 5.44 and confirm that the azimuthal wavenumber $m = 1$ is more susceptible to absolute instability. In the present case, we found that when $m = 1$ is unstable, the instability is always of absolute nature. In the spatial DNS, the global bending mode develops behind the axial station where the second smaller bubble is located. This has been observed considering both the evolution from the axisymmetric breakdown state or from the columnar vortex. The local analysis predicts that between the two bubbles, at $z = 4$, mode $m = 1$ is fully stabilised. There is no doubt that this local stabilisation, developing in the wake of the bubble, is reflected in the DNS, and is the reason why the helical instabilities are initiated outside of the first vortex bubble. We point out that at $Re=400$ the behaviour has been observed to be similar, but mode $m = 1$ was never found to be completely stable. This means that a more intense breakdown may effectively induce a stronger stabilisation. Mode $m = 1$ becomes again absolutely unstable at $z = 5$, and preserves this character in the wake. As expected, the streamwise evolution of mode $m = 2$ is different. It exhibits absolute instability only within the two recirculating regions. For $z > 6$, it remains always

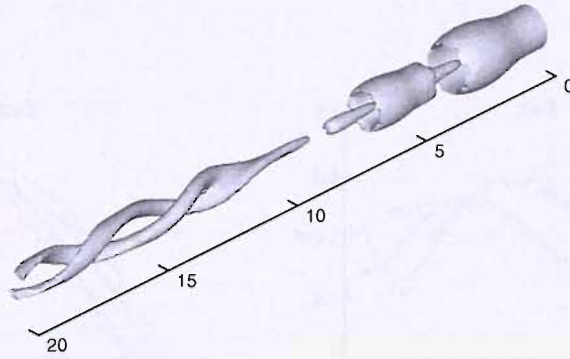


Figure 5.42: $Re=800$ $S = 0.95$ case excited by an “even” perturbation. Iso-surface of vorticity magnitude. $|\xi| = 2.18$.

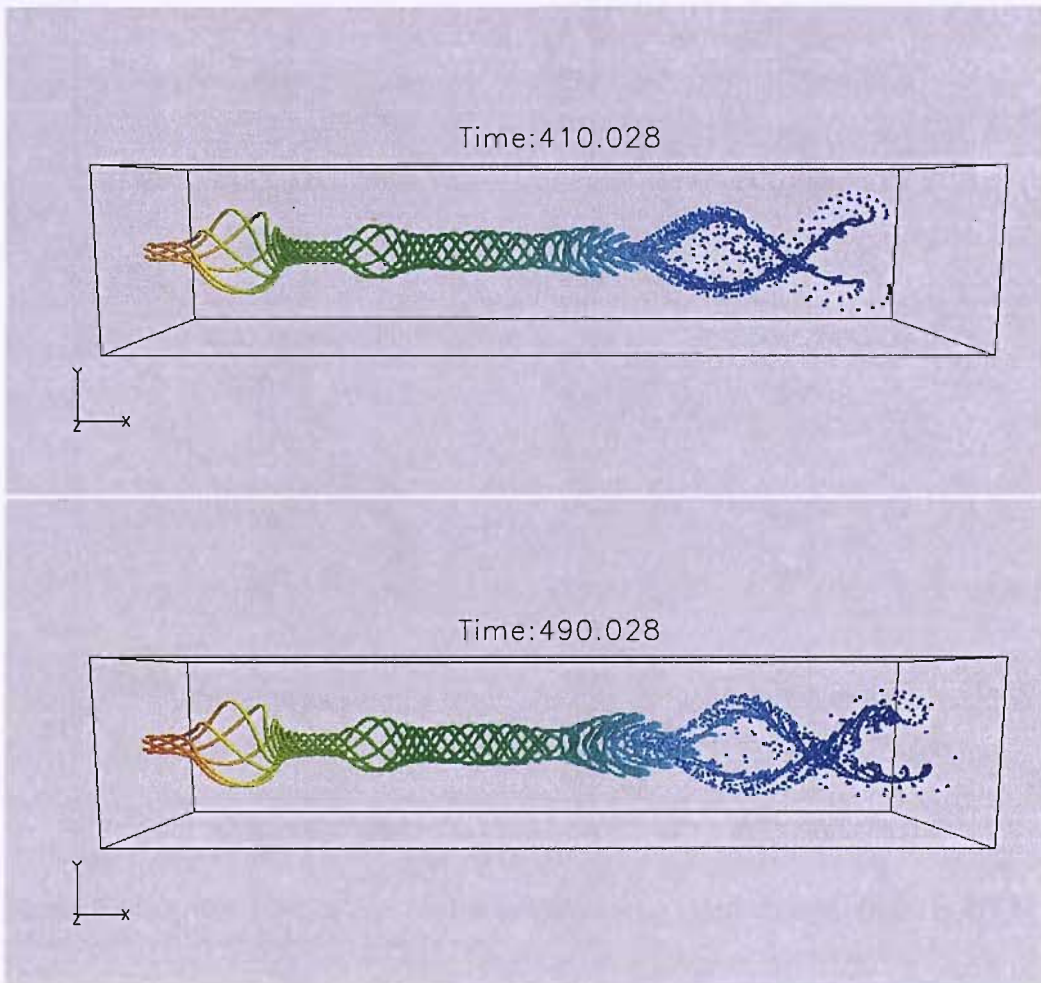


Figure 5.43: $Re=800$ $S = 0.95$ case excited by an “even” perturbation. The multiple breakdown configuration remains preserved.

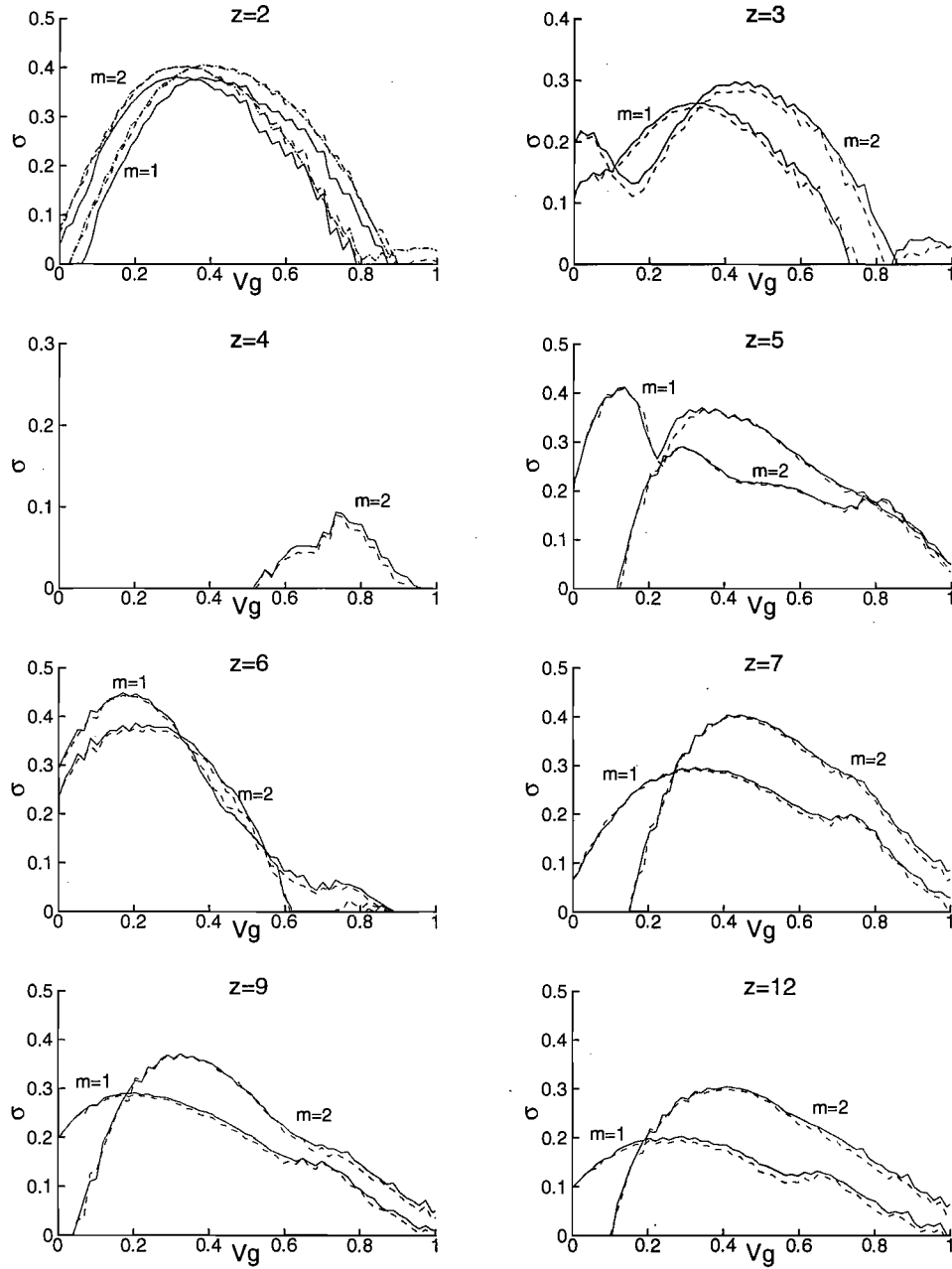


Figure 5.44: $Re=800$ $S = 0.95$ case. Absolute growth rate $\sigma(V_g)$ of helical modes retrieved by LTS for velocity profiles extracted at different axial stations z .

convectively unstable, a result confirming that the two global mode $m = 1, 2$ revealed in the spatial DNS, are of different nature.

5.4 Higher wavenumber structures

Before proceeding, it appears convenient to summarise the main points of the present discussion. In agreement with most of the existing studies, we have found that vortex breakdown is characterised by a self-sustained dominant mode with azimuthal wavenumber $m = 1$. However, double-helical structures may also be present; these may eventually be enhanced by nonlinear interactions, but their identification based on streakline visualisation (as done in physical experiments) becomes generally problematic as they are overwhelmed by the more unstable bending mode.

If the disturbance is *ad hoc* introduced, but not exciting $m = 1$, double-helical breakdown can be clearly revealed, as testified by the cases ($\text{Re}=200$, $S = 1.5$) and ($\text{Re}=800$, $S = 0.95$). The two cited examples are representative of two distinct global modes. In the former one, low Reynolds high swirl, the unsteadiness concerns the overall wake, following the analog behaviour of the bending mode $m = 1$. The latter case, conversely, is representative of a self-sustained convective amplification developing in the wake.

It is of interest now to examine the possibility of activating self-sustained higher modes, increasing one (or both) the control parameters. The study is relevant to the present investigation since our initial purpose was to establish to what extent results of local analysis can be manifested for this class of spatially developing flow. The study of Loiseleux *et al.* [67] and that of Gallaire *et al.* [29], performed on parallel flows, show that a further increase of the swirl leads to absolute instability of higher modes.

The question has been investigated adopting the usual procedure: introducing high order disturbances. The DNS presented so far has been obtained with an azimuthal discretisation $n_\theta = 64$. Since n_θ is a multiple of 4, we can introduce an initial noise obtained by quadrupling a random signal. The corresponding spectrum has non-zero modes only for $m = 4k$ with $k = 0 \dots 8$. Hereafter such a perturbation will be labelled “m4” perturbation, to distinguish it from the “even” perturbation introduced earlier. Following this procedure, we have found that a further increase of the swirl number does not activate the global mode $m = 4$. At $\text{Re}=200$, the flow field has been observed to remain perfectly axisymmetric up to a swirl level $S = 1.9$. An analogous operation was performed keeping constant the swirl

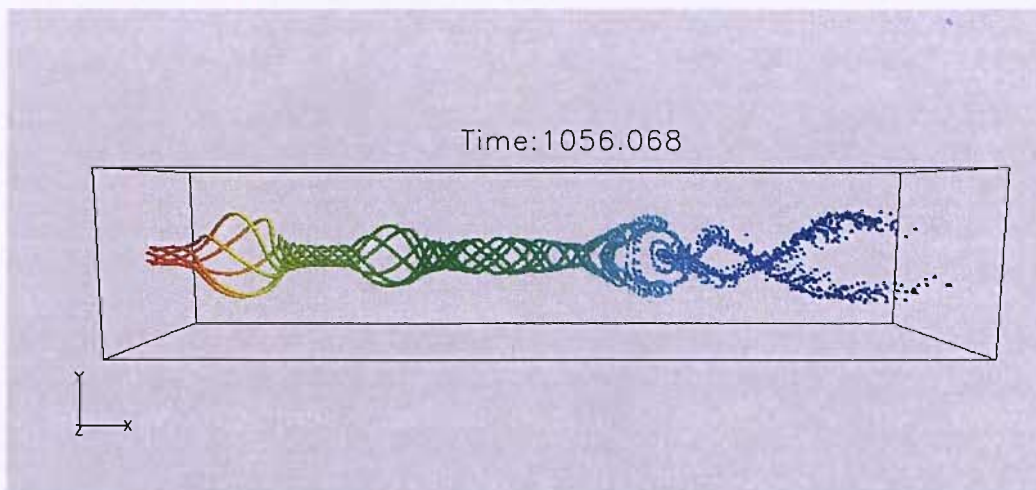


Figure 5.45: $Re=1200$ $S = 0.95$ case excited by an “even” perturbation.

and increasing the Reynolds number. At $S = 0.95$, we moved up to $Re=1600$: if the initial disturbance is an “even” perturbation, the behaviour obtained resembles what was discussed at $Re=800$. Double-helical wave packets saturate in the wake after a spatial amplification. For example, figure 5.45 refers to the $Re=1200$ case and shows a snapshot of the streaklines at $Time=1056$ (restart from the axisymmetric solution is at $Time=900$). Conversely, if the initial disturbance is given by a “m4” perturbation, the solution remains helically stable. At $Re=1600$, we also increased the amplitude of the initial disturbance, but the perturbation was seen to leave the computational domain. Figure 5.46 shows the temporal evolution of mode $m = 4$ measured at different axial stations. The amplification of the disturbance is evident, because the flow is actually highly unstable, but the global mode does not develop. In a final attempt, we performed a calculation increasing both the swirl and the Reynolds number. The set of parameters was chosen as $Re=1600$, $S = 1.4$. Under these conditions, the flow field reveals three big vortex bubbles (see fig. 5.48). Some unsteadiness is observed and correlated to the second and third bubble which are periodically “emptied” at their downstream end. Beside this feature, which is mainly axisymmetric, in the region close to the outlet structures revealing the existence of a mode $m = 4$ can be identified by the vorticity isosurfaces (fig. 5.47). These structures are very irregular, and for large transient they are damped before reappearing again. The large degree of irregularity may be a consequence of the axisymmetric unsteadiness, but the observation that those modes develop far away from the recirculating regions suggest they are of convective nature.

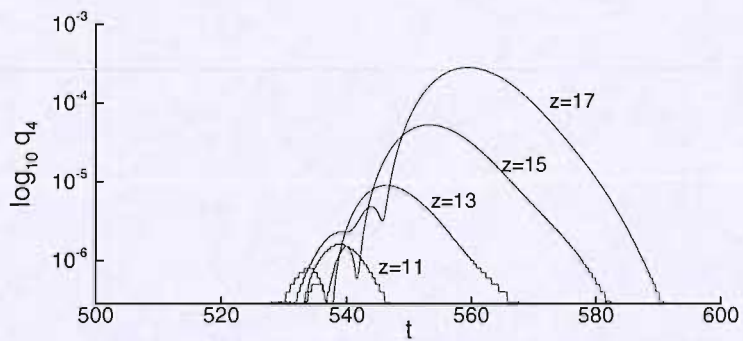


Figure 5.46: $Re=1600$ $S = 0.95$ excited by a “m4” perturbation. Temporal evolution of mode $m = 4$ at different axial stations.

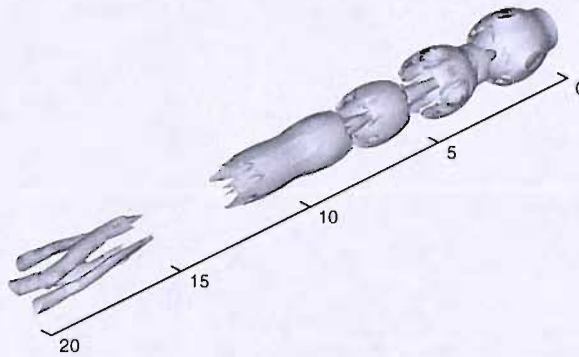


Figure 5.47: $Re=1600$ $S = 1.4$ case excited by a “m4” perturbation. Iso-surface of vorticity magnitude. $|\xi| = 3.12$.

5.5 Vortex breakdown in a restricted pipe

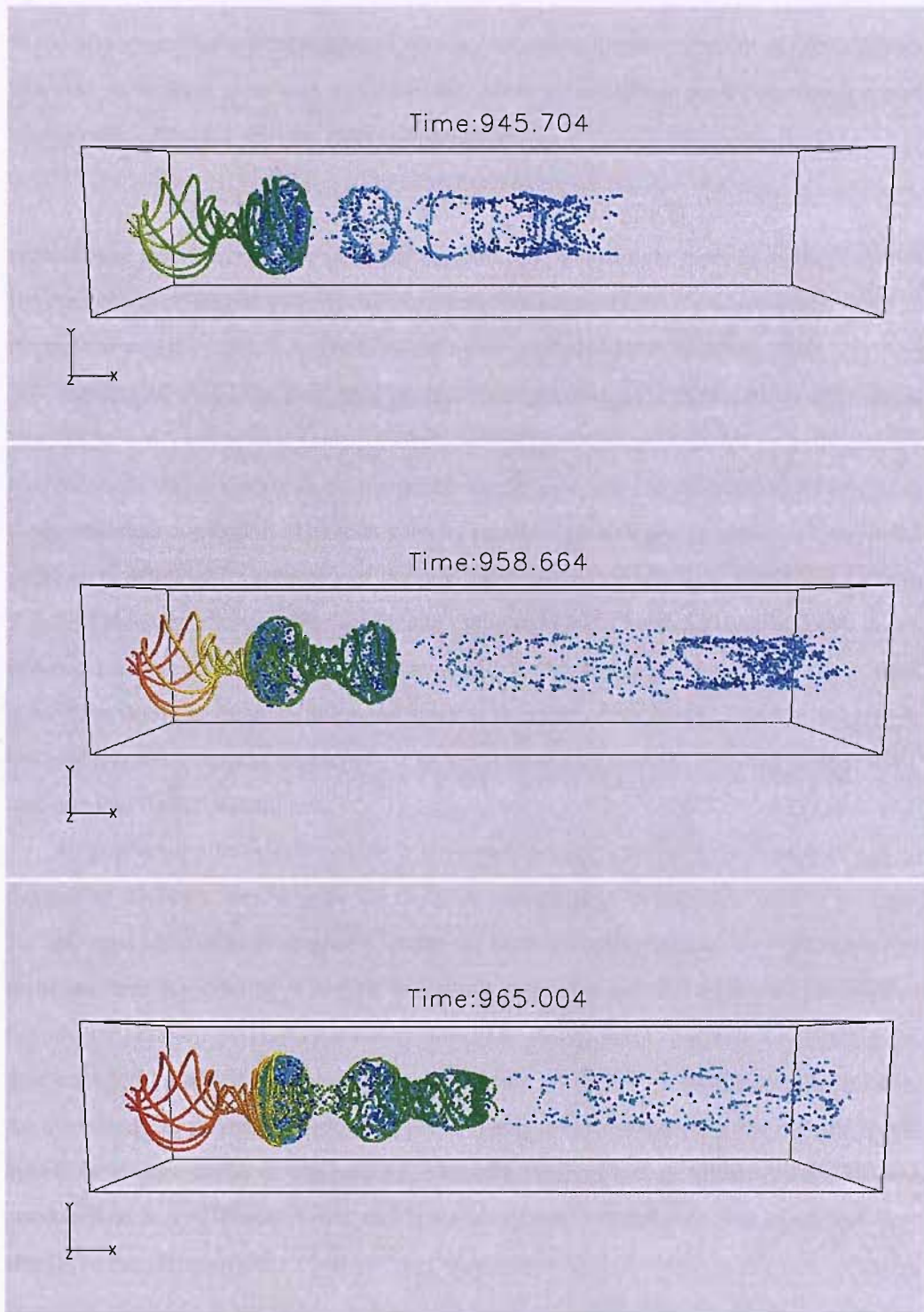


Figure 5.48: $Re=1600$ $S = 1.4$ case excited by an “ $m=4$ ” perturbation.

5.5 Vortex breakdown in a constricted pipe

In the present section we present some results concerning the development of vortex breakdown in an inviscid pipe with a contraction. More precisely, we have considered a pipe whose radius R varies with the axial coordinate as:

$$R(z) = \begin{cases} R_0[1 - \beta(1 - \cos(2\pi z/L_1))] & 0 \leq z \leq L_1 \\ R_0 & L_1 \leq z \leq L, \end{cases} \quad (5.5)$$

representing a convergent-divergent nozzle followed by a straight pipe. L_1 is the length of the convergent-divergent part, whose contraction is measured by β ($\beta = 0$ corresponds to the case of straight pipe). L is length of the whole pipe, and R_0 is the inlet radius.

Figure 5.49 shows the flow field of the converged axisymmetric solutions obtained at $Re=200$, $M = 0.5$ and several values of swirl. Streamlines are superimposed on axial velocity contour maps which clearly show the initial acceleration and the subsequent decay due to the geometrical constraints. The inlet velocity profile is given by (4.1) with $\alpha = 1$, while the parameters defining the geometry of the pipe are $L = 20$, $L_1 = 10$, $R_0 = 5$ and $\beta = 2$. Up to $S = 0.77$ the streamlines appear essentially cylindrical but a localised axial velocity decay is present outside the constriction; consistent with the analysis carried out in chapter 4, even if the flow does not stagnate, the breakdown is in some sense already existing, but due to the low Reynolds number employed, it is manifested as a trapped localised perturbation, undetectable by the streamlines.

At $S = 0.8$ the flow field reveals a large recirculating region in the divergent part of the nozzle. Thus the critical point for the flow to stagnate is in the range $0.77 < S < 0.8$. For the open jet studied in chapter 4, under the same set of parameters the critical level of swirl has been found to be $S = 0.89$: this result highlights how the additional presence of the adverse pressure gradient renders the flow more susceptible to stagnate. Conversely, the inlet contraction, which ensures a favorable pressure gradient and a positive contribution to the azimuthal component of vorticity, appears to reduce the upstream excursion of the vortex bubble (it may be useful to compare fig. 5.49 with those of 4.7). A further calculation was conducted at $S = 0.89$ and $\beta = 0$, that is for an entirely straight pipe. The result was very similar to the corresponding open jet case, demonstrating that replacing the non-reflective boundary condition at the radial outflow with an inviscid wall does not produce significant modifications.

Figure 5.50 shows the three-dimensional evolution computed at $S = 0.8$ and $S = 0.85$. Self-sustained global modes with azimuthal wavenumbers $m = 1, 2$ develop and interact

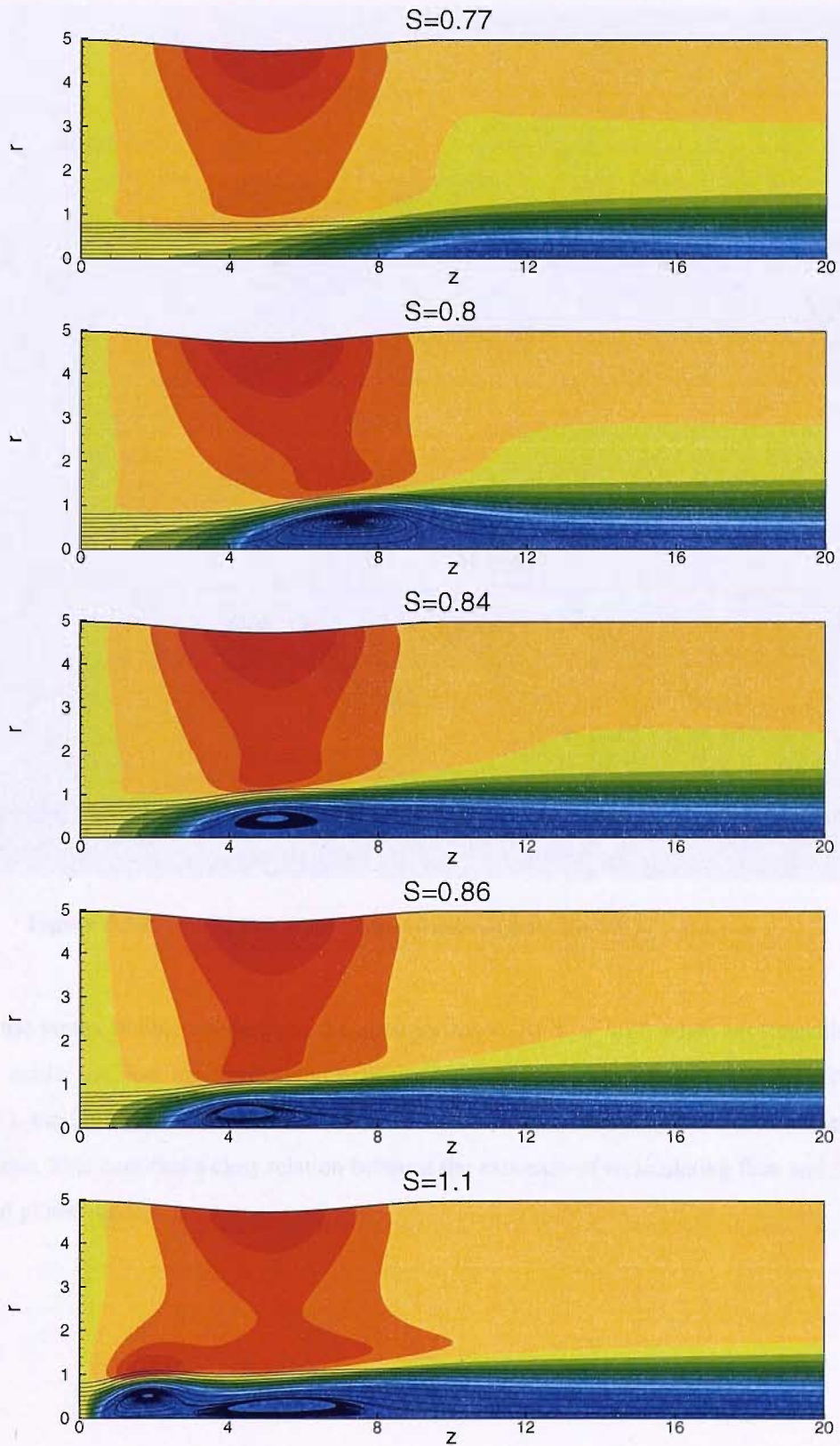


Figure 5.49: Swirling flow in pipe: steady axisymmetric solutions obtained at different swirl numbers. $Re=200$, $M = 0.5$, $\alpha = 1$.

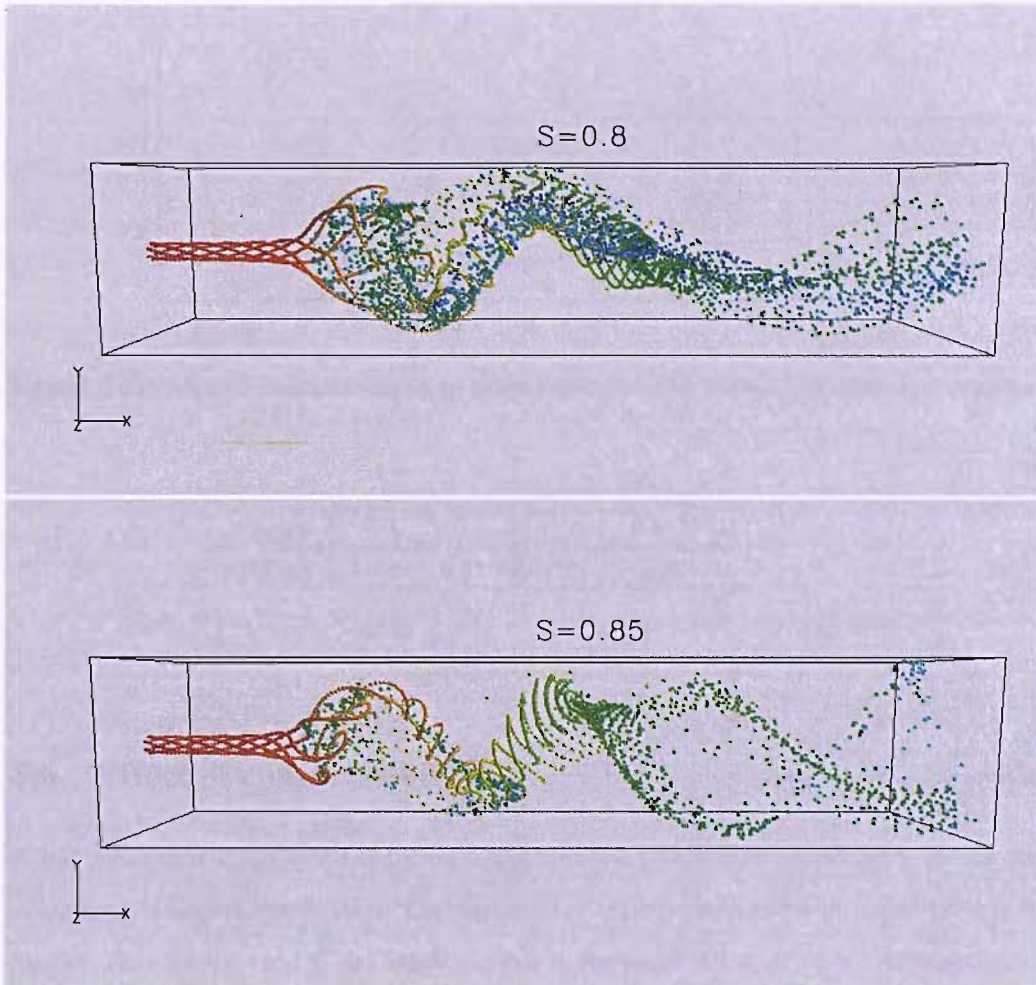


Figure 5.50: Swirling flow in pipe: Saturated unstable states. $Re=200$ $M = 0.5$, $\alpha = 1$.

with the vortex bubble similarly to the open jet cases. At $S = 0.77$, when no stagnation point exists, the flow has been found helically stable. Thus, as for the open jet case (cfr. §5.3.1), the limit point S_1 and that associated with the loss of stability to 3D disturbances are close. This confirms a clear relation between the existence of recirculating flow and the helical global modes.

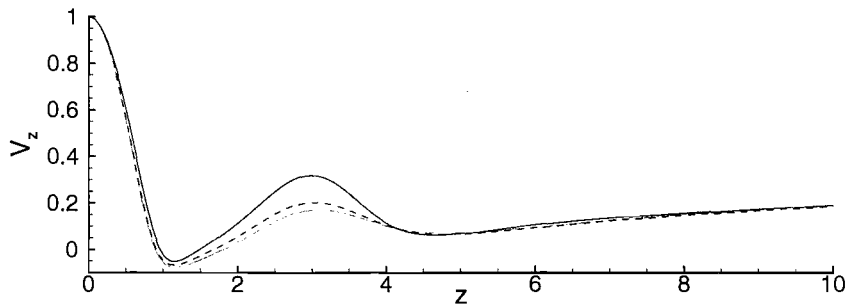


Figure 5.51: Effect of compressibility on the axisymmetric vortex breakdown. Centerline axial velocity at $M = 0.3$ (solid), $M = 0.6$ (dash-dotted) and $M = 0.7$ (dotted). $Re=200$, $S=1.1$.

M	0.3	0.4	0.5	0.6	0.7
$\hat{\omega}_1$	0.059	0.051	0.039	0.028	0.014

Table 5.5: Linear growth rate of mode $m = 1$ measured for different Mach numbers.

5.6 Effect of compressibility

A last parametric study was conducted to evaluate the effect of compressibility on the development of helical instabilities. The analysis has been performed on the open jet case at $Re=200$, $S = 1.1$ by varying the Mach number in the range $0.3 \leq M \leq 0.7$. Computations with Mach numbers outside this range become problematic for the compressible code used here, due to the absence of both low Mach preconditioning and filtering techniques for the treatment of shock waves.

Among the previous studies, the effect of compressibility has been investigated by Khorrani [49] in the parallel context, and by Herrada *et al.* [41] for the axisymmetric vortex breakdown in pipes. According to these results, compressibility reduces the value of the critical point S_1 [41] and enlarges the stability region of a parallel swirling jet [49].

In our analysis, in order to distinguish between three-dimensional and purely axisymmetric effects, we preferred to compute the 3D evolution starting from converged axisymmetric solutions. Results discussed in previous sections (cfr. §5.1.3) have demonstrated that, at the low Reynolds number employed here, the growth rates of unstable helical modes do not depend on the initial condition adopted.

The steady solutions corresponding to the axisymmetric cases reveal a very small sensitivity to the Mach number, with the flow field preserving a very similar spatial structure.

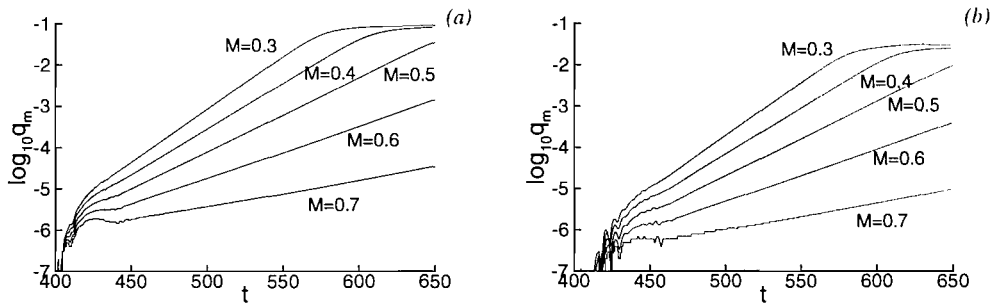


Figure 5.52: Effect of compressibility on the development of helical instabilities. Temporal evolution of mode $m = 1$ at different axial positions. (a): $z = 4, r = 0.3$. (b): $z = 16, r = 0.3$. $Re=200$ $S = 1.1$.

Figure 5.51 shows the centerline axial velocity obtained at $M = 0.3$, $M = 0.6$ and $M = 0.7$ (streamlines are not reported since they do not allow us to detect any difference). The compressibility has therefore a negligible effect on vortex breakdown, although it slightly reduces the acceleration in the wake of the vortex bubble. This observation renders more interesting the comparison made on the 3D calculations, since any difference can be attributed with more confidence to a pure effect of compressibility, and not associated with a structural change in the base flow. The three-dimensional DNS reveal a clear damping effect on the growth of helical instabilities. Figure 5.53 shows the time history of the first harmonic for the axial velocity component (all simulations restart at Time=400). In order to stress the global character of the instability the temporal evolution of mode $m = 1$ has been monitored at two distinct positions, namely $z = 5$ and $z = 16$. The growth rates have been found to be equal at both the stations, and their values are reported in table 5.5. The maximum growth rate, obtained at $M = 0.3$, is $\hat{\omega}_1 = 5.9 \cdot 10^{-2}$. The result is consistent with the value predicted by Ruith *et al.* [88] who have found, for the incompressible case, $\hat{\omega}_1 = 6.63 \cdot 10^{-2}$.

Conclusions

A DNS code in cylindrical coordinates has been developed to carry out a comprehensive theoretical and numerical study of vortex breakdown and instability of swirling flow. Our computations have revealed the main features of the phenomenon, *i.e.* large amplitude axisymmetric waves and instability to small helical perturbations. A linearised version LTS of the code has allowed the discussion of the elements in relation to the general dynamics of swirling flows. The main achievements are summarised as follows:

- The formation of a large region of recirculating flow (the vortex bubble) is seen to be related to the ability of a vortex core to sustain axisymmetric waves generated by a localised perturbation. These are inertial waves, whose propagation has been explained analysing the response of the perturbed Rankine vortex and in terms of vorticity considerations (cfr. §3.3). In synthesis, the wave motion is provided by a coupling mechanism between the tilting and the stretching of axial vorticity. When the base vortex flow is strictly one-dimensional, the inertial waves can propagate in the upstream and downstream direction marginally, *i.e.* no amplification is observed. When streamwise inhomogeneities are introduced, an unstable mode can be generated as a superimposition of waves propagating upstream. This mechanism has been observed in the axisymmetric DNS for an incipient vortex breakdown (cfr. §4.2). The introduction of physical boundary conditions breaks the one-dimensionality of the flow. By diffusion, negative axial circulation gradient is created, and plays the role of a continuous localised forcing. At this point, the flow evolves into breakdown if, for any mechanism, the wave motion in the upstream direction is inhibited. This may be caused by two different reasons: the existence of inlet boundary conditions where the velocity is kept constant, or a streamwise dynamical evolution of the base flow which switches from a supercritical condition (when any perturbation is convected downstream by the axial velocity support) to a subcritical one (when the base axial

support is slower than the marginal waves).

- In the axisymmetric framework, several parametric studies have been conducted and special emphasis has been given to illustrate the dependence on the Reynolds number. More precisely, we have tried to explain the hysteresis loop found at high Reynolds numbers in terms of the vortex bubble motion. Our results (cfr. §4.4) support the idea that multiple steady solutions exist when the vortex bubble is so strong as to be able to migrate downstream when the level of swirl is sequentially reduced under the critical point S_1 . In this case, solutions on branch (II) of the bifurcation diagram represent standing waves localised at different axial positions. The critical point S_2 *always* represents a small wave. It will be located in the proximity of the outlet boundary if the Reynolds number is high enough, while its axial position moves away from it as the dissipative effect of viscosity increases. The minimum Reynolds number such that the vortex bubble is unable to move downstream represents the limit point when the bifurcation diagram loses branch (II) and multiple steady solutions disappear.
- In the three-dimensional DNS, the breakdown regime has been shown to be characterised by the onset of self-sustained global modes with low azimuthal wavenumbers $m = 1, 2$. In most of the cases, computations suggest a causal relation between vortex breakdown and helical instabilities, *i.e.* the loss of stability appears to be a consequence of the structural change generated by vortex breakdown itself. After the vortex bubble has formed, the flow field evolves into a limit cycle represented by the saturated state.

Solving the Navier-Stokes equations linearised (LTS) around one-dimensional velocity profiles extracted from converged axisymmetric solutions, we have examined possible correlations between the response obtained by the global nonlinear DNS and the local stability characteristics of the base flow. The local analysis of swirling flows (cfr. §3.1) indicates the destabilisation of higher azimuthal modes $|m| \geq 2$ as a typical effect of the swirl. Now, examining the response to controlled perturbations (cfr. §5.1.4), we have actually found that the spatial amplification produced by an axisymmetric swirling flow in breakdown configuration on higher helical modes $m \geq 3$ is quite well predicted by the local analysis. However, due to their convective nature, these higher modes are unable to trigger a global mode in the spatial DNS because in the absence of a continuous forcing they leave the computational domain. Conversely,

the bending mode $m = 1$, although “less unstable” in a local analysis, gives rise to self-sustained oscillations completely independent on the forcing applied. This global mode is initiated following the scenario predicted by the theory of Pier and Huerre [85], *i.e.* it is determined by an extended region of local absolute instability whose upstream border represents the wave-maker. This station acts as a front imposing the local frequency to the global response (cfr. §5.2.2) and delimiting (at least initially) the region where unsteadiness develops. For the $Re=200$, $S = 0.95$ case, the wave-maker has been identified behind the vortex bubble, which on the other side does not partake in the frequency selection revealed in the nonlinear DNS. The reason appears to be related to a local stabilisation caused by the inward motion in the lee of the bubble.

The discussion is more complicated for mode $m = 2$. The local analysis highlights that *only* localised regions of absolute instability exist, and they are located within the recirculating regions (cfr. §5.2.2 and §5.3.3). It should be noted that currently available weakly non-parallel formulations do not provide theoretical indications for such a non-parallel object. An important result, obtained however in the parallel framework, is that the absolute instability region can be too small to be active [17]. Our study suggests that the vortex bubble, limited, strongly non-parallel, region of absolute instability, does not play a completely passive role: wave packets are irregularly sent out beating at a specific internal frequency. A second kind of global mode can then be observed at higher values of the control parameter (the swirl or the Reynolds numbers) (cfr. §5.3). In fact, the wave packets are subjected to a spatial amplification in the wake leading to a saturated state. The local analysis (cfr. §5.3.3) confirms that the instability developing in the wake is purely convective, demonstrating a clear, substantial difference from the predictions of Pier and Huerre.

Future work

During our investigation, we have continually made reference to a collection of results produced by theoretical studies on the forced Ginzburg-Landau (GU) equation, the simplest system exhibiting absolute instability. In the last decade, it has been common practice to apply these results to different physical situations. In most of the circumstances, the generality of these concepts has been validated regardless of the physical context in which they were analysed.

The second kind of global mode revealed in our computations ($Re=800$, $S = 0.95$, $m = 2$) may be interpreted as a counter-example. It is important to notice, however, that it does not represent the first case in which the indications given by the GU equation are not fulfilled (Davies and Carpenter [20] have shown some discrepancies for the rotating-disc boundary layer, although the nature of their results is very different from what is discussed here). We are aware that spurious numerical effects, feedback instability and, more generally, an improper simulation of conditions at infinity represent possible sources of error leading to equivocal conclusions in DNS. This eventuality is here moderated by the observation that careful inspections of other numerical studies on vortex breakdown [88] seem to identify similar dynamics.

The question which should now be addressed is to understand which element renders the transitional behaviour of a swirling flow in the breakdown regime not fully describable by the Ginzburg-Landau model. Guided by this objective, some considerations offer the possibility of interesting future work.

In our discussion, we have implicitly assumed that the *linear* absolute stability represents a sufficient condition for the *nonlinear* absolute stability. Under this working hypothesis, we have assumed valid a result which has been numerically confirmed by Delbende and Chomaz [22] for a family of two-dimensional wakes. If this condition is not satisfied for swirling flows, the existence of the second kind of global mode might be explained in terms of local absolute instability with respect to nonlinear perturbations. There are good reasons

to believe that this is not the case: first, the structure itself of this global mode demonstrates features of convective instability also in the nonlinear DNS (cfr. §5.3.3); in addition, how could be then explained the difference with the behaviour revealed by the first kind of global mode?

In order to remove any doubt, we believe it may be worth extending the nonlinear wave packet analysis of Delbende and Chomaz to the current swirling flow. Alternatively, one may conduct direct numerical simulations of the complete linearised Navier-Stokes equations around a base flow given by an axisymmetric vortex breakdown state. The latter approach is particularly recommended, as it would also provide a complete set of information about the role played by nonlinearity. It should tell us whether the frequency selection is affected and would clarify the presence and nature of convective wave packets.

The irregular self-sustained structures giving rise to the second kind of global mode are seen to be initiated in the vortex bubble. This region is strongly non-parallel, whereas the Ginzburg-Landau equation provides indications only for slowly developing flow. Despite this simple evidence, we cannot be sure that our results are a manifestation of a pure non-parallel effect. In fact, there exist other physical situations which are similar to the context studied here. Flows over cylindrical bluff bodies are a typical class of flow characterised by large regions of recirculating flow and strong non-parallelism, but instability mechanisms of this kind are not reported in the literature. The application of the same filtering technique adopted in this work, to three-dimensional wakes (for example over a sphere) may provide interesting answers. If the same elements are captured, we gain confidence that they actually result from a complicated non-parallel effect whose analysis has to be sent back to theoretical studies. Conversely, the complete absence of these dynamics would suggest a more intimate relation to the physical context in which they have emerged.

In this latter case, the starting point should be the scenario arising from the $Re=200$ $S = 1.1$ case (cfr. §3.1.3) regarding the transient growth characterising the evolution of mode $m = 2$. This is self-sustained, of short duration and with a convective long-term character. The transient growth is reminiscent of a typical non-normal effect, occurring when the linear operators are actually stable but support solutions exhibiting large transient energy growth. Our local analysis does not show any sign of algebraic growth, and there is no reason to believe that this effect might be invisible to LTS, since no assumption is undertaken regarding the orthogonality of the eigenmodes expansion. However, a secure guarantee on this argument can be provided only comparing the LTS results with those

obtained by a matrix formulation of the stability analysis.

We believe that the non-normal effect retrieved in the DNS has more likely a global origin, in the sense that it might be caused simply by a too limited extension of local absolute instability. On this point, the analogy with three-dimensional wakes over bluff bodies ceases to exist, because the stabilisation encountered behind the vortex bubble is an inertial effect associated with the swirl. On the other hand, the theoretical predictions based on the GU model would be closer to this condition, since the appearance of local absolute instability is only a necessary condition for the onset of a global mode. In this direction, further numerical studies should be conducted in order to determine a more precise correlation between the base morphology of an axisymmetric breakdown state (so much dependent on parameters like the Reynolds and the swirl) and the details of the convective wave packet produced.

Bibliography

- [1] Adams B., Jones M., Hourigan K. and Thompson M. 1999. Hysteresis in the open pipe flow with vortex breakdown. *CSIRO Conference*, Melbourne, Australia.
- [2] Amirante D., Luo K.H. 2005. A numerical investigation on vortex breakdown in swirling jets. *IASME Transactions.*, Vol. 7, pp. 1221-1228.
- [3] Arendt S., Fritts D.C. and Andressen O. 1997. The initial value problem for Kelvin waves. *J. Fluid Mech.*, Vol 344, pp. 181-212.
- [4] Batchelor G.K. 1967. *An introduction to fluid dynamics.*, Cambridge University Press.
- [5] Batchelor G.K., Gill A.E. 1962. Analysis of the stability of axisymmetric jets. *J. Fluid Mech.*, Vol. 14, pp. 529-551.
- [6] Benjamin B. 1962. Theory of the vortex breakdown phenomenon. *J. Fluid Mech.*, Vol. 14, pp. 593-629.
- [7] Beran P.S., Culik F.E.C. 1992. The role of nonuniqueness in the development of vortex breakdown in tubes. *J. Fluid Mech.*, Vol. 242, pp. 491-527.
- [8] Bers A. 1975. Linear waves and instabilities. *Physique des Plasmas*, ed. C De Witt, J. Peyraud, pp. 117-215. New York: Gordon & Breach.
- [9] Billant P., Chomaz J.M. and Huerre P. 1998. Experimental study of vortex breakdown in swirling jets. *J. Fluid Mech.*, Vol. 376, pp. 183-219.
- [10] Boersma B.J., Lele S.K. 1999. Large eddy simulation of compressible turbulent jets. *Center for Turbulence Annual Research Briefs*, Stanford Univ..
- [11] Broadhurst M. 2006. Vortex Stability and Breakdown: Direct Numerical Simulation and Stability Analysis using BiGlobal and Parabolised Formulations. *PhD thesis, Aero. Dept.*, Imperial College London.

- [12] Brown G.L., Lopez J.M. 1990. Axisymmetric vortex breakdown. Part 2. Physical mechanisms. *J. Fluid Mech.*, Vol. 221, pp. 553-576.
- [13] Carnevale G.F., Kloosterziel R.C. 1994. Emergence and evolution of triangular vortices. *J. Fluid Mech.*, Vol. 259, pp. 305-331.
- [14] Carpenter M.H., Gottlieb D. and Abarbanel S. 1993. The stability of numerical boundary treatments for compact high-order finite-difference schemes. *J. Comput. Phys.*, Vol. 108, pp. 272-295.
- [15] Chen P. 2000. Numerical simulations of swirling flows. *PhD thesis, Dept. Aerosp. and Mech. Engin.*, Univ. South. California.
- [16] Chomaz J.M. 2005. Global instabilities in spatially developing flows: non-normality and nonlinearity. *Annu. Rev. Fluid Mech.*, Vol. 37, pp. 357-392.
- [17] Chomaz J.M., Huerre P. and Redekopp L. 1991. A frequency selection criterion in spatially developing flows. *Stud. Appl. Math.*, Vol. 84, pp. 119-144.
- [18] Conte E. 1996. *Lezioni di teoria dei segnali*, ed. Liguori, Napoli.
- [19] Darmofal D. 1993. The role of vorticity dynamics in vortex breakdown. *AIAA Pap.*, Vol. 93, pp. 3036-3049.
- [20] Davies C., Carpenter P.W. 2003. Global behaviour corresponding to the absolute instability of the rotating-disc boundary layer. *J. Fluid Mech.*, Vol. 486, pp. 287-329.
- [21] Delbende I., Chomaz J.M. and Huerre P. 1998. Absolute/convective instabilities in the Batchelor vortex: a numerical study of the linear impulse response. *J. Fluid Mech.*, Vol. 355, pp. 229-254.
- [22] Delbende I., Chomaz J.M. 1998. Nonlinear convective/absolute instabilities in parallel two-dimensional wakes. *Phys. Fluids*, Vol. 10 no.11, pp. 2724-2736.
- [23] Delery J. 1994. Aspects of vortex breakdown, *Prog. Aerospace Sci.*, Vol. 30, pp. 1-30.
- [24] Drazin P.G. 2002. *Introduction to hydrodynamic stability*, Cambridge University Press, 2002.
- [25] Emanuel K.E. 1984. A note on the stability of columnar vortices. *J. Fluid Mech.*, Vol. 145, pp. 235-238.

- [26] Escudier M. 1998. Vortex breakdown: observation and explanations. *Prog. Aerospace Sci.*, Vol. 25, pp. 189-229.
- [27] Faler J.H., Leibovich S. 1977. Disrupted states of vortex flow and vortex breakdown. *Phys. Fluids*, Vol. 20, pp. 1385-1400.
- [28] Freund J.B. 1999. Acoustic sources in a turbulent jet: a direct numerical simulation study. *AIAA Pap.*, Vol. 99, pp. 1858-1967.
- [29] Gallaire F., Chomaz J.M. 2003. Mode selection in swirling jet experiments: a linear stability analysis. *J. Fluid Mech.*, Vol. 494, pp. 223-253.
- [30] Gallaire F., Chomaz J.M. 2003. Instability mechanisms in swirling flows. *Phys. Fluids*, Vol. 15 no.9, pp. 2622-2638.
- [31] Gallaire F., Chomaz J.M. 2004. The role of boundary conditions in a simple model of incipient vortex breakdown. *Phys. Fluids*, Vol. 16 no.2, pp. 274-286.
- [32] Gallaire F., Rott S. and Chomaz J.M. 2004. Experimental study of a free and forced swirling jet. *Phys. Fluids*, Vol. 16 no.8, pp. 2907-2917.
- [33] Gallaire F., Ruith M., Meiburg E., Chomaz J.M and Huerre P. 2006. Spiral vortex breakdown as a global mode. *J. Fluid Mech.*, Vol. 549, pp. 71-80.
- [34] Garg A., Leibovich S. 1979. Spectral characteristics of vortex breakdown flowfields. *Phys. Fluids*, Vol. 22, pp. 2053-2064.
- [35] Grabowski W.J., Berger S.A. 1976. Solutions of the Navier-Stokes equations for vortex breakdown. *J. Fluid Mech.*, Vol. 75, pp. 525-544.
- [36] Griffin M.D., Jones E. and Anderson J.D. 1979. A computational fluid dynamic technique valid at the centerline for non-axisymmetric problems in cylindrical coordinates. *J. Comp. Phys.*, Vol. 30, pp. 352-365.
- [37] Jameson A. 1991. Time dependent calculations using multigrid, with application to unsteady flows past airfoils and wings. *AIAA Pap.*, Vol. 91, pp. 1596-1608.
- [38] Jiang X., Luo K.H. 2000. Spatial direct numerical simulation of the large vortical structures in forced plumes. *Flow, Turbulence Combust.*, Vol. 64, pp. 43-69.

- [39] Hall M. 1972. Vortex breakdown. *Annu. Rev. Fluid Mech.*, Vol. 4, 195-218.
- [40] Harvey J.K. 1962. Some observations of the vortex breakdown phenomenon. *J. Fluid Mech.*, Vol. 14, pp. 585-592.
- [41] Herrada M.A., Perez-Saborid M. and Barrero A. 2003. Vortex breakdown in compressible flows in pipes. *Phys. Fluids*, Vol.15 no.8, pp. 2208-2218.
- [42] Herrada M.A., Fernandez-Feria R., 2006. On the development of three-dimensional vortex breakdown in cylindrical regions. *Phys. Fluids*, Vol. 18 no.8, pp. 1-15.
- [43] Hirsch C. 1990. *Numerical computation of internal and external flows*. John Wiley and sons.
- [44] Howard L., Gupta A. 1962. On the hydrodynamic and hydromagnetic stability of swirling flows. *J. Fluid Mech.*, Vol. 14, pp. 463-476.
- [45] Huerre P., Monkewitz P. 1990. Local and global instabilities in spatially developing flows. *Ann. Rev. Fluid Mech.*, Vol. 22, pp. 473-537.
- [46] Huerre P. 2000, Open shear flow instabilities. In *Perspective in Fluid Dynamics*, ed. G.K. Batchelor, H.K. Moffat and M.G. Worster, Cambridge University Press, pp. 159-229.
- [47] Jumper E.J., Nelson R.C and Cheung K. 1993. A simple criterion for vortex breakdown. *AIAA J.*, Vol.32, pp. 763-767.
- [48] Khorrami M.R. 1991. On the viscous modes of instability of a trailing line vortex. *J. Fluid Mech.*, Vol. 225, pp. 197-212.
- [49] Khorrami M.R. 1995. Stability of a compressible axisymmetric swirling jet. *Phys. fluids*, Vol. 33 no.4, pp.650-657.
- [50] Kim J.W., Lee D.J. 1996. Optimized compact finite difference schemes with maximum resolution. *AIAA J.*, Vol. 34, pp. 887-893.
- [51] Koch W. 1985. Local stability characteristics and frequency determination on self-excited wake flows. *J. Sound Vibr.*, Vol. 99, pp. 53-83.
- [52] Kollmann W., Ooi A.S.H., Chong M.S. and Soria J. 2001. Direct numerical simulations of vortex breakdown in swirling jets. *J. Turbulence*, Vol. 2, pp. 5-21.

- [53] Kopecky R.M., Torrance K.E. 1973. Vortex breakdown in an axisymmetric flow. *Computers and Fluids*, Vol. 1, pp. 289-302.
- [54] Krause E., Shi X.G. and Hartitch P.M. 1983. Computation of leading edge vortices. *AIAA 6th Computational Fluid Dynamics Conference*, Washington, USA.
- [55] Kribus A., Leibovich S. 1994. Instability of strongly nonlinear waves in vortex flows. *J. Fluid Mech.*, Vol. 269, pp. 247-264.
- [56] Le Dizes S., Lacaze L. 2005. An asymptotic description of vortex Kelvin modes. *J. Fluid Mech.*, Vol. 542, pp. 69-96.
- [57] Leibovich S. 1970. Weakly nonlinear waves in rotating fluids. *J. Fluid Mech.*, Vol. 42, pp. 803-822.
- [58] Leibovich S., Randall J.D. 1973. Amplification and decay of long nonlinear waves. *J. Fluid Mech.*, Vol. 53, pp. 481-493.
- [59] Leibovich S. 1978. The structure of vortex breakdown. *Annu. Rev. Fluid Mech.*, Vol. 10, pp. 221-284.
- [60] Leibovich S. 1983. Vortex stability and breakdown: survey and extension. *AIAA J.*, Vol. 22 no.9, pp. 1192-1205.
- [61] Leibovich S., Stewartson K. 1983. A sufficient condition for the instability of columnar vortices. *J. Fluid Mech.*, Vol. 126, pp. 335-356.
- [62] Lele S.K. 1992. Compact finite differences schemes with spectral-like resolution. *J. Comput. Phys.*, Vol.103, pp. 16-42.
- [63] Lessen M., Singh P.J. and Paillet F. 1974. The stability of a trailing line vortex. Part I. Inviscid theory. *J. Fluid Mech.*, Vol. 63, pp. 753-763.
- [64] Lewis H.R., Bellan P.M. 1990. Physical constraints on the coefficients of Fourier expansions in cylindrical coordinates. *J. Math. Phys.*, Vol. 31, pp.2592-2596.
- [65] Liang H., Maxworthy T. 2005. An experimental investigation of swirling jets. *J. Fluid Mech.*, Vol. 525, pp. 115-159.
- [66] Lighthill J. 1996. *Waves in fluids*, Cambridge University Press.

- [67] Loseleux T., Chomaz J.M. and Huerre P. 1997. The effect of swirl on jets and wakes: linear stability of the Rankine vortex with axial flow. *Phys. Fluids*, Vol. 10 no.5, pp. 1120-1134.
- [68] Loiseleux T., Delbende I. and Huerre P. 2000. Absolute and convective instabilities of a swirling jet/wake shear layer. *Phys. Fluids*, Vol. 12, pp. 375-380.
- [69] Lopez J.M. 1994. On the bifurcation structure of axisymmetric vortex breakdown in a constricted pipe. *Phys. Fluids*, Vol. 6 no.11, pp. 3683-3693.
- [70] Ludweig H. 1960. Stabilität der Stromung in einem zylindrischen Ringraum. *Z. Flugwiss*, Vol. 9, pp. 135-140.
- [71] Luo K.H., Sandham N.D. 1997. Instability of vortical and acoustic modes in supersonic round jets. *Phys. Fluids*, Vol. 9 no.4, pp. 1003-10013.
- [72] Mahesh K. 1996. A model for the onset of breakdown in an axisymmetric compressible vortex. *Phys. Fluids*, Vol. 8 no.12, pp. 3338-3345.
- [73] Maxworthy T., Hopfinger E.J. and Redekopp L.G. 1985. Wave motions on vortex cores. *J. Fluid Mech.*, Vol. 151, pp. 141-168.
- [74] Mayer E.W., Powell K.G. 1992. Viscous and inviscid instabilities of a trailing vortex. *J. Fluid Mech.*, Vol. 245, pp. 91-114.
- [75] Melander M.V, Hussain F. 1993. Polarized vorticity dynamics on a vortex column. *Phys. Fluids*, Vol. 5 no.8, pp. 1992-2003.
- [76] Melson N.D., Sanetrik M.D 1995. Multigrid acceleration of time accurate Navier-Stokes calculations. *7th Cooper Mountain Conferences on Multigrid Methods*.
- [77] Michalke A. 1984. Survey on jet instability theory. *Prog. Aerospace Sci.*, Vol. 21, pp. 159-199.
- [78] Mohseni K., Colonius T. 2000. Numerical treatment of polar singularities. *J. Comput. Phys.*, Vol. 157, pp. 787-795.
- [79] Monkewitz P., Sohn K., 1988. Absolute instability in hot jets. *AIAA J.*, Vol. 26, pp. 911-916.

- [80] Monkewitz P. 1988. A note on vortex shedding from axisymmetric bluff bodies. *J. Fluid Mech.*, Vol. 192, pp. 561-575.
- [81] Muller S.B., Kleiser L. 2006. Large-eddy simulation of vortex breakdown in compressible swirling jets flow. *Conference on Turbulence and Interactions*, Porquerolles, France.
- [82] Olendraru C., Sellier A. 2002. Viscous effects in the absolute instability of the Batchelor vortex. *J. Fluid Mech.*, Vol. 459, pp. 371-396.
- [83] O'Sullivan P.L., Breuer K.S. 1994. Transient growth in circular pipe flow. 1. Linear disturbances. *Phys. Fluids*, Vol. 6 no.11, pp. 3643-3651.
- [84] Pedley T.J. 1968. On the instability of viscous flow in a rapidly rotating pipe. *J. Fluid Mech.*, Vol. 35, pp. 97-115.
- [85] Pier B., Huerre P. 2001. Nonlinear self-sustained structures and fronts in spatially developing wake flows. *J. Fluid Mech.*, Vol. 435, pp. 145-174.
- [86] Poinso T.J., Lele S.K. 1992. Boundary conditions for direct simulations of compressible viscous flows. *J. Comput. Phys.*, Vol.101, pp. 104-129.
- [87] Quadrio M., Luchini P. 2002. Direct numerical simulation of the turbulent flow in a pipe with annular cross-section. *Eur. J. Mech. B*, Vol. 21 pp. 413-427.
- [88] Ruith M.R., Chen P., Meiburg E. and Maxworthy T., 2003. Three-dimensional vortex breakdown in swirling jets and wakes: direct numerical simulations. *J. Fluid Mech.*, Vol.486, pp. 331-378.
- [89] Randall J.D., Leibovich S. 1973. The critical state: a trapped wave model of vortex breakdown. *J. Fluid Mech.*, Vol. 58, pp. 495-515.
- [90] Saffman P.G. 1992. *Vortex dynamics*, Cambridge university Press.
- [91] Sandberg R.D., Fasel H.F. 2006. Numerical investigation of transitional supersonic axisymmetric wakes. *J. Fluid Mech.*, Vol. 563, pp. 1-41.
- [92] Sandham N.D., Reynolds W.C. 1989. A numerical investigation of the compressible mixing layer. *Report No. TF-45*, Stanford Univ..

- [93] Sarpkaya T. 1971. On stationary and travelling vortex breakdowns. *J. Fluid Mech.*, Vol. 45, pp. 545-559.
- [94] Spall R.E., Gatski T.B. and Grosh C.E. 1987. A criterion for vortex breakdown. *Phys. Fluids*, Vol. 30 no.11, pp. 3434-3440.
- [95] Spall R.E., Gatski T.B. and Ash R.E. 1990. The structure and dynamics of bubble-type vortex breakdown. *Proc. R. Soc. Lond.*, Vol. 429, pp. 613-637.
- [96] Squire H.B. 1960. Analysis of the vortex breakdown phenomenon. Part I. *Aero. Dept. Rep. no. 102*, Imperial College London.
- [97] Thompson K.W. 1987. Time dependent boundary conditions for hyperbolic systems. *J. Comput. Phys.*, Vol. 68, pp. 1-24.
- [98] Tromp J.C., Beran P.S. 1995. Temporal evolution of three-dimensional vortex breakdown from steady, axisymmetric solutions. *AIAA J.*, Vol. 34 no. 3, pp.632-634.
- [99] Tromp J.C., Beran P. 1996. The role of nonunique axisymmetric solutions in 3-D vortex breakdown. *Phys. Fluids*, Vol. 9 no.5, 1996.
- [100] Visbal M.R., Gaitonde D.V. 2001. Very high-order spatially implicit schemes for computational acoustics on curvilinear meshes. *J. Comp. Acoustics*, Vol. 9 no.4, pp. 1259-1286.
- [101] Wang S. and Rusak Z. 1997. The dynamics of a swirling flow in a pipe and transition to axisymmetric vortex breakdown. *J. Fluid Mech.*, Vol.340, pp. 177-223.
- [102] Bessel functions. *Wikipedia, the free encyclopedia*, www.en.wikipedia.org.
- [103] Yin X., Sun D., Wei M. and Wu J. 2000. Absolute and convective instability character of slender viscous vortices. *Phys. Fluids*, Vol. 12, pp. 1062-1072.